

# **Searches for Supersymmetry with compressed mass spectra using monojet events with the CMS detector at the LHC**

Robyn Elizabeth Lucas

High Energy Physics

Blackett Laboratory

Imperial College London

A dissertation submitted to Imperial College London  
for the degree of Doctor of Philosophy

## Abstract

A novel search for supersymmetric particles in events with one high transverse momentum jet and large missing transverse energy is performed using an integrated luminosity of  $19.7 \text{ fb}^{-1}$  of pp collision data collected using the CMS detector at the Large Hadron Collider. By using events with an energetic radiated jet, sensitivity to supersymmetric models with compressed mass spectra is gained where the decay products have very low energy. Standard Model background estimates are evaluated with the use of data control samples. No excess over Standard Model expectations is observed, and limits are placed on third generation squark production at the 95% confidence level using supersymmetric simplified models.

The development of a Level 1 trigger algorithm to reconstruct jets in the Phase 1 Upgrade of the CMS detector is presented. Utilising the full granularity of the CMS calorimeter and time-multiplexed-trigger technology, a new algorithm with increased flexibility and resolution is presented. It is possible to measure and subtract the contribution to calorimeter deposits of soft particles originating from multiple pp vertices in an event, on an event-by-event basis, in order to decrease the trigger rates associated with high luminosity future run conditions. This will enable CMS to maintain, or better, its ability to do physics as the LHC ramps up energy and luminosity in the years to come.

## Declaration

I, the author of this thesis, hereby declare the material presented here to be the result of my own work, except where explicit reference is made to the work of others. It has not been submitted for another qualification to this or any other university. All figures labelled “CMS” have been sourced from CMS publications, referenced in the caption, and include those produced by the author. Those figures labelled “CMS Preliminary” have been sourced from a CMS public preliminary document or an unpublished CMS document. Figures labelled “CMS Simulation” are made using CMS simulation only, and those labelled “CMS Unpublished” do not feature in any CMS documents. All figures taken from external sources are referenced appropriately throughout this thesis.

Robyn Lucas

*The copyright of this thesis rests with the author and is made available under a Creative Commons Attribution Non-Commercial No Derivatives licence. Researchers are free to copy, distribute or transmit the thesis on the condition that they attribute it, that they do not use it for commercial purposes and that they do not alter, transform or build upon it. For any reuse or redistribution, researchers must make clear to others the license terms of this work.*

## Acknowledgements

Firstly, I would like to thank my parents and family for their support and encouragement throughout my academic career. Secondly, I thank my supervisors Alex Tapper and Steve Worm for their advice and guidance. I also express huge thanks to the Monojet analysis team; without Phat Srimanobhas my research would not have been possible, and whose patience, help and hard work I am eternally grateful for; Anwar Bhatti, Sarah Malik, Shuichi Kunori and Teruki Kamon, whose discussions and guidance have been invaluable. Thanks also to Michele Pioppi and Andrew Rose for their patience in helping a fresh faced first year who could not code in the work on upgrade jets. My friends and colleagues; Sam Cunliffe, Darren Burton, Andrew Gilbert, Matthew Kenzie and Patrick Owen you provided much needed distractions and laughs, as well as more than a little bit of help over the years. Sam Hall must get my particular thanks for the many occasions where he fixed my code and made me dinner! I cannot express enough thanks to my boyfriend Ed. His unfaltering support, both in Geneva and London, were at times the only thing keeping me going. Sorry I never found the Lucas boson! Finally, I thank the STFC for providing the funding that enabled me to conduct the research presented here, and for the 15 months spent out at CERN.

# Contents

<b>1</b>	<b>Introduction</b>	<b>2</b>
<b>2</b>	<b>Theory and Motivations</b>	<b>5</b>
2.1	The Standard Model of Particle Physics . . . . .	5
2.1.1	Fundamental particles and forces . . . . .	6
2.1.2	Gauge symmetries . . . . .	9
2.1.3	Electroweak unification . . . . .	12
2.1.4	Electroweak symmetry breaking and the higgs mechanism . . . . .	14
2.2	Motivation for Physics Beyond the Standard Model . . . . .	18
2.3	Supersymmetry . . . . .	20
2.3.1	R parity and dark matter . . . . .	22
2.3.2	Unifying the forces . . . . .	23
2.3.3	Breaking supersymmetry and naturalness . . . . .	24
2.3.4	Searching for supersymmetry at colliders . . . . .	25
2.3.5	Supersymmetry with compressed mass spectra . . . . .	29
2.4	Decays of the Top Squark . . . . .	30
<b>3</b>	<b>The LHC and CMS experiment</b>	<b>33</b>
3.1	The Large Hadron Collider (LHC) . . . . .	33
3.1.1	LHC run conditions, past and present . . . . .	35
3.2	The CMS Detector . . . . .	36
3.2.1	The tracking system . . . . .	39
3.2.2	The electromagnetic calorimeter . . . . .	40
3.2.3	The hadronic calorimeter . . . . .	43
3.2.4	The muon system . . . . .	45
3.3	Event Reconstruction . . . . .	47
3.3.1	Jets . . . . .	48
3.3.2	Missing transverse momentumenergy . . . . .	51
3.3.3	Muons . . . . .	52

3.4	The Trigger . . . . .	54
3.4.1	The L1 trigger . . . . .	55
3.4.2	The high level trigger . . . . .	57
<b>4</b>	<b>Jet Algorithms for the L1 Trigger Upgrade</b>	<b>58</b>
4.1	The LHC Upgrade . . . . .	58
4.1.1	Motivations for a new L1 jet algorithm . . . . .	59
4.2	CMS Trigger Upgrade . . . . .	61
4.2.1	Calorimeter trigger upgrade . . . . .	61
4.3	Algorithm for Jet Reconstruction at L1 . . . . .	64
4.3.1	Jet reconstruction . . . . .	65
4.3.2	Jet filtering . . . . .	67
4.3.3	Event-by-event estimation of pile-up . . . . .	68
4.3.4	Calibration to the jet energy scale . . . . .	69
4.4	Upgrade L1 Jet Algorithm Performance . . . . .	71
4.4.1	Angular and energy resolutions . . . . .	71
4.4.2	Trigger efficiencies . . . . .	73
4.4.3	Jet trigger rates . . . . .	75
4.4.4	Other jet variables . . . . .	76
4.5	Conclusion . . . . .	79
<b>5</b>	<b>Searching for SUSY with compressed mass spectra using monojet events</b>	<b>81</b>
5.1	Introduction . . . . .	81
5.2	Data samples . . . . .	83
5.3	Background MC simulation . . . . .	86
5.4	Object reconstruction . . . . .	87
5.4.1	Jets and $p_T^{\text{miss}}$ . . . . .	87
5.4.2	Leptons . . . . .	87
5.5	Event selection . . . . .	90
5.5.1	Event Cleaning . . . . .	90
5.5.2	Search region event selection . . . . .	91
5.6	Background estimation and systematic uncertainties . . . . .	95
5.6.1	Data-driven $Z(\nu\bar{\nu}) + \text{jets}$ background estimation . . . . .	99
5.6.2	Data-driven $W(\ell\nu) + \text{jets}$ background estimation . . . . .	105
5.6.3	QCD Background Estimation . . . . .	110
5.6.4	$t\bar{t}$ background estimation . . . . .	112
5.6.5	Diboson background estimation . . . . .	114

5.6.6	Single top quark and Drell–Yan background estimations	116
5.7	Summary	116
<b>6</b>	<b>Results and Interpretation</b>	<b>118</b>
6.1	Results	118
6.2	Interpretation	120
6.2.1	Simulation of signal events	120
6.3	Signal acceptance	121
6.3.1	Signal acceptance in 2- and 3-parton simulation	123
6.3.2	Systematic Uncertainties on Signal	124
6.4	Exclusion limits	126
6.5	Summary	135
<b>7</b>	<b>Conclusions and Future Outlook</b>	<b>138</b>
7.1	Upgrade L1 Jet Algorithm	138
7.2	Search for Compressed SUperSYmmetry (SUSY) in Monojet Events	139
<b>Bibliography</b>		<b>142</b>
<b>List of Figures</b>		<b>160</b>
<b>List of Tables</b>		<b>170</b>
1	Acronyms	172

*“For Peter”*

---

# Chapter 1

## Introduction

*“Everything starts somewhere, although many physicists disagree.”*

— Terry Pratchett, 1948–2015

The Standard Model (SM) of particle physics, a theory developed during the second half of the 20<sup>th</sup> Century, represents mankind’s best understanding of the universe around us: what we are made of, the interactions in the world around us, how we got here. A multitude of theoretical leaps and experimental discoveries have cemented it as one of the cornerstones of physics. It has withstood unparalleled experimental scrutiny [1] and is incredibly successful at explaining the vast majority of experimental phenomena we observe.

However, the SM fails to explain some fairly crucial aspects of the universe that we observe on both a daily basis and through more in depth inspections. Gravity has no place within the SM; it is not one of the fundamental forces of nature that it describes. The presence of any matter at all in the universe, and lack of any antimatter raises a crucial question: why did everything not annihilate in the instants after the big bang? Cosmological observations tell us that Dark Matter (DM) accounts for 27% of the [observable](#)[visible](#) universe - an additional, non-luminous but gravitating matter must account for the extra gravity seen in observations of gravitational lensing, galaxy rotation curves, and the Cosmic Microwave Background (CMB). Yet, there is no candidate for such a particle in the SM. Questions which are more theoretical in nature persist - why are there four forces, and why do they have such different strengths? And why do we observe three generations of particles? Further, why is the third generation’s top quark,

for example, so much heavier than the other quarks, and why is the neutrino’s mass so small? In fact, why do neutrinos have a mass at all?

The SM, then, is thought to be some low-energy approximation of a more complete picture. One widely considered theory, which goes some way to solving many of the issues with the SM, is SUSY. It introduces a new symmetry of nature between fermions and bosons, postulating a new partner sparticle for every SM particle. In common forms of the theory, in which a sparticle will always decay into another sparticle, the Lightest Supersymmetric Particle (LSP) provides a DM candidate. It can enable the weak, strong and electromagnetic forces to unite, and provide a solution to the problem of quadratic divergences in the Higgs boson’s mass. A detailed description of the theory of the SM, the motivation for new physics, and SUSY, is given in Chapter 2.

The LHC was built to probe our understanding of fundamental physics. Its primary aim, to discover the Higgs boson, the last remaining piece of the SM, was a resounding success with the discovery [of a neutral boson](#) from both the A Toroidal LHC ApparatuS (ATLAS) and Compact Muon Solenoid (CMS) collaborations unveiled to the world on 4<sup>th</sup> July [2012](#)[2014](#)[2, 3], [which, with further observations, looks to be compatible with the SM Higgs boson. As well as Higgs exploitation,](#) attention has now shifted to Beyond the Standard Model (BSM) physics, including the search for SUSY and DM. A description of the LHC apparatus and the CMS detector is given in Chapter 3.

In Chapter 2 we discuss the arguments for a particular type of SUSY where the various sparticles are close in mass to one other: the mass spectra of the models are “compressed”. Sparticle decay products in these scenarios are typically very low energy as most of the mass-energy of the parent sparticle is taken in creating the daughter sparticle, leaving very little phase space for the accompanying SM decay products. Traditional SUSY searches are insensitive to these scenarios because of these soft, SM decay products are obscured by the SM backgrounds, largely in multijet production.

Chapter 5 describes a search dedicated to looking for compressed SUSY, using a novel method of looking for events with a monojet topology; events with a high transverse momentum jet which is balanced by large missing transverse momentum. The idea is to trigger on compressed SUSY events by looking for objects created in association with sparticles; i.e. radiated jets in the initial state, and ignoring the soft sparticle decay products. The search is therefore independent of the visible decay products, and therefore has a reach to sparticle-LSP degeneracy. The event selection is optimised to search for compressed scenarios and backgrounds to the search are estimated using data driven

methods alongside simulation. Chapter 6 shows the results of the search. No excess above the SM expectations is observed, so limits are set on models of compressed SUSY in the third generation.

The author was responsible for the search described in Chapters 5 and 6 as a part of the CMS monojet group. This search has been released as a CMS Physics Analysis Summary, [4]. It has very recently been combined with two other CMS SUSY analyses into a legacy Run I paper [5] on third generation squark production in all-hadronic final states. The author was the main editor of this paper and it has just been acceptedsubmitted to the Journal of High Energy Physics (JHEP).

The LHC was built to be at the frontier of fundamental physics for decades to come. A programme of upgrades is planned well into the 2020's, which will continue to extend the reach of the accelerator and detectors in terms of both energy and integrated luminosity. As well as increasing the energy up to 13 TeV, and eventually the design energy of 14 TeV, the LHC will deliver proton beams at increasingly high instantaneous luminosities, to enable precision measurements of very rare processes such as the properties of the newly discovered boson. The CMS detector must be prepared to cope with the enormous challenges that such increases in the instantaneous luminosity will bring: many overlapping pp vertices in each bunch crossing lead to much higher detector occupancies and many more events per second. The trigger system, used to filter out the events of interest from the vastly more numerous ‘uninteresting’ events, will therefore have to cope with huge increases in rates while maintaining sensitivity to new physics processes. The CMS Level 1 Trigger (L1) system, the first stage of this sieve, is therefore undergoing an upgrade. Chapter 4 details the development of a new jet algorithm for the L1 trigger upgrade that the author conducted during 2012–2013, which as well as being far more flexible than the current algorithm, has event-by-event pile-up (PU) subtraction and shows a reduction in rates for hadronic triggers.

# Chapter 2

## Theory and Motivations

*“Absence of evidence is not evidence of absence.”*

— Carl Sagan, 1934 – 1996

This chapter introduces the SM as a gauge invariant Quantum Field Theory (QFT), and gives a description of the fundamental particles and their interactions. The shortcomings of the SM, outlined in Section 2.2, imply however that it must be an incomplete description of nature. A Supersymmetric extension of the SM can address many of these limitations and is described in Section 2.3. Particular emphasis is placed on the arguments for SUSY with compressed mass spectra in Section 2.3.5, as this is the subject of this thesis.

### 2.1 The Standard Model of Particle Physics

The SM of particle physics provides a fantastically accurate description of the fundamental particles of nature and their interactions via the strong, electromagnetic, and weak forces at the electroweak energy scale. It has proved itself incredibly robust during the first years of LHC running. Many high precision measurements of production cross sections (which can be understood as the number of events produced) are consistent with their loop level SM predictions, see Figure 2.1, which shows many different experimental measurements and theory expectations [agreeing](#) over 6 orders of magnitude. Even very rare processes have been measured to agree with their SM predictions: the decay  $B_s \rightarrow \mu\mu$ , very sensitive to new physics processes, has been observed at the level of three

in every billion decays of the  $B_S$  meson [6]. Such tests of the SM cement its place as one of the major successes of 20<sup>th</sup> century physics.

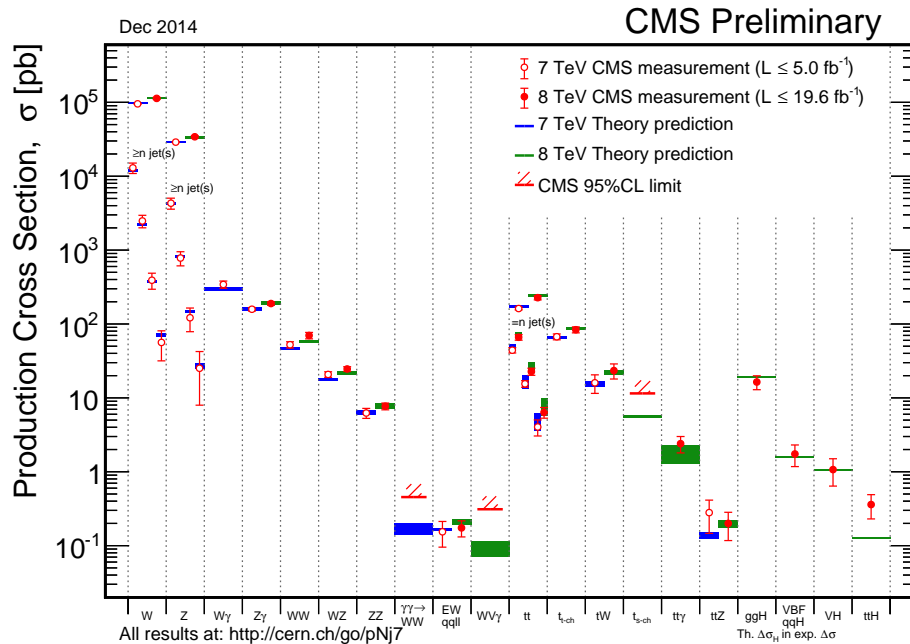


**Figure 2.1:** Combined results from CMS of many SM measurements made at LHC centre-of-mass energies of 7 and 8 TeV, taken from [7]. Theory and experiment agree over a vast range of production cross section values, for many different SM processes.

Developed in the 1960's and 1970's [8–11], the SM is a relativistic QFT in which particles are excitations of fields. It is gauge invariant, guaranteeing its renormalizability, and contains three symmetries:  $SU(3)_C \otimes SU(2)_L \otimes U(1)_Y$ .  $SU(3)$  describes the strong force, felt by coloured particles, and  $SU(2) \otimes U(1)$  describes the unified Electromagnetic and Weak forces, felt by particles with weak isospin and weak hypercharge. The Higgs mechanism [12–17] describes the spontaneous symmetry breaking of the  $SU(2) \otimes U(1)$  gauge symmetry which allows for massive gauge bosons in a gauge invariant way. The discovery of the Higgs boson [2, 3] in July 2012, the mediator of the Higgs field, provided the last piece of the SM.

### 2.1.1 Fundamental particles and forces

All known matter in the universe can be described by the fundamental matter particles, which can be separated into quarks – those that feel the strong force, and leptons – those that do not. Matter particles are all spin- $\frac{1}{2}$  fermions that conform to Fermi statistics

Matter fermions: spin- $\frac{1}{2}$						
Generation	Leptons			Quarks		
	Particle	Mass (MeV)	Charge	Particle	Mass (MeV)	Charge
1	$\nu_e$	$\sim 0$	0	d	2.3	$-\frac{1}{3}$
	e	0.511	-1	u	4.8	$+\frac{2}{3}$
2	$\nu_\mu$	$\sim 0$	0	s	95	$-\frac{1}{3}$
	$\mu$	106	-1	c	1270	$+\frac{2}{3}$
3	$\nu_\tau$	$\sim 0$	0	b	4180	$-\frac{1}{3}$
	$\tau$	1780	-1	t	173200	$+\frac{2}{3}$

**Table 2.1:** Summary of the particles of the SM of particle physics. Fermions, of spin- $\frac{1}{2}$  are shown, split into the three generations of leptons and quarks. Masses are taken from Ref. [1].

and obey the Dirac equation<sup>1</sup>:

$$(i\gamma^\mu \partial_\mu - m)\psi = 0, \quad (2.1)$$

where  $\gamma^\mu$  are the Dirac matrices, which are defined by their anti-commutation relation  $\{\gamma^\mu, \gamma^\nu\} = \gamma^\mu \gamma^\nu + \gamma^\nu \gamma^\mu = 2\eta^{\mu\nu} I_4$ , where  $\eta^{\mu\nu}$  is the Minkowski metric  $(+, -, -, -)$ , and  $I_4$  is the four-dimensional identity matrix;  $\delta_\mu$  is the covariant derivative; and  $m$  is the mass of the particle [18]. Repeated indices are summed over.

A summary of the matter particles of the SM can be found in Table 2.1. A similar table exists for the anti-particles of the leptons and quarks. There are both positive and negative energy solutions of Equation 2.1, so, rather than interpreting the negative solutions as particles travelling backwards in time, , a consequence of Equation 2.1, which has both positive and negative energy solutions. Rather than particles travelling backwards through time, as the negative energy solutions suggest anti-particles are interpreted to have all of the same properties as their partner particles but with opposite charge.

Leptons are fundamental, free particles in nature. Conversely, quarks are fundamental but not free particles; they form hadrons: baryons, which consist of 3 quarks or anti-quarks, and mesons, a bound quark–anti-quark pair. This difference is due to the colour charge that quarks carry: they interact with the strong force. The force carrier of the strong force, the gluon, is both massless and self-interacting, which results in colour

---

<sup>1</sup>The convention  $c = \hbar = 1$  is used throughout and the four vector indices are labelled  $\mu$  and  $\nu$ .

Force carrying gauge bosons: spin-1				
Force	Particle	Symbol	Mass (GeV)	Charge
Electromagnetic	Photon	$\gamma$	0	0
	W boson	$W^+$	80.4	1
Weak	W boson	$W^-$	80.4	-1
	Z boson	Z	91.2	0
Strong	Gluons (8)	$g$	0	0
Higgs Boson: spin-0				
-	Higgs	$H^0$	126	0

**Table 2.2:** Summary of the gauge bosons of the SM. The force carrying bosons of spin-1 are shown, with the Higgs boson to complete the picture. Masses are taken from Ref. [1].

confinement and hadronization. Rather than separate a quark from another quark or gluon into a ‘free’ quark, it is more energetically favourable for a quark–anti-quark pair to pop out of the vacuum via the exchange of a gluon, creating a hadronization process. Both quarks and leptons~~gluons~~ exist in three families or generations, with each subsequent family increasing in mass. Within the SM neutrinos are massless; however neutrino oscillations observed in nature imply a non-zero mass [19]. However, due to the negligible mass as compared to the other SM particles as well as to the energy scales probed, here, and throughout, their mass is neglected.

Matter particles interact via the exchange of spin-1 gauge bosons. The photon ( $\gamma$ ) mediates the electromagnetic interaction and the heavy  $W^\pm$  and Z bosons mediate the weak interaction, through the mixing of the gauge fields when the respective forces are unified. There are 8 coloured~~colourless~~ gluons ( $g$ ) that mediate the strong force. The properties of these bosons, and similarly the properties of the interactions, are a direct result of their gauge symmetry groups, detailed in Section 2.1.2. A summary of the bosons can be found in Table 2.2.

Discoveries of sub-atomic particles throughout the 19<sup>th</sup> and 20<sup>th</sup> Centuries drove the formulation of the SM. The electron was discovered by J.J. Thomson in the Cavendish Laboratory in 1897 [20], and the electron (anti)-neutrino was first proposed by Pauli in 1930 to explain the energy spectrum of beta decay [21], though it was not discovered until 1956 by Cowan and Reines at Los Alamos [22]. The muon was discovered in 1936 by Anderson and Neddermeyer at Caltech in studies of cosmic rays [23], and confirmed a

year later in a cloud chamber experiment [24]. The muon neutrino was then discovered in 1962 by Lederman, Schwartz and Steinberger [25], after being proposed in the early 1940’s. The  $u$ ,  $d$ , and  $s$  quarks were first proposed in 1964 by Gell-Man and Zweig to explain the ‘Eightfold’ hadron structure [26, 27], and the three quarks were observed in deep inelastic scattering experiments at the Stanford Linear Accelerator Center (SLAC) four years later [28, 29]. The proposal of the GIM mechanism [30] in 1970 predicted the completion of the second generation – the charm quark in order to explain the observed suppression of Flavour Changing Neutral Currents (FCNC). The discovery of the  $\text{J}/\Psi$  meson in 1974 [31, 32] confirmed the existence of the charm quark. The third generation was more of a surprise. The  $\tau$  lepton was proposed to explain an excess of events at the  $e^+e^-$  colliding ring at SLAC in the mid 1970’s [33], and so postulating another generation of leptons. It was not until 2000 that the  $\nu_\tau$  was discovered [34], completing the lepton family. CP violation in kaon decay drove the proposal of the third quark generation in 1973 [35]. The bottom quark was first observed in 1977 at Fermilab with the observation of the bottomonium state, known as the  $\Upsilon$  meson [36]. The top quark, after years of dedicated searches at SLAC, Deutsches Elektronen-Synchrotron (DESY) and European Organisation for Nuclear Research (CERN), was finally discovered in 1995 at the Tevatron [37, 38] and it remains the heaviest SM particle today.

The SM was thus built as a theory over several decades; driven by the need to explain experimental observations, and predicting the existence of particles that were then found later after dedicated searches. This is particularly evident in the discoveries of the  $W$  and  $Z$  bosons. The unification of electromagnetism and the weak nuclear force [8–10] around 1968 predicted the existence of both the charged  $W$  bosons and the neutral  $Z$  boson. They were discovered at CERN in 1983 using the UA1 and UA2 experiments on the Super Proton Synchrotron (SPS) collider ring [39–42]: experiments specifically designed to search for traces of the  $W$  and  $Z$ . Due to the non-perturbative nature of the strong force, interactions between quarks and gluons were (and remain) less certain, and theory is driven by experiment. The observation of three-jet events at PETRA [43, 44], DESY, provided direct evidence of gluons in 1979.

### 2.1.2 Gauge symmetries

Noether’s theorem [45] states that **continuous** symmetries lead to conserved quantities in nature. If a physical process is unaffected by location or time, then its Lagrangian is symmetric under space and time translations. As a result, both energy and linear

momentum are conserved quantities. If it is unaffected by spatial orientation, its Lagrangian is rotationally symmetric, leading to the conservation of angular momentum. The symmetries found in a Lagrangian which attempts to describe a system therefore reveal important and useful properties of that system. It is certainly reasonable that we should expect a theory to give the same answer 10 minutes ago as it does now; and in 10 minutes, or 10 years, or 10 millennia – any Lagrangian which is not invariant under time transformations should perhaps be revised<sup>2</sup>. Indeed, the conserved quantity associated with invariance under time transformations, energy, is a cornerstone of physics. Energy is always conserved. Symmetries are therefore very powerful in forming conserved quantities, and vice versa. By demanding that any theory which describes the particle nature of our universe has the appropriate conserved quantities, we are demanding that its Lagrangian formalism is invariant under the various transformations.

The principle of Gauge Invariance drives the formalism of the SM. The SM Lagrangian is invariant under local gauge transformations: transformations which are space-time dependent. A gauge transformation takes the wavefunction describing a system to a different ‘gauge’, and in this gauge the Lagrangian is symmetric compared to the original state – there is a ‘gauge symmetry’. Such gauge symmetries result in symmetry, or ‘gauge’ groups, and it is the generators of these gauge groups which lead to the gauge bosons. The generators manifest themselves as vector, or gauge fields – one for each degree of freedom in the symmetry group. Mathematically, the substitution of

$$\partial_\mu \rightarrow D_\mu = \partial_\mu - igA_\mu \quad (2.2)$$

for the covariant derivative in the Dirac equation, where  $g$  are the coupling constants of the gauge group indicating interaction strength and  $A_\mu$  are the gauge fields which transform as

$$A_\mu \rightarrow A_\mu + \frac{1}{g}\partial_\mu\theta \quad (2.3)$$

ensures gauge invariance under the transformation

$$\psi \rightarrow \psi' = e^{i\theta}\psi \quad (2.4)$$

by construction, where  $\theta$  is any gauge transformation.

---

<sup>2</sup>Unless the Lagrangian is not symmetric under Charge Parity (CP) symmetry: for Charge Parity Time (CPT) must always be invariant.

The formulation of Quantum Electro-Dynamics (QED) gives the simplest demonstration of the use of gauge symmetries. Under a local  $U(1)$  abelian gauge transformation, the wavefunction transforms as

$$\psi(x) \rightarrow \psi'(x) = e^{i\theta(x)}\psi(x) \quad (2.5)$$

where  $\theta(x)$  implies a local rotation of the phase angle of the electron field. Taking the free Lagrangian, which follows from Eq. 2.1,

$$\mathcal{L} = \bar{\psi}(x)(i\gamma^\mu\partial_\mu - m)\psi(x) \quad (2.6)$$

and substituting in for the gauge covariant derivative,

$$\mathcal{L} = \bar{\psi}(x)(i\gamma^\mu D_\mu - m)\psi(x), \quad (2.7)$$

we can demonstrate the gauge invariance. Transforming the wavefunction according to Eq. 2.5, where  $\psi$  and  $\theta$  are functions of  $x$ , and substituting in Eq. 2.3 for the gauge transformation of  $A_\mu$ ,

$$\mathcal{L}' = e^{-i\theta}\bar{\psi}(i\gamma^\mu(\partial_\mu - ig(A_\mu + \frac{1}{g}\partial_\mu(\theta)) - m)e^{i\theta}\psi \quad (2.8)$$

$$\mathcal{L}' = \bar{\psi}(i\gamma^\mu(\partial_\mu - igA_\mu) - me^{i\theta})\psi + e^{-i\theta}\bar{\psi}i\gamma^\mu(i e^{i\theta}\psi\partial_\mu(\theta) - i\partial_\mu(\theta)e^{i\theta}\psi) \quad (2.9)$$

$$\mathcal{L}' = \mathcal{L} \quad (2.10)$$

as the last term equates to zero. QED is therefore gauge invariant under a local gauge transformation, which guarantees its renormalizability as a theory.  $A_\mu$  is interpreted as the massless photon field which has coupling  $g = e$ . In order to regard  $A_\mu$  as a physical field a kinetic term must be added to the Lagrangian of Eq. 2.7. To maintain gauge invariance, the kinetic term is of the form  $F_{\mu\nu} = \partial_\mu A_\nu - \partial_\nu A_\mu$ . The full QED Lagrangian can thus be written as

$$\mathcal{L}_{QED} = \mathcal{L}_{int} + \mathcal{L}_{kin} \quad (2.11)$$

$$= \bar{\psi}i\gamma^\mu D_\mu\psi - \frac{1}{4}F_{\mu\nu}F^{\nu\mu} - m\bar{\psi}\psi \quad (2.12)$$

The lack of any photon mass term, of the form  $m^2 A_\mu A^\mu$  (which would not be gauge invariant), implies the photon is massless. Thus, by requiring gauge invariance and using the simple free particle Dirac Equation, which is invariant under  $U(1)_{EM}$  symmetry, we

arrive at the QED Lagrangian that gives a massless photon field,  $A_\mu$ , with interaction strength  $e$ .

### 2.1.3 Electroweak unification

The requirement of local gauge invariance in the weak sector, in conjunction with QED, can be used to unify the electromagnetic and weak forces. The Electroweak (EWK) sector is defined by the symmetry groups  $SU(2)_L \otimes U(1)_Y$ .

The special unitary group  $SU(2)_L$ , of order 2, is generated by the  $2 \times 2$  matrices  $T_i = \tau_i/2$ , where  $\tau_i$  are the three Pauli spin matrices<sup>3</sup>. The three generators are manifested in the three gauge fields  $W_\mu^1$ ,  $W_\mu^2$ , and  $W_\mu^3$ . They act only on the left handed chiral component of the field  $\psi_L$ , where  $\psi = \psi_L + \psi_R$  and  $\psi_{L/R} = (1 \mp \gamma_5)\psi$ ; where  $\gamma^5 = i\gamma^0\gamma^1\gamma^2\gamma^3$ . This reflects the experimental observation of parity violation in weak interactions:  $W_\mu^i$  couple only to the left handed component of the fermion wavefunctions, hence the  $L$  subscript. The weak isospin  $t_i$  are the corresponding conserved quantities. The unitary group  $U(1)_Y$  brings an additional generator, hypercharge  $Y$ , which is manifested in the gauge field  $B_\mu$ . Here, the conserved quantity is hypercharge  $y$ , where electric charge  $Q = t_3 + y/2$ . Incidentally,  $U(1)_Y$  is a different representation of the  $U(1)_{EM}$  gauge group used in Section 2.1.2, which instead has generator  $Q$ , and gauge field  $A_\mu$ , where electric charge is the conserved quantity.

Due to the parity violating nature of the electroweak representation, the left and right handed components of the fermion wavefunction are written separately as  $\chi_L$ , a doublet, and  $\psi_R$ , a singlet. Their  $SU(2)_L \otimes U(1)_Y$  gauge transformations can then be written as:

$$\chi_L \rightarrow \chi'_L = e^{i\theta(x) \cdot T + i\theta(x)Y} \chi_L \quad (2.13)$$

$$\psi_R \rightarrow \psi'_R = e^{i\theta(x)Y} \psi_R. \quad (2.14)$$

Gauge invariance is maintained by modifying the covariant derivative accordingly:

$$\partial_\mu \rightarrow D_\mu = \partial_\mu - ig_1 \frac{Y}{2} B_\mu - ig_2 \frac{\tau_i}{2} W_\mu^i. \quad (2.15)$$

---

<sup>3</sup>The  $SU(2)$  generators are labelled  $i$ ,  $j$ , and  $k$

To recover the familiar physical bosons of Table 2.2, the  $SU(2)_L$  and  $U(1)_Y$  symmetries are combined via a rotation of the separate gauge bosons:

$$W_\mu^\pm = \frac{1}{\sqrt{2}}(W_\mu^1 \mp W_\mu^2) \quad (2.16)$$

$$Z_\mu = \cos \theta_W W_\mu^3 - \sin \theta_W B_\mu \quad (2.17)$$

$$A_\mu = \sin \theta_W W_\mu^3 + \cos \theta_W B_\mu, \quad (2.18)$$

where  $A_\mu$  is the photon field and the Weinberg angle,  $\theta_W$ , is determined by the ratio of the electromagnetic coupling constant ( $g_1$ ) and the weak coupling constant ( $g_2$ ):

$$\frac{g_1}{g_2} = \frac{\sin \theta_W}{\cos \theta_W}. \quad (2.19)$$

The fermion wavefunctions are then written in terms of left-handed states (the electroweak doublet), and right-handed states (the electroweak singlet). For the leptons, these are:

$$\chi_L = \begin{pmatrix} \nu_e \\ e \end{pmatrix}_L, \begin{pmatrix} \nu_\mu \\ \mu \end{pmatrix}_L, \begin{pmatrix} \nu_\tau \\ \tau \end{pmatrix}_L = L \quad (2.20)$$

$$\psi_R = e_R, \mu_R, \tau_R = e_R, \quad (2.21)$$

where there is no right-handed neutrino, using the notation where  $L$  and  $e_R$  are implicitly summed over the three generations of left-handed lepton doublets and right-handed electron-like right-handed singlets. For the quarks,

$$\chi_L = \begin{pmatrix} u \\ d \end{pmatrix}_L, \begin{pmatrix} c \\ s \end{pmatrix}_L, \begin{pmatrix} t \\ b \end{pmatrix}_L = Q_L \quad (2.22)$$

$$\psi_R = u_R, d_R, c_R, s_R, t_R, b_R = u_R, d_R \quad (2.23)$$

where, similarly,  $Q_L$  is summed over the three generations, and  $u_R$  and  $d_R$  are summed over the three generations of up-type and down-type quarks. This gives five types of fermion wavefunction. We can then write  $\psi$ , the total fermion wavefunction, as  $\psi^i$ , for  $i \in 1 - 5 = e_R, L, u_R, d_R, Q_L$ , and the sum over three generations is implicit.

Compressing the fermion wavefunction as such allows a concise definition of the fermion interaction Lagrangian:

$$\mathcal{L}_{int} = \bar{\psi} i\gamma^\mu D_\mu \psi \quad (2.24)$$

where  $D_\mu$  is defined in Eq. 2.15. In the same way as for QED, to describe a physical system and allow the propagation of the gauge fields, a kinetic term of the form  $\frac{1}{4}F_{\mu\nu}F^{\mu\nu}$  is required. The term for the  $B_\mu$  gauge field follows from Eq. 2.12, and a similar expression for  $W_\mu^i$  is necessary, which is given by the field strength tensor for the  $SU(2)$  group:

$$B_{\mu\nu} = \partial_\mu B_\nu - \partial_\nu B_\mu \quad (2.25)$$

$$W_{\mu\nu} = \partial_\mu W_\nu^i - \partial_\nu W_\mu^i - g_2 \epsilon^{ijk} W_\mu^j W_\nu^k \quad (2.26)$$

The kinetic term of the Lagrangian can thus be defined,

$$\mathcal{L}_{kin} = -\frac{1}{4}F_{\mu\nu}F^{\mu\nu} = -\frac{1}{4}(B_{\mu\nu}B^{\mu\nu} + W_{\mu\nu}W^{\mu\nu}), \quad (2.27)$$

and the full  $SU(2)_L \otimes U(1)_Y$  Lagrangian is simply written as

$$\mathcal{L}_{EWK} = \mathcal{L}_{int} + \mathcal{L}_{kin}. \quad (2.28)$$

Notice that here, as for QED, there are no boson mass terms of the form  $m^2 X_\mu X^\mu$ . While this is sensible for the photon field, as the photon is known to be massless, the W and Z bosons are heavy. Similarly, mass terms such as  $m\bar{\psi}\psi$  for the fermions are absent: this, too, is at odds with nature. Adding such mass terms to the Lagrangian would break the gauge symmetry. Masses are instead generated using the Higgs mechanism. By introducing an extra scalar field (with an associated massive scalar boson), spontaneous symmetry breaking is induced in order to give mass to the electroweak bosons, and SM fermions, in a gauge invariant way.

### 2.1.4 Electroweak symmetry breaking and the higgs mechanism

The previous discussion tells us that if we are to believe  $\mathcal{L}_{EWK}$  to be an accurate description of the electroweak force, both the bosons and fermions must be massless: something which observation tells us is clearly not true. Mass terms cannot be introduced

to the Lagrangian as they break gauge invariance; the masses of what we know to be the heavy vector bosons  $W^\pm$  and  $Z^0$  (as well as the fermions) are instead generated by the Higgs mechanism. The  $SU(2)$  symmetry is broken spontaneously, while preserving the invariance of the Lagrangian itself and the renormalizability of the theory.

To start with, we introduce a scalar  $SU(2)$  field  $\phi$ :

$$\Phi = \begin{pmatrix} \phi_1 \\ \phi_2 \end{pmatrix}, \quad (2.29)$$

where  $\phi_i$  are complex fields:  $\phi_i = \text{Re}(\phi_i) + i\text{Im}(\phi_i)$ ; in total then, there are four real scalar fields. The additional term in the Lagrangian takes the form

$$\mathcal{L}_H = (D_\mu \Phi)^\dagger (D^\mu \Phi) - V(\Phi), \quad (2.30)$$

and in order to break the  $SU(2)$  symmetry spontaneously, the potential term  $V(\Phi)$  must take a very specific form:

$$V(\Phi) = -\mu^2 \Phi^\dagger \Phi + \lambda (\Phi^\dagger \Phi)^2 \quad (2.31)$$

where  $\mu^2 < 0$  and  $\lambda > 0$ . Compared to the Lagrangian for a complex scalar, the  $\mu$  term has the wrong sign: it is *not* the mass. Instead, the potential has a ‘Mexican hat’ shape, see Figure 2.2, and gives a non-zero expectation value as it forms a circle in phase space. Any point on this circle gives the same solution, and the vacuum state, at which point the potential gives the Vacuum Expectation Value (VeV), can be in any direction. This choice of direction, to determine where the field acquires a non-zero VeV, causes the symmetry to become spontaneously broken. The field no longer looks the same in all directions of the  $SU(2)$  phase space;  $SU(2)$  is no longer invariant.

The convention is to choose the VeV as

$$\langle 0 | \Phi | 0 \rangle = \begin{pmatrix} 0 \\ v/\sqrt{2} \end{pmatrix} \text{ where } v = \sqrt{\frac{-\mu^2}{\lambda}} \quad (2.32)$$

as the minimum of the Higgs potential, given by  $\Phi^\dagger \Phi = \frac{1}{2}(-\mu)^2/\lambda$ , which is chosen to be consistent with the ground state of the vacuum. Fluctuations from this zero point are

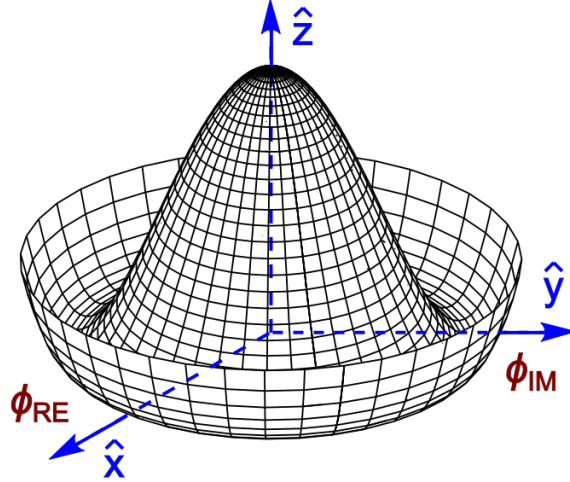


**Figure 2.2:** Higgs ‘Mexican Hat’ potential

then parametrized in terms of the four real scalar fields  $\theta_1, \theta_2, \theta_3$ , and  $h(x)$ .

$$\Phi(x) = \begin{pmatrix} \theta_2 + i\theta_1 \\ v/\sqrt{2} + h(x)/\sqrt{2} - i\theta_3 \end{pmatrix} = e^{i\tau \cdot \theta(x)/v} \begin{pmatrix} 0 \\ v/\sqrt{2} + h(x)/\sqrt{2} \end{pmatrix} \quad (2.33)$$

The four scalar fields can be interpreted as four massless Goldstone bosons. The exponential factor is recognised as an  $SU(2)$  gauge transformation, so by moving to a different gauge in which this term becomes unity (the unitary gauge), we can arrive at

$$\Phi(x)' = \frac{1}{\sqrt{2}} \begin{pmatrix} 0 \\ v + h(x) \end{pmatrix}. \quad (2.34)$$

Substituting this expression for  $\Phi'(x) = \Phi(x)$  into the covariant derivative term of  $\mathcal{L}_H$ , using Eq. 2.15, the mass terms for the three gauge bosons we require to complete the electroweak unification present themselves:

$$(D_\mu \Phi)^\dagger (D^\mu \Phi) = \frac{1}{2} (\partial_\mu h)^2 + \frac{g_2^2 v^2}{8} (W_\mu^+ W^{+\mu} + W_\mu^- W^{-\mu}) + \frac{(g_1^2 + g_2^2)v^2}{8} Z_\mu Z^\mu + 0 A_\mu A^\mu. \quad (2.35)$$

Here, we have substituted in the physical gauge bosons  $W_\mu^\pm, Z_\mu$  and  $A_\mu$  for the fields  $W_\mu^i$  and  $B_\mu$ . This mechanism for spontaneous symmetry breaking gives the expected mass

terms of the form  $\frac{1}{2}m^2X_\mu X^\mu$  for the  $W^\pm$  and  $Z$  in terms of their couplings:

$$m_W = \frac{g_2 v}{2} \quad (2.36)$$

$$m_Z = \frac{\sqrt{g_1^2 + g_2^2} v}{2} = \frac{m_W}{\cos \theta_W}. \quad (2.37)$$

Crucially, the photon remains massless. By moving to the unitary gauge, we have lost three of the Goldstone bosons, or equivalently three degrees of freedom. The fourth massless Goldstone boson has become a massive scalar boson, the SM Higgs boson, with mass  $m_H = \sqrt{-2\mu^2}$ . The three lost degrees of freedom correspond to the longitudinal polarizations of the new massive  $W^\pm$  and  $Z$  bosons.

Adding the Higgs potential to the SM Lagrangian has allowed massive gauge bosons in a gauge invariant way. The remaining missing fermion mass terms can now be filled in using a similar method. By adding a Yukawa coupling (that is invariant under  $SU(2)$ ) between the Higgs field and the fermions in the Lagrangian, the same Higgs **fieldboson** can generate their masses. The additional terms in the Lagrangian are of the form

$$\mathcal{L}_{Yukawa} = k_e \bar{L} \Phi e_R + h.c. + \left( k_u \bar{Q}_L \Phi d_R + k_d \bar{Q}_L \tilde{\Phi} u_R \right) + h.c. \quad (2.38)$$

where  $\tilde{\Phi} = i\tau_2 \Phi^*$  for up-type quark wavefunctions is necessary for gauge invariance. In the same unitary gauge of Eq. 2.34, we find the couplings of the fermions to the Higgs field are then equal to their masses;  $m_e = k_e v / \sqrt{2}$  and similarly for  $m_u, m_d$  where  $k_u$  and  $k_d$  are arbitrary, non-diagonal  $3 \times 3$  matrices. These are the Cabibbo-Kobayashi-Maskawa (CKM) matrices and dictate the flavour structure of the SM [35, 46].

The remaining piece of the SM not mentioned above is the description of the strong interaction. It only affects coloured particles, and as a result of its  $SU(3)$  gauge invariance, the generators are the Gell-Mann matrices  $\lambda_a$  where  $a = 1, 2, \dots, 8$  which give rise to eight gluons  $G_a$ . To incorporate the strong force, which gives rise to Quantum Chromo-Dynamics (QCD), we simply add the  $SU(3)$  terms to the covariant derivative and  $\mathcal{L}_{kin}$ :

$$D_\mu = \partial_\mu - ig_1 \frac{Y}{2} B_\mu - ig_2 \frac{\tau_i}{2} W_\mu^i - ig_3 \frac{\lambda_a}{2} G_\mu^a \quad (2.39)$$

$$\frac{1}{4} F_{\mu\nu} F^{\mu\nu} = \frac{1}{4} (B_{\mu\nu} B^{\mu\nu} + W_{\mu\nu} W^{\mu\nu} + G_{\mu\nu}^a G_a^{\mu\nu}). \quad (2.40)$$

Gauge invariance dictates the form of the electroweak Lagrangian. Spontaneous symmetry breaking via the Higgs mechanism leads to three massive gauge bosons, one massless gauge boson, and one massive scalar boson. The SM Lagrangian can then be written by summing the various terms discussed above:

$$\mathcal{L} = \mathcal{L}_{int} + \mathcal{L}_{kin} + \mathcal{L}_H + \mathcal{L}_{Yukawa} \quad (2.41)$$

$$= \bar{\psi} i\gamma^\mu D_\mu \psi - \frac{1}{4} F_{\mu\nu} F^{\mu\nu} + |D_\mu \Phi|^2 + \mu^2 |\Phi|^2 - \lambda |\Phi|^4 + (\bar{\psi}_i k_{ij} \psi_j + h.c) \quad (2.42)$$

## 2.2 Motivation for Physics Beyond the Standard Model

Despite its many successes, fundamental theoretical flaws in the SM, as well as observed phenomena it fails to explain, imply there must be new physics at some energy scale. Various experimental observations – gravity, the matter-antimatter imbalance in the universe, neutrino oscillations, dark matter – all have no explanation in the SM. Questions of the naturalness of the theory with regard to fine tuning the mass of the Higgs boson, the non-unification of the fundamental forces, and the seemingly arbitrary number of parameters lead many theorists to believe the SM to be a low energy approximation of some new form of physics – physics which solves the underlying theoretical problems, as well as filling in the ‘holes’.

Gravity has no place within the SM; there is no interaction to explain the gravitational attraction felt by the fundamental particles which is so evident at large distance scales. Despite its negligible influence on subatomic particles at the energy scales probed by the LHC, the gravitational force cannot be reconciled with a quantum theory.

In addition, there is insufficient CP violation within the SM to explain the observed matter dominance in the Universe. The CP violation in the kaon,  $B_0$  and  $D_0$  meson sectors is not enough to explain why only matter remains from the Big Bang, in which matter and antimatter are thought to have been produced in even quantities. Physics BSM is necessary to introduce another source of it in order to explain **why we were why** are here at all; why all matter did not annihilate soon after it was created.

The solar neutrino problem, in which there were far less  $\nu_e$  arriving at the Earth from the Sun than solar models predicted, was solved with the discovery of neutrino oscillations [47]. The  $\nu_e$ , on their flight from the sun, were changing state so that when

they were measured on Earth they were no longer in the electron-like weak eigenstate. They had oscillated into a different weak eigenstate, and so appeared to have disappeared when measured in electron-like charged current interactions. Atmospheric neutrinos are produced in cosmic ray interactions in the atmosphere (resulting largely from charged pion decay), in the ratio of approximately 2:1 of  $\nu_\mu:\nu_e$ . There is similarly observed to be a deficit of the muon-like weak eigenstate in experiments on (or under) the ground [48, 49]. Experiments using neutrinos from accelerator and reactor sources have seen similar behaviours [50–53]. Neutrino oscillations imply that there is a mass difference between the different mass eigenstates of the neutrinos,  $\nu_1, \nu_2, \nu_3$ , which are a superposition of their weak flavour eigenstates  $\nu_e, \nu_\mu, \nu_\tau$ . A mass difference means each type of neutrino must have a mass (albeit small) – in contradiction of the massless, left handed neutrinos present in the SM. New physics is needed to explain massive neutrinos.

The flaw in the SM getting perhaps the most attention at the moment, in the current post-Higgs boson discovery era, is that it has no candidate for DM. Astronomical observations of galaxy rotation curves [54], gravitational lensing [55, 56], the CMB [57], the Bullet Cluster [58], and large scale structures [59] imply that there is a ‘dark’ matter present in the universe; dark because it does not interact with electromagnetic radiation. Its presence is only inferred by its gravity. Therefore it must be also stable and weakly interacting – we have found no unequivocal evidence of DM decay products (although recent gamma-line spectra from the centre of the galaxy could suggest DM annihilation [60]). Astronomical observations imply that DM makes up around 26.8% of the energy budget of the universe, compared to the 4.9% of the matter the SM is comprised of. For our model of the fundamental forces and particles of the universe, the SM, to have no DM candidate leads us to question it – and come to the conclusion there must be something more. It is perhaps worth mentioning that Dark Energy, which is theorized to constitute the remaining 68.3% of the energy budget, and is responsible for the observed expansion of the universe, is not understood at all!

While the above are pieces of experimental evidence that cannot be explained by the SM, there are also theoretical problems with the model when calculating the radiative corrections to the Higgs boson mass. We saw in Eq. 2.31 that the scalar potential giving rise to the Higgs boson  $h$  is of the form

$$V \sim m_{H0}^2 h^2 + \lambda h^4. \quad (2.43)$$

The presence of the quartic term, proportional to  $\lambda$ , implies the Higgs interacts with itself at loop level. This self-interaction adds another, quadratically divergent term to the mass of the Higgs,  $m_H$ :

$$m_H^2 \sim m_{H0}^2 + \frac{\lambda}{4\pi^2} \Lambda^2 + \delta M_H^2, \quad (2.44)$$

where  $\Lambda$  is some cut-off energy scale to where the physics is valid. If there is no new physics between the electroweak scale at  $\sim 100$  GeV and the Planck scale, then  $\Lambda$  is of the same order as the Planck scale. Indirect constraints on the Higgs mass from measurements of the W and top quark masses [61, 62] imply that the Higgs mass is around the electroweak scale, and indeed direct measurements of the Higgs boson mass are around 125 GeV [63, 64] – not  $M_{Pl}$ . The term  $\delta M_H^2$  then must cancel out the term in  $\Lambda$ ; ie there must be a cancellation of order  $M_{Pl} \sim 10^{18}$ . To put this hierarchy problem another way, there is a precise fine-tuning necessary, of one part in  $10^{18}$ . Although possible, this is very unnatural, and drives [the](#) much of the theoretical motivation for BSM physics.

SUSY [65, 66] is one example of an extension to the SM which can solve many of its problems, and is the subject of [the](#) remainder of this chapter, as well as the analysis work done in this thesis. It is probably the most popular and well studied BSM theory in the community, however is not alone: models of Large Extra Dimensions [67], the SeeSaw Mechanism [68, 69], and Little Higgs [70] are just a few examples of many theories which attempt to explain the shortcomings of the SM by introducing new physics.

## 2.3 Supersymmetry

SUSY first emerged in the 1970’s as a result of the mathematical considerations of QFT. The Coleman-Mandula theorem [71], which states that space time and internal symmetries cannot be combined anything but trivially, was found to have a hole in it [72]. This allows a symmetry between fermions (f) and bosons (b):

$$\hat{O}|f\rangle = |b\rangle; \quad \hat{O}|b\rangle = |f\rangle \quad (2.45)$$

where  $\hat{O}$  is the supersymmetric operator generating the transition. SUSY relates particles of different spin, where they differ by a half integer unit, and the Lagrangian remains invariant under transformations such as those in Eq. 2.45. The generated particles, or

sparticles, have [the](#) all of the same quantum numbers as those particles they have been generated with (but for the spin) – so they have the same mass.

If we reconsider the one loop corrections to the Higgs field,  $h$ , with massive fermions  $\psi$  and massive scalars  $\phi$  [73] (which can be generated by a supersymmetric transition as they differ in spin by a half-integer unit), we see additional terms in  $m_H^2$ :

$$\begin{aligned} m_H^2 \sim & m_{H0}^2 + \frac{\lambda_F^2}{4\pi^2}(\Lambda^2 + m_F^2) - \frac{\lambda_S^2}{4\pi^2}(\Lambda^2 + m_S^2) \\ & + \text{logarithmic divergences} + \text{uninteresting terms}. \end{aligned} \quad (2.46)$$

Crucially, there is a relative minus sign between the two quadratic terms in  $\Lambda$ , a result of Fermi statistics. If the couplings between the Higgs and the fermion  $\lambda_F$  and scalar  $\lambda_S$  are equal, then the quadratic terms in  $\Lambda$  cancel, and all that remains of the troubling quadratic divergence of Eq. 2.44 are the mass terms:

$$m_H^2 \sim m_{H0}^2 + \frac{\lambda_F^2}{4\pi^2}(m_F^2 - m_S^2). \quad (2.47)$$

Here, the fermion and scalar have been generated by a supersymmetric transition, and thus have the same quantum numbers. They have the same mass – and so the quadratic term completely cancels out. The fine tuning problem has been solved. However, no scalar particle has been observed with the same quantum numbers, and mass, of any fermion. No scalar particle with the same quantum numbers and different mass have been observed either, up to the energies probed – which, at the LHC, is of order 1 TeV.

It was the theoretical breakthrough in the 1980’s that allowed SUSY to be a broken symmetry: the mathematical framework remains consistent even if the masses are not the same. Then, the second term in Eq. 2.47 remains – but, provided the masses are ‘not too different’ (where the allowed differences are seemingly a matter of opinion, deemed ‘naturalness’, but general consensus is of order a few TeV so reachable at LHC energies) - the issue of the fine-tuning of the Higgs mass is resolved, as the huge corrections necessary with no SUSY are now far more manageable.

SUSY, then, is a BSM theory with a foundation in the mathematics of QFTs, which, as a consequence of its symmetry, cancels out the huge quadratic divergences in the Higgs mass, making it very appealing. The SM becomes a part of a wider supersymmetric model that maintains the same  $SU(3) \otimes SU(2) \otimes U(1)$  gauge symmetry. [In the Minimal Supersymmetric Standard Model—\(MSSM\),](#) Every SM particle gets a supersymmetric particle (sparticle) partner which has the same quantum numbers but

differs a half integer unit in spin and has a greater mass. In the MSSM [74], there is the minimum number of new particle states, with one extra Higgs doublet. A rich sparticle phenomenology results, as the entire spectrum of SM particles is doubled. For example, the left-handed quark doublet gets a doublet of left handed scalars:

$$Q_L = \begin{pmatrix} u \\ d \end{pmatrix}_L ; \quad \tilde{Q}_L = \begin{pmatrix} \tilde{u}_L \\ \tilde{d}_L \end{pmatrix} \quad (2.48)$$

and similarly,  $L, e_R, u_d, d_R$  defined in Section 2.1.3 get  $\tilde{L}, \tilde{e}_R, \tilde{u}_d, \tilde{d}_R$  which are both contained in the respective  $SU(2)_L$  or  $U(1)$  superfields. Additional superfields contain the SM bosons and their fermionic partners: the gluons  $g^a$  and gluinos  $\tilde{g}^a$ ; the three weak bosons  $W_i$  and the winos  $\tilde{w}_i$ ; and the  $U(1)$  boson  $B$  and its partner the bino  $\tilde{b}$ . To cancel out gauge anomalies, the SM  $SU(2)_L$  Higgs doublet of scalars becomes two doublets  $H_u$  and  $H_d$ , which then require two Higgs doublets of fermions for the higgsinos  $\tilde{h}$ .

### 2.3.1 R parity and dark matter

The full MSSM Lagrangian can be found elsewhere [73]. Suffice to say, there are terms which permit lepton and baryon number violating interactions that can mediate proton decay, and give rise to interactions such as the one in Fig. 2.3. There are very stringent

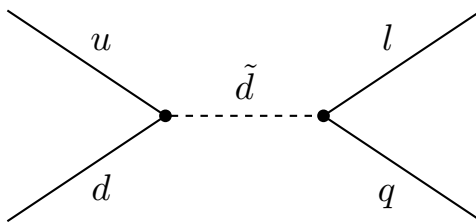


**Figure 2.3:** Example of a lepton and baryon number interaction which would mediate proton decay.

limits on proton decay;  $\tau > 10^{33}$  years [1], so interactions such as these must be highly suppressed, if allowed at all. The class of SUSY models which do not permit lepton and baryon violating interactions have an additional symmetry in R parity, which is defined as

$$R = (-1)^{3(B-L)+2s}, \quad (2.49)$$

where  $B$  is the baryon number,  $L$  the lepton number, and  $s$  the spin of the particle. A consequence of R parity conserving SUSY is that sparticles are always produced in pairs, and any sparticle decay will always result in another sparticle being produced. So any SUSY decay chain, as well as producing many SM particles, will always result in a single sparticle – the lightest of the SUSY spectra, so cannot decay further. This is then the LSP, and must be stable. Cosmological bounds on light charged or coloured stable particles [1] imply the LSP (if it exists) must be neutral. A stable, neutral, weakly interacting LSP, key to the popularity of SUSY, then very naturally gives a DM candidate. The LSP, with a collider signature much like a neutrino, will exit a detector having deposited no energy as it interacts with none of its material. There will instead be an imbalance in momentum, leading to a missing transverse [momentumenergy](#) signature.

Proton decay requires both lepton and baryon number violation, so certain models that have partial R-parity violation in either B or L can be compatible with limits on proton decay. These do not give rise to the same missing transverse momentum signatures as R-parity conserving SUSY, as the LSP becomes unstable eventually decays into SM particles. There are dedicated searches for such models, and these are discussed elsewhere [75–77].

### 2.3.2 Unifying the forces

Another feature of SUSY which makes it very popular with the theory community is the natural unification of the weak, electromagnetic and strong forces at the Grand Unified Theory (GUT) scale. The strengths of each of these forces change with distance, or equivalently energy – their coupling constants ‘run’. At very small distances, or very high energies, such as those at the time of the Big Bang, masses of any particles involved are completely negligible, and the strengths of interactions can be investigated. With the vanilla SM of Section 2.1, there is not a single point where the three coupling constants unite, or become one, unified interaction. However, when SUSY is added in, all three forces become unified at a single point around  $10^{16}$  GeV [78], see Fig. 2.4.

This very elegant picture of the early universe is very attractive: one single force dominated while the energy density was high enough, and then later, a transition occurred when the three forces became distinct. The idea of a GUT, with some higher symmetry group, that can dictate all of the behaviour we observe in the universe is very appealing to theorists.

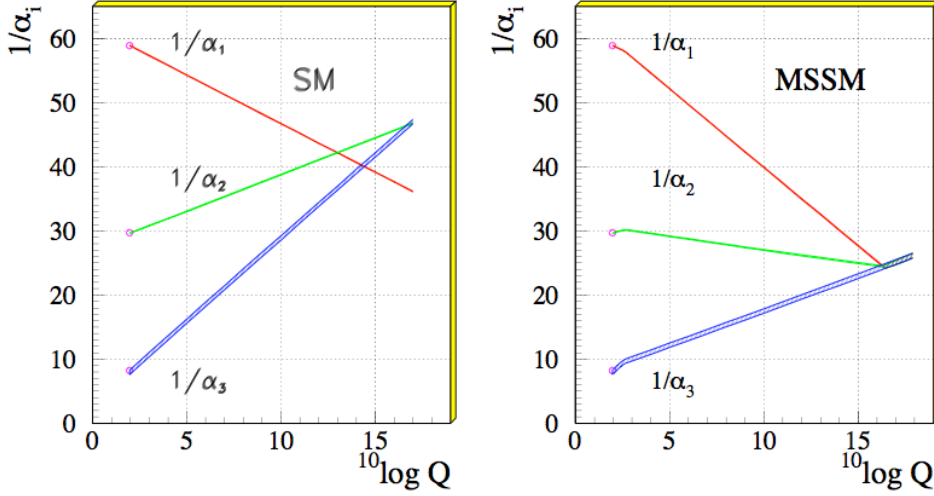


**Figure 2.4:** The running coupling constants of the electromagnetic, strong and weak forces with increasing energy or decreasing distance. Once SUSY has been added in, the three unify around  $10^{16}$  GeV, hinting at a GUT. Taken from [79].

### 2.3.3 Breaking supersymmetry and naturalness

We have mentioned that SUSY is a broken symmetry if it exists in nature. The possible mechanism of the spontaneous symmetry breaking is beyond the scope of this thesis, but different SUSY breaking mechanisms lead to many different sparticle phenomenologies [66]. It is usually assumed that the SUSY breaking occurs at some high scale  $\sim M_{Pl}$ , and that it is “soft” [80], which leads to logarithmic, rather than quadratic divergences. The correction to the Higgs mass then takes the form

$$\delta m_H^2 \sim (m_{\tilde{q}}^2 - m_q^2) \log \Lambda. \quad (2.50)$$

The largest contribution to  $\delta m_H$  is from the top quark, because it is so much more massive than all other SM fermions at 173 GeV. To keep  $\delta m_H$  reasonably small, and the fine tuning issue minimal, the supersymmetric partner to the top quark, the top squark  $\tilde{t}$  should be fairly close in mass to 173 GeV. Figure 2.5 shows the correction to the Higgs mass due to the top quark loop, and the corresponding loop correction from the top squark, which acts to cancel the divergence in the Higgs mass out.

Such naturalness arguments motivate a light  $\tilde{t}$ , and a bottom-up approach to any SUSY spectrum. The biggest Yukawa couplings come from the heaviest SM particles, i.e. the third generation. To keep corrections to the Higgs mass small, the third SUSY generation is expected to be the lightest, and in reach of the LHC [81, 82]. First generation

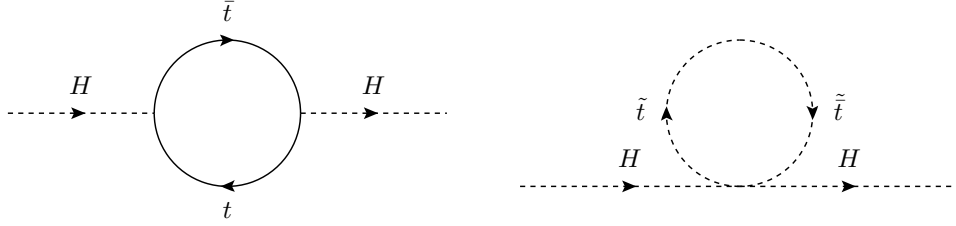


**Figure 2.5:** The loop contributing to the Higgs mass due to the top quark, left, and the cancellation of the loop due to the top squark, right.

squarks and sleptons can be much heavier, even up at the Plank scale, while keeping a natural SUSY.

### 2.3.4 Searching for supersymmetry at colliders

Having motivated SUSY as a extension of the SM which has the potential to very nicely solve the hierarchy problem, give us a DM candidate and unify the three fundamental forces at the GUT scale, we ask ourselves how best to search for any possible signs of it at a collider. In R parity conserving SUSY, the LSP exits the detector leaving nothing but an imbalance of momentum; at hadron colliders, this imbalance is evident in the transverse plane as  $p_T^{\text{miss}}$ . In addition, typical SUSY decay chains have multiple legs, as a heavy sparticle produced in the pp collision decays down the SUSY spectrum. A SM particle (which may itself decay) is emitted at each step until the energy is small enough that only the LSP can be emitted, along with a final SM particle. Each event has two such decay chains as the original sparticle is pair produced. The array of decays possible, as well as the energies involved, depend entirely on the SUSY spectrum considered, which in turn is dependent on the type of SUSY breaking. An example of this kind of SUSY decay chain is shown in Fig. 2.6. Here, the LSP is shown as  $\tilde{\chi}_1^0$ . Such  $\tilde{\chi}^0$  states are a neutral superposition of higgsino, wino and bino states; the exact composition is again SUSY model dependent. Charged superpositions are written as  $\tilde{\chi}^\pm$  and often feature in such decay chains.

To be sensitive to these SUSY signatures, which have high particle multiplicity and lots of energy in the final state, traditional searches have revolved around looking for multiple final state objects, plus a significant amount of  $p_T^{\text{miss}}$ . To be as model independent as possible, searches are generic. There are searches for multijet events (arising from a decay chain similar to that in Fig. 2.6), same or opposite sign dilepton events, multi-lepton events, events which have both leptons and jets, or photons, jets which are tagged

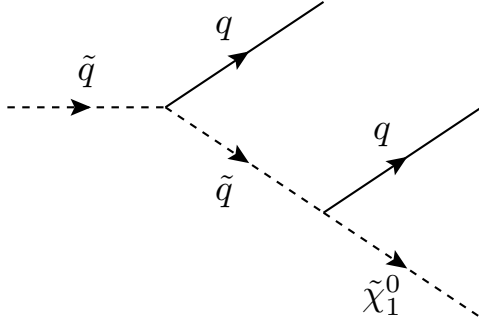
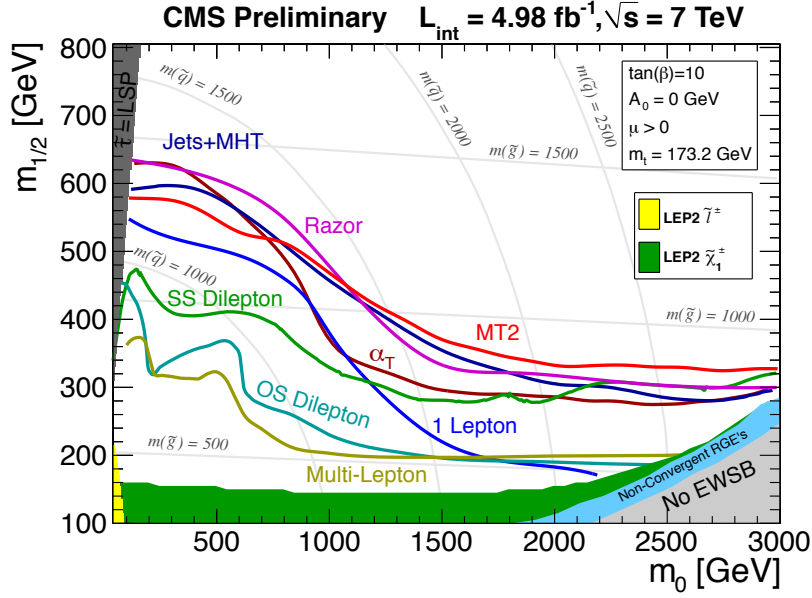


**Figure 2.6:** Example of a SUSY decay chain, in which there are several quarks emitted as well as the LSP. Two of these decay chains will be present in each event due to the pair production of the parent  $\tilde{q}$ .

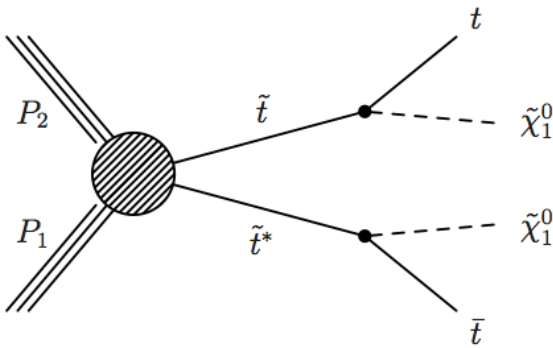
as arising from a b-quark, events with lots of hadronic energy deposited ( $H_T$ ): see Refs. [83–91]. Innovative methods of controlling the large backgrounds, particularly as a result of QCD multijet events, have been developed [92–94].

Stringent bounds were placed on the Constrained Minimal Supersymmetric Standard Model (CMSSM) during the first LHC run [95, 96]. It is a popular SUSY model which simply reduces the multitude of free parameters in the MSSM down to 5 by setting many of the masses to be equal. All scalar masses become  $m_0$ , all gaugino masses  $m_{1/2}$ , trilinear couplings are set to  $A_0$ , and the ratio of the VeV of the two Higgs doublets is  $\tan\beta$ . The fifth parameter is the sign of  $\tan\beta$ . Traditionally, searches are interpreted using the CMSSM as it produces a simple phenomenology, enabling mass scans in four dimensions (plus a sign) rather than over one hundred in the full MSSM. The phenomenology is also ‘easily’ discoverable: parameters are fixed at the GUT scale and extrapolated down to the electroweak scale (for example, the Z pole mass), making mass differences between particles relatively large and so decay products reasonably energetic. Limits from searches using the CMS detector are shown in Fig. 2.7. The lack of any sign of SUSY in these direct searches, as well as limits from indirect searches sensitive to the parameters of the CMSSM (such as  $B_S \rightarrow \mu\mu$  [6]) have led the community to pursue less specific, alternative scenarios.

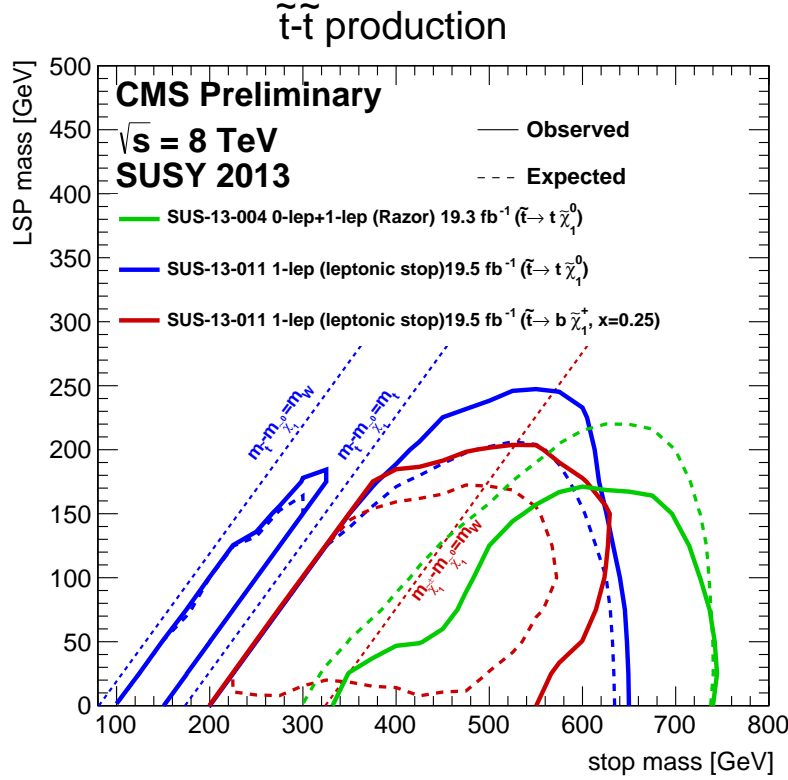
A more model independent approach has been adopted more recently at CMS, with the use of Simplified Model Spectra (SMS) [98–101], which allow searches to be interpreted in the mass planes of various sparticles: in the mass of the  $\tilde{t}$ ,  $\tilde{b}$ ,  $\tilde{q}$  and  $\tilde{\chi}_1^0$  for example. All other sparticles than those probed are assumed to be very heavy and are integrated out.



**Figure 2.7:** The limits on the  $m_{1/2}, m_0$  CMSSM mass plane from CMS with the full 7 TeV dataset, taken from [97].



**Figure 2.8:** An example of a SUSY decay of the top squark. This is one of the simplified models probed by CMS at the LHC.



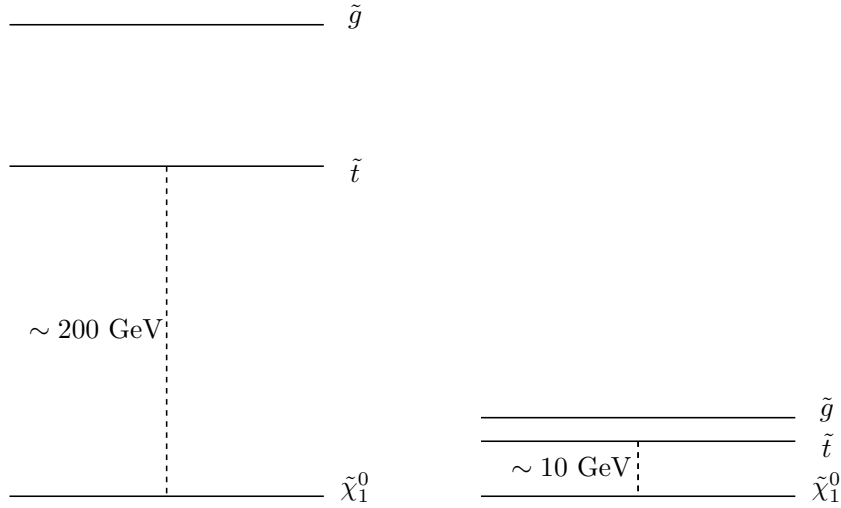
**Figure 2.9:** The limits on the  $\tilde{t}, \tilde{\chi}_1^0$  mass plane from CMS at SUSY 2013 [102].

Figure 2.8 shows an example Feynman diagram for a particular decay of the  $\tilde{t}$ , one of the SMS hypotheses probed, which dominates if the top squark is heavy enough to produce an on-shell top quark when it decays. Other decays dominate when this is not true, which can then be targeted with searches that have different kinematics than that of Fig. 2.8: this will be the subject of Chapter 5. Such generic searches can also be simply applied to other models of BSM physics.

At 7 and 8 TeV, no evidence for SUSY has been found at the LHC; exclusion limits on squarks and gluinos are around 1 TeV at 95% Confidence Level (CL). Searches have ruled out huge swathes of phase space, see Fig. 2.7 and Fig. 2.9 that show the limits on the CMSSM and the combined CMS results on the  $\tilde{t}, \tilde{\chi}_1^0$  mass plane, as shown at SUSY 2013, respectively.

If SUSY is to persist as a convincing BSM theory, naturalness arguments in conjunction with a Higgs mass of  $\sim 125$  GeV imply that the third generation squarks should be light [103]<sup>4</sup>. Either SUSY does not exist in a natural way and doesn't solve the theoretical

<sup>4</sup>Recent work may indicate that a light stop is not necessarily the only route to ‘natural’ SUSY; light higgsinos can also give a small amount of fine-tuning [104].



**Figure 2.10:** An example SUSY spectrum in the bulk region, left, and for a compressed spectrum, right. The mass difference between the NLSP and the LSP, here the  $\tilde{t}$  and  $\tilde{\chi}_1^0$  respectively, is much reduced for the compressed scenario.

problems in the SM that it has been proclaimed to, it is just out of reach at the 8 TeV LHC, or SUSY is somehow hidden. Fig. 2.9 has areas which are not covered by the exclusion regions, where it has been suggested that SUSY may be ‘hiding’. Traditional searches loose sensitivity in these regions. For example, in the strip close to the kinematic limit, when the parent sparticle –  $m_{\tilde{t}}$  in this case – is close in mass to  $m_{\tilde{\chi}_1^0}$ , decay products become very soft, so would be hidden amongst the high QCD background. This kind of mass spectrum, which is compressed, would not show up in the traditional SUSY searches that demand lots of visible energy: a different approach is necessary.

### 2.3.5 Supersymmetry with compressed mass spectra

SUSY has compressed mass spectra when the symmetry breaking dictates that the various states are close in mass, for example see Fig. 2.10. Particularly, the LSP is close in mass to the Next-to-Lightest Supersymmetric Particle (NLSP), which, in many scenarios, is the  $\tilde{t}$ . There is no reason to assume that nature would not ‘prefer’ a compressed spectra: to keep as wide a net as possible over the SUSY phase space, compressed scenarios should be probed – we should look for both the types of spectra shown in Fig. 2.10. Further, it is not just the lack of any evidence for SUSY in the bulk phase space regions, where the mass difference between the LSP and the next lightest sparticle is typically  $> 100$  GeV, but there are also phenomenological arguments which motivate the search for compressed SUSY, with a light  $\tilde{t}$ .

Any BSM candidate for DM must give the correct energy density of dark matter, which has been accurately measured by Wilkinson Microwave Anisotropy Probe (WMAP) and the Planck space telescope [57, 105]. Any SUSY model, if it is to explain the origin of DM as the LSP, must therefore give the correct DM relic density (if nothing else is acting to increase or decrease the relic density). This requirement can dictate the nature of the neutralino (the DM candidate) [106, 107]. If the neutralino is a superposition of bino states, then the relic density is too large; if it is instead a composition of higgsino or wino states, then it is too small. However, if the neutralino is bino-like but has a few tens of GeV mass splitting with the lightest  $\tilde{t}$ , the correct relic density can be achieved [108–110].

Any compressed scenario will lead to soft decay products, as the energy from the parent sparticle goes mostly into producing the daughter particles with little left to boost the decay products. The question of how to efficiently select these events then presents itself – it is very difficult to pick out events that contain only a few soft particles; they would be lost in the SM electroweak,  $t\bar{t}$  and QCD events. Similarly, the  $\tilde{\chi}_1^0$  at the end of the decay chain will also be very soft, so the  $p_T^{\text{miss}}$  in each event is also small. Instead of looking for the decay products themselves, it is then more useful to search for states which are produced in association with the parent sparticles. Initial State Radiation (ISR) can lead to the emission of a high energy gluon or quark, giving a hard jet. It will also give a boost to the system, such that the  $\tilde{\chi}_1^0$  also have more momentum, and thus there will be a significant amount of  $p_T^{\text{miss}}$ . Such an event will then have a clear signature of one high momentum jet and large  $p_T^{\text{miss}}$ , where the decay products are too soft to observe. While the production cross section of a process with an ISR jet is of course lower than without, due to the additional factor of  $\alpha_S$ , the gain in sensitivity to the signal far outweighs the lower event yield.

## 2.4 Decays of the Top Squark

We have discussed in the previous section the importance of a light top squark for natural SUSY. In order to optimise any search for such a light top squark, it is important to consider its decays in different regions of parameter space [111, 112].

For the case when the mass difference between the top squark and the LSP is greater than the mass of the top quark,  $m_{\tilde{t}} - m_{\tilde{\chi}_1^0} > m_t$ , the dominant decay mode is simply

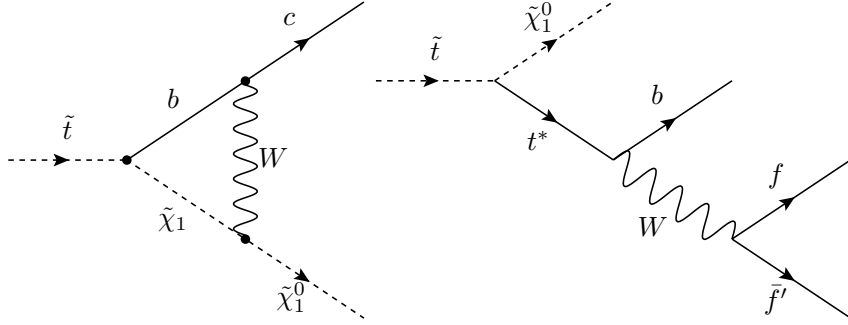


**Figure 2.11:** Feynman diagrams to show two contributing processes to the decays of the top squark:  $\tilde{t} \rightarrow c\tilde{\chi}_1^0$  (left) and  $\tilde{t} \rightarrow b\tilde{\chi}_1^0 f\bar{f}'$  (right). **The intermediate top quark on the right,  $t^*$ , is produced off-shell.**

$\tilde{t} \rightarrow t\tilde{\chi}_1^0$ . The Feynman diagram for  $\tilde{t}$  pair production followed by this decay is shown in Fig. 2.8.

However, when the mass difference is less than the top quark,  $m_{\tilde{t}} - m_{\tilde{\chi}_1^0} < m_t$ , things become more complicated. While the mass difference is above the mass of the W,  $m_{\tilde{t}} - m_{\tilde{\chi}_1^0} > m_W$ , the three body decay mode  $\tilde{t} \rightarrow Wb\tilde{\chi}_1^0$  dominates, as the W can be produced on-shell. As the mass difference becomes smaller still,  $m_{\tilde{t}} - m_{\tilde{\chi}_1^0} < m_W$ , both the flavour changing neutral current decay  $\tilde{t} \rightarrow c\tilde{\chi}_1^0$  and the four body decay  $\tilde{t} \rightarrow b\tilde{\chi}_1^0 f\bar{f}'$  can occur, where  $f$  is any fermion, and **the intermediate top quark is produced off-shell**. Examples of Feynman diagrams that contribute to these are shown in Fig. 2.11. While the precise branching fraction of these decay modes is rather model dependent, it is usually assumed that due to phase space arguments, the four body decay is suppressed and  $\tilde{t} \rightarrow c\tilde{\chi}_1^0$  dominates [111]. Figure 2.12 summarizes the decays of the top squark, showing the relevant decay for the different kinematic regimes of  $\tilde{t}$  and  $\tilde{\chi}_1^0$  mass **in the  $\tilde{t}-\tilde{\chi}_1^0$  mass plane**.

In light of the arguments for searching for compressed SUSY, particularly in the third generation, Chapters 5 and 6 will describe a search for light stops decaying to a charm quark and a neutralino, using events with a monojet topology. **This search is applicable to many new physics scenarios, being more usually applied to dark matter searches and the like.** Here, it is interpreted for these particular third generation compressed SUSY scenarios, and equally could be applied to other compressed SUSY scenarios.

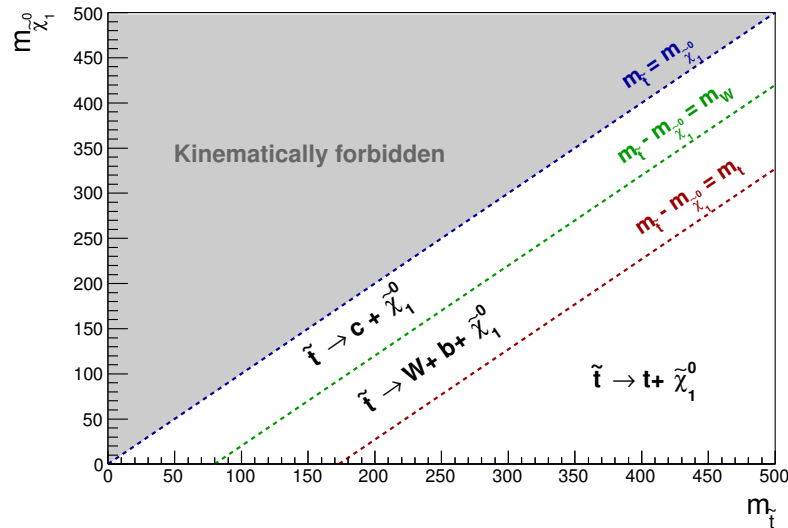


**Figure 2.12:** Phase space of the top squark and LSP. The grey region is kinematically forbidden:  $m_{\tilde{\chi}_1^0} > m_{\tilde{t}}$  is at odds with the LSP definition. The coloured dotted lines and labels define each kinematic region, and the dominant  $\tilde{t}$  decays are shown, where we have neglected the four body decay in the region where  $m_{\tilde{t}} - m_{\tilde{\chi}_1^0} < m_W$ .

# Chapter 3

## The LHC and CMS experiment

*“Insanity: doing the same thing over and over again and expecting different results.”*

— Albert Einstein, 1879-1955

Probing the physics of the SM and beyond at the TeV scale is only possible with the technologically unparalleled apparatus situated at CERN. This chapter will introduce the hugely complex machinery of the LHC, which provides proton-proton collisions at centre-of-mass energies in excess of  $\sqrt{s} = 7$  TeV, and outline the main features of the CMS experiment, of which the author is a member, with particular focus on those features relevant to the material presented in this thesis. Section 3.1 presents the main features of the LHC, and Section 3.2 provides an overview of the CMS detector. Physics object reconstruction is described in Section 3.3 and the CMS trigger system is discussed in Section 3.4.

### 3.1 The LHC

The LHC is the world’s largest and most energetic synchrotron particle collider [113]. Housed in the tunnel built for the Large Electron-Positron Collider (LEP) that operated during the 1990’s at CERN, the LHC is a double ring circular collider 27 km in circumference, and sits on the bedrock beneath the Franco-Swiss border, close to Geneva, Switzerland. It is designed for both proton-proton (pp) and heavy ion (PbPb) collisions at a centre of mass energy  $\sqrt{s} = 14$  TeV and instantaneous luminosity of  $10^{34}\text{cm}^{-2}\text{s}^{-1}$ .

Currently the world's only operating collider able to study physics directly at the TeV scale, the LHC consists of thousands of superconducting magnets which act to accelerate, bend and focus two beams of protons (or heavy ions) that circulate in opposite directions around the accelerator. A chain of accelerators, shown in Figure 3.1 and culminating with the SPS, inject bunches of approximately one hundred billion protons 25 or 50 ns apart at  $\sqrt{s} = 450$  GeV into the two beampipes of the LHC. 16 Radiofrequency (RF) cavities along the LHC ring provide electric fields which oscillate at 400 MHz Oseillating electric fields provided by 1232 superconducting dipole magnets and act to accelerate the beams up to the operating centre of mass energy. For the data used in this thesis, this was  $\sqrt{s} = 8$  TeV, with bunches crossing every 50 ns. Once protons are accelerated to the operational  $\sqrt{s}$ , the LHC acts as a storage ring with 1232 superconducting dipole magnets bending the beams around the 27 km circumference, and collisions can occur. Either side of four points around the LHC ring, very high precision magnetic fields, provided by quadrupole and higher order multipole magnets, position and focus the beams such that each bunch has a diameter of  $16 \mu\text{m}$ . The chance of a pp collision with large momentum transfer at the four interaction points around the LHC ring is thereby increased, and the number of such collisions per bunch crossing, termed PU for the data used in this thesis was  $\sim 20$ .

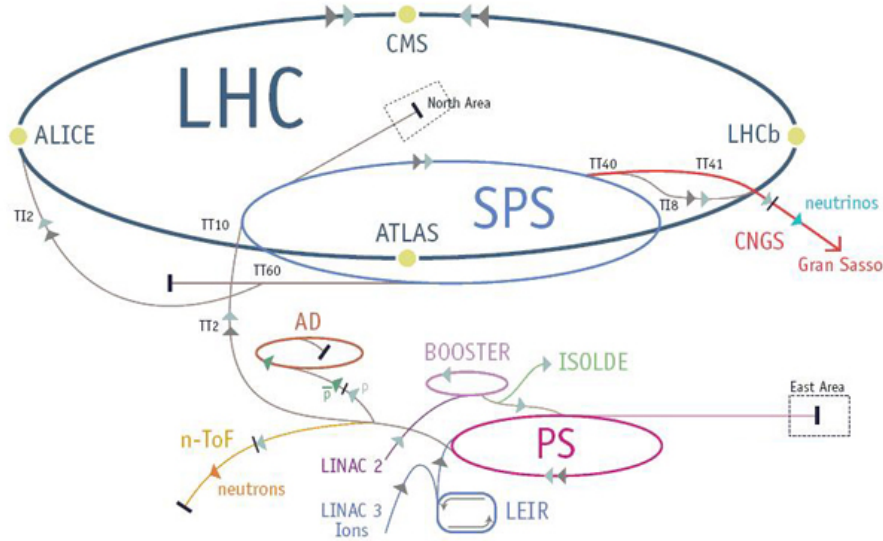


**Figure 3.1:** The LHC accelerator ring, showing the locations of the four main experiments at the four collision points.

Interaction points are at the centre of four large particle detectors, shown in Figure 3.1: A Large Ion Collider Experiment (ALICE) [114], ATLAS [115], CMS [116] and Large

Hadron Collider Beauty (LHCb) [117]. They act to identify particles produced as a result of a pp or PbPb bunch crossing through a combination of tracking and calorimetry, in order to reconstruct and measure physical processes, to test currently accepted theories and search for new physics.

### 3.1.1 LHC run conditions, past and present

The first physics runs of the LHC were incredibly successful, both for the machine and the experiments. The LHC achieved the highest ever energy per beam, with sustained running at 3.5 TeV per beam and then at 4 TeV per beam, and provided record-breaking integrated luminosities. As a result, in Run 1, the CMS and ATLAS experiments collected around  $5 \text{ fb}^{-1}$  of integrated luminosity at  $\sqrt{s} = 7 \text{ TeV}$  and  $20 \text{ fb}^{-1}$  of integrated luminosity at  $\sqrt{s} = 8 \text{ TeV}$ , with bunch crossings every 50 ns. The data collected allowed for the discovery of the last missing piece of the SM [2, 3, 118], enabled us to probe many new regions of parameter space, and set limits on a huge array of new physics models. It is the  $20 \text{ fb}^{-1}$  data set collected by the CMS detector at  $\sqrt{s} = 8 \text{ TeV}$  that is used to search for evidence of SUSY in Chapters 5 and 6.

On 13<sup>th</sup> February 2013 the LHC was shut down in order to undergo an upgrade. This period is termed Long Shutdown 1 (LS1), and is due to end in early 2015. Magnet interconnections are being replaced and the dipole magnets are undergoing a quench training programme. These improvements to the LHC magnets will allow safe acceleration of protons up to 7 TeV in each beam, and sustained operation at  $\sqrt{s} = 13 \text{ TeV}$ , eventually to achieve the design energy of 14 TeV. This will nearly double the available centre of mass energy as compared to Run I, potentially making Run 2 a discovery run — opening up more phase space and therefore opportunities for finding new physics. Instantaneous luminosity will also increase, with the aim of providing the number of events to give the statistical precision required to search for the rarest processes, as well as shed more light on the properties of the boson discovered during Run 1. The exact scenarios for running after LS1, in Run 2, are not concrete; however two potential luminosity scenarios with associated PU conditions are shown in Table 3.1. For comparison, figures typical of Run 1 operation are also shown. The jet algorithm described in Chapter 4 is for the period of running from 2016 when either of these luminosity scenarios, or similar, will be in operation.

Scenario	# bunches	$\mathcal{L}$ ( $\text{cm}^{-2}\text{s}^{-1}$ )	Pile-up	$\text{L}$ ( $\text{fb}^{-1}/\text{year}$ )
Run 1: 50 ns	2760	$0.4 \times 10^{34}$	15	10
Run 2: 25 ns	2760	$0.9 \times 10^{34}$	21	24
Run 2: 50 ns	1260	$0.9-1.7 \times 10^{34}$	40-76	45

**Table 3.1:** Alongside typical numbers from Run 1 of LHC operation, two of the possible luminosity performances for LHC after LS1, i.e. for running during Run 2 [119].

Years	Name	$\sqrt{s}$
2010–2013	Run 1	7 & 8 TeV
2013–2015	LS1	-
2015–2018	Run 2	13 TeV
~2018–2020	LS2	-
~2020 onwards	Run 3	14 TeV

**Table 3.2:** Summary of periods of running of the LHC.

In approximately 2018, the LHC will again be shutdown for Long Shutdown 2 (LS2). Improvements to the accelerator injector chain will be made — with the aim of providing much greater instantaneous luminosities. The different stages of LHC running are summarized in Table 3.2.

## 3.2 The CMS Detector

The CMS detector is a general purpose particle detector situated at Point 5 on the LHC ring, designed to carry out many different measurements for various physics goals. Close to  $4\pi$  solid angle reconstruction with efficient particle identification and reconstruction allows measurements of photons, muons, electrons, taus, hadronic showers and missing transverse momentum. A diagram of CMS is shown in Figure 3.2. It is 21.6 m long, 14.6 m in diameter and weighs 12500 T. It consists of different sub-detectors, each of which measures a different particle or property, and is built around a central 12.5 m long 4 T superconducting solenoid magnet and its iron return yoke. CMS consists of a barrel region, containing the solenoid, and endcaps to extend the forward and backward coverage.

The different sub-detectors are arranged in an onion structure. Closest to the beam line is the silicon tracking system. A very high-resolution pixel detector lies closest to the interaction region, followed by a granular strip detector. Measurements of charged particle momenta are made using the curvature of tracks in the uniform magnetic field provided by the solenoid, as well as measurements of displaced vertices and impact parameters which are essential for identifying heavy flavour decays. Energy measurements are provided by the calorimeters, which lie outside the tracker; the Electromagnetic Calorimeter (ECAL) and Hadronic Calorimeter (HCAL). The highly granular ECAL consists of 70,000 transparent lead tungstate crystals. As electrons and photons pass through, they cause electromagnetic showers in the crystals, which produce scintillation light. The sampling HCAL consists of slabs of brass interleaved with plastic. Incident hadrons shower when passing through the absorber (brass), causing scintillation light to be produced in the active material (plastic) as the shower passes through. Scintillation light produced in the crystals, or plastic, is collected by photodetectors and used to infer the incident particle energy and position. The solenoid lies outside the HCAL and provides a 3.8 T axial magnetic field. Embedded in the iron return yoke of the magnet sits the muon system. Three different types of muon detectors are used to identify muons and make momentum and charge measurements over a large kinematic range. More information on the CMS detector can be found in Ref. [116].

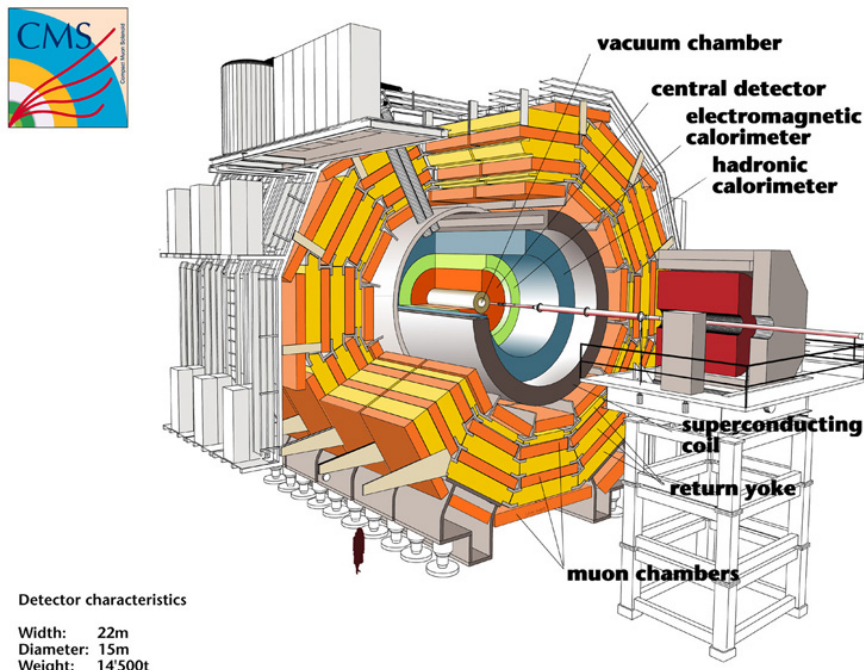


**Figure 3.2:** The CMS detector, with the main subsystems labelled.

CMS uses a right-handed coordinate system: the  $x$ -axis points south towards the centre of the LHC ring, the  $y$ -axis points vertically upwards and the  $z$ -axis is in the direction of the beam, where positive  $z$  is to the West. More natural is the coordinate system defined in terms of  $r$ ,  $\phi$  and  $\theta$ . The azimuthal angle  $\phi$  is measured from the  $x$ -axis in the  $xy$  plane, where the radial component is denoted  $r$ . The polar angle  $\theta$  is defined in the  $rz$  plane, and the pseudorapidity is defined by

$$\eta = -\ln \tan(\theta/2). \quad (3.1)$$

Convention is that the position of a particle is described in terms of  $\eta$  and  $\phi$ , where  $\eta = 0$  is along the  $y$ -axis and  $\eta = \infty$  is along the beam direction; and  $-\pi < \phi < \pi$ . The distance between particles is commonly described in terms of the variable  $\Delta R = \sqrt{\Delta\phi^2 + \Delta\eta^2}$ .

The LHC is a hadron collider, and as such, collides non-fundamental particles. Inelastic collisions with large momentum transfer can occur between component quarks and gluons, however in a single bunch crossing there will also be many low energy, elastic, soft scatters, as well as the remnant part of any protons that have had a hard collision. As a result, the forward and backward directions are highly populated environments and therefore difficult to instrument due to high occupancy and radiation damage. CMS has endcaps to extend the detector coverage at high  $\eta$ , however it is not possible to reconstruct the momentum of a single interaction in the direction of the beam. Additionally, interesting physics results from a hard collision, where energy is available for the creation of new particles. It can be characterized by the amount of energy in the transverse ( $xy$ ) plane. Most importantly, however, we cannot conserve momentum in the plane parallel to the beam because we cannot know the initial momentum of the quark or gluon which collides in the hard collision. Protons are not fundamental particles. The colliding parton has a fraction of the incoming proton's momentum; but we cannot know what this fraction is. Parton Density Functions (PDFs) try to predict these fractions, however the probabilistic nature of quantum mechanics means we cannot know it exactly. This is not the case for  $e^+e^-$  colliders such as LEP, in which the collisions occur between fundamental particles.

For these reasons, particle energy and momenta are described only in the transverse plane, where conservation laws can be applied. By conserving energy and momentum in the transverse plane, any imbalance can be assigned to a particle leaving the detector without any trace; for example from a neutrino, or, from new physics processes such as DM production. A nearly hermetic detector (with close to  $4\pi$  coverage in solid angle) allows excellent particle reconstruction and measurements of missing transverse energy,

the ‘tell-tale’ sign of new physics, and make CMS perfectly suited to searching for physics beyond the SM.

### 3.2.1 The tracking system

The tracker is designed for precise and efficient measurement of charged particle trajectories (and therefore position and momentum) as they emerge from the interaction point. Additionally, reconstruction of any secondary vertices is crucial for identifying heavy flavour decays such as jets that originate from b-quarks.

The LHC provides bunch crossings every 25 or 50 ns, resulting in  $\sim 20$  pp interactions, giving rise to of order 1000 particles. All of these traverse the tracker. The granularity of the tracker must be such that one can determine which of the  $\sim 20$  pp vertices each of the particles come from, and the electronics fast enough that the information is sent on in time for the next bunch crossing to arrive. With such high particle fluxes, the tracker is also subject to a huge amount of radiation damage. These conditions must be dealt with using the least amount of material possible in order to limit multiple scattering, photon conversion, bremsstrahlung and nuclear interactions. To meet such criteria, and to have an estimated lifetime of 10 years, the tracker is constructed entirely from silicon.

The tracker consists of an all silicon pixel and strip detector. Measuring 5.8 m in length and 2.5 m in diameter, with a total active area of  $200 \text{ m}^2$ , it surrounds the interaction region. The pixel detector has three layers in the barrel, at radii of 4.4 cm, 7.3 cm and 10.2 cm. In the endcaps, there are two disks at distances  $z = \pm 34.5, \pm 46.5$  cm. The strip detector has a length of 5.8 m and a diameter of 2.4 m, and is composed of four subsystems: the Tracker Inner Barrel (TIB), Tracker Outer Barrel (TOB), Tracker Inner Disks (TID) and Tracker Endcaps (TEC). The CMS tracker geometry is shown in Figure 3.3.

Both the energy and spatial resolutions of the tracker are excellent. The energy resolution of the tracker is shown in the left hand plot of Figure 3.4, for samples of single muons with  $p_T$  of 1, 10 and 100 GeV. For a 100 GeV muon, the resolution is 1–2% up to  $|\eta| = 1.6$  [116]. Lower momentum objects have a better energy resolution as their tracks have increased curvature. Excellent spatial resolution is vital for identifying displaced vertices, important for tagging jets as originating from b-quarks. The relatively long lived b-hadron decays  $\sim 1$  cm away from the primary vertex, leading to a displaced vertex. The resolution of transverse and longitudinal impact parameters, which characterize the

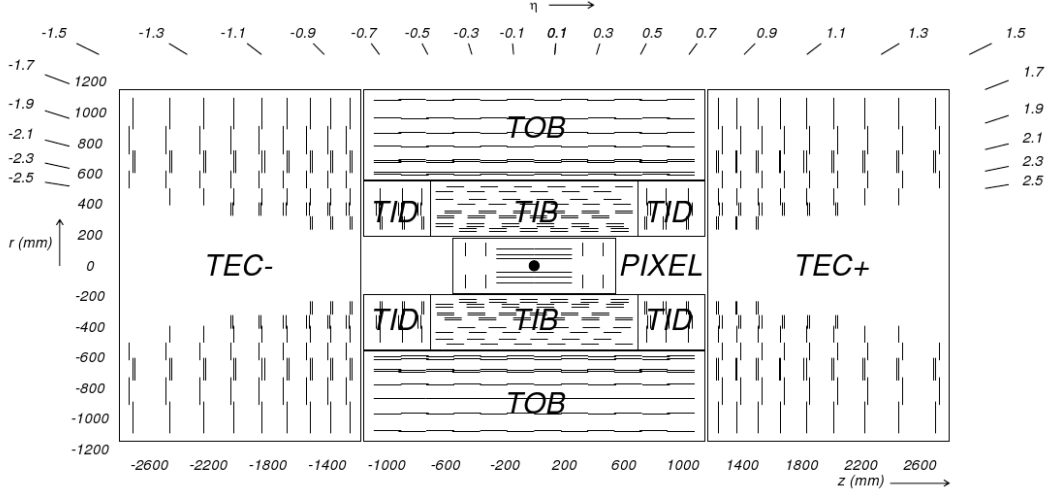


**Figure 3.3:** The CMS tracker, shown in the  $r z$  plane. The pixel detector is shown at the centre of the tracker, closest to the interaction region (shown by the black dot), and the strip detector surrounds it. The different subsystems of the strip detector are shown [116].

position of the displaced vertex, are shown in the center and right plot of Figure 3.4, for samples of single muons with  $p_T$  of 1, 10 and 100 GeV. The transverse impact parameter resolution is as good as  $10 \mu\text{m}$  for high  $p_T$  tracks [116]; evidence of the excellent spatial resolution of the tracker.

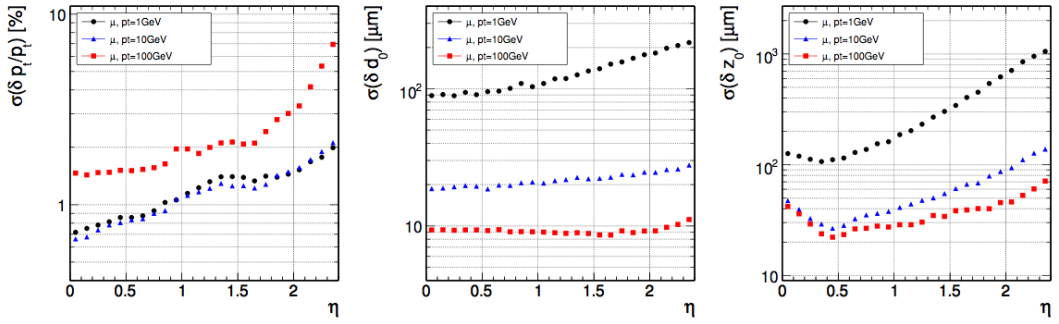


**Figure 3.4:** The energy resolution (left), transverse and longitudinal impact parameters (center, right) as a function of  $|\eta|$  for CMS tracker, shown for single muons with  $p_T = 1, 10$  and  $100 \text{ GeV}$  [116].

### 3.2.2 The electromagnetic calorimeter

High resolution photon and electron position and energy measurements are provided by the lead tungstate ( $\text{PbWO}_4$ ) crystal ECAL, which covers pseudorapidities up to

$|\eta| < 3$ . It is made up of the Electromagnetic Calorimeter Barrel (EB), covering the range  $0 < |\eta| < 1.479$ , and the Electromagnetic Calorimeter Endcap (EE), covering the range  $1.479 < |\eta| < 3$ .

Both fast response times (80% of scintillation light is emitted in 25 ns) and radiation hardness are required from the ECAL, motivating the choice of material. In addition, it is very dense ( $8.28 \text{ gcm}^{-3}$ ), has a short radiation length ( $X_0 = 0.89 \text{ cm}$ ), and small Molière radius (2.2 cm), making it well suited to a compact, fine granularity calorimeter. Arranged in a quasi-projective geometry, 61,200 crystals in the barrel and 7,324 crystals in the endcaps are tapered in shape and angled at  $3^\circ$  to ensure that particle trajectories avoid cracks between them. Barrel crystals have a front face of  $22 \times 22 \text{ mm}^2$  and a length of 23 cm, corresponding to  $25.8 X_0$ . Endcap crystals have a front face of  $28.6 \times 28.6 \text{ mm}^2$  and length corresponding to  $24.7 X_0$ . Electromagnetic showers are therefore expected to be contained within one crystal length, so only a single layer of crystals is needed. A preshower detector is placed in front of the endcaps, with a thickness of  $3X_0$ , in the range  $1.653 < |\eta| < 2.6$ , in order to distinguish between single photons and photon pairs resulting from neutral pion decay. The ECAL geometry is shown in Figure 3.5.

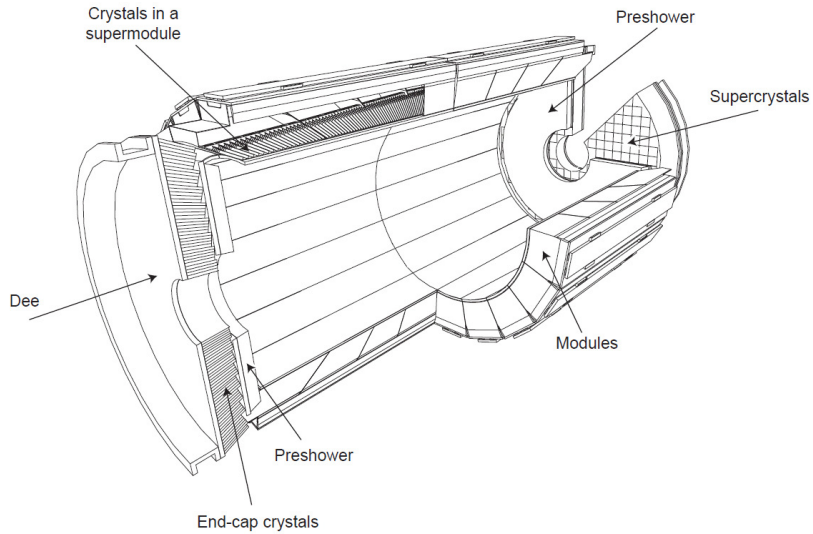


**Figure 3.5:** Geometric view of the CMS ECAL [116]. Barrel crystals are arranged in modules and supermodules, and endcap crystals arranged in supercrystals. Also shown is the preshower detector.

The very dense material  $\text{PbWO}_4$  causes incident photons and electrons to shower. Resulting pair produced electrons and positrons, and radiated photons, cause scintillation light in the transparent, polished crystals. The amount of light produced is proportional

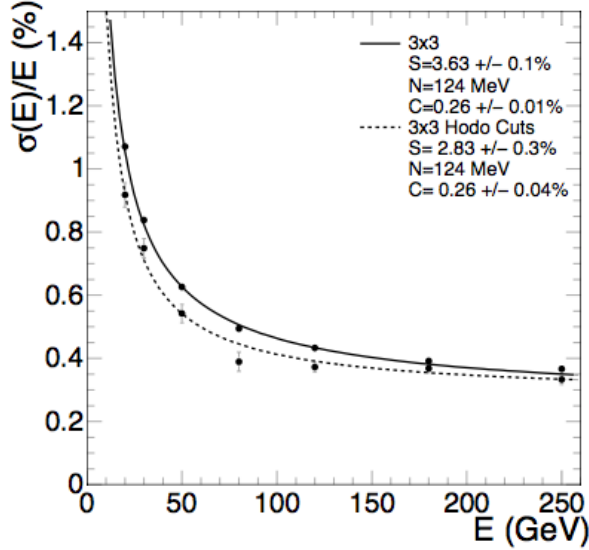


**Figure 3.6:** The energy resolution of an ECAL supercrystal, measured in a test beam. The lower set of points along the dashed line correspond to the energy measured in an array of  $3 \times 3$  crystals, where events fall within a  $4 \times 4$  mm region in the central crystal [120].

to the incident particle energy, and is collected by an avalanche photo-diode on the end of each crystal in the barrel, and a vacuum photo-triode in the endcaps. These photodetectors also have to be radiation hard and operate successfully in the 3.8 T magnetic field, while providing significant amplification of the signal. Both the crystal and photodetector performance has a strong temperature dependence, so the ECAL is kept at a constant temperature of  $18^\circ$  via a water cooling system, and is stable to  $\pm 0.05^\circ\text{C}$ .

The energy resolution of the ECAL can be parametrised using the following equation:

$$\left(\frac{\sigma}{E}\right)^2 = \left(\frac{S}{\sqrt{E}}\right)^2 + \left(\frac{N}{E}\right)^2 + C^2, \quad (3.2)$$

where  $S$  is due to stochastic scattering,  $N$  is due to noise and  $C$  is the constant term. Measurements from test beam are shown in Figure 3.6, where the terms were found to be:  $S = 2.8\%$ ,  $N = 0.12$  GeV and  $C = 0.30\%$  [116].

### 3.2.3 The hadronic calorimeter

The HCAL provides complementary energy measurements of hadronic showers, crucial for measuring jets and missing transverse energy. It is a sampling brass calorimeter, built from alternating layers of large, absorbing brass plates, interleaved with scintillating plastic tiles arranged in trays. Sitting within the bore of the solenoid, the Hadron Barrel (HB) covers pseudorapidities up to  $|\eta| < 1.3$ , and the Hadron Endcaps (HE) on each side enclose  $1.3 < |\eta| < 3$ . To attain an almost hermetic detector, there is also a Hadron Forward (HF), which extends coverage right up to  $|\eta| < 5.2$ .

The quality of the HCAL's measurements is dictated by the fraction of the hadronic shower that passes through the scintillator; the plastic must be thick enough to catch the majority of the shower. This demand for radial extension is at odds with the location of the HCAL, from the outer edge of the ECAL at  $r = 1.77$  m, to the inner edge of the solenoid at  $r = 2.95$  m. Providing a compromise, an outer hadronic calorimeter, Hadron Outer (HO), is placed outside of the vacuum tank of the magnet and supplements the HB. Using the solenoid coil as absorber material, it can identify late starting showers, providing sufficient containment for 11.8 interaction lengths. Five rings of HO are arranged along the  $z$ -axis of the detector, where the central ring at  $\eta = 0$  has two layers at  $r = 3.82$  m and  $4.07$  m, and the rest have a single layer at  $r = 4.07$  m. Figure 3.7 shows the geometry of the HCAL.

Hadron showers are created in the brass absorber plates, through nuclear interactions in the material, and the plastic scintillator tiles produce blue-violet light when the shower passes through. It is read out using wavelength shifting fibres, sending the now green light down transparent fibres to hybrid photodetectors (HPD) which produce an electrical signal proportional to the incident hadron energy. The first layer of plastic tiles is placed in front of the first absorber plate in order to sample the incoming shower as it develops in the material between the ECAL and the HCAL. The final layer of scintillator is placed after the final brass plate to catch any late developing showers. There are 70,000 plastic scintillator tiles in the HB and 20,916 tiles in the HE.

The HF uses a different technology in order to cope with the much harsher environment in which it is situated. With an average energy of 760 GeV deposited in the HF per pp collision at LHC design energy, peaking at the highest rapidity point closest to the beam line, radiation hardness and occupancy requirements demand alternative materials. Steel absorber plates are embedded with scintillating quartz fibres, which act to detect the

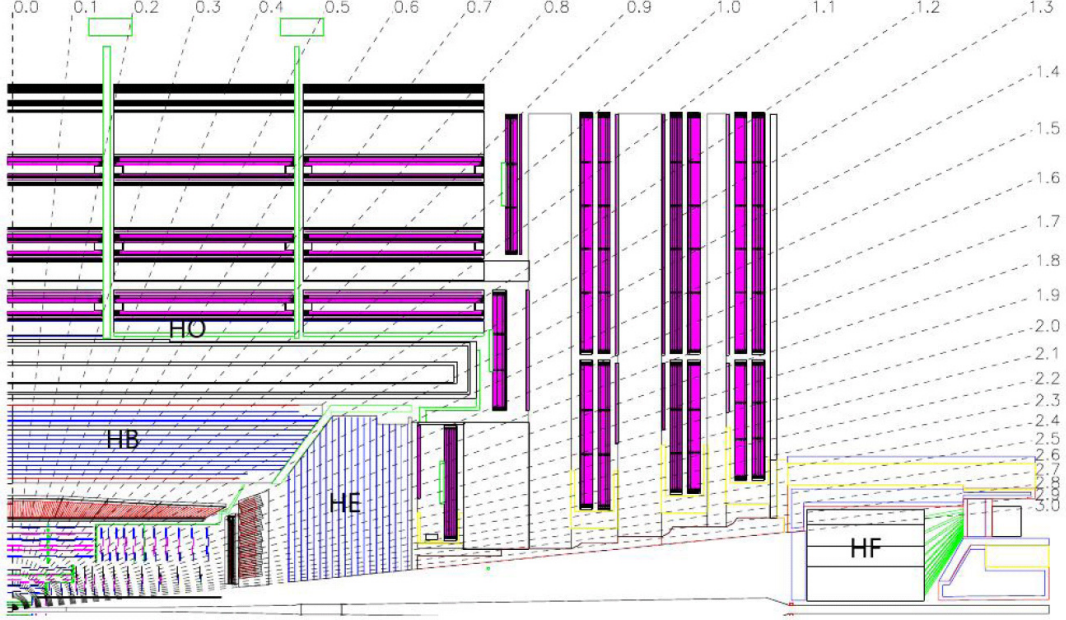


**Figure 3.7:** Longitudinal view of the CMS HCAL [116]. Locations of the HB, HO, HE and HF are shown with values of  $\eta$ . The purple regions represent the muon detectors which further restrict the volume of the HO.

Cherenkov light emitted by charged particles in the shower. It is therefore most sensitive to the electromagnetic component of the shower.

The energy resolution of the HCAL was measured in pion beam tests. The energy response and resolution are shown in Figure 3.8, and the fractional energy response is parametrised as  $\frac{\sigma}{E} = \frac{120\%}{\sqrt{E}} \oplus 6.9\%$  [120].

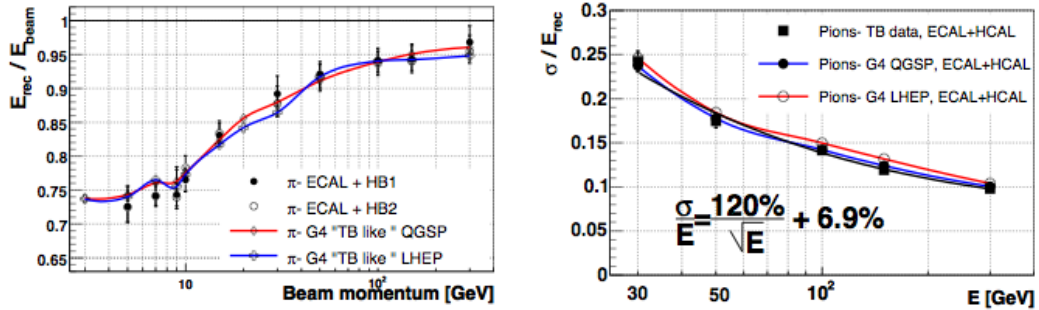


**Figure 3.8:** The raw energy response (left) and fractional energy resolution (right) as a function of energy, for pions, in team beam data [120].

### 3.2.4 The muon system

Muons are a powerful tool for recognising signs of interesting physics. A relatively easy experimental signature to identify, muons can provide excellent 2- or 4-particle mass resolutions as, due to their larger mass, they do not suffer large radiative losses (as electrons do). Muon reconstruction is therefore a central design feature. Embedded in the iron flux-return yoke of the solenoid, the muon system combines three methods of gaseous detection to identify mass, carry out high-resolution measurements of, and trigger events, up to  $|\eta| < 2.4$ . Figure 3.9 shows a cross section of one of the five wheels that make up the barrel section of the muon system; there are also two planar endcaps which sit at either end of the detector and enclose it.

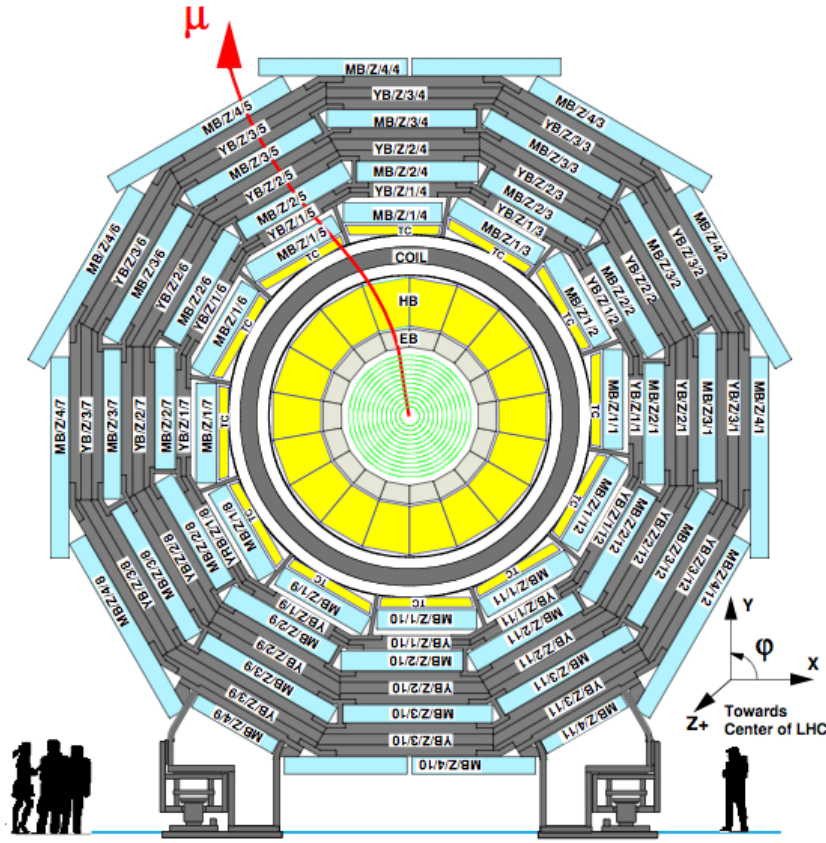


**Figure 3.9:** One of the 5 wheels of the barrel of the CMS muon system [116]. Gaseous detectors are embedded in the iron return yoke of the solenoid.

In the barrel ( $|\eta| < 0.9$ ), the magnetic flux is concentrated in the iron return yoke so the residual field is very small. There is also a low muon rate and neutron induced background, so Drift Tube (DT) chambers are used. In the endcaps ( $0.9 < |\eta| < 2.4$ ), the magnetic field and muon rates are much higher, so Cathode Strip Chambers (CSCs) are

used instead; they have a faster response time, higher granularity and better radiation hardness. Both the DTs and CSCs have excellent position resolution. An additional system of Resistive Plate Chambers (RPCs) in both the barrel and endcaps provide an independent signal which has good time resolution (and poorer position resolution) and serves as a trigger.

By combining information from the tracker, and from either the DTs or CSCs and RPCs, CMS has excellent muon reconstruction. Precise momentum resolution is achieved for the kinematic range, from 10 GeV to  $> 500$  GeV, as shown in Figure 3.10.

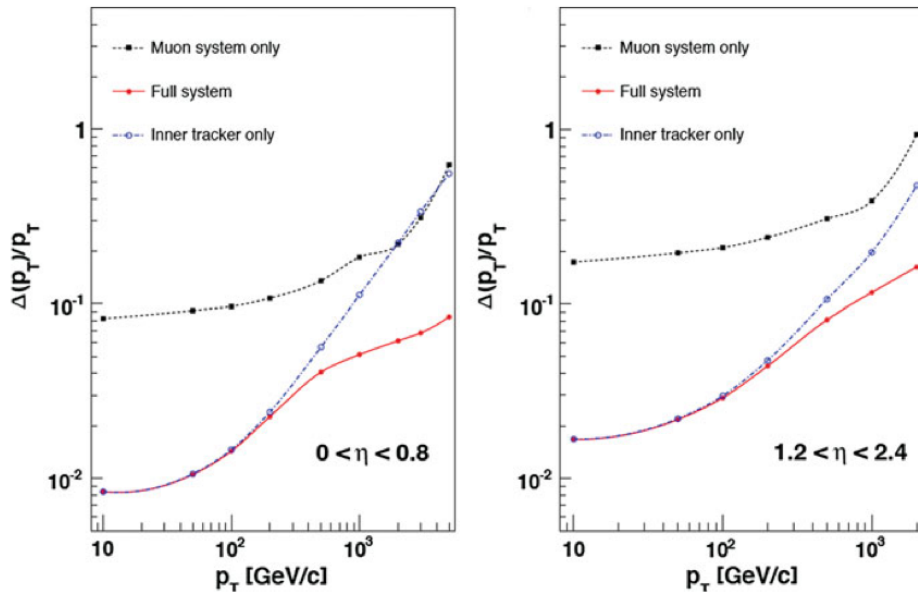


**Figure 3.10:** Muon transverse momentum resolution, shown as a function of muon  $p_T$  in the barrel (left) and the endcaps (right) [116]. The resolution of the tracker and muon system is shown, and the enhancement gained by combining the information. Here, and in several of the following plots, the units shown are not natural, indicated by the presence of  $c$  in the specified unit.

### 3.3 Event Reconstruction

It is by piecing together the information from the various subsystems of the CMS detector that, for example, a track in the tracking system, or an energy deposit in the HCAL, can be attributed to a particle or “physics object”. Figure 3.11 shows a slice of the whole detector with each of the main physics objects traversing it: muons, electrons, photons, and charged and neutral hadrons. Each of these leaves a different signature. Charged particles leave tracks in the silicon tracker, curved under the influence of the magnetic field. Electrons and photons cause electromagnetic showers, leaving energy deposits in the ECAL. Hadrons penetrate further, showering and leaving energy deposits in the HCAL. Muons are the only visible particles to reach the muon system, where they leave tracks.

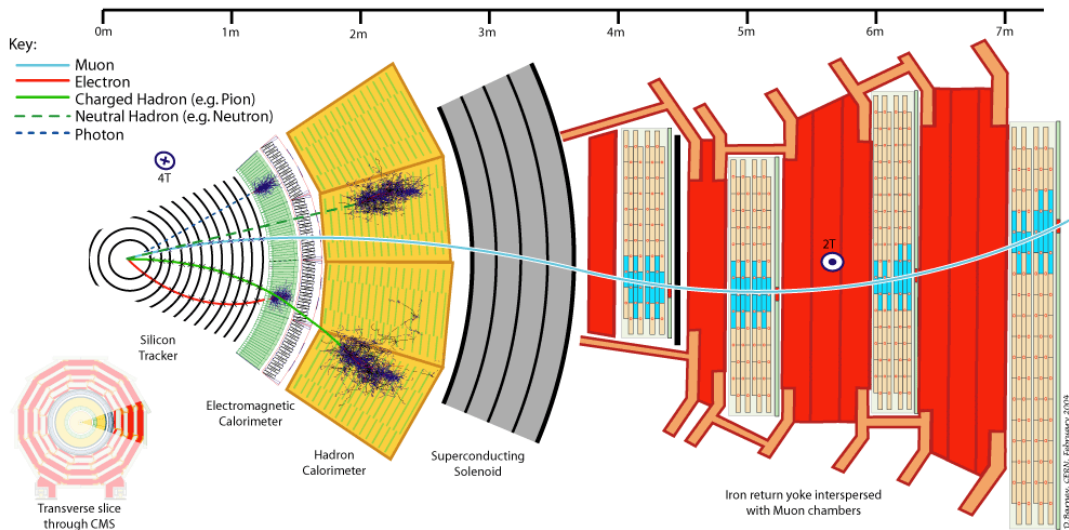


**Figure 3.11:** A slice of the CMS detector is shown, with various particles, or physics objects, traversing it. By combining information from each of the subdetectors, each of the particles produced in an event can be identified and the whole event reconstructed.

Particles can then be identified by combining tracking information with data from the calorimeters and muon system. If there is an energy deposit in the ECAL, the only way to distinguish between a photon or electron is by looking to see if there are hits in the tracker, leading to the position of the electromagnetic shower in the calorimeter. Similarly, the momentum measurement of the electron, determined using the curvature of the track it leaves (also used to reconstruct its charge), can be combined with the energy measurement made using the amount of scintillation light produced in the ECAL to get a better resolution. If there is no track leading to the electromagnetic shower,

a photon is instead reconstructed. Hadronic showers in the HCAL due to charged and neutral incident hadrons can also be distinguished by their tracks. A muon will leave the tell-tale sign of hits in the tracker, and hits in the outer muon chambers, where position, momentum and charge measurements from both ensure the initial track in the silicon tracker matches up to the track in the muon system. Dual measurements also lead to enhanced resolution.

Below is a summary of the object reconstruction most relevant to the physics analysis described in Chapter 5. More information can be found in Ref. [120].

### 3.3.1 Jets

Copious numbers of quarks and gluons are produced during pp collisions in CMS, a consequence of the huge QCD cross section. Through the strong interaction they fragment and immediately hadronize, and a spray of hadrons is produced in the direction of an initial quark or gluon. Various algorithms have been developed in order to group the spray of hadrons into a “jet”, and assign an energy, direction and transverse momentum to it.

In the analysis presented in this thesis (and in general at CMS), the anti- $k_t$  algorithm [121] is used with a distance parameter,  $R = 0.5$ . It behaves like an idealised cone algorithm, using a distance parameter to cluster particles into cone shapes, with a radius  $R$ . Soft particles are clustered with nearby hard particles rather than with themselves, leading to conical jets, which — crucially — are resilient to soft radiation on the boundary of the cone. Likewise, the area of the jet is unaffected by soft radiation on the boundary, and is equal to  $\pi R^2$ . These features make the anti- $k_t$  algorithm the preferential jet algorithm at CMS, due to its insensitivity to soft radiation that arises from sources such as PU; see Figure 3.12.

Several types of jets exist at CMS, in which the anti- $k_t$  algorithm is given different inputs. Calorimeter (Calo) jets use information from the calorimeter only. ECAL crystals are grouped in  $5 \times 5$  arrays into “towers”, which measure  $0.087 \times 0.087$  in  $\Delta\phi \times \Delta\eta$  space (in the barrel region) and are matched to aligning blocks of HCAL. The sum of the energy deposits in both layers of the calorimeter are used as inputs to the jet algorithm, where towers are treated as massless and an  $\eta$  dependent energy threshold has been placed on each tower to reduce the effect of instrumental noise.

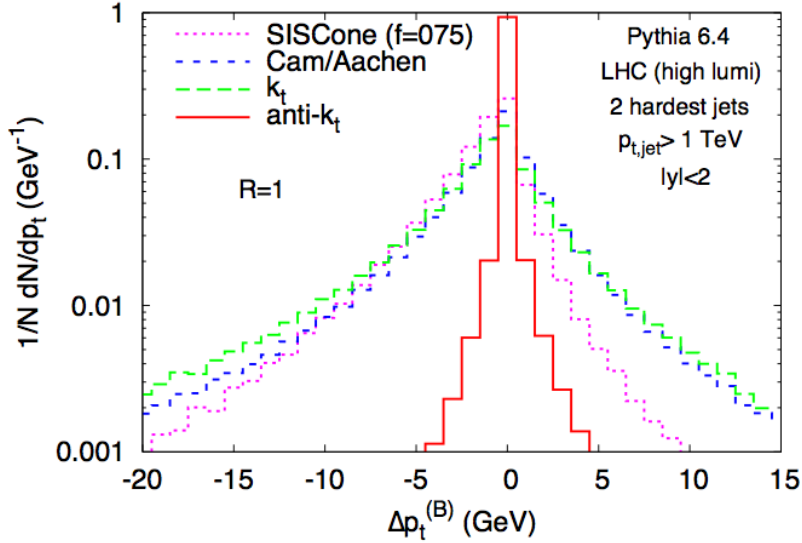


**Figure 3.12:** The relative insensitivity of the anti- $k_t$  algorithm to PU is shown, compared to other common jet algorithms. The distribution of back reaction, corresponding to the net change in  $p_T$  to each of the two hardest jets (where each jet has  $p_T > 200 \text{ GeV}$ ), when adding PU  $\sim 25$  to the event, corresponding to LHC running conditions in the next phase of data taking starting in 2015 [121].

The Particle Flow (PF) algorithm [122] creates a list of all stable particles in an event: photons, electrons, muons, neutral hadrons and charged hadrons. Particle momentum, direction and type are determined using all of the subdetectors of CMS, which, with its silicon tracker, highly granular ECAL and strong magnetic field is ideally suited to the task. The reconstruction of the fundamental constituents of a typical jet — largely photons, charged hadrons and neutral hadrons — uses charged particle tracks and calorimeter clusters, termed “elements”. A traversing particle is expected to give rise to one, or several, elements arising from separate subdetectors. To reconstruct a particle, these elements are therefore grouped into “blocks”: links of one, two or three elements that have arisen due to the same object. Blocks can then be interpreted as individual particles, and the resulting list of reconstructed particle flow particles gives a global description of each event. This list of particles is used as the input to the anti- $k_t$  algorithm, producing PF anti- $k_t$  jets.

The energy of a typical jet consists of energy from charged particles (65%), photons (25%) and neutral hadrons (10%). Therefore, typically, 90% of the jet energy can be reconstructed with good precision, utilising measurements from the high resolution silicon tracker and ECAL. Only 10% of the energy, arising from neutral hadrons, is reconstructed using the relatively poor resolution hadron calorimeter. Therefore, PF jets, made of

reconstructed particles, are much closer to **hadron-level** jets made of simulated, Monte Carlo (MC) generated particles than those that rely just on calorimeter information alone (such as Calo jets), see Figure 3.13. PF jets consequently have excellent position and energy resolution. Jet momentum resolution, defined as the ratio  $(p_T^{\text{rec}} - p_T^{\text{gen}})/p_T^{\text{gen}}$  is shown in Figure 3.14. Here, “rec” is for jets taken from **hadron-level** simulation, i.e. PF or Calo jets, and “gen” is for **parton-level jets taken from simulation jets taken from simulation**. It is because of the excellent performance of the PF algorithm, as input to the anti- $k_t$  algorithm, that it is used most commonly across CMS analyses, including in the analysis presented in this thesis.

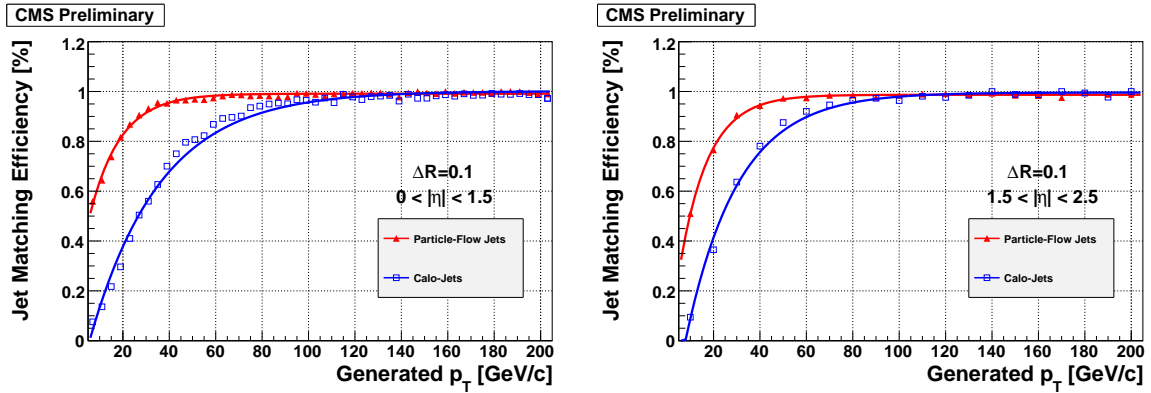


**Figure 3.13:** The efficiency of PF jets, and Calo jets, matched to generated jets in the barrel region (left) and the endcap (right), taken from [122]. The superior performance of PF jets is evident because they are more efficiently matched to the generator, “truth” jets, at a lower  $p_T$  threshold: termed a sharper turn-on.

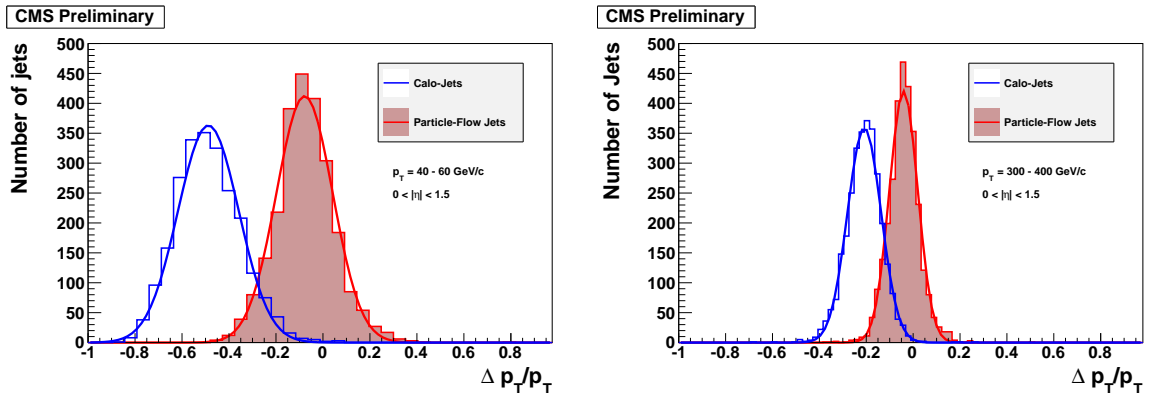


**Figure 3.14:** The momentum resolution,  $(p_T^{\text{rec}} - p_T^{\text{gen}})/p_T^{\text{gen}}$  of PF jets, and Calo jets, for low energy jets ( $40 \text{ GeV} < p_T < 60 \text{ GeV}$ ) (left) and for high momentum jets ( $300 \text{ GeV} < p_T < 400 \text{ GeV}$ ) (right) in the barrel region, taken from [122]. Not only are the peaks sharper for PF jets, meaning a smaller (and therefore better) overall momentum resolution, but it is also peaking much closer to zero, meaning the jet measurement is much closer to the generated jet momentum.

### 3.3.2 Missing transverse momentumenergy

As discussed in the previous sections, CMS is nearly hermetic, has coverage up to  $|\eta| = 5$  and excellent particle reconstruction; a very complete picture of each event is available. As such, is it very well suited to make measurements of weakly interacting particles, such as neutrinos, that do not leave any trace within any subsystem of the detector; and are only evident through an imbalance of [transverse](#) momentum. [This momentum balance is evident in the transverse plane](#), that is, in the plane perpendicular to that of the beam, as discussed in Section 3.2. Due to the unknown momenta of the initial colliding partons, as the proton is a non-fundamental particle, we are unable to conserve momentum in the direction of the beam. We are, however, able to conserve momentum [in the transverse plane; it sums vectorially to zero](#). New physics processes, such as R-parity conserving SUSY, would also lead to signatures involving a large imbalance in transverse momentum as the weakly interacting LSP exits the detector. DM production would also lead to such a signature. Measurements of missing transverse energy and momentum are therefore crucial to the search for new physics at CMS, as they have been crucial in previous discoveries — for example of the W boson [123], and in searches for other related processes [124, 125].

The missing transverse [momentumenergy](#) vector,  $\vec{p}_T^{\text{miss}}$  is formed by adding the transverse [momentumenergy](#) vectors  $\sum \vec{p}_T$  of all the particles formed in an event. The missing transverse [momentumenergy](#) vector  $\vec{p}_T^{\text{miss}} = -\sum \vec{p}_T$ , where  $|\vec{p}_T^{\text{miss}}| = p_T^{\text{miss}} = |\sum \vec{p}_T|$ ; i.e., it is equal in magnitude and opposite in direction to the total visible [momentumenergy](#) in the event. It is worth noting that the missing transverse momentum is often written as the missing transverse energy,  $\vec{E}_T^{\text{miss}}$ . Although technically wrong, as energy is not a vector quantity, the two are used interchangeably as any masses involved are negligible and we usually take the magnitude of the transverse momentum vector, a scalar quantity. In an analogous way to jets (and usually using such jets),  $p_T^{\text{miss}}$  can be built using various algorithms. Calorimeter (Calo)  $p_T^{\text{miss}}$ , in the same way as Calo jets, is built from calorimeter information alone while PF  $p_T^{\text{miss}}$  is calculated from all of the transverse energies of reconstructed particles in an event. In a similar way to the jet algorithms, a better resolution is achieved using the PF algorithm over calorimeter information alone, see Figure 3.15. However, because energy measurements of particle flow objects are driven by calorimeter resolution, particularly for large  $E_T$  objects, the improvement is less marked. In the analysis presented in this thesis, PF  $p_T^{\text{miss}}$  is used, where any muons present have been removed from the calculation. It therefore mimics Calo  $p_T^{\text{miss}}$ , only with an enhanced resolution.

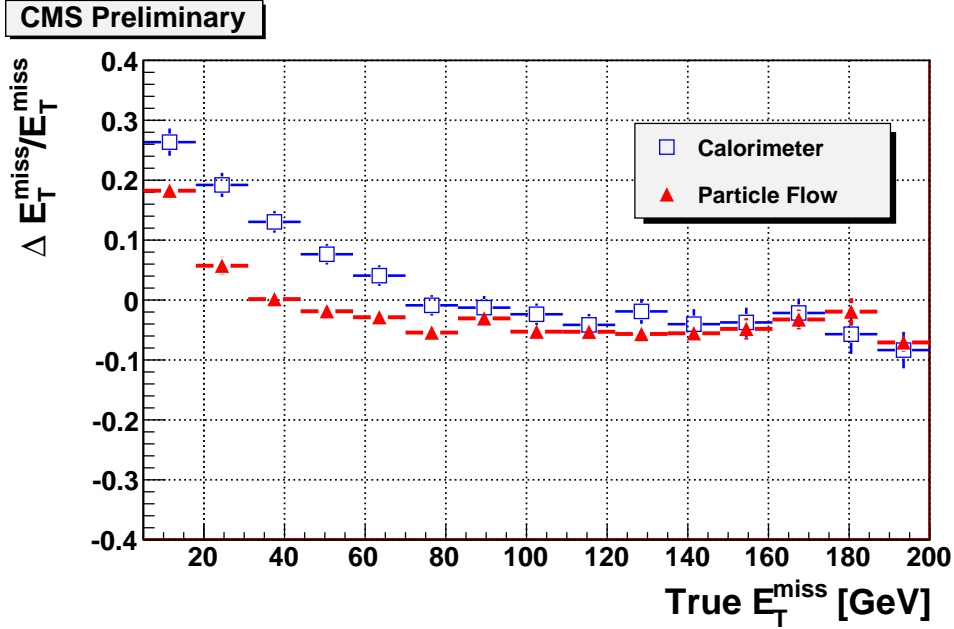


**Figure 3.15:** The missing transverse momentum resolution,  $(p_{T,\text{rec}}^{\text{miss}} - p_{T,\text{gen}}^{\text{miss}})/p_{T,\text{gen}}^{\text{miss}}$  of PF and Calo  $p_T^{\text{miss}}$ , taken from [122]. An improved resolution is seen using the PF algorithm, particularly at low values of  $p_T^{\text{miss}}$ . At higher  $p_T^{\text{miss}}$  values, energy measurements are dominated by the calorimeter resolution and values using the two different methods converge.

### 3.3.3 Muons

Muons are reconstructed using the muon systems and the tracker, and the reconstruction algorithms use the concept of “regional reconstruction”. On the basis of an input or seed from the muon systems, the software only reconstructs the part of the tracker from which the muon causing the seed could originate. This means that only a very small part (typically a few percent) of the tracker volume must be processed to reconstruct a muon; thereby speeding up the procedure and reducing the CPU power necessary to process an event.

Muon reconstruction has three stages: local, standalone and global reconstruction. Starting with a seed which defines a region of interest, which could be from the L1 Trigger seeds (from the RPCs) or from patterns of hits found in the CSCs and/or DTs, a local reconstruction is performed in surrounding compatible muon chambers. The standalone reconstruction uses information from just the muon system; measurements of track position, momentum and direction of travel are taken, and extrapolated to the nominal interaction point. Global reconstruction then extends the resulting muon trajectories to include hits in the silicon tracker. A track is extrapolated from the innermost

muon chamber to the outer tracker surface, and compatible silicon layers determined. Candidates for the muon trajectory are built from pairs of hits in separate layers of the tracker and the  $\chi^2$  of the fit is used to ensure a “good” muon candidate; to detect any bremsstrahlung or significant energy loss. High energy muons present particular difficulty as they suffer huge energy loss and undergo large severe electromagnetic showers in the muon system; the  $\chi^2$  probability of the fit compared to the  $\chi^2$  probability of the tracker only trajectory allows accurate momentum reconstruction of such objects.

### 3.4 The Trigger

The pp interaction cross section is 100 mb, while for example, the W boson production cross section is some 6 orders of magnitude less than this, and the rare physics processes that CMS was built to search for, such as Higgs boson and SUSY production, many times smaller still; see Figure 3.16. The LHC delivers an unprecedentedly high instantaneous luminosity so that such rare physics processes occur, but this also implies that the vast majority of the collisions result in ‘uninteresting’ physics: namely relatively low energy, soft scattering events. It would be impossible to record the very high volumes of data that come out of CMS, some Petabytes per second, and not useful to do so. Therefore, a very efficient method of recording those events that appear ‘interesting’ is necessary.

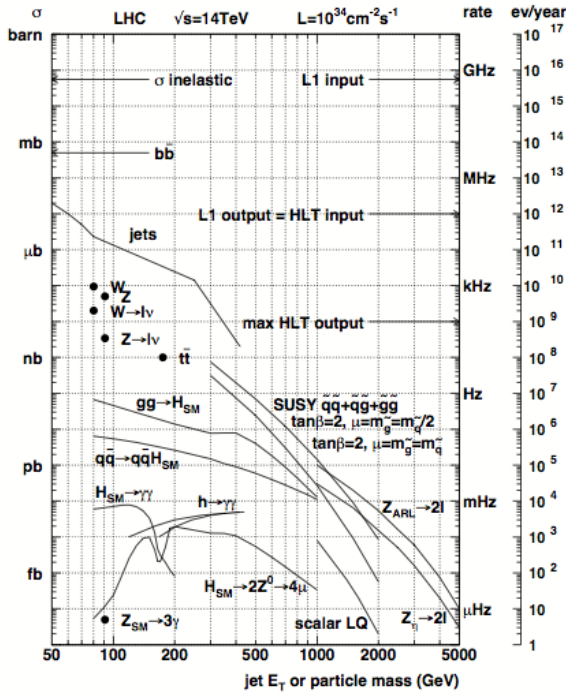


**Figure 3.16:** Inclusive pp cross sections ( $\sigma$ ) for basic and rarer physics processes, showing some of the phenomena on the physics programme at CMS. Shown on the right are the interaction rates for LHC design luminosity,  $10^{34}\text{cm}^{-2}\text{s}^{-1}$  [126].

A two tier trigger system reduces the 40 MHz LHC bunch crossing rate to an output of 100 Hz, which is then saved offline to be reconstructed ready for physics analysis. The hardware based L1 trigger uses fast algorithms with coarse inputs from the calorimeter and muon system to efficiently select, online (that is at the same rate as LHC bunch crossings), those events that appear interesting. This reduces the 40 MHz collision rate to 100 kHz. A software based Higher Level Trigger (HLT) running on the event filter PC

farm at Point 5 takes the output of the L1 trigger and reduces it further to 100 Hz, using more sophisticated inputs and algorithms. Performance of the subdetectors and readiness to collect data, monitored by the Data Acquisition System (DAQ) system, is supervised by the trigger control system. Events passing HLT selection requirements are sent to the CERN Computing Centre where complex algorithms using all the information from the CMS detector are used to fully reconstruct the event. More information on the CMS trigger can be found in Ref. [126].

### 3.4.1 The L1 trigger

Low granularity inputs from the calorimeter and muon system are used to quickly select possibly interesting events, based on predefined and programmable algorithms and criteria. Parts of the hardware are Field Programmable Gate Array (FPGA) based, allowing some flexibility in algorithms, while other parts are Application Specific Integrated Circuit (ASIC) based, with predefined criteria. Events are selected if they show signs of interesting physics; for example have jets, electrons/photons, or muons. Global quantities such as total transverse energy and total missing transverse energy are also used. In order to see if an event contains any of these physics objects above a pre-defined energy threshold or multiplicity, the L1 trigger is separated into the Calorimeter Trigger, which looks for jets, photons and electrons, and the Muon Trigger, which looks for muons. Global quantities are computed at the Global Trigger (GT) and combined with information from the Calorimeter and Muon triggers, and here a decision is made to keep or reject an event.

In the Calorimeter Trigger, information from the ECAL, HCAL and HF are combined. First, the calorimeter is split into different (geographical) regions, and electron, photon and jet finding algorithms run on the separate parts of the subdetectors at the Regional Calorimeter Trigger (RCT). Information from the different regions is then combined *inat* the Global Calorimeter Trigger (GCT). In the Muon Trigger, information from the DT, CSCs and RPCs are combined. Muon track finding algorithms are applied to data from the DT and CSCs *inat* the Regional Muon Trigger (RMT), and the Global Muon Trigger (GMT) combines information from all of the three subdetectors to get an enhanced resolution. Inputs from the GCT and GMT are then combined *inat* the GT, where the decision to keep or discard an event is made. The architecture of the L1 trigger is shown in Figure 3.17.

There is an inbuilt latency of  $3.2 \mu\text{s}$  in the L1 trigger, meaning that on the first bunch crossing, it takes up to  $3.2 \mu\text{s}$  to transmit the necessary information, and make a decision. This is driven by the data storage available for information from the tracker and preshower detectors; they need so much data storage that it must be saved before a L1 accept decision, and subsequent event read out, can be made. The decisions on the rest of the bunch crossings follow at the rate of collisions, and the architecture is ready to accept another event every 25 ns.

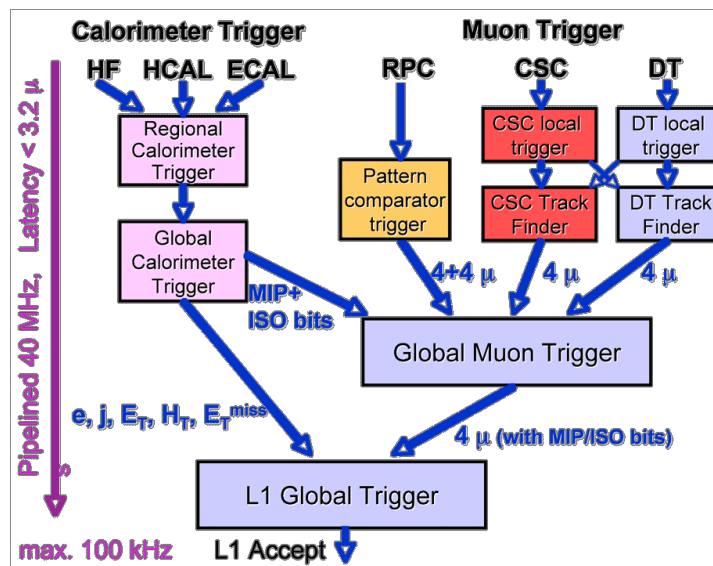


**Figure 3.17:** Architecture of the L1 trigger. The calorimeter trigger takes inputs from the ECAL, HCAL and HF. The muon trigger takes inputs from the DT, CSCs and RPCs. A decision is made at the L1 GT, using inputs from the GCT and the GMT, of whether to pass an event onto the HLT or discard it.

A L1 accept decision is based upon the results of the various physics object reconstruction algorithms. Typically, every physics analysis has a type of event it is searching for; a particular topology. For example, the monojet analysis looks for events with a final state of one high  $p_T$  jet and large missing transverse energy. At L1, it requires the global variable **of an event, total missing transverse momentum to be energy** above 36, 40 or 50 in L1 units of energy. A L1 trigger menu, comprised of all of the required L1 seeds for the whole physics programme at CMS, gives a certain bandwidth to each of the seeds. A low threshold seed will typically demand a large amount of bandwidth as more events are likely to be lower in energy, whereas a high threshold will require a lower bandwidth. Combined, the output to the HLT of all of the L1 seeds in the trigger menu must not exceed the design rate of 100 kHz.

### 3.4.2 The high level trigger

When an event is accepted by the L1 trigger, the full detector information for that event (consisting of around 1 MB of data) is passed onto the HLT. On the event filter farm, which consists of over 1000 PC's, all of the detector information for each event is processed. Information not available at L1 becomes available. The additional computing power and longer time scales mean the full granularity of the calorimeter and tracker information (as well as L1 objects) can be used as inputs to more complex algorithms. As a result, much more stringent requirements are used to select events of interest, creating datasets which are used for offline analysis.

An analysis will typically use more than one HLT trigger, and similarly more than one analysis might use the same trigger (and an event pass more than one trigger). For example, the monojet analysis uses a combination of three triggers which demand large missing transverse momentum in every event, or a single high momentum jet in addition to large missing transverse momentum. This allows events with a monojet topology to be selected efficiently; further kinematic and topological selections are applied offline to a dataset formed of events passing these trigger requirements. Similarly, every physics analysis uses a trigger (or triggers) suited to the topology under investigation.

In the same way that there is a L1 trigger menu, there is also an HLT menu comprised of all of the HLT trigger paths, and the bandwidths they require, which meets the needs of all of the physics analyses at CMS. The total bandwidth of the HLT menu must not exceed 100 Hz or 100 events saved offline per second; it is limited by the resources necessary to process and store events, namely the number of Computer Processing Unit (CPU)s and the disk space available.

# Chapter 4

## Jet Algorithms for the L1 Trigger Upgrade

In the hadron rich environment of the LHC, jets are very important. Whether for SM analyses, Higgs searches, SUSY searches or exotic analyses, jet reconstruction is vital for both online event selection and offline analysis, for a wide range of kinematic requirements. Efficient and reliable triggering on jets is therefore of key importance and the first stage of event selection, the L1 trigger, must have an effective jet algorithm. This is of particular significance as we look towards the LHC upgrade, when running conditions become increasingly challenging. Up to double the instantaneous luminosity and centre-of-mass energy lead to an increase in PU up to  $\sim 70$  and far higher detector occupancies. Jet algorithms must maintain a similar performance in this next phase of LHC running as exhibited in the previous period of data collection. A new L1 jet algorithm is proposed, which exploits the full granularity of the calorimeter and uses event-by-event PU subtraction.

### 4.1 The LHC Upgrade

There are various phases of planned LHC upgrades, as discussed in Chapter 3. The algorithm described in this chapter is for implementation in Run 2, from 2016. The new trigger architecture is being installed during LS1, and the system will be commissioned during 2015 (the first year of Run 2), ready to be brought online in 2016 when it will replace the current system. The two trigger systems (current and upgrade) will run in parallel during 2015, to make sure that CMS is never without a functional L1 trigger.

### 4.1.1 Motivations for a new L1 jet algorithm

If, during Run 2, the machine operates at 50 ns, the instantaneous luminosity will double compared to that of Run 1, with PU expected to more than double from around 20 inelastic collisions per bunch crossing to, perhaps, in excess of 70. Not only will the number of interactions per second increase due to the higher instantaneous luminosity, but the increased centre of mass energy means the energy of these interactions will also increase. Consequently, for a particular trigger (say, for example a single jet trigger), many, many more events will pass a particular energy threshold as compared to Run 1. As a result, the trigger rate will soar.

For a single jet trigger, where the jet (reconstructed offline) is required to be above 128 GeV, 95% of jets which have been matched to this offline jet and reconstructed using the existing L1 jet algorithm are above 150 GeV—where the higher L1 threshold is due to poorer L1 reconstruction than offline reconstruction. In a typical Run 1 run during 2012 ( $\text{PU}=15$ ,  $\mathcal{L} = 0.4 \times 10^{34} \text{ cm}^{-2}\text{s}^{-1}$ ), a L1 jet threshold of 150 GeV corresponds to a rate of 1.1 kHz. In the high PU test runs during 2012, this trigger rate rose to 3.6 kHz ( $\text{PU}=45$ ,  $\mathcal{L} = 1.1 \times 10^{34} \text{ cm}^{-2}\text{s}^{-1}$  equivalent); and simulation shows that in similar conditions but at 14 TeV, a trigger rate of 14 kHz is expected. The total rate of all of the L1 triggers is capped at 100 kHz by design, and a balanced trigger menu is desirable to satisfy all of the physics demands of CMS. Therefore, individual trigger rates must be kept reasonably low to ensure the total L1 trigger rate is acceptable. The only way to maintain low trigger rates in the more challenging run conditions is to increase energy thresholds. Figure 4.1 shows an illustrative L1 trigger menu for the upgraded LHC during Run 2, for two luminosity scenarios which have bunch spacings of 50 ns (centre column) and 50 ns (right column). Thresholds have had to be significantly raised to maintain a total rate below 100 kHz; for example, the single jet threshold is increased from 128 GeV in Run 1 to 170 GeV and 205 GeV for 50 and 25 ns bunch crossings respectively.

For the physics requirements of CMS the necessary increase in L1 thresholds, and corresponding increase in offline (analysis) thresholds, is an unacceptable compromise as lower energy final states are crucial to many analyses and keeping as much physics, at as low thresholds as possible, is desirable. To cope with the challenges of the LHC upgrades, and to enable new algorithms (with better performance) to be developed so the physics performance of Run 1 can be maintained, or bettered, the CMS L1 trigger is undergoing upgrades.

Trigger Algorithm	Current Level-1 $L = 1.1 \times 10^{34} \text{ cm}^{-2}\text{s}^{-1}$			Current Level-1 $L = 2.2 \times 10^{34} \text{ cm}^{-2}\text{s}^{-1}$		
	Rate [kHz]	95% Threshold [GeV]	Plateau Efficiency	Rate [kHz]	95% Threshold [GeV]	Plateau Efficiency
Single e/ $\gamma$	12	46	1.0	10	67	1.0
Single iso e/ $\gamma$	10	38	0.9	9.4	52	0.9
Single Mu	12	23	0.95	11	42	0.95
Single isoTau	10	65	0.3	9.2	72	0.3
iso e/ $\gamma$ + e/ $\gamma$	10	24 15	0.9	16	26 16	0.9
Mu + Mu	6.3	18 10	0.9	7.4	20 12	0.9
Tau + Tau	7.5	36 36	0.1	8.2	36 36	0.1
iso e/ $\gamma$ + Mu	9.6	21 11	0.85	6.2	24 12	0.85
Mu + e/ $\gamma$	3.3	18 14	0.95	5.0	20 15	0.95
Single Jet	6.4	170	1.0	5.4	205	1.0
Double Jet	4.6	140 140	1.0	5.8	170 170	1.0
Quad Jet	9.4	4@71	1.0	4.8	4@96	1.0
Single iso e/ $\gamma$ + Jet	7.5	32 68	0.9	8.5	38 82	0.9
Single Mu + Jet	8.6	22 43	0.95	7.5	27 54	0.95
Single iso e/ $\gamma$ + $H_T^{\text{miss}}$	10	29 110	0.9	8.2	38 120	0.9
Single Mu + $H_T^{\text{miss}}$	4.6	18 89	0.95	9.8	20 93	0.95
$H_T$	3.9	500	1.0	5.4	580	1.0
Total Rate	94			92		

**Figure 4.1:** A possible Run 2 L1 trigger menu, using the current L1 system and algorithms, where  $\sqrt{s} = 14 \text{ TeV}$  [119]. The numbers here are for illustration purposes only - they are not a proposed trigger menu. In the left hand column, all of the different triggers contributing to the menu are shown. In the centre (right-hand) columns, the projected L1 trigger rate, 95% threshold and plateau efficiency are shown for possible Run 2 running conditions with bunch spacing of 50 ns,  $\mathcal{L} = 1.1 \times 10^{34} \text{ cm}^{-2}\text{s}^{-1}$ , PU=50 (25 ns,  $\mathcal{L} = 2.2 \times 10^{34} \text{ cm}^{-2}\text{s}^{-1}$ , PU=50).

## 4.2 CMS Trigger Upgrade

Upgrades to the electronics of the calorimeter trigger, muon trigger and global trigger are under way in order to meet the triggering demands of CMS. These upgrades involve installing additional interconnections between the systems, reducing the current huge diversity of electronics cards to a small number of multi-purpose and adaptable cards, using high bandwidth optical links and modern, high powered FPGA processing chips. These upgrades not only allow more information from the detector subsystems to be used as inputs to improved (more sophisticated) algorithms, due to increased logic resources and fast links, but crucially also allow far more flexibility in the L1 trigger system. In Run 1, the ability to adapt the trigger algorithms and menu to evolving LHC run conditions proved vital in reducing trigger rates and improving efficiencies. Increasing the flexibility by making more of the system adaptable, and more of the cards standardised, will only improve the trigger and enhance its longevity. Having the ability to easily update software and firmware, as well as trigger architecture, in response to unforeseen circumstances — not just in the planned LHC upgrades to 2016 but far beyond — will put CMS in an excellent position for data collection.

The new L1 trigger is being installed during LS1, and will be commissioned and run concurrently with the existing trigger during Run 2. The upgraded system will be available for physics in 2016. Here, I discuss in detail the calorimeter trigger upgrade, as this is what the proposed jet algorithm, detailed in this chapter, relies upon. More information on the muon trigger and global trigger upgrade can be found in Ref. [119].

### 4.2.1 Calorimeter trigger upgrade

The calorimeter trigger uses information from the ECAL and HCAL to look for electrons/photons and jets, as described in the previous chapter. It currently is based upon a traditional trigger design; where the detector is spatially segmented into different processing nodes, each of which deals with the data from each geographical region, and does so at every bunch crossing. The desire for far more flexibility in triggering motivates a new approach to the upgrade trigger architecture, known as time-multiplexing. Instead of splitting the detector into geographical regions and sending the data to different processors at every bunch crossing, a Time-Multiplexed Trigger (TMT) [127] places all of the data from the detector in a single processor across several bunch crossings. No data

are thrown away at any stage of the process, and all of the data, at its full granularity, is available in the same card making many more algorithms possible.

### Traditional trigger architecture

A conventional trigger architecture is shown in Figure 4.2. The calorimeter is split into geographical regions in  $\eta - \phi$ , and at every bunch crossing data from the individual regions are sent to different processors. Boundaries between these regions must be duplicated in each implicated processor, to ensure that any objects found along the boundary are sufficiently dealt with. To achieve a compact implementation, at each stage of the trigger process the volume of data is reduced and the minimal information with which to make a decision is passed onto the GT. Therefore, a lot of the information from an event is discarded before a decision at the GT is made. In addition, the current calorimeter trigger does not use the full granularity of information available, and the combined ASIC and FPGA hardware, although permitting some flexibility in algorithms and parameters, is restricted by a fixed data flow. Not all algorithms can therefore be implemented, and the coarse inputs limit the possible performance.

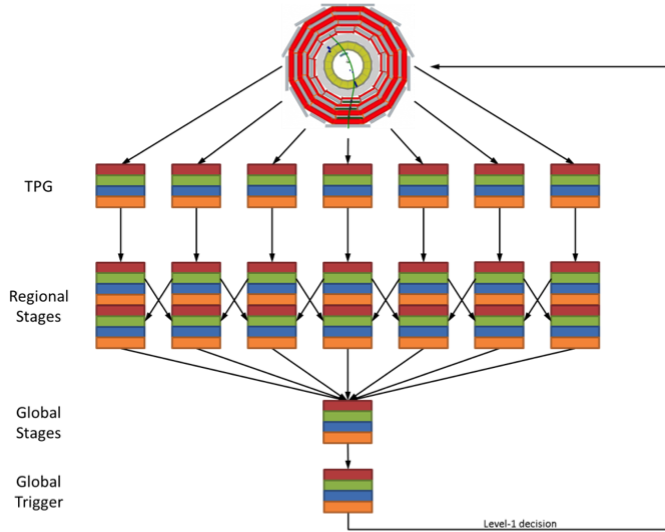


**Figure 4.2:** Conventional trigger architecture, showing data processing in regions [128]. Here, and in Figure 4.3, ‘TPG’ stands for trigger primitive generators.

Energy clusters are built into physics objects with which the GT can make a decision over two processing layers. Trigger towers, consisting of groups of  $5 \times 5$  crystals in the ECAL, and the corresponding blocks of the HCAL, are themselves grouped into  $4 \times 4$  arrays or “regions”. These regions are used as inputs to the various object algorithms.

In the first layer, the ‘Regional stages’ in Figure 4.2, the regions, or clusters of transverse energy are assigned a type; electron/photon-like, if the energy is predominantly in the ECAL, otherwise hadron-like. In the second processing layer, the ‘Global Stages’, the cluster type is identified as an electron/photon or tau (for high energy or isolated deposits respectively), and non-isolated clusters are grouped together to form jets. The jet finding algorithm looks for energy deposits in windows of  $3 \times 3$  regions, with the requirement that the central region has a larger transverse energy deposit. The top four candidates are passed onto the global trigger, with the rest discarded. Also in this layer of processing, the value and direction of the total missing transverse momentum are calculated from the sum of energy deposits across the calorimeter, and jet candidates above threshold are summed to give the total hadronic energy content, known as  $H_T$ .

### Time multiplexed trigger

A time-multiplexed trigger architecture is shown in Figure 4.3. In a similar way as the HLT, it will consist of parallel nodes, each of which process individual events concurrently [127]. All of the data from an event — from the whole  $\eta - \phi$  range of the calorimeter and at full granularity — are sent to an individual processor. The first processor receives the data from the first bunch crossing over  $N$  clock cycles (where the length of a clock cycle is equal to the time between bunch crossings, 25 or 50 ns). The data from the second bunch crossing are sent to the second processor, again over  $N$  clock cycles, and so on; where there are more than  $N$  processors in total, as each processor needs time to process each event. After the first processor has processed all of the data from the first bunch crossing and passed it on to the next stage of the trigger, the ‘Demux’ in Figure 4.3 (some  $N + X$  clock cycles after the first bunch crossing where  $X$  is the time taken to process and send on the data), it can then receive data from another bunch crossing. Developments in large FPGA chips and increased rate and volume of data transmission in optical fibres make this kind of architecture possible for the upgraded CMS L1 calorimeter trigger, whereas it was not when the current trigger was designed and built. The system latency,  $N + X$ , is now small enough, due to the increased processing power and bandwidths, that it is viable in hardware for the huge amounts of data and short time-scale that the trigger demands [127].

With all of the data, at full granularity, in one single processor, many more algorithms for object reconstruction are possible. Tower level calorimeter inputs (rather than region level inputs) will be available, increasing the granularity by a factor of  $4^2$ , with similarly

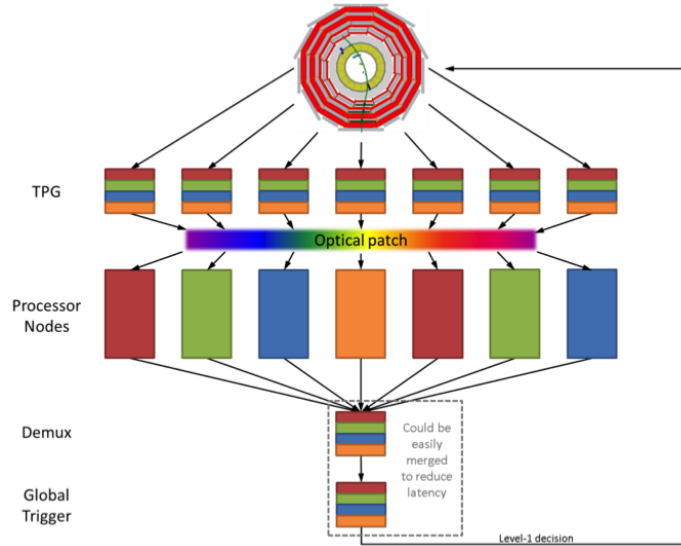


**Figure 4.3:** Time-multiplexed trigger architecture, showing data pipe-lining to different processing nodes [128].

improved spatial resolutions. There is also scope for an array of additional variables, using information from the whole calorimeter. For example, the average energy deposit for each row in  $|\eta|$  or ring of  $\phi$  can be calculated, and used to give an estimate of PU on an event-by-event basis. In the remainder of this chapter, a jet algorithm is proposed for the upgraded L1 calorimeter trigger. More detail on the CMS L1 calorimeter trigger upgrade can be found in Ref. [129].

### 4.3 Algorithm for Jet Reconstruction at L1

A jet algorithm to reconstruct, filter and calibrate L1 jets is proposed, for the upgraded CMS calorimeter trigger. It is assumed that all of the L1 calorimetric information for a single event streams through a single processor; that is, all of the information from a single bunch crossing can be processed in one single chip. This is compatible with the TMT architecture which will be available after LS1 [at CMS, ready to be brought online fully in 2016](#)[LS2 at CMS](#).

Using tower level information, the algorithm creates a tunable sized jet at each site on the calorimeter, filters out zero-energy jets and repeats, to get the ‘best’ 13 jet candidates per event. The [medianaverage](#) jet energy density for each event is calculated, and subtracted from the energy deposited across the calorimeter in order to perform PU

subtraction on an event-by-event basis. The 13 jet candidates are then calibrated to offline energy. This algorithm is compared to the current L1 jet algorithm: a much improved spatial resolution is seen, as well as enhanced, and crucially, more PU independent, energy resolution. The resulting trigger turn-on curves for various jet energy thresholds, and trigger rates for single and multijet triggers are improved compared to the current algorithm, as well as rates for the global variable  $H_T$  trigger. This jet algorithm was the proposed jet algorithm in the CMS L1 Trigger Upgrade Technical Design Review, Ref. [119]. With help from A. Rose for the initial algorithm idea, the author was responsible for all of the work that follows on this jet algorithm: designing and implementing the algorithm, refining and testing it, calibrating the jets, and characterizing performance.

### 4.3.1 Jet reconstruction

The proposed jet algorithm uses the full granularity of the calorimeters available at L1; that is,  $5 \times 5$  ECAL crystals grouped together into towers, with the corresponding block of HCAL. In the centre of CMS, each tower measures  $0.087 \times 0.087$  in the  $\eta - \phi$  plane, with the  $\eta$  dimension increasing as  $\eta$  increases; see Figure 4.4. In total there are 72 towers in the  $\phi$  direction, and for  $|\eta| \leq 3.0$  (the barrel region), 56 towers in the  $\eta$  direction. The sum of energy deposits in both the ECAL and HCAL at each tower is used as input to the algorithm.

A group of  $n \times n$  towers is combined to form a jet candidate, where the energy of that jet candidate is the sum of the  $n \times n$  towers it consists of. The jet size,  $n$ , is completely flexible, as well as the jet shape. Jet sizes of  $8 \times 8$  to  $12 \times 12$  were studied, and both circular and square jets. This compares with the current L1 jet algorithm, which consists of equivalent  $12 \times 12$  square jets - where the towers are incorporated into regions, each measuring  $4 \times 4$  towers; see Figure 4.5 for a comparison of the current and proposed upgrade jet geometry. For circular jets the size  $n$  represents the length of the diameter, for square jets it represents the length of the side.

A candidate is created at each individual tower, using a “sliding window” approach. Only jet candidates with non-zero energies are passed onto the next stage, however there remains a huge jet multiplicity at this first stage of jet creation. There is a jet for every non-zero tower, and a huge number of overlapping jets as each tower contributes to  $n^2$  different jets, or, equivalently, each jet candidate has  $(2n - 1)^2$  overlapping jets. Figure 4.6 shows some of the jet candidates which overlap, shown in red, with a single jet

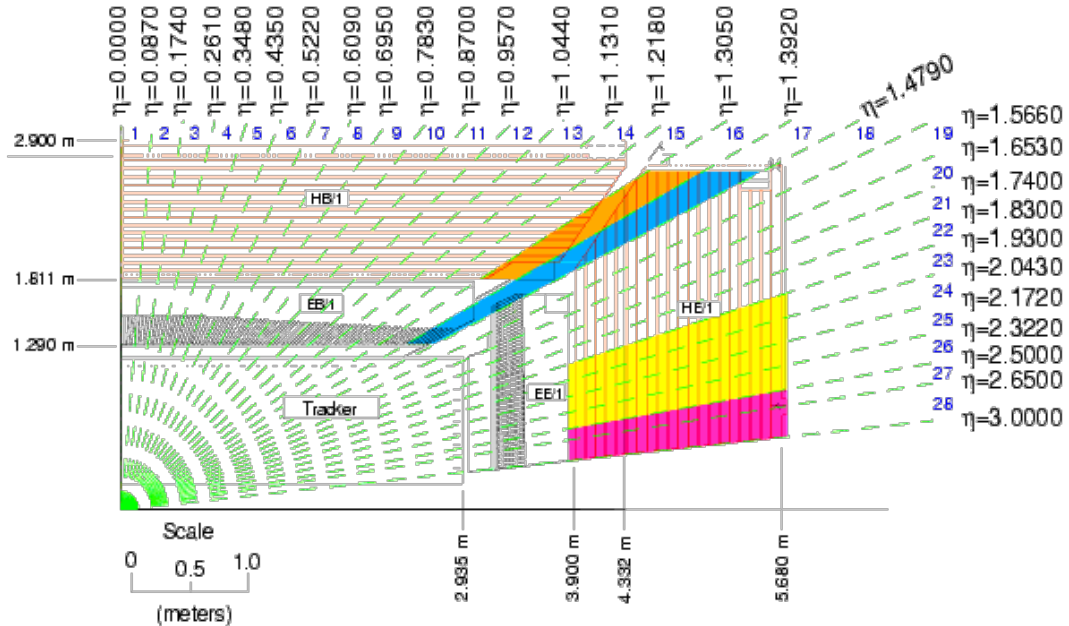


**Figure 4.4:** Layout of trigger towers in the  $r - z$  projection, for  $0 < \eta < 3.0$ . Both ECAL and HCAL towers are shown.

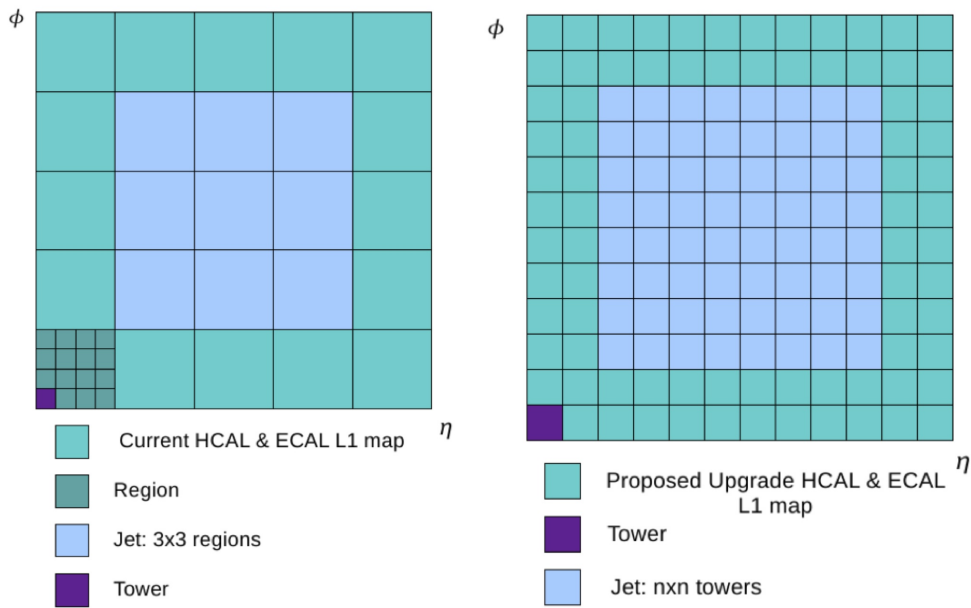


**Figure 4.5:** Comparison of the current L1 jet map, left, with the proposed upgrade jet map, showing a  $8 \times 8$  square jet, right.

candidate measuring  $4 \times 4$  towers and square in shape, shown in purple. The window of all overlapping candidates is shown in blue; and measures  $10 \times 10$  towers. The resulting

numerous overlapping jets must be sorted and filtered to find the highest energy jet of the candidates.

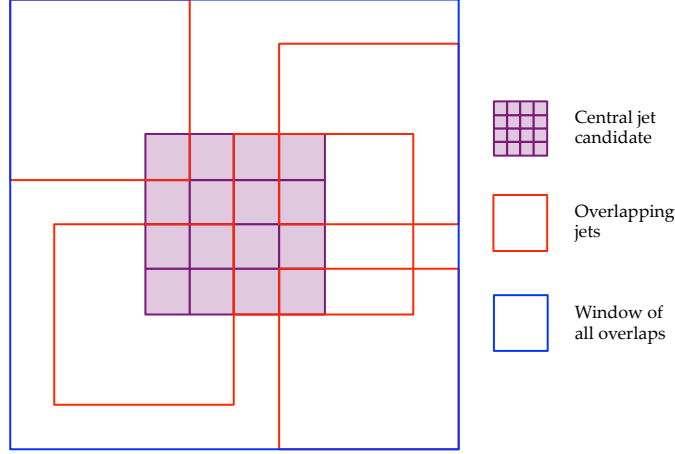


**Figure 4.6:** A few of the overlapping jets of one  $4 \times 4$  jet (centre, purple), are shown in red. The window of all of the jet overlaps is shown in blue, measuring  $10 \times 10$ . These overlapping jets must be sorted and filtered to keep only the most energetic jet.

To give the best angular resolution, the  $\eta$  and  $\phi$  coordinates of the jets are energy weighted,

$$\eta_{jet} = \frac{\sum \eta_{tower} \cdot E_{tower}}{\sum E_{tower}} \quad (4.1)$$

$$\phi_{jet} = \frac{\sum \phi_{tower} \cdot E_{tower}}{\sum E_{tower}}. \quad (4.2)$$

Here, the sum is over all of the towers in a jet window and  $\eta_{tower}$ ,  $\phi_{tower}$  are the coordinates of the individual towers within a jet,  $E_{tower}$  is the transverse energy deposit in the tower and  $\eta_{jet}$ ,  $\phi_{jet}$  are the coordinates of the jet.

In my previous studies diameter 8 circular jets, because they are smallest, gave the best angular resolution, so these are presented here.

### 4.3.2 Jet filtering

The jet collection must be sorted and filtered to remove the numerous overlaps. Firstly, all jets in each event are ordered in energy using a bitonic sort. This is a recursive parallel sorting algorithm suitable for implementation in hardware. It takes  $2^N$  inputs and sorts in  $N$  steps using a series of bitonic sequences and splits.

However, there is often more than one overlapping jet of a particular energy. An asymmetry parameter in  $\eta$  and  $\phi$  is also considered for each jet when this is the case:

$$A_{\eta,\phi} = \sum (\text{Constituent tower energies in positive } \eta, \phi) - \sum (\text{Constituent tower energies in negative } \eta, \phi), \quad (4.3)$$

where positive and negative values are defined with respect to the jet centre. A jet with all of its energy in the central tower will have  $A_{\eta,\phi} = 0$  whereas a jet of the same energy with all energy deposits in an outer tower will have large  $|A_{\eta,\phi}|$ . If overlapping jets have the same energy, they are instead sorted to give the lowest asymmetry parameter. The first element in the sorted list is then the most energetic jet, with its energy concentrated most centrally within the  $n \times n$  window.

The sorted list is then filtered to remove jets which overlap with this first jet. The process is repeated until 13 separate jets are found. This number is somewhat arbitrary, and is limited by hardware at some high number.

Jets are sorted initially in one dimension, along  $\eta$  or  $\phi$ , and overlaps in one dimension are removed. The resulting list of the most energetic jets along or around the calorimeter is then sorted in the other direction to give the final jet collection.

### 4.3.3 Event-by-event estimation of pile-up

The measurement of the PU contribution to the jet energy is evaluated event by event using a method inspired by the paper of Cacciari and Salam [130] and already used to correct offline jets. In a pp collision with a large number of overlapping proton-proton interactions, a large number of relatively soft jets originate from PU and are distributed roughly evenly across the calorimeter. The median jet transverse energy is therefore very likely to come from PU and the underlying event, and gives a good estimate of the typical transverse energy of a PU jet in the event. Further, the energy density of the median jet transverse energy gives a good estimation of the energy density due to PU across the calorimeter. The energy released by PU per unit area in each event, denoted by  $\rho$ , can therefore be estimated using the median jet transverse energy, and the area of the jet:

$$\rho^{\text{L1}} = \frac{\langle E_{\text{T}}^{\text{L1 jet}} \rangle}{A_{\text{L1 jet}}} \quad (4.4)$$

where  $\langle E_T^{\text{L1 jet}} \rangle$  denotes the median jet transverse energy, and  $A_{\text{L1 jet}}$  denotes the jet area. The energy of all jets in an event can then be corrected for the energy density due to PU and the underlying event by simply subtracting from all jets in an event using

$$\text{PU corrected } E_T = E_T - \rho^{\text{L1}} \times A_{\text{L1 jet}}, \quad (4.5)$$

because the energy density due to PU across the calorimeter is assumed to be uniform. This assumption is valid for PU values of order  $\sim 50$ , however as PU increases above 100 pp collisions in each bunch crossing, simulation shows many more soft PU jets are expected to lie in the forward regions of the detector, so an  $\eta$  dependent PU subtraction may be more suitable for very high PU scenarios. This is not investigated here, but is within the capabilities of the upgraded trigger system.

In the following we show the effect of PU subtraction in the measurement of the jet energy. The same quantity could also be used to correct the contribution of PU to quantities used to define electrons/photons; isolation parameters, and the ratio of transverse energy deposits in the HCAL and ECAL.

#### 4.3.4 Calibration to the jet energy scale

Different regions of the detector do not necessarily give the same response to an incoming jet. Certain regions may be less-well instrumented, and produce an energy measurement that is smaller than a more highly instrumented region would give to the same jet, for example. The raw jet energies from the calorimeter towers must be corrected to the jet energy scale in order to take into account this effect. Different regions of the calorimeter give different responses so A set of calibration constants in  $p_T$  and  $\eta$  are therefore derived, in order to provide a look-up table to be used online, so that energy deposits can be calibrated to the jet energy scale in real time.

A non linear regression method is used on an independent samplesubseetion of 20,000 events collected using a single muon trigger. Events which contain a least one muon often have hadronic activity in the opposite hemisphere to the muon and so the data sample provides a sufficient number of jets to do a statistically meaningful calibration. This sample of events is subsequently removed from data sets used to characterize performance of the algorithm in the following sections: they are statistically independent.

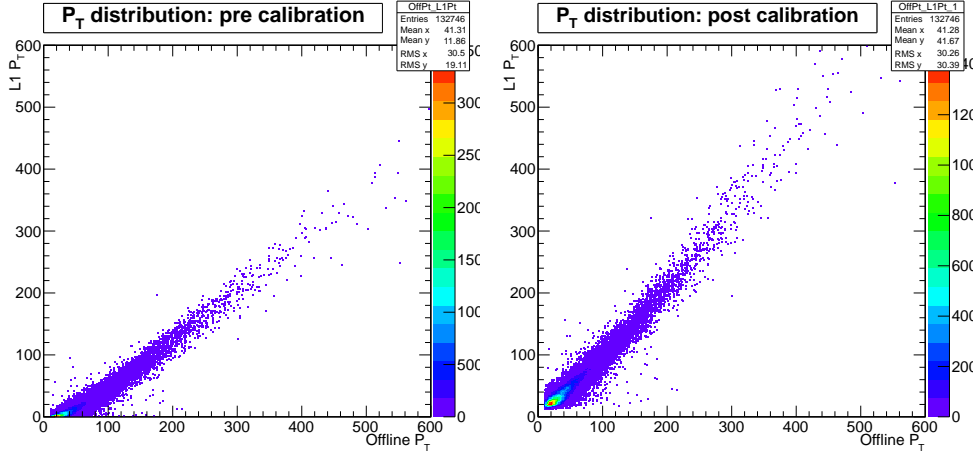


**Figure 4.7:** The  $p_T$  distribution of L1 jets that have been matched, within a cone of  $\Delta R < 0.5$ , to offline jets reconstructed with the anti- $k_t$  algorithm using a radius parameter of 0.5 and calorimeter information as input only. The distribution shown before a  $p_T$  and  $\eta$  calibration has been applied is shown on the left, and after the calibration has been applied on the right. In both distributions, PU has been subtracted from both jet collections.

Once the L1 upgrade jets have been created, sorted and filtered, the value of the average energy density due to PU,  $\rho^{L1}$ , which is calculated on an event-by-event basis, is calibrated to the jet energy scale by comparing it to a lookup table of  $\rho$  values, created by comparing the online  $\rho$  with that calculated offline for each event in an independent sample. The corrected PU subtraction parameter is applied to the L1 jets in the event according to Equation 4.5, in order that they can be calibrated to the offline jets which have been similarly PU subtracted. The leading offline jet in each event, where the jet is formed using the anti- $k_t$  algorithm with radius parameter of 0.5 and inputs from the calorimeter alone, “AK5 Calo jets”, is matched to a L1 jet within a cone of  $\Delta R = \sqrt{(\eta_{L1} - \eta_{offline})^2 + (\phi_{L1} - \phi_{offline})^2} < 0.5$ . The use of AK5 Calo jets, rather than AK5 PF jets, gives reconstructed offline jets as close as possible to those created at L1, as both are built using calorimeter information alone. The values of  $p_T$  and  $\eta$  for the matched L1 and offline jets are used as inputs to a multi-variate analysis. This provides a lookup table of multiplication factors binned in values of the L1 jet  $\eta$  and  $p_T$ . Applying this calibration to the L1 jets gives a calibration independent of PU.

The distribution of L1 jet  $p_T$ , where each jet has been matched to an offline jet, before and after the calibration has been applied is shown in Figure 4.7. Momenta are much more closely matched after the calibration has been applied.

## 4.4 Upgrade L1 Jet Algorithm Performance

Jet performance can be characterised by angular and energy resolutions, efficiency of reconstruction and trigger rates. The proposed upgrade L1 jets were simulated using data that were collected in high PU conditions during 2012, where events were selected at random from the whole dataset, for example every 10<sup>th</sup> event kept — termed “Zero Bias” data. The LHC run used for the study had an average of 45 primary vertices per bunch crossing, and had integrated luminosity of 0.03 pb<sup>-1</sup>.

### 4.4.1 Angular and energy resolutions

Resolutions are measured as compared to offline AK5 Calo jets, as described in Section 4.3.4. The leading offline jet (which must have  $p_T > 20$  GeV) is matched to a L1 jet within  $\Delta R < 0.5$ , and the resolutions are defined as:

$$\sigma_\eta = \eta_{offline} - \eta_{L1} \quad (4.6)$$

$$\sigma_\phi = \phi_{offline} - \phi_{L1} \quad (4.7)$$

$$\sigma_{p_T} = \frac{p_T^{offline} - p_T^{L1}}{p_T^{offline}} \quad (4.8)$$

Angular and energy resolutions of the proposed upgrade algorithm compared to the current system are shown in Figure 4.8. There is a much improved angular resolution as the upgrade jets take advantage of the full granularity of the calorimeter. In high PU data, the energy resolution is improved due to the PU subtraction. With the current L1 jet algorithm, there are a significant number of events in which the energy of the L1 jet has been falsely boosted by PU, and it is matched to a relatively soft offline jet, the leading offline jet has been matched to low energy PU L1 jets, giving a negative value of  $\sigma_{p_T}$  and giving rise to the significant negative tail in the distribution.

Crucially, the energy resolution of the upgrade jet algorithm shows a much reduced dependence on PU, shown in Figure 4.9. This is evidence that the event-by-event PU subtraction has the intended effect, reducing the worsening effect of additional primary vertices on the jet energy resolution, and the upgrade jet algorithm is therefore expected to show a reduction in rate compared to the current algorithm.

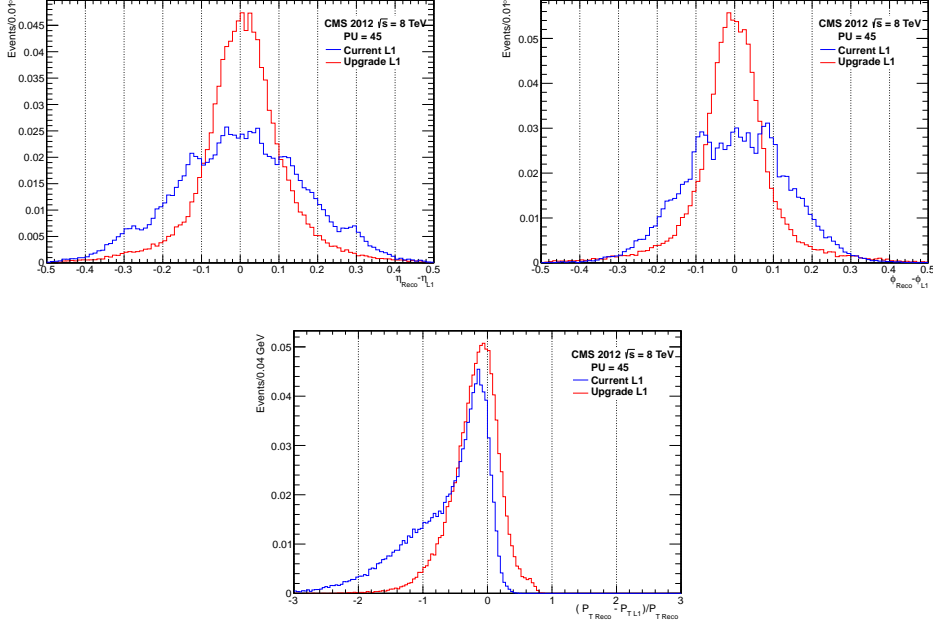


**Figure 4.8:** Resolution in  $\eta$ ,  $\phi$  and  $p_T$  for high PU data taken by the CMS detector in 2012. There is a clear improvement with the upgrade jets, plotted in red, in both angular resolutions and energy resolution. These plots can be found in [119].

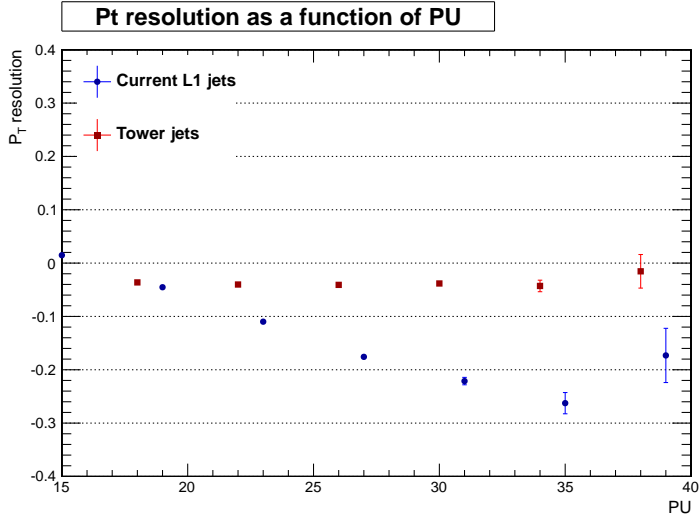


**Figure 4.9:** The PU dependency of the L1 jet energy resolution for both the current algorithm and the upgrade algorithm, where the resolution is taken as the RMS of the PU distribution shown in Figure 4.8, for different PU bins. There is a clear improvement with the upgrade jets, plotted in red, which shows independence of PU up to PU  $\sim 40$ .

#### 4.4.2 Trigger efficiencies

The trigger efficiencies for various L1 jet transverse energy thresholds are measured, as compared to AK5 Calo jets, to show the effectiveness of the proposed algorithm at reconstructing jets which have been measured offline, which are treated as the “truth”. If the leading L1 jet in each event above a certain energy threshold is matched to an offline jet, the energy of the matched offline jet is plotted. All matched offline jet energies are also plotted. By taking the ratio between these two distributions we attain trigger turn on curves, shown in Figures 4.10 and 4.11.

The sharpness of the turn on curve is due to the energy resolution of the jet algorithm. If all of the L1 jets have reconstructed energies that exactly equal the energies of the offline jets to which they are matched, i.e.  $\sigma_{p_T} = 0$ , there would be a step function at the value of the jet energy threshold of the trigger. The turn on would be instant at the specified trigger threshold. The plateau efficiency of the turn on is dictated by the matching efficiency of the jet algorithm. If all L1 jets are perfectly matched to offline jets then the algorithm is fully efficient at reconstructing jets at L1 and the plateau efficiency is 1.

The turn on curves shown in Figure 4.10 are taken from data taken using the same single muon trigger as was used for the jet calibration, where the presence of at least one muon in each event implies there is often hadronic activity in the opposite hemisphere of the detector to the muon. This is a relatively low PU set of events, with approximately 20 pp interactions per bunch crossing. While the plateau efficiency for both algorithms is 1, as you would expect, there is a slightly slower turn-on for the upgrade algorithm – it does worse than the current algorithm. This is down to non-optimal calibration, and could be improved with a better method and more statistics with which to perform the calibration (particularly for high momentum jets). However, it is in the high PU data where the improvement can be seen.

Figure 4.11 shows the performance at PU of approximately 45, a data sample which has lower statistical precision, hence the larger error bars. The sizeable negative tail shown in the momentum resolution for the current algorithm in Figure 4.8 is evident in the bump at low momentum in the left hand plot. Relatively soft jets due to PU have been falsely boosted, and are reconstructed using the current L1 algorithm to be above the L1 threshold. These are then matched to very soft PU jets, reconstructed offline, causing the behaviour at low  $p_T$  where many L1 jets are over the L1 threshold, whereas

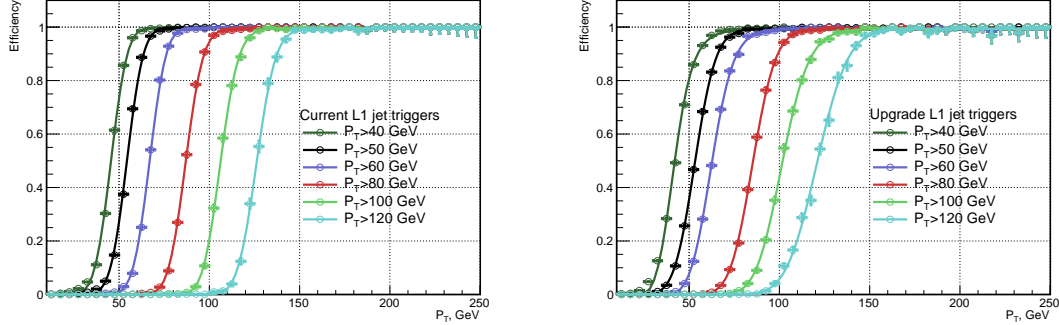


**Figure 4.10:** On the left are the trigger turn on curves for the current jet algorithm and on the right are the trigger turn on curves for the upgrade jet algorithm, for various single jet trigger thresholds, calculated using relatively low PU data. The right hand plot can be found in [119].

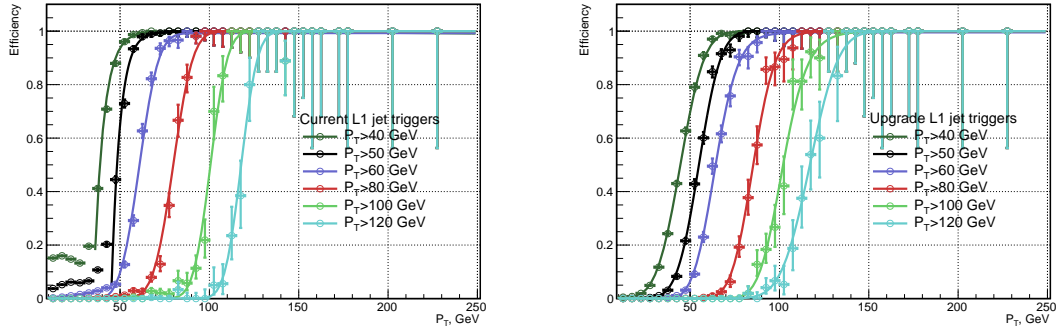


**Figure 4.11:** On the left are the trigger turn on curves for the current jet algorithm and on the right are the trigger turn on curves for the upgrade jet algorithm, for various single jet trigger thresholds, using relatively high PU data.

their offline counterparts are not. Because the effect of PU has effectively been removed from the upgrade L1 jet collection, this is not the case for the upgrade trigger turn ons.

The PU subtraction of the proposed upgrade algorithm is also evident in the upward shift in energy of the turn on curves, going from the current algorithm to the upgrade algorithm; the sharper turn ons for the current algorithm are now because the L1 jet energy is falsely boosted by PU. For a requirement of, for example, one 40 GeV jet at L1, the offline value at which 95% of events pass the trigger is 51.4 GeV for the current algorithm in the high PU dataset; and 62 GeV for the upgrade algorithm. Table 4.1 shows the offline transverse momentum value at which the trigger is 95% efficient for the various turn on curves shown in Figure 4.11. A lower typical hadronic energy at L1 in events reconstructed using the upgrade algorithm, due to the PU subtraction, drives the

95% efficiency values up. While for offline analysis variables to stay as low as possible we ideally want the 95% efficiency values to be as low as possible, we also want to maintain a low rate. With the current algorithm, we will be allowing many more events to pass the threshold, increasing the rate the trigger fires. Further, the energy values are falsely high, so the fake rate of events that don't actually contain a jet above threshold will also be high; this is a ‘waste’ of bandwidth as these events will be discarded in offline analysis.

Plateau efficiency values are 1 in both algorithms, meaning the upgrade jet algorithm (like the current algorithm) is fully efficient at large jet  $p_T$  values.

**Table 4.1:** The 95% efficiency values for various L1 jet transverse momentum thresholds, in GeV, and plateau efficiency values for the current and upgrade algorithm, for turn on curves taken in high PU data and shown in Figure 4.11.

L1 threshold	Current L1		Upgrade L1	
	95% efficiency	Plateau	95% efficiency	Plateau
40	51.4	1	62.0	1
50	59.5	1	70.9	1
60	75.4	1	83.7	1
80	94.1	1	103	1
100	112.9	1	123.6	1

#### 4.4.3 Jet trigger rates

As discussed in Section 4.1, the purpose of building a new trigger is to be able to better control the trigger rates at reasonable energy thresholds in the future LHC running, which is not possible with the current system. The projected trigger rates of the proposed jet algorithm in the next phases of LHC running are therefore compared to the current system, in order to show the improvement in rates, and subsequent reduction in energy thresholds possible with the upgraded CMS L1 calorimeter trigger.

Without any requirements on events that are recorded, i.e. Zero Bias data where all events are kept, the rate is equivalent to the instantaneous luminosity multiplied by the inelastic proton-proton cross section,  $R = L \times \sigma_{pp}$ . In events where there are additional primary vertices in the bunch crossing, PU > 1, it takes the number of interacting vertices to get the process in question to occur, so there is an inverse proportionality to the PU, and the rate, per vertex,  $R = L \times \sigma_{pp}/PU$ . The rate of events passing a particular trigger

at L1,  $R_{L1}$ , for a given luminosity and PU scenario can then be written as

$$R_{L1} = R_{L1}^{\text{ev}} \cdot \frac{L \times \sigma_{pp}}{\text{PU}}, \quad (4.9)$$

where  $R_{L1}^{\text{ev}}$  is the normalised trigger pass rate per `vertexevent`, which for a given set of events is simply the number of events passing a certain trigger divided by the total number of events. Using this equation, the L1 trigger rates can then be extrapolated to a given luminosity and PU scenario.

The rates for several jet triggers are plotted in Figure 4.12, in terms of the L1 jet energy. Usually, the offline cut used in analysis is dictated by the allowed trigger rate, which corresponds to a particular L1 threshold, and therefore to a 95% efficiency value — where the 95% efficiency value is as low as possible to maintain as much phase space as possible (given the rate restrictions). It is therefore also helpful to show the rate in terms of the 95% efficiency, which enfolds both trigger rate and efficiency of the proposed algorithm and enables a fair comparison between the current and proposed upgrade algorithm. The conversion from the online, L1 jet energy to offline 95% threshold is taken from the turn on curves shown in Figure 4.11, using the linear conversion function shown in Figure 4.13. Figure 4.14 shows the single, `double`, `triple` and quad jet (where one, two, three or four jets are required) trigger rates vs the 95% efficiency. The current and upgrade single jet rates are comparable, as the PU subtraction does very little to the leading jet in the event, whereas the multi jet triggers, such as the quad jet trigger, see a significant reduction in rate as PU jets are removed from the event.

#### 4.4.4 Other jet variables

Other offline variables, constructed from jets, have been widely used in the data analyses at CMS at 7 and 8 TeV, both at trigger level and offline. They therefore will also benefit from the upgraded calorimeter trigger, and shown here are the improvements in rates for  $H_T$ , the transverse hadronic energy which is defined as the scalar sum of jet transverse momenta in each event:

$$H_T = \sum |p_T^{\text{jet}}| \quad (4.10)$$

where the sum is over all jets in each event.  $H_T$  is commonly used in analyses which search for SUSY, for example in Ref. [131]. It gives a good indication of the amount of hadronic energy in an event and so the energy transfer in the original inelastic pp

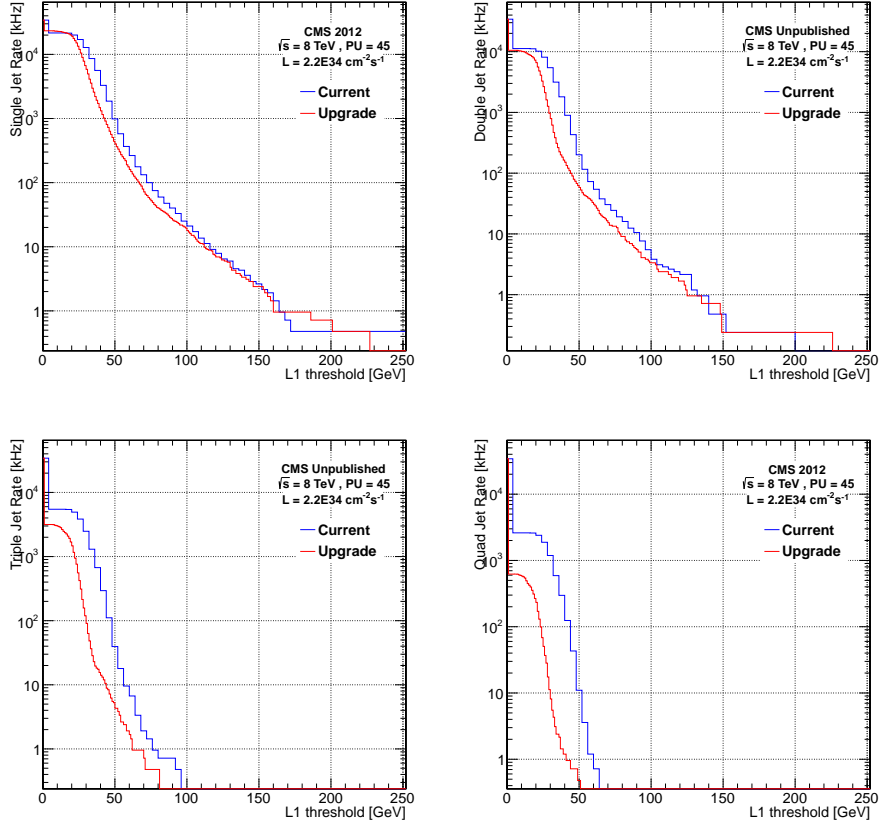


**Figure 4.12:** Rates of single, double, triple and quad jet triggers. The single jet trigger shows similar performance to the current system, while the multi-jet trigger show a large reduction in rate.

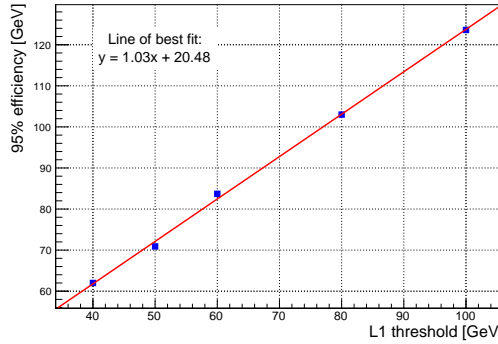


**Figure 4.13:** Conversion between the L1 jet threshold and the 95% efficiency as measured offline, for the proposed upgrade jet algorithm, using the turn on curves shown in Figure 4.11.

collision, which should be high for new physics processes to occur. It is particularly sensitive to the number of primary vertices in each bunch crossing, as soft PU jets are

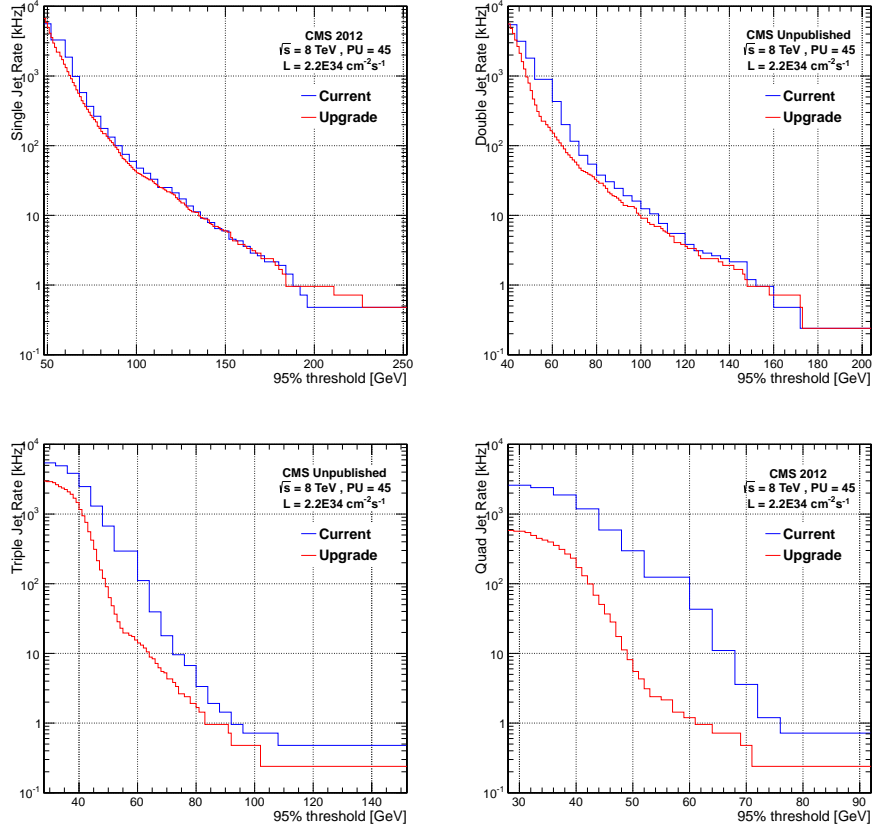


**Figure 4.14:** Rates of single, double, triple and quad jet triggers. The single jet trigger shows similar performance to the current system, while the multi-jet trigger show a large reduction in rate. The single and quad jet rate plots can be found in [119].

included in the sum. The addition of PU subtraction on an event-by-event basis in the proposed upgrade jet algorithm therefore has the potential to lead to significant improvements in the rate. The trigger turn on curves for various  $H_T$  thresholds using the upgrade jet algorithm are shown in Figure 4.15 together with the conversion between the L1 threshold and the 95% offline efficiency. The trigger rate of the  $H_T$  in terms of both the L1 threshold and the 95% efficiency are shown in Figure 4.16, which shows a rate reduction of nearly an order of magnitude when using the upgrade algorithm compared to the current algorithm, in terms of the 95% efficiency. This is a much fairer comparison between the two algorithms than the rate in terms of the L1 threshold, as the current  $H_T$  and  $H_T^{\text{miss}}$  values at L1 are not corrected to the jet energy scale.

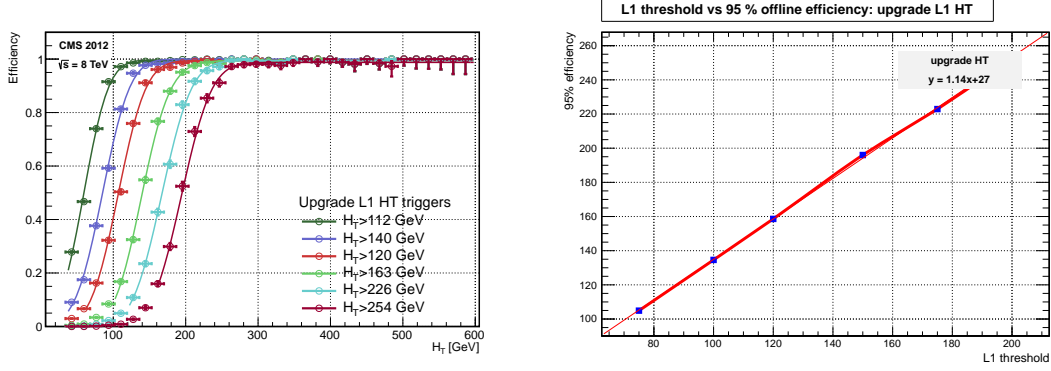


**Figure 4.15:** The trigger turn on curves for the  $H_T$  variable, left, and the conversion between the L1  $H_T$  threshold and the 95% efficiency as measured offline, using  $H_T$  constructed with the proposed upgrade algorithm.

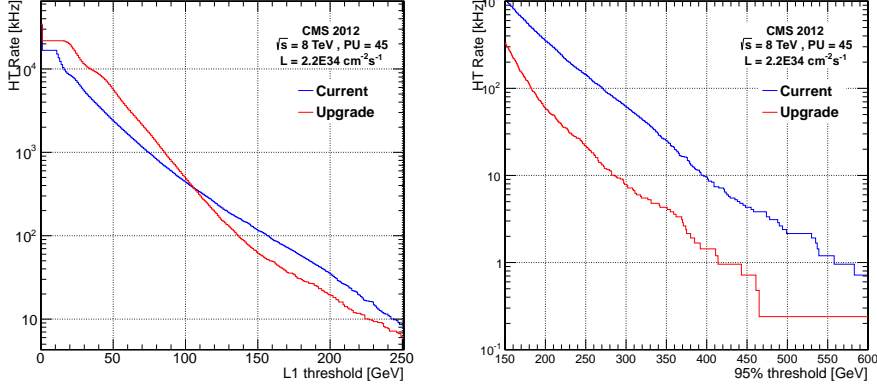


**Figure 4.16:** Rates of  $H_T$  triggers, vs L1 threshold (left) and 95% offline threshold (right), where the conversion between L1 threshold and 95% efficiency is taken from Figure 4.15. There is a significant reduction in rates with the proposed upgrade algorithm.

## 4.5 Conclusion

The proposed upgrade jet algorithm, which is possible to implement with the upgraded CMS calorimeter trigger based upon a TMT architecture, shows significant improvements over the current L1 jet algorithm. By utilising event-by-event PU subtraction at L1 for the first time, the dependency of PU of the L1 jet algorithm is much reduced. By taking advantage of the full tower level granularity of the calorimeter, the angular resolutions of the algorithm are also much improved. This will lead to large improvements in topological calculations at the GT, where two or more objects are used to calculate some quantity which is used in triggering; for example transverse mass, and determining jets arising

from Vector Boson Fusion processes such as Higgs boson production. While similar trigger rates are seen for the single jet triggers, there are big improvements in the multijet trigger rates. The double jet rate is reduced by a factor of around 2, the triplet jet rate by a factor of about 3, and the quad-jet trigger rate is reduced by a factor of about 4. ~~and a factor of two reduction in the quad-jet trigger rate.~~ The  $H_T$  variable sees a factor 10 reduction in rate. These rate reductions will allow lower energy thresholds in the upgraded CMS L1 calorimeter trigger, as compared to the current L1 jet algorithm, and help to maintain the energy thresholds and jet rates that were used in 7 and 8 TeV data taking.

This upgrade jet algorithm was proposed in Ref. [119], and the majority of the work was done during 2012. Many improvements to the algorithm are possible, using different PU subtraction techniques, different jet shapes, and additional parameters such as jet substructure variables. Indeed, since this work was completed improvements have been made, and documented elsewhere [132].

# Chapter 5

## Searching for SUSY with compressed mass spectra using monojet events

*“Physics, as we know it, will be over in six months.”*

— (1928) Max Born, 1882 – 1970

This chapter and the next describe a search for events containing a single energetic jet and missing transverse momentum, using a data sample collected at 8 TeV by the CMS detector at the LHC and corresponding to an integrated luminosity of  $19.7 \text{ fb}^{-1}$ . In this chapter, we describe the data samples used in the search, the reconstruction of events, the selection of the search regions, and the SM background estimations with their associated uncertainties.

### 5.1 Introduction

The monojet signature of a high  $p_T$  jet and an imbalance of momentum in the transverse plane is the discovery signal for many new physics scenarios that have genuine missing energy in the final state. Searches for Large Extra Dimensions in the framework of the Arkani-Hamed, Dimopoulos, and Dvali (ADD) model [67], for DM using effective field theory and simplified models, and Unparticle production [133] have been presented in previous searches both at the LHC and the Tevatron [134–141] using the monojet channel.

~~Note to Gavin: UED models typically produced KK excitations in pairs, so don't give rise to monojet final states. arXiv:hep-ph/0510350 gives a special case where monojets can be formed, but I can't see any theory re-interpretations of results from monojet LHC data in UED – ATLAS diphoton paper and trilepton theory paper is all I can find so I won't mention about UED here!~~ Signals are commonly invisible; for example the theorized DM is a Weakly Interacting Massive Particle (WIMP) candidate, and as such, does not interact with any part of the detector. It therefore leaves no signal but an imbalance of momentum in the transverse plane, which is balanced by an ISR particle. In this case, the ISR particle is a quark or gluon, leading to a high  $p_T$  jet. Searches have also been conducted using other radiated particles: photons (termed “monophoton”) and W or Z bosons (“mono-W” or “mono-Z”) [135, 142–148]. However, because monojet searches have the advantage of higher production cross sections (as the strong coupling constant  $\alpha_s$  is greater than the electromagnetic or weak coupling constants), they typically lead to stronger limits.

A search for compressed SUSY in the third generation is motivated in Chapter 2. SUSY signals are slightly different: Feynman diagrams are shown in Fig. 5.1. The final state does not just consist of missing transverse momentum balanced by an ISR jet; there are also sparticle decay products. These are therefore not pure monojet signals. However, when the mass difference between the parent sparticle and the LSP decreases below 80 GeV ([the mass of the W boson](#)), decay products have increasingly low  $p_T$ , are very soft, and become indistinguishable from SM backgrounds. Events that have an energetic ISR jet produced in association with parent sparticles, which recoils against the missing transverse momentum due to the LSP leaving the detector (“boosted events”), provide a clear signature in such scenarios. One high  $p_T$  jet alongside large  $p_T^{\text{miss}}$  gives rise to a monojet final state, in events where the sparticle decay products are too soft to observe.

Searches are interpreted in the context of pair production of third generation squarks followed by their decay to jets and the LSP, where the LSP is taken to be the lightest neutralino  $\tilde{\chi}_1^0$ , and the LSP is close in mass to the parent squark. Top squarks,  $\tilde{t}$ , are assumed to undergo the FCNC loop-induced decay  $\tilde{t} \rightarrow c\tilde{\chi}_1^0$  with 100% branching fraction, and bottom squarks,  $\tilde{b}$ , are assumed to decay via  $\tilde{b} \rightarrow b\tilde{\chi}_1^0$  with 100% branching fraction. By selecting events using particles produced alongside the  $t\bar{t}$  or  $b\bar{b}$  pair, and being independent of the soft final-state jets, the search is sensitive to mass differences of less than 10 GeV. The search presented here is a [simple counting experiment conducted in multiple inclusive search regions](#). It was conducted by the author as part of the CMS monojet group and loosely follows the well-established searches in Refs. [139–141]. The

author was responsible for all of the analysis; including developing the alternative event selection in order to be sensitive to SUSY signatures, developing techniques to improve the  $Z(\nu\bar{\nu}) + \text{jets}$ ,  $t\bar{t}$ , QCD, and diboson background estimations, as well as setting limits in the SUSY parameter space. Here, we have increased the jet counting threshold and bin signal regions in leading jet threshold, rather than  $p_T^{\text{miss}}$ , as compared to the standard CMS monojet search.

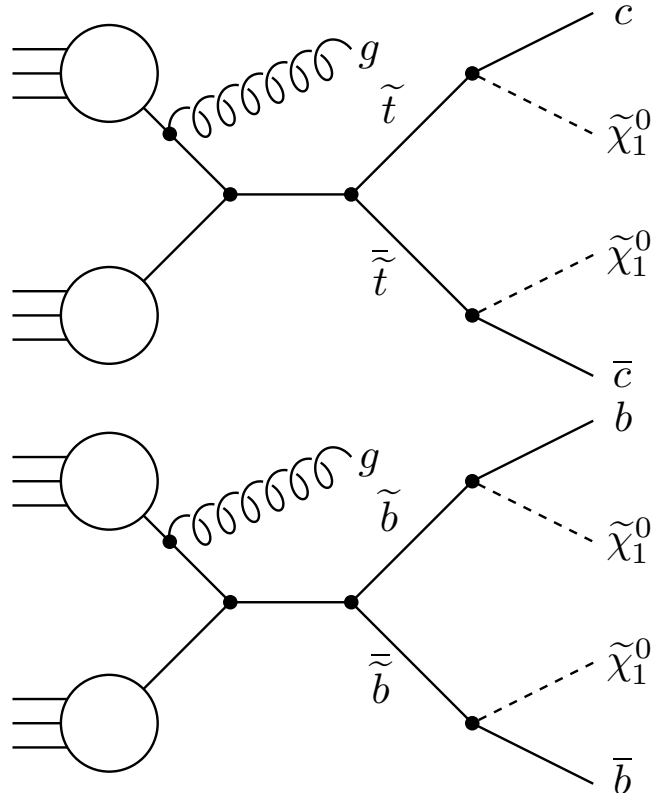


**Figure 5.1:** Feynman diagrams of the signals probed. The top diagram shows the FCNC process  $\tilde{t}\bar{\tilde{t}} \rightarrow c\bar{c} \tilde{\chi}_1^0 \tilde{\chi}_1^0$  and the bottom diagram shows the process  $\tilde{b}\bar{\tilde{b}} \rightarrow b\bar{b} \tilde{\chi}_1^0 \tilde{\chi}_1^0$ . In both cases, an ISR gluon leads to an energetic jet, and balances the  $p_T^{\text{miss}}$  due to LSPs escaping the detector leaving no trace.

## 5.2 Data samples

The data for this search were collected using a combination of `threetwo` triggers at the HLT. The first requires events to have  $p_T^{\text{miss}} > 120$  GeV. The second, a dedicated monojet trigger, requires a central jet ( $|\eta| < 2.6$ ) with  $p_T > 80$  GeV and  $p_T^{\text{miss}}$  (calculated without muons) to be greater than 95 or 105 GeV. These triggers also have coarse noise cleaning filters applied. The first `trigger` has various requirements on the energy deposits in the

HCAL to cut out noisy events, and the [latter two](#)[second](#) demand that the neutral energy deposited in the ECAL is less than 95% of the total energy deposited. They are seeded by L1 triggers which require the missing transverse momentum, calculated using the coarse inputs available at L1, to be greater than 36, 40 or 50 GeV for the first trigger, or greater than 40 GeV for the second [and third](#) triggers.

Very few events with  $p_T^{\text{miss}}$  below 100 GeV, where it is calculated offline using optimal object reconstruction, will pass the analysis triggers described above that require  $p_T^{\text{miss}}$  calculated online to be above 120 GeV, or to be above 95 or 105 GeV without muons. However, most events with  $p_T^{\text{miss}}$  (reconstructed offline) above 200 GeV will pass the same analysis triggers. It is therefore necessary to calculate the efficiency of these triggers in terms of the key analysis variables,  $p_T^{\text{miss}}$  and the  $p_T$  of the leading jet, in order to find where best to place offline analysis cuts. An independent sample of events collected using a trigger requiring a single isolated muon with  $p_T > 24$  and  $|\eta| < 2.4$  is used. The efficiency is given by the ratio of the number of events passing the analysis triggers to the number of events passing the reference trigger. Efficiencies are shown in the trigger turn-on curves in Figure 5.2 as a function of  $p_T^{\text{miss}}$  and the  $p_T$  of the leading jet, as reconstructed offline. Here, the different colours show the different runs (A–D) of the LHC during Run I. The dedicated monojet trigger described above was introduced for Run C, which increased the efficiency of the combination of the triggers for lower values of  $p_T^{\text{miss}}$  and leading jet  $p_T$  as compared to Runs A and B. The plots in Figure 5.2 show that the trigger paths become almost 100% efficient at  $p_T(j_1) \sim 110$  GeV and  $p_T^{\text{miss}} \sim 220$  GeV.

The fluctuations evident in the low  $p_T^{\text{miss}}$  region of the left-hand plot arise from low statistical precision in these bins with data from the new trigger, evident only in Runs C and D. These events are removed from the dataset as the offline analysis cut is placed at  $p_T^{\text{miss}} > 250$  GeV.

The specific datasets used for this analysis, along with their integrated luminosities, can be found in Table 5.1. The data are from a ‘good-run’ list of LHC runs, in which each of the subsystems of the CMS detector were operating well, and therefore event reconstruction was optimal. Events were re-reconstructed using the `CMSSW_5_3_9_patch3` release of the CMS software (CMSSW), and form a part of the legacy dataset from Run I of CMS running.

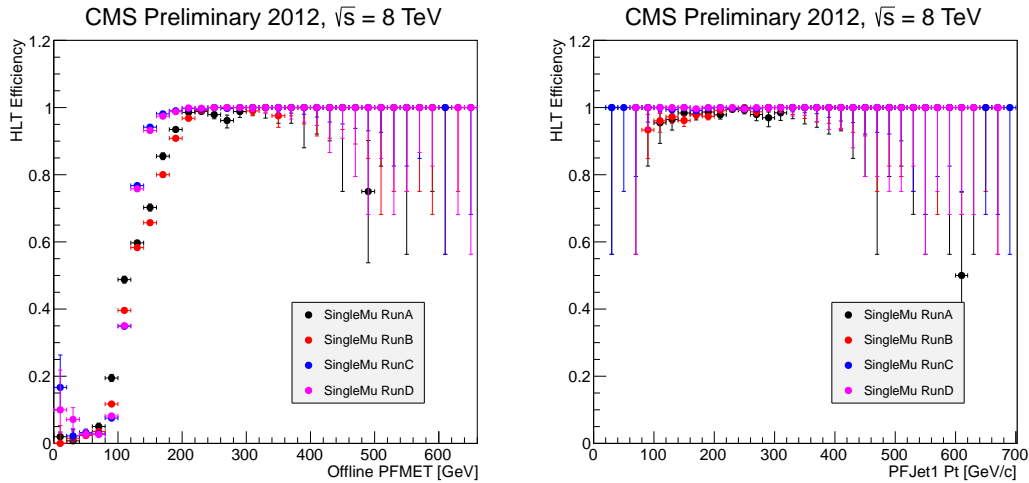


**Figure 5.2:** The trigger efficiency as a function of the  $p_T^{\text{miss}}$  (left) and  $p_T$  of the leading jet (right).

**Table 5.1:** Datasets used in the search, which combine to give a total integrated luminosity of  $19.7 \text{ fb}^{-1}$ .

Era	Dataset	Int. Lumi. [ $\text{pb}^{-1}$ ]
2012A	/MET/Run2012A-22Jan2013-v1/AOD	889
2012B	/MET/Run2012B-22Jan2013-v1/AOD	4429
2012C	/MET/Run2012C-22Jan2013-v1/AOD	7152
2012D	/METParked/Run2012D-22Jan2013-v1/AOD	7315

### 5.3 Background MC simulation

MC simulation of SM backgrounds are used, directly and indirectly, to estimate the contribution of SM backgrounds to the number of events in the search regions. The SM processes considered are; W or Z bosons produced in association with jets, top quark pair production ( $t\bar{t}$ ), diboson (WW, WZ, ZZ,  $W\gamma$  and  $Z\gamma$ ) production, single top quark events, and QCD multijet processes.

The simulation of each sample follows a similar procedure. Events are generated using a matrix element event generator such as MADGRAPH [149, 150], which simulates the underlying process at parton level. The event is then passed through a parton showering programme, usually PYTHIA [151, 152] with tune Z2\* [153]. Partons are showered – QCD processes are simulated and cascades of quarks and gluons are produced from individual partons, which then hadronize and form jets. It is finally passed through a simulation of the CMS detector in order to mimic the detector’s response to the event. All simulated SM background events have gone through a GEANT4 [154, 155] simulation of the detector. This is a ‘full’ simulation, computationally expensive and providing accurate responses to the simulated physics objects. For simulation of signal (detailed later), a ‘fast’ simulation [156] is used instead as it is around 100 times faster to process each event and has a comparable accuracy.

Samples of Z bosons decaying invisibly ( $Z(\nu\bar{\nu}) + \text{jets}$ ),  $t\bar{t}$ , and diboson events are simulated using MADGRAPH5 interfaced with PYTHIA6.4.24. To evaluate the content of the proton in the initial state, the CTEQ 6L1CTEQ6L PDFs are used [157]. Simulated Drell–Yan ( $Z(\ell^+\ell^-) + \text{jets}$ ) and  $W + \text{jets}$  events are generated in the same way, where a cut has been placed on the transverse momentum of the boson,  $p_T > 100$  GeV, in order to increase the number of generated events that pass offline selection requirements (and where the production cross section has been modified accordingly). QCD multijet events are generated with PYTHIA6.4.24, using the CTEQ 6L1 PDFs. Single top quark processes (s-channel, t-channel and tW-channel production) are generated using POWHEG [158, 159] interfaced with PYTHIA6.4.24 and CTEQ 6.6M PDFs. Decays of the  $\tau$  lepton are simulated using the TAUOLA 27.121.5 package [160].

To ensure no double counting in phase space between the matrix element and the parton shower, underlying event and the fragmentation and hadronization process, the MLM shower matching prescription [161] is used, in which partons from the matrix element calculation are matched to jets resulting from the parton shower. In order to avoid double

counting photons from the PYTHIA shower in  $W + \text{jets}$  and  $W\gamma$  samples (and similarly for  $Z(\ell^+\ell^-) + \text{jets}$  and  $Z\gamma$  samples), events from the  $W + \text{jets}$  and  $Z(\ell^+\ell^-) + \text{jets}$  simulation which have a photon from ISR or Final State Radiation (FSR), of  $p_T(\gamma) > 5 \text{ GeV}$ , are removed.

## 5.4 Object reconstruction

In Chapter 3 the CMS detector and reconstruction methods are discussed at length, including those used in this analysis. Here, the important features of the object reconstruction are recapped with additional details on the object definitions.

### 5.4.1 Jets and $p_T^{\text{miss}}$

Jets and  $p_T^{\text{miss}}$  are reconstructed using a PF technique [122]. The algorithm produces a unique list of particles in each event, using the combined information from all CMS subdetectors. This list is then used as input to the jet clustering, which reconstructs jets using the anti- $k_t$  algorithm [121] with a distance parameter of 0.5. The missing transverse momentum vector  $\vec{p}_T^{\text{miss}}$  is computed as the negative vector sum of the transverse momenta of all particles reconstructed in the event. Its magnitude is referred to as  $p_T^{\text{miss}}$ . Used throughout is the modification of this variable to exclude muons: the vector  $\vec{p}_T^{\text{miss},\mu}$  is computed without muons, and its magnitude is referred to as  $p_T^{\text{miss},\mu}$ .

Jet energies are corrected to establish a uniform calorimeter response in  $\eta$  and an absolute response in  $p_T$ , calibrated at the particle level. Jet Energy Scale (JES) corrections are derived from simulation, and a residual correction calculated by measuring the  $p_T$  balance in dijet and  $\gamma + \text{jets}$  events is applied to events in data [162] to account for differences in the JES between data and simulation. To resolve any ambiguity in the reconstruction of jets and leptons, a jet is removed from the event if the energy fraction of an electron or muon in the jet is greater than 0.5.

### 5.4.2 Leptons

Lepton reconstruction is used at various stages in the analysis. We identify events with leptons — electrons, muons, and hadronically decaying  $\tau$  leptons — in order to veto these

events and reduce the electroweak backgrounds. The identifications used for this purpose are “loose”, that is, satisfying basic selection criteria, in order to reject as much of these backgrounds as possible. Muon control samples are also used to estimate the electroweak —  $Z(\nu\bar{\nu}) + \text{jets}$  and  $W + \text{jets}$  — backgrounds. The identifications used here are both “loose” and “tight”, where muons satisfying the tight requirement satisfy more extensive selection criteria. A data control sample of  $Z(\mu\mu) + \text{jets}$  events is selected using one loose and one tight muon, and a data control sample of  $W(\mu\nu) + \text{jets}$  events is selected using one tight muon. We further use a data control sample consisting of loose muons and tight electrons to provide a data-driven estimate for the  $t\bar{t}$  background.

Leptons are also reconstructed using the PF algorithm and the definitions of objects are in accordance with the CMS recommendations. In addition to muons, electrons and  $\tau$  leptons are also used in the analysis. Muons either pass a “loose” or “tight” selection criteria (which has more stringent requirements). Electrons must pass a “loose” selection criteria, and the Hadron–Plus–Strips (HPS) algorithm with “loose” criteria is used to reconstruct hadronically decaying  $\tau$  leptons ( $\tau_h$ ).

A loose muon must have  $p_T$  greater than 10 GeV, and be tagged as a Global or Tracker muon — meaning that it must have independent tracks from both the tracker and the muon systems that join together, or that a series of hits in the tracker matches up with at least one hit in the muon system [163]. A tight muon must have  $p_T$  greater than 20 GeV and be central —  $|\eta| < 2.4$ . It must also be considered a Global muon, with additional requirements on the global muon track. There must be at least one hit from the muon chambers included in the global track, and the  $\chi^2$  of the global track must be less than 10. These requirements suppress mistaken muon identification as a result of hadronic punch-through from the HCAL and the magnet, and suppress muons originating from in-flight decays. There must also be hits in at least two of the muon stations, which acts to reduce the number of accidental track-to-segment matches. In order to suppress the number of cosmic-ray muons (and further suppress muons from in-flight decays), the transverse impact parameter of the track ( $d_{xy}$ ) as reconstructed in the tracker must be less than 2 mm from the primary vertex. Requiring the longitudinal impact parameter ( $d_z$ ) to be less than 5 mm has a similar effect, as well as reducing the number of muons which originate from PU. Additional demands on the number of hits in the pixel system ( $> 0$ ) and the number of tracker layers with hits ( $> 5$ ) further suppress in-flight muon decays, and guarantee a good measurement of the muon  $p_T$ .

The electron identification used in the analysis is loose. To be classified as an electron, a track in the tracker must match to a supercluster in the ECAL. The electron  $p_T$

must be greater than 10 GeV. If the electron originates in the gap between the ECAL barrel and endcap, where there is no instrumentation (and thus reconstruction is far from optimal):  $1.44 < |\eta| < 1.56$ , the event is rejected. In addition, various simple parameters regarding the supercluster shower shape, matching between the ECAL cluster and track, the ratio of energy deposited in the ECAL and HCAL, and impact parameters distinguish between primary electrons and those originating from bremsstrahlung and photon conversion. More information can be found in Ref. [164].

To ensure that electrons and muons are isolated — not close to a jet or other object — they must satisfy requirements on the isolation parameter  $I_{\text{so}}$ , defined as

$$I_{\text{so}} = \frac{\sum E_{\text{T}}^{\text{charged hadrons}} + \sum E_{\text{T}}^{\text{neutral hadrons}} + \sum E_{\text{T}}^{\text{photons}}}{p_{\text{T}}}, \quad (5.1)$$

where the hadrons and photons are considered in a cone with radius  $\Delta R = \sqrt{\Delta\phi^2 + \Delta\eta^2} = 0.4$  around the lepton direction. Tight muons must have  $I_{\text{so}} < 0.12$ , and loose muons must have  $I_{\text{so}} < 0.2$ . Loose electrons must also have  $I_{\text{so}} < 0.2$ . The effect of PU is corrected for. For charged particles, only those which are associated with the primary vertex in the event are considered, where this primary vertex is defined as that which has the largest sum of  $p_{\text{T}}^2$  of all the tracks associated with it. The hadronization of PU vertices leads to approximately twice the number of charged hadrons than neutral hadrons [165], so the energy within the isolation cone deposited by charged particles from PU vertices is multiplied by 0.5 and subtracted from the neutral component.

The  $\tau$  lepton decays hadronically 65% of the time, with the dominant decay modes consisting of one or three charged  $\pi^\pm$  mesons, and up to two neutral  $\pi^0$  mesons. The HPS algorithm first reconstructs the  $\pi^0$  component of the  $\tau_h$  decay using a PF anti- $k_t$  seed jet with distance parameter 0.5, and then combines with charged hadrons to build a  $\tau_h$ . ‘Strips’ are constructed from PF photons and electrons, starting with the most energetic electromagnetic particle within the seed jet, and combining all surrounding electromagnetic particles. Strips with  $p_{\text{T}} > 1$  GeV are then combined with charged hadrons to provide a  $\tau_h$  candidate. Here, the candidate must have  $p_{\text{T}} > 20$  GeV and  $|\eta| < 2.3$  and the loose requirements of the algorithm are used which correspond to approximately 1% of jets to be misidentified as a  $\tau_h$ . Similar corrections to account for PU are applied as described above for the isolation parameter. More information can be found in Ref. [166].

## 5.5 Event selection

The aim is to select signal candidate events while rejecting as much background as possible. A final state with one, high  $p_T$  leading jet, and large  $p_T^{\text{miss}}$  from the LSPs leaving the detector form the basis of the event selection in order to be sensitive to compressed SUSY signatures.

### 5.5.1 Event Cleaning

The first stage of the event selection, after the trigger, is to reject any events that have passed the trigger due to instrumental noise or non-collision backgrounds.

Events are required to have at least one well-reconstructed primary vertex [167], where it is reconstructed in a 24 cm window along the beam axis, within a radius of  $\rho < 2$  cm orthogonal to the plane of the beam. To reject events that have “scraping” tracks due to beam-gas interactions close to the interaction point, in events where there are 10 or more tracks at least 25% must be good quality; that is, satisfy various requirements on the number of hits, the  $p_T$  of the track, the  $\chi^2$  of the combination of hits which build the track etc. To remove events with spurious  $p_T^{\text{miss}}$  reconstruction, different methods of calculating the  $p_T^{\text{miss}}$  are compared. The value of  $p_T^{\text{miss}}$ , reconstructed using the PF algorithm, must be comparable with the  $p_T^{\text{miss}}$  calculated using calorimetric information only: events with  $(\text{PF } p_T^{\text{miss}} - \text{calo } p_T^{\text{miss}}) > 2 \times \text{calo } p_T^{\text{miss}}$  are discarded.

Beam-halo and other beam-related backgrounds [168], which arise when the beams interact with the beam pipes, can deposit energy in both the ECAL and HCAL leaving no associated tracks. Cosmic muons also can give rise to fake  $p_T^{\text{miss}}$ , or leave similarly spurious deposits - leading to fake jets - as they deposit energy in one or more of the subdetectors while leaving no tracks, or tracks which do not originate from the primary vertex. Similarly, instrumental noise can lead to large apparent deposits in the ECAL or HCAL. Stringent requirements are therefore placed on the neutral and charged hadronic and electromagnetic content of jets:

- Leading jet charged electromagnetic fraction  $< 0.7$
- Leading jet charged hadronic fraction  $> 0.2$
- Leading jet neutral electromagnetic fraction  $< 0.7$
- Leading jet neutral hadronic fraction  $< 0.7$

- Second jet neutral electromagnetic fraction  $< 0.9$
- Second jet neutral hadronic fraction  $< 0.7$

These conditions also reject high  $p_T$  photons and electrons which are misidentified as jets due to energy deposits in the HCAL; the energies associated with neutral hadrons in the ECAL and HCAL must sum to less than 70% of the total jet energy. In addition, jets are also required to pass a loose identification criterion which rejects fake jets due to calorimeter noise.

The distributions for the neutral and charged energy fractions of the first and second jet in events (where jets are  $p_T$  ordered) before and after these noise cleaning cuts are applied are shown in Figures 5.3 and 5.4. They are very effective at removing noisy events, with good data/MC agreement after the cuts have been applied.

### 5.5.2 Search region event selection

Once events passing the trigger have been filtered to remove noise and fakes, events are selected to optimize signal acceptance while rejecting as much background as possible.

To satisfy trigger requirements, and ensure most events comfortably pass the HLT trigger selection, events are required to have  $p_T^{\text{miss},\mu} > 200 \text{ GeV}$  and the most energetic jet ( $j_1$ ) in the event is required to have  $p_T(j_1) > 110 \text{ GeV}$  and  $|\eta(j_1)| < 2.4$ . Signal acceptance is increased by allowing events where there is a second jet ( $j_2$ ) originating from ISR (or FSR); however the signal also has soft final-state jets originating from the sparticle decay products. To ensure that these soft final-state jets coming from charm or bottom quarks remain invisible within the event selection, and a monojet signature is maintained, the  $p_T$  threshold at which the second and third jets are counted must be high enough that the soft-hadronic (signal) decay products fall below it for a good range of signal phase space while keeping the QCD multijet background at a manageable level.

Figure 5.5 shows the  $p_T$  distribution of charm quarks, taken from simulation, for a few representative mass hypotheses in the process  $\tilde{t}\tilde{t} \rightarrow c\bar{c}\tilde{\chi}_1^0\tilde{\chi}_1^0$ . Placing the jet counting threshold at  $p_T > 60 \text{ GeV}$ , and requiring  $|\eta| < 4.5$ , is a good compromise between signal efficiency and background rejection. Events are therefore vetoed if they contain more than two jets, where  $p_T(j_1) > 110 \text{ GeV}$  and  $|\eta| < 2.4$ ;  $p_T(j_2) > 60 \text{ GeV}$  and  $|\eta| < 4.5$ ; and the third jet is counted (and the event rejected) if it has  $p_T(j_3) > 60 \text{ GeV}$  and  $|\eta| < 4.5$ . A monojet-like topology in signal events is therefore maintained, allowing the search to

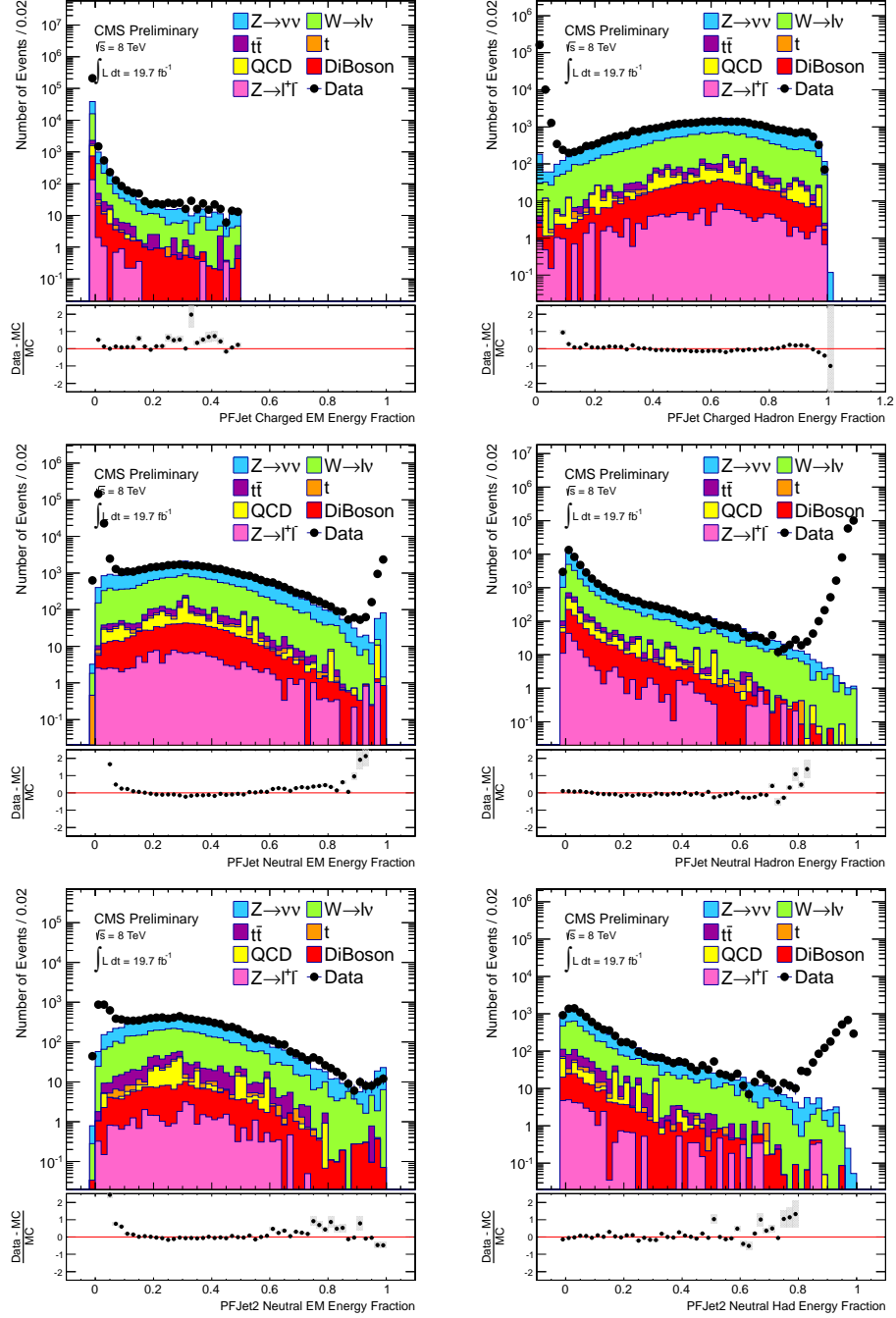


**Figure 5.3:** Hadronic and EM energy fractions from charged and neutral particles, before clean-up cuts on these quantities are applied. In the leading jet, the charged hadronic energy fraction is required to be  $> 20\%$  and the neutral EM and hadronic energy fractions must be  $< 70\%$ . In the second leading jet, the neutral EM energy fraction is required to be  $< 90\%$  and the neutral hadronic energy fraction must be  $< 70\%$ . The shaded band in the ratio plot shows the statistical uncertainty and all distributions are normalized to the cross sections shown in Table 5.2.

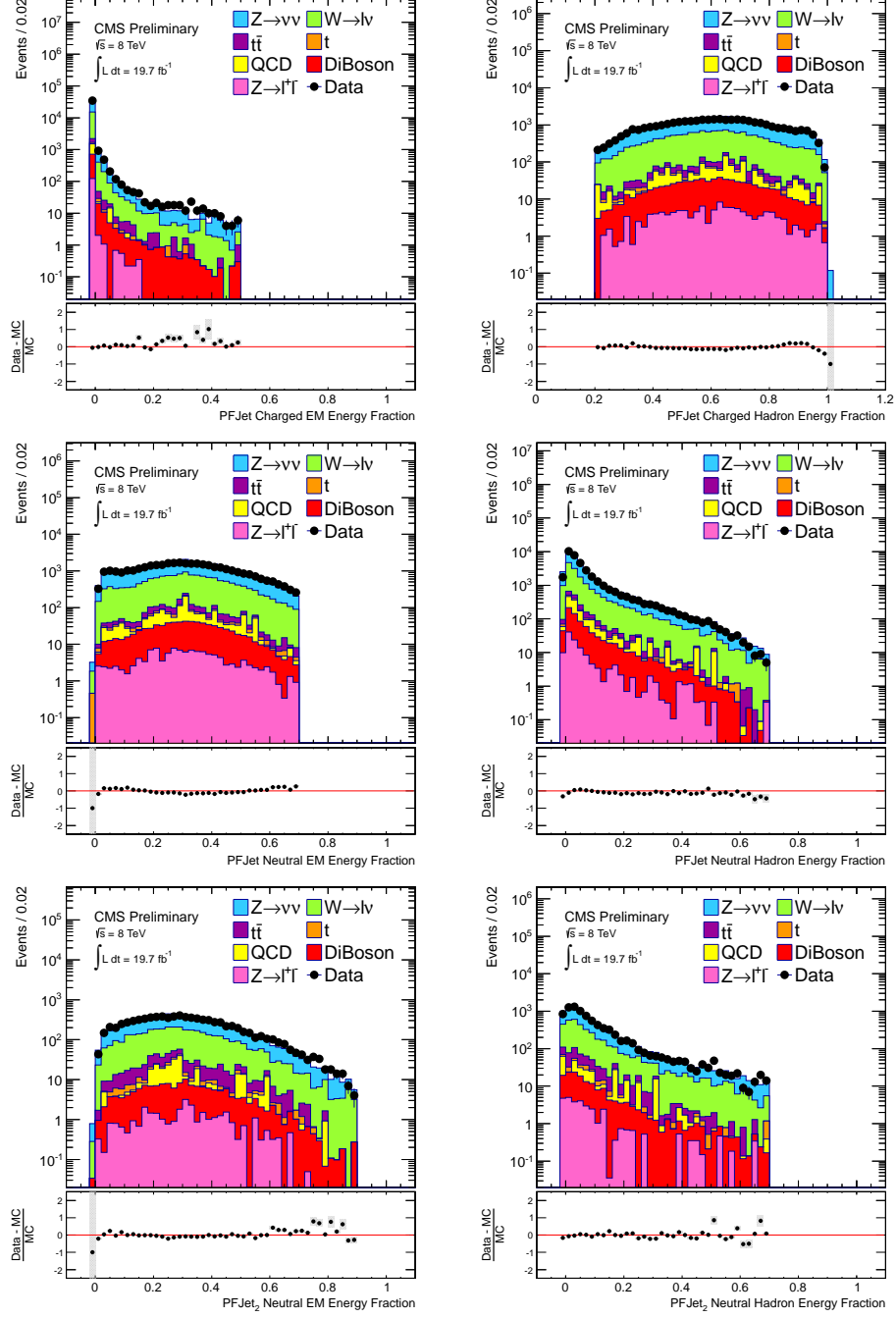


**Figure 5.4:** Hadronic and EM energy fractions from charged and neutral particles, after clean-up cuts on these quantities are applied. The shaded band in the ratio plot shows the statistical uncertainty and all distributions are normalized to the cross sections shown in Table 5.2.

be sensitive to both highly compressed spectra and extending the scope to larger mass differences.

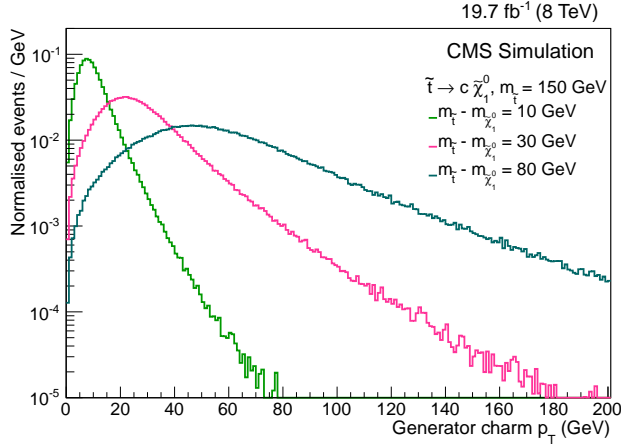


**Figure 5.5:** Charm quark  $p_T$  spectra for mass splittings across the phase space range,  $m_{\tilde{t}} - m_{\tilde{\chi}_1^0} = 10, 30, 80$  GeV, for a top squark mass of 150 GeV. Taken from Ref. [5].

To reduce the QCD dijet background, if two jets are present in the event, they must not be back-to-back:  $\Delta\phi(j_1, j_2) < 2.5$ . The multijet background is largely rejected by the  $N_{\text{jets}} \leq 2$  requirement.

Electroweak backgrounds in which a W or Z-boson is produced in association with a jet can lead to large  $p_T^{\text{miss}}$  as leptonic decays can lead to neutrinos and/or to mismeasured energy. In order to reduce the background from such Z and W-boson decays in the search regions, events with leptons are rejected. Events containing one or more loose electrons [with  \$p\_T > 10\$  GeV](#) (where the loose requirements are detailed in Section 5.4) are rejected. Similarly, events containing any loose muons [with  \$p\_T > 10\$  GeV](#) are also rejected. In addition, events containing hadronically decaying  $\tau$  leptons are vetoed, where  $\tau_h$  are reconstructed using the HPS algorithm as described in Section 5.4. The vetoes here use loose requirements of object reconstruction, to reject as many leptons — and as much of the electroweak background — as possible.

A trigger efficiency of unity is ensured by requiring  $p_T^{\text{miss},\mu} > 250$  GeV. Search regions are then defined by thresholds of the leading jet  $p_T$ ;  $p_T(j_1) > 250, 300, 350, 400, 450, 500$  and 550 GeV. These are inclusive search regions, determined by the hardness of the ISR jet in each event. Typically, for a larger  $\tilde{t}$  mass, there is a larger boost to the  $\tilde{t}\tilde{t}$  system — see Figure 5.6. By having many, inclusive, search regions, sensitivity to a range of  $\tilde{t}$  (and  $\tilde{b}$ ) masses is gained. The baseline search region is defined by the above selection requirements and a leading jet threshold of 250 GeV.

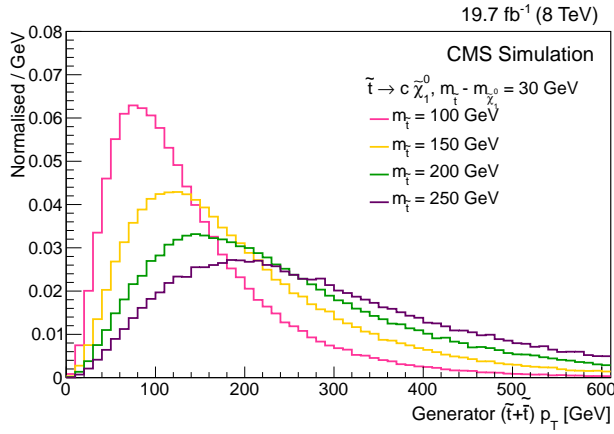


**Figure 5.6:** Total  $p_T$  of the  $\tilde{t}\tilde{t}$  pair for various signal hypotheses, where the mass splitting  $m_{\tilde{t}} - m_{\tilde{\chi}_1^0} = 30$  GeV. The  $\tilde{t}\tilde{t}$  system has a larger boost for larger  $\tilde{t}$  masses.

Various kinematic distributions are shown in Figure 5.7, before selection cuts are applied to that variable. The corresponding distribution after the cut has been applied is shown in Figure 5.8. Superimposed on the plots in Figure 5.8 are signal distributions for  $\tilde{t}\tilde{t} \rightarrow c\bar{c}\tilde{\chi}_1^0\tilde{\chi}_1^0$  where  $m_{\tilde{t}} = 250$  GeV and  $m_{\tilde{\chi}_1^0} = 240$  GeV. Table 5.2 lists the event yields from the various SM backgrounds at each step of the analysis, where numbers are taken from simulation and normalized to the integrated luminosity of the data. The cross section used to normalize each background is also listed [169–174]. [The total background yield is seen to be dominated by  \$Z\(\nu\bar{\nu}\) + \text{jets}\$  and  \$W + \text{jets}\$  events.](#)

## 5.6 Background estimation and systematic uncertainties

As is evident in Table 5.2, the dominant backgrounds in the search regions after the monojet event selection are expected to be electroweak backgrounds. The largest contribution is due to invisible  $Z$  boson decays,  $Z(\nu\bar{\nu}) + \text{jets}$ , which is irreducible as the neutrinos mimic the LSPs and there is genuine  $p_T^{\text{miss}}$  in the final state. The secondary background is due to leptonic  $W$  boson decay,  $W(\ell\nu) + \text{jets}$ , where the lepton (electrons and muons, including those from leptonically decaying taus) is not reconstructed, outside of the kinematic acceptance of the lepton vetoes or not isolated. Both of these backgrounds are estimated from data by selecting a control sample of  $\mu+\text{jet}$  events, where  $Z(\mu\mu) + \text{jets}$  events are used to predict the invisible  $Z$  background and  $W(\mu\nu) + \text{jets}$  events are used

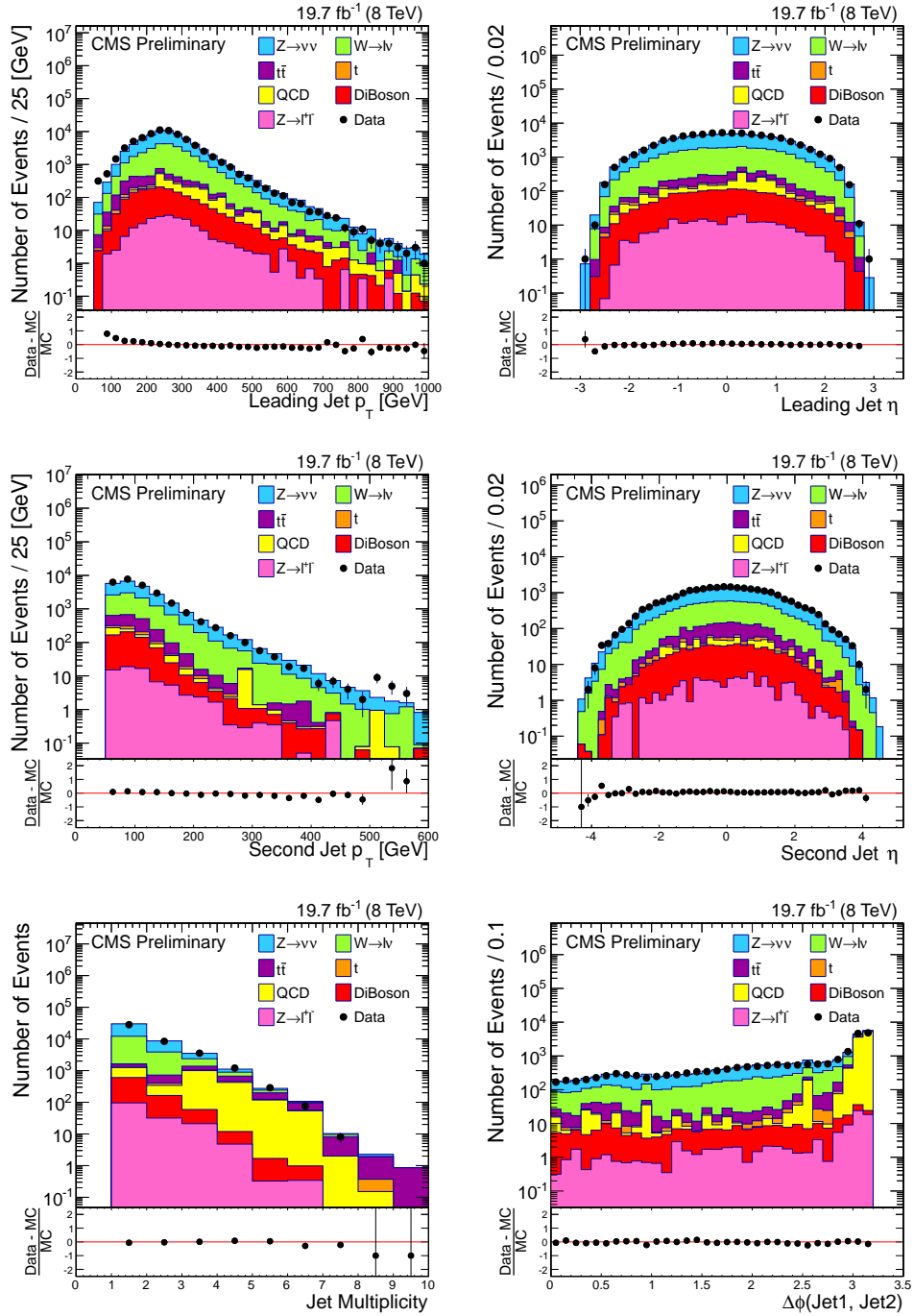


**Figure 5.7:** Plots of basic selection variables. All figures except for the  $p_T$  and  $\eta$  of the second leading jet show distributions after all cuts are applied except the one being plotted (the leading jet  $p_T$  cut for all plots except the jet  $p_T$  and jet  $\eta$  is set to 110 GeV). SM backgrounds are taken from simulation and normalized to the integrated luminosity using the cross sections shown in Table 5.2. The error bars in the ratio plots show the statistical uncertainties.

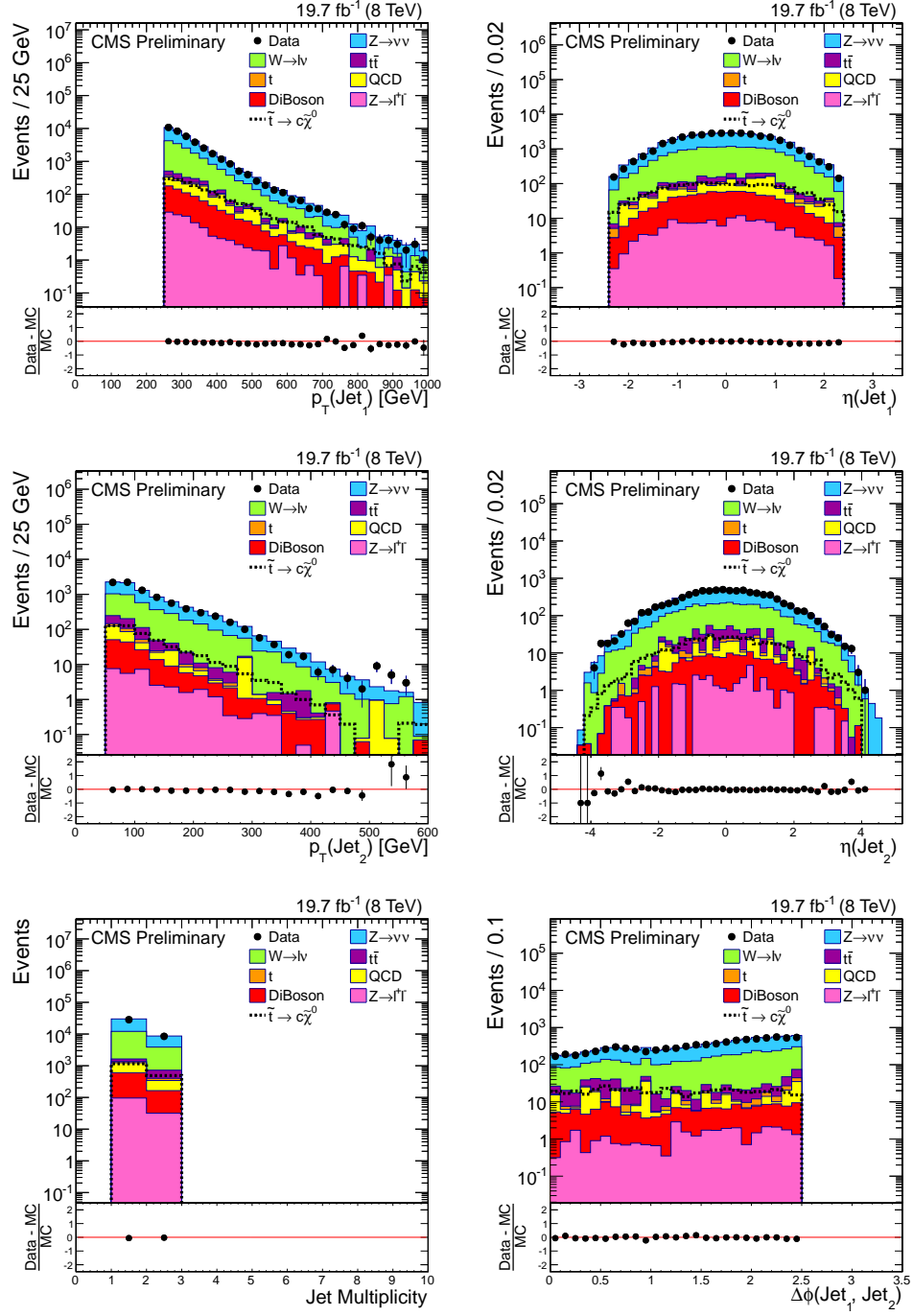


**Figure 5.8:** Plots of selection variables in the baseline search region, where  $p_T(\text{jet}) > 250 \text{ GeV}$ . Superimposed are kinematic distributions for the signal  $\tilde{t}\tilde{t} \rightarrow c\tilde{\chi}_1^0\tilde{\chi}_1^0$  where  $m_{\tilde{t}} = 250 \text{ GeV}$  and  $m_{\tilde{\chi}_1^0} = 240 \text{ GeV}$ . SM backgrounds are taken from simulation and normalized to the integrated luminosity using the cross sections shown in Table 5.2. The error bars in the ratio plots show the statistical uncertainties.

**Table 5.2:** For illustrative purposes, event yields from different simulated samples for the SM backgrounds at each step of the event selection including the search regions. Backgrounds are obtained directly from simulation and normalized to an integrated luminosity of  $19.7 \text{ fb}^{-1}$  using the cross sections shown in the table.

Selection	W + jets	Z( $\ell^+\ell^-$ ) + jets	Z( $\nu\bar{\nu}$ ) + jets	Diboson	t $\bar{t}$	Single-top	QCD multijet	Total BG
Cross section (pb)	228.9	40.5	588.3	234.0	1.085e6	114.8	105.7	
Event cleaning	2514352	190332	4337526	65666	461413	77284	5429269	13075841
$p_T^{\text{miss},\mu} > 200 \text{ GeV}$	317656	30242	134578	9572	63174	9289	87605	652117
Noise cleaning	292550	27880	123420	8706	59412	8525	81668	602162
$p_T(j_1) > 110 \text{ GeV}$	279323	26652	117513	8045	53353	7752	80844	573484
$N_{\text{jets}} \leq 2$	254058	24413	109313	7287	29364	5596	44247	474278
$\Delta\phi(j_1, j_2) < 2.5$	237533	22947	104158	6984	25312	4815	8433	410181
$\mu$ veto	106236	1511	104152	4051	9826	1892	7444	235112
$e$ veto	79407	1004	104065	3459	6557	1325	7401	203218
$\tau_h$ veto	71808	807	103106	3248	5599	1147	7047	192762
$p_T(j_1) > 250 \text{ GeV}$ & $p_T^{\text{miss},\mu} > 250 \text{ GeV}$	13641	127	22615	639	602	172	819	38615
$p_T(j_1) > 300 \text{ GeV}$	6873	75	11093	369	344	97	546	19397
$p_T(j_1) > 350 \text{ GeV}$	3182	40	5231	206	178	49	332	9218
$p_T(j_1) > 400 \text{ GeV}$	1501	25	2617	113	91	21	181	4549
$p_T(j_1) > 450 \text{ GeV}$	751	17	1335	64	48	11	92	2318
$p_T(j_1) > 500 \text{ GeV}$	376	11	727	36	27	5.2	61	1244
$p_T(j_1) > 550 \text{ GeV}$	204	7.4	406	21	18	3.2	34	693

to predict the  $W(\ell\nu) + \text{jets}$  background. Small contributions from QCD multijet and t $\bar{t}$  events are estimated using simulation and corrected for differences in MC and data using dedicated control samples. Diboson (WW, WZ and ZZ) processes are taken from simulation. Events due to  $V\gamma$  processes are estimated as a part of the electroweak data driven backgrounds. Very small contributions from single top quark and Drell–Yan processes are taken directly from simulation.

The control sample of  $\mu + \text{jets}$  events used to estimate the electroweak background is obtained by applying the full monojet selection with the exception of the muon veto. The definition of  $p_T^{\text{miss},\mu}$  to exclude muons and therefore allowing muons to mimic neutrinos or missing leptons at both the trigger level and in reconstructed events, allows the use of the same trigger for both the search and control regions. As well as being rather simple, this has the advantage of reducing the systematic uncertainties associated with combining two data samples.

### 5.6.1 Data-driven $Z(\nu\bar{\nu}) + \text{jets}$ background estimation

The large and irreducible  $Z(\nu\bar{\nu}) + \text{jets}$  background is estimated using a muon control sample of  $Z(\mu\mu) + \text{jets}$  events. By exploiting the similar kinematics of  $Z \rightarrow \nu\bar{\nu}$  and  $Z \rightarrow \mu^+\mu^-$  processes, and their known branching ratios, we extrapolate from the number of dimuon events in muon control regions to the number of  $Z(\nu\bar{\nu}) + \text{jets}$  events in the signal regions.

From the muon control sample defined using the monojet event selection with the exception of the muon veto, we select events to form a dimuon control sample enriched in  $Z(\mu\mu) + \text{jets}$  events. Two muons of opposite sign are required, where at least one must satisfy the tight muon requirements of Section 5.4.2 and the other satisfies the loose muon requirements. The invariant mass of the  $\mu^+\mu^-$  pair must be within the  $Z$  mass window, which we take to be within  $60 < m_{\mu^+\mu^-} < 120$  GeV. These criteria of one tight and one loose muon represent a good compromise between having a well-reconstructed  $Z$  boson while maintaining reasonable statistical precision. Event yields in the dimuon control sample are shown in Table 5.3. The control region requirements are very effective at selecting  $Z \rightarrow \ell^+\ell^-$  events, however there are a small number of non- $Z$  events that contribute to the event yield in data - namely from  $t\bar{t}$ , diboson and single top quark processes.

**Table 5.3:** Event yields for the dimuon control regions in data and MC simulation. 50% uncertainty is assigned to each background (i.e. from  $t\bar{t}$ , single top, and diboson events) and these are combined in quadrature to get the total uncertainty on the number of background events in the  $Z \rightarrow \mu^+\mu^-$  sample.

$p_T(j_1)$ GeV	> 250	> 300	> 350	> 400	> 450	> 500	> 550
$Z(\ell^+\ell^-) + \text{jets}$	3067	1577	757	382	198	109	62
$W + \text{jets}$	0	0	0	0	0	0	0
$Z(\nu\bar{\nu}) + \text{jets}$	0	0	0	0	0	0	0
$t\bar{t}$	37	21	9.9	4.8	0.7	0	0
Single-top	5.7	2.2	0.9	0.9	0	0	0
QCD multijet	0	0	0	0	0	0	0
Diboson	68	41	24	13	8.2	4.4	2.6
Total MC	3177	1641	791	401	207	113	65
Data	2547	1235	567	277	150	79	40

The  $Z \rightarrow \mu^+\mu^-$  and  $Z \rightarrow \nu\bar{\nu}$  events share similar kinematic characteristics and by interpreting the pair of muons as missing energy, the topology of the process in which the  $Z$  boson decays to neutrinos can be reproduced. A comparison between data and MC for the dimuon invariant mass and momentum after all the selection cuts and requiring

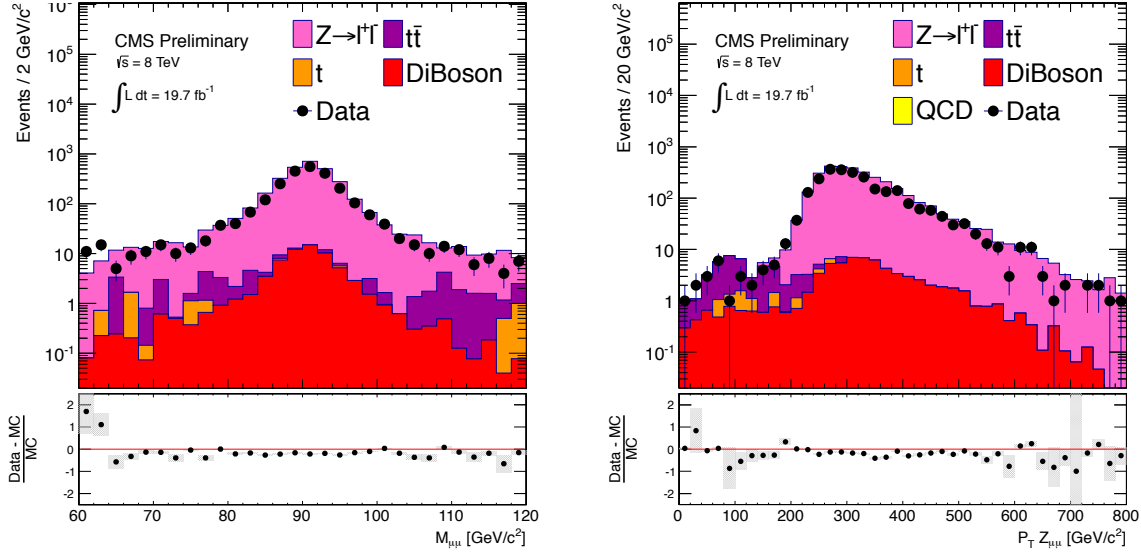


**Figure 5.9:** Invariant mass and transverse momentum of the dimuon pair in the  $Z \rightarrow \mu^+\mu^-$  control sample.

$p_T(j_1) > 250$  GeV is shown in Figure 5.9. The number of  $Z \rightarrow \nu\bar{\nu}$  events can then be predicted using:

$$N(Z \rightarrow \nu\nu) = \frac{N_{\mu\mu}^{\text{obs}} - N_{\mu\mu}^{\text{bgd}}}{A * \epsilon} \cdot R, \quad (5.2)$$

where  $N_{\mu\mu}^{\text{obs}}$  is the number of observed dimuon events,  $N_{\mu\mu}^{\text{bgd}}$  is the number of non- $Z(\mu\mu)$  events contributing to the dimuon sample,  $A$  is the acceptance of the control sample criteria and  $\epsilon$  is the selection efficiency of a reconstructed event provided it was produced within the acceptance of the criteria, and  $R$  is the ratio of branching fractions for the  $Z$  decay to neutrinos and a pair of muons. These factors are determined as follows:

- $N_{\mu\mu}^{\text{bgd}}$  : The dimuon sample comprises predominantly of  $Z \rightarrow \mu^+\mu^-$  events with contamination from other, non- $Z(\mu\mu)$  processes at the level of 5%. These backgrounds are taken from simulation and a relative 50% uncertainty is assigned their yields;
- $A$  : The acceptance  $A$  is defined as the fraction of all generated events, prior to hadronization and reconstruction (i.e. at quark and lepton level as described by the event generator), that satisfy the requirements of the control sample. One muon must satisfy  $p_T > 20$  GeV and  $|\eta| < 2.1$ , and the other, of opposite sign, must satisfy  $p_T > 10$  GeV. The invariant mass of these muons must lie between 60 GeV and 120 GeV. This is obtained from  $Z + \text{jets}$  simulation;

- $\epsilon$  : The event selection efficiency  $\epsilon$  is defined as the efficiency of reconstructing two muons passing all the identification and isolation criteria that have a reconstructed invariant mass between 60 and 120 GeV, given that they are within the detector acceptance  $A$ . The efficiency is taken from simulation, once it has passed through the hadronization and reconstruction stages (unlike for  $A$ ). The efficiency of reconstructing a  $Z(\mu\mu)$  event with [one tight and one loose muon](#)~~two tight muons~~ is calculated in both data and simulation (for all MC simulated samples) in the  $Z \rightarrow \mu^+\mu^-$  control sample. The difference in efficiencies is averaged across the search region jet  $p_T$  thresholds, and the resulting correction factor of 1.005 is applied to  $\epsilon$  to account for the difference in muon selection efficiency between data and MC;
- $R$  : The ratio of the branching fraction  $R = (\frac{BF(Z(\nu\bar{\nu}))}{BF(Z(\ell^+\ell^-))})$  is obtained from Ref. [1] and is  $5.942 \pm 0.019$  when  $l = \mu$ .

The prediction of the  $Z(\nu\bar{\nu}) + \text{jets}$  background in the search regions relies on counting the number of  $Z(\mu\mu) + \text{jets}$  events at each  $p_T(j_1)$  threshold, which is in turn correlated to the  $p_T^{\text{miss},\mu}$  requirement. In the definition of  $p_T^{\text{miss},\mu}$ , we interpret the muons as missing energy: muon  $\vec{p}_T$  is added into the  $\vec{p}_T^{\text{miss}}$  to calculate  $\vec{p}_T^{\text{miss},\mu}$ . As the  $\vec{p}_T^{\text{miss},\mu}$  in an event is largely balanced by  $\vec{p}_T(j_1)$ , the values of  $p_T^{\text{miss},\mu}$  and  $p_T(j_1)$  thus rely on successfully identifying both muons arising from a  $Z \rightarrow \mu^+\mu^-$  decay.

If either (or both) of the muons in a  $Z \rightarrow \mu^+\mu^-$  decay is not properly identified, then the value of  $p_T^{\text{miss},\mu}$  may be wrong. For example, if one of the muons does not pass identification requirements but the track is reconstructed, then the energy of that muon will be included within the  $\vec{p}_T^{\text{miss}}$  calculation (reconstructed using the PF algorithm). However, the muon will not be identified using tight or loose requirements, and its  $\vec{p}_T$  will not be included in the  $\vec{p}_T^{\text{miss},\mu}$  calculation. The value of  $\vec{p}_T^{\text{miss},\mu}$  will then be incorrect, and the event is likely to fail the selection requirements on  $p_T^{\text{miss},\mu}$  or  $p_T(j_1)$ . It will not contribute to the total number of  $Z(\mu\mu) + \text{jets}$  events and therefore reduce the total  $Z(\nu\bar{\nu}) + \text{jets}$  background estimation. However, if it had been a  $Z(\nu\bar{\nu}) + \text{jets}$  event, both neutrinos would lead to  $p_T^{\text{miss}}$ — in neglecting such events we underestimate the  $Z(\nu\bar{\nu}) + \text{jets}$  background.

Figure 5.10 shows the distribution of the ratio of  $p_T^{\text{miss},\mu}$  to the  $p_T$  of the  $Z$  boson  $p_T(Z)$ , taken from  $Z(\mu\mu) + \text{jets}$  and  $Z(\nu\bar{\nu}) + \text{jets}$  simulation. The larger tail at low values of  $p_T^{\text{miss},\mu}/p_T(Z)$  in  $Z(\mu\mu) + \text{jets}$  events is attributed to events where one or both muons is not properly identified as described above. In order to correct for this effect we count the number of events in simulation where the ratio  $p_T^{\text{miss},\mu}/p_T(Z) < 0.7$ , at each

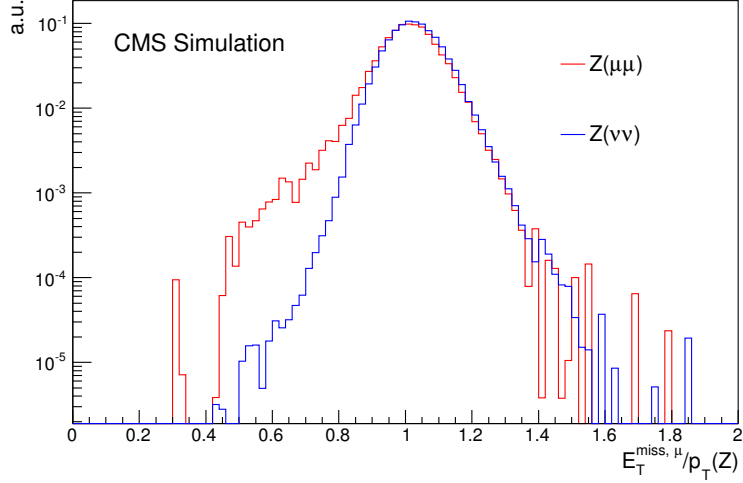


**Figure 5.10:** The ratio of  $p_T^{\text{miss}, \mu}$  to the Z boson  $p_T$ , taken from simulation, in  $Z(\mu\mu) + \text{jets}$  and  $Z(\nu\bar{\nu}) + \text{jets}$  events. Distributions are normalized to unit area.

**Table 5.4:** The fraction of events that sit in the tail of the  $p_T^{\text{miss}, \mu}/p_T(Z)$  spectrum, which give correction factors used to predict the  $Z \rightarrow \nu\bar{\nu} + \text{jets}$  background.

$p_T(j_1)$ (GeV)	> 250	> 300	> 350	> 400	> 450	> 500	> 550
$p_T^{\text{miss}, \mu}/p_T(Z) < 0.7$	0.037	0.046	0.060	0.063	0.083	0.097	0.098

$p_T(j_1)$  threshold in the dimuon control sample, with the additional criteria that the  $p_T(Z) > 250$  GeV to ensure  $p_T^{\text{miss}, \mu}$ , when measured correctly,  $> 250$  GeV. The value of 0.7 is chosen because the resolution of the Z boson mass peak is  $\sim 0.3$ , and we wish to count events in the tail of the spectrum. This gives an estimation of the number of events where we have not properly measured or identified one or two of the muons. The ratio in each search region is shown in Table 5.4. This correction factor is summed with the difference in data and simulation for muon selection efficiency (1.005, described above), and applied to  $\epsilon$  in each search region. For example, for  $p_T(j_1) > 250$  GeV, the correction factor for  $\epsilon$  becomes  $0.037 + 1.005 = 1.042$ .

A correction factor is applied to R in order to account for contamination from  $\gamma^*$  events in the data that fall within the selection criteria of the control sample, as well as efficiency of the mass window requirement. Using  $Z(\mu\mu) + \text{jets}$  and  $Z(\nu\bar{\nu}) + \text{jets}$  simulated events, the  $\gamma^*$  contamination  $R^{\gamma^*}$  can be estimated using

$$R^{\gamma^*} = \frac{1 - \alpha}{1 - \beta}, \quad (5.3)$$

**Table 5.5:** Observed yields in the dimuon control sample, background yields from non-Z( $\mu\mu$ ) processes,  $A$  and  $\epsilon$  of control sample requirements and the corrected ratio of branching fractions in each of the search regions.

$p_T(j_1)$ (GeV)	> 250	> 300	> 350	> 400	> 450	> 500	> 550
$N_{\mu\mu}^{\text{obs}}$	2547	1235	567	277	150	79	40
$N_{\mu\mu}^{\text{bgd}}$	111	64	35	19	8.9	4.4	2.7
Acceptance $A$	0.805	0.833	0.851	0.864	0.881	0.905	0.896
Efficiency $\epsilon$	0.862	0.843	0.822	0.802	0.775	0.751	0.754
$R$	6.043	6.043	6.043	6.043	6.043	6.043	6.043

where  $\alpha$  is the difference in the normalized yield of Z( $\mu\mu$ ) + jets and Z( $\nu\bar{\nu}$ ) + jets events in the Z mass window,  $60 < m_Z < 120$  GeV, and  $\beta$  is the fraction of events lying outside the Z mass window in Z( $\nu\bar{\nu}$ ) + jets simulation. [Because this factor has no dependence on  \$p\_T\(j\_1\)\$ , we](#) normalize across all  $p_T(j_1)$  bins, and find a correction factor of 1.017.

Table 5.5 shows the observed dimuon event yields, non-Z( $\mu\mu$ ) event yields, the acceptance  $A$  and efficiency  $\epsilon$ . The ratio of branching fractions  $R$  is corrected by  $R^{\gamma^*}$ , and given (it is the same for each threshold). The uncertainties on these factors are discussed below.

### Uncertainties on data-driven Z( $\nu\bar{\nu}$ ) + jets background estimation

The dominant source of uncertainty on the Z( $\nu\bar{\nu}$ ) + jets background estimation arises from statistical uncertainties on  $N_{\mu\mu}^{\text{obs}}$ . It increases as the  $p_T(j_1)$  threshold is increased, and contributes 2.1–17%.

The uncertainty on  $N_{\mu\mu}^{\text{bgd}}$ , arising from non-Z( $\mu\mu$ ) processes, is taken as 50% of the respective yields, where the total uncertainty on  $N_{\mu\mu}^{\text{bgd}}$  is the quadratic sum of the individual contributions. As the total contribution from non-Z( $\mu\mu$ ) processes in the control region is small, of order 5%, this uncertainty has a relatively minor contribution to the total uncertainty, varying from 1.6–3.5%.

The total uncertainty on  $A$  arises from both statistical and systematic sources. The statistical uncertainty is due the number of simulated events used to derive the ratio. A 2% systematic uncertainty is added to this, [calculated using the PDF4LHC recommendations \[175\]](#), to incorporate the uncertainty on the PDFs used to describe the colliding protons. Similarly, the total uncertainty on  $\epsilon$  is due to the statistics of the

**Table 5.6:** Summary of the contributions, in %, to the total uncertainty on  $Z \rightarrow \nu\bar{\nu} + \text{jets}$  background from the various factors used in the data-driven estimation.

$p_T(j_1)$ (GeV)	> 250	> 300	> 350	> 400	> 450	> 500	> 550
Statistics ( $N_{\mu\mu}^{\text{obs}}$ )	2.1	3.0	4.5	6.5	8.7	12	17
Background ( $N_{\mu\mu}^{\text{bgd}}$ )	1.6	2.0	2.4	2.7	2.9	2.9	3.5
Acceptance	2.0	2.1	2.1	2.2	2.4	2.5	2.9
Efficiency	2.1	2.1	2.3	2.6	3.3	4.4	5.5
R	2.0	2.0	2.0	2.0	2.0	2.0	2.0
Total	5.3	5.9	7.0	8.8	11	14	19

**Table 5.7:** The predicted  $Z(\nu\bar{\nu}) + \text{jets}$  event yield in each of the search regions, calculated as detailed in the text. The uncertainty contains both systematic and statistical sources.

$p_T(j_1)$ (GeV)	> 250	> 300	> 350	> 400	> 450	> 500	> 550
$Z(\nu\bar{\nu}) + \text{jets}$	$21209 \pm 1115$	$10077 \pm 592$	$4597 \pm 324$	$2250 \pm 197$	$1250 \pm 137$	$663 \pm 94$	$334 \pm 65$

simulation and incorporates a 2% systematic uncertainty on the hadronization process. For  $\epsilon$  in the lower jet threshold bins, and for  $A$  in all search regions, these systematics dominate over the statistical uncertainties, where the total uncertainty on  $A$  varies from 2.0–2.9%, and on  $\epsilon$  from 2.1–5.5%. There are fewer events with muons reconstructed within the kinematic acceptance of the control sample than are generated within the kinematic acceptance, hence the statistical uncertainty - and therefore total uncertainty - on  $\epsilon$  is larger than the uncertainty on  $A$ .

A 2% systematic uncertainty is assigned to  $R$ , in order to incorporate the uncertainties on the ratio of branching fractions (which are much smaller than 2%), and on the correction factor  $R\gamma^*$  (itself less than 2%), which incorporates the uncertainty due to the restriction of the  $Z$  mass window on branching fractions, and on the contribution of  $\gamma^*$  events in the control sample.

The uncertainties from the various sources are added in quadrature, and are listed in Table 5.6. The total uncertainty varies between 5.3 and 19%.

The final data-driven evaluation of the  $Z(\nu\bar{\nu}) + \text{jets}$  background using the methods outlined above is shown in Table 5.7.

### 5.6.2 Data-driven $W(\ell\nu) + \text{jets}$ background estimation

The second largest contribution to the total SM background arises from  $W(\ell\nu) + \text{jets}$  events. The lepton ( $e$  and  $\mu$ , including those from leptonically decaying  $\tau$  leptons) fails the respective lepton veto and hence is “lost”, i.e. it is not isolated, not identified, or outside of the acceptance of the analysis. Similarly,  $\tau_h$  leptons which are not identified contribute to this lost-lepton background. The contributions in the search regions from lost-lepton events are evaluated in a similar way to the  $Z(\nu\bar{\nu}) + \text{jets}$  background, using a muon control sample enriched in  $W(\mu\nu) + \text{jets}$  events.

From the muon control sample defined using the same triggers as the search regions with the exception of the muon veto, a sample enriched in  $W(\mu\nu) + \text{jets}$  events is obtained by requiring one muon satisfying the tight muon criteria with a reconstructed W-boson transverse mass  $m_T = \sqrt{2p_T^{\mu\nu} p_T^{\text{miss}}(1 - \cos \Delta\phi)}$  that lies between 50 and 100 GeV, where  $\Delta\phi$  is the azimuthal angle between the  $\vec{p}_T^{\text{miss},\mu}$  and  $\vec{p}_T^\mu$  vectors. Event yields in the  $W(\mu\nu) + \text{jets}$ -enriched single muon control sample are listed in Table 5.8 with the predicted SM processes from simulation. [Here, as in Table 5.3, simulation is greater than data across all search regions. We do not expect MC to model the data very well in this very boosted corner of phase space, hence why we use data to estimate these backgrounds.](#) A comparison between data and MC for the transverse mass and momentum of the W boson after the full selection and for  $p_T(j_1) > 250$  GeV is shown in Figure 5.11.

**Table 5.8:** Event yields for the  $W \rightarrow \mu\nu$  data control sample with SM backgrounds from MC simulation. A relative uncertainty of 50% is assigned to each background (i.e. from  $Z + \text{jets}$ ,  $t\bar{t}$ , single top, QCD and diboson events) and these are combined in quadrature to get the total uncertainty on the number of background events in the  $W \rightarrow \mu\nu$  sample.

$p_T(j_1)$ (GeV)	> 250	> 300	> 350	> 400	> 450	> 500	> 550
W + jets	11436	5712	2694	1349	712	389	223
$Z(\ell^+\ell^-) + \text{jets}$	183	94	44	22	9.9	6.6	3.7
$Z(\nu\bar{\nu}) + \text{jets}$	0	0	0	0	0	0	0
$t\bar{t}$	608	313	151	76	41	20	11
Single top quarks	158	80	41	22	13	7.8	4.8
QCD multijet	0.3	0.3	0.3	0.3	0.3	0.3	0.3
Diboson	197	121	71	41	22	13	6.5
Total MC	12582	6320	3001	1509	798	437	249
Data	11371	5477	2547	1258	668	352	184

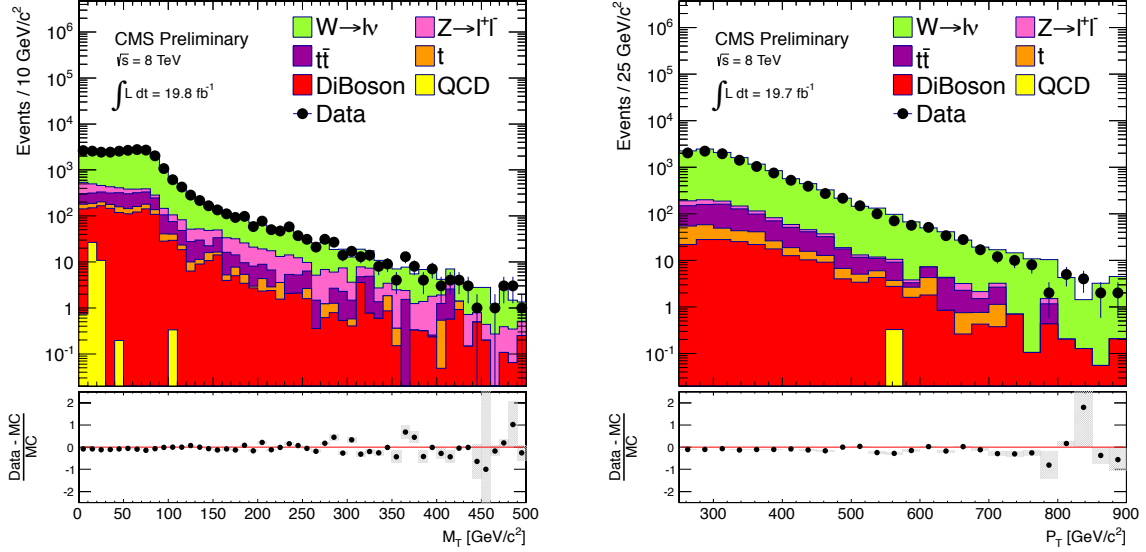


**Figure 5.11:** Transverse mass  $m_T$  of the muon (left) and  $p_T$  of  $W^\pm$  candidates in the  $W$  mass window,  $50 - 100$  GeV in the single muon control sample.

The total number of  $W(\mu\nu) + \text{jets}$  events is estimated in an analogous way to the  $Z(\nu\bar{\nu}) + \text{jets}$  background, correcting the observed number of single muon events in the control sample  $N_\mu^{\text{obs}}$  by events due to non- $W + \text{jets}$  processes  $N_\mu^{\text{bgd}}$ . The resulting  $W \rightarrow \mu\nu$  events are then corrected for the kinematic acceptance  $A'$  of the control sample, and the efficiency  $\epsilon'$  of reconstructing events within the acceptance of the detector to obtain the total number of generated events ( $N_\mu^{\text{tot}}$ ):

$$N_\mu^{\text{tot}} = \frac{N_\mu^{\text{obs}} - N_\mu^{\text{bgd}}}{A'\epsilon'}. \quad (5.4)$$

The resulting number of  $W \rightarrow \mu\nu$  events produced in the detector is subsequently weighted by a muon veto inefficiency factor in order to obtain the predicted number of  $W(\mu\nu) + \text{jets}$  events that would not be rejected by the lepton veto and thus remain in the search regions. The total number of  $W(\mu\nu) + \text{jets}$  events that are out of the acceptance and not identified or isolated can be written as:

$$N_\mu^{\text{lost}} = N_\mu^{\text{tot}}(1 - A_\mu\epsilon_\mu). \quad (5.5)$$

where  $A_\mu$  is the acceptance of the loose muon selection requirements (used in the muon veto) before any reconstruction has taken place, and  $\epsilon_\mu$  is the efficiency of the reconstruction for muons satisfying selection requirements when produced (i.e. for muons within the acceptance  $A_\mu$ ).  $A_\mu$  and  $\epsilon_\mu$  are estimated using simulation, and  $\epsilon_\mu$  is corrected

for differences in muon selection efficiency between data and MC in the same way as for  $\epsilon$  in the  $Z(\nu\bar{\nu}) + \text{jets}$  background estimation.

To estimate the lost electron background, we begin by finding the total number of  $W \rightarrow e\nu$  events produced  $N_e^{\text{tot}}$ . The ratio of the number of  $W(e\nu) + \text{jets}$  to  $W(\mu\nu) + \text{jets}$  events produced, before any reconstruction has taken place, is taken from simulation and labelled  $f_e$ . Then,  $N_e^{\text{tot}} = N_\mu^{\text{tot}} f_e$ . The number of lost  $W \rightarrow e\nu$  events can subsequently be found by correcting for the electron veto inefficiency factor:

$$N_e^{\text{lost}} = N_e^{\text{tot}}(1 - A_e \epsilon_e). \quad (5.6)$$

Both the  $A_e$  and  $\epsilon_e$  factors are obtained using simulation, where  $A_e$  is the acceptance of the loose electron selection requirements (used in the electron veto) before any reconstruction has taken place, and  $\epsilon_e$  is the efficiency of reconstruction for electrons satisfying selection requirements when produced (i.e. for electrons within the acceptance  $A_e$ ). A data/MC scale factor of 1.0 is assumed [with an assigned systematic that covers the variation in efficiency between data and MC](#).

The component of the  $W + \text{jets}$  background from  $\tau_h$  events is estimated in the same way. The ratio of the number of  $W(\mu\nu) + \text{jets}$  to  $W(\tau_h\nu) + \text{jets}$  events ( $f_{\tau_h}$ ) produced prior to reconstruction is taken from simulation and used to obtain  $N_{\tau_h}^{\text{tot}}$ . This is subsequently weighted by the inefficiency of the tau selection used in the  $\tau_h$  veto to obtain the lost-lepton background due to  $\tau_h$  events:

$$N_{\tau_h}^{\text{tot}} = N_\mu^{\text{tot}} f_{\tau_h}, \quad (5.7)$$

$$N_{\tau_h}^{\text{lost}} = N_{\tau_h}^{\text{tot}}(1 - A_{\tau_h} \epsilon_{\tau_h}). \quad (5.8)$$

The  $\tau_h$  identification acceptance and efficiency is estimated from simulation with a data/MC scale factor of 1.0 and assigned an uncertainty of 6% as recommended by the CMS Tau Physics Object Group. The electron and muon discriminants in the tau identification can also result in the tau veto rejecting electron and muon events. The probability of an electron or muon to fake a tau is estimated from  $W + \text{jets}$  simulation and found to be negligible, below 0.1%.

All of the above components can be summarised in a ‘master’ equation for estimating the lost-lepton background:

$$N_{\text{lep}}^{\text{lost}} = \frac{N_\mu^{\text{obs}} - N_\mu^{\text{bkgd}}}{A' \epsilon'} \left[ (1 - A_\mu \epsilon_\mu) + f_e(1 - A_e \epsilon_e) + f_{\tau_h}(1 - A_{\tau_h} \epsilon_{\tau_h}) \right] \quad (5.9)$$

**Table 5.9:** Estimation of the remaining  $W + \text{jets}$  background from the lost electron, muon and hadronic tau contributions.

$p_T(j_1)$ (GeV)	>250	>300	>350	>400	>450	>500	>550
$N_\mu^{\text{obs}}$	11371	5477	2547	1258	668	352	184
$N_\mu^{\text{bgd}}$	1146	608	307	160	86	48	26
$A'\epsilon'$	0.345	0.345	0.341	0.346	0.349	0.361	0.371
$N_\mu^{\text{tot}}$	29666	14125	6573	3176	1666	841	425
<b>Lost <math>\mu</math></b>							
$A_\mu\epsilon_\mu$	0.887	0.895	0.901	0.908	0.908	0.906	0.907
$N_\mu^{\text{lost}}$	3350	1484	649	292	152	79	40
<b>Lost <math>e</math></b>							
$A_e\epsilon_e$	0.615	0.684	0.734	0.771	0.793	0.815	0.823
$f_e$	0.374	0.465	0.548	0.610	0.653	0.706	0.727
$N_e^{\text{lost}}$	4273	2077	958	444	225	110	55
<b>Lost <math>\tau_h</math></b>							
$A_{\tau_h}\epsilon_{\tau_h}$	0.253	0.284	0.298	0.296	0.294	0.341	0.325
$f_{\tau_h}$	0.212	0.235	0.235	0.228	0.212	0.201	0.195
$N_{\tau_h}^{\text{lost}}$	4704	2377	1083	510	249	112	56

The factors in Eq. 5.9 used to estimate the lost muon, electron and hadronic tau backgrounds are listed in Table 5.9.

### Uncertainties on the data-driven lost-lepton background

The fractional contributions to the total uncertainty on the lost-lepton background are shown in Table 5.10. The statistical uncertainty on the number of events in the single muon control sample contributes 1.0–8.6% to the total uncertainty on the lost-lepton background, becoming dominant as the jet threshold increases and the number of  $W(\mu\nu) + \text{jets}$  events surviving the high leading jet  $p_T$  requirement decreases. The statistical precision could be increased by using  $W(e\nu) + \text{jets}$  events in addition to  $W(\mu\nu) + \text{jets}$  events, however this would require an additional electron-based trigger. The extra systematic uncertainties associated with combining the triggers mean there is little to be gained by doing this in this analysis.

The uncertainty on the non- $W + \text{jets}$  processes in the single muon control sample contributes 3.3–4.4% to the total uncertainty. It is taken to be 50% of each individual contribution added quadratically, in the same way as for the  $Z(\nu\bar{\nu}) + \text{jets}$  background

**Table 5.10:** Summary of the fractional contributions (in %) to the total uncertainty on the W + jets background from the various factors used to estimate it.

$p_T(j_1)$ (GeV)	> 250	> 300	> 350	> 400	> 450	> 500	> 550
Statistics ( $N_\mu^{\text{obs}}$ )	1.0	1.5	2.3	3.2	4.4	6.2	8.6
Background ( $N_\mu^{\text{bgd}}$ )	3.3	3.7	4.0	4.2	4.2	4.3	4.4
$A'$	2.0	2.0	2.0	2.0	2.0	2.1	2.1
$\epsilon'$	2.0	2.1	2.2	2.4	2.7	3.1	3.7
$A_\mu$	0.1	0.1	0.2	0.2	0.3	0.4	0.5
$\epsilon_\mu$	0.1	0.1	0.2	0.2	0.3	0.4	0.6
$A_e$	0.7	0.9	1.0	1.1	1.2	1.3	1.3
$\epsilon_e$	0.7	0.9	1.0	1.1	1.2	1.3	1.4
$A_\tau$	0.2	0.2	0.2	0.2	0.2	0.3	0.3
$\epsilon_\tau$	0.2	0.2	0.2	0.2	0.2	0.3	0.3
Total $A$ & $\epsilon$ 's	4.5	4.7	4.9	5.2	5.5	6.1	7.1
Total	5.7	6.2	6.7	7.4	8.2	9.7	12

estimation — here there is a larger yield from background processes, hence this uncertainty is larger than the similar numbers in Table 5.6.

Systematic uncertainties due to PDF, 2%, (hadronization, 2%) uncertainties are absorbed into the uncertainties on  $A'$ ,  $A_e$  and  $A_{\tau_h}$  ( $\epsilon'$ ,  $\epsilon_e$  and  $\epsilon_{\tau_h}$ ). No factor is added into  $A_\mu$  and  $\epsilon_\mu$  to avoid double-counting — these uncertainties, related to the generation and reconstruction of simulated muon events, have already been considered in the calculation of  $N_\mu^{\text{tot}}$ . They are reconsidered in the case of the lost electron and  $\tau_h$  lepton events in order to account for any differences in their generation as compared to muon events. The uncertainties on acceptance and efficiency in each calculation are considered fully correlated, because efficiency is dependent on acceptance and we wish to be conservative. The uncertainties on data/MC scale factors and on the number of simulated events in the control samples are also considered. The combined uncertainties on acceptances and efficiencies in the lost-lepton background estimation dominate the total uncertainty, contributing 4.5–7.1%.

A summary of the lost-lepton background in the search regions is shown in Table 5.11.

**Table 5.11:** Summary of the estimated total remaining W + jets background.

$p_T(j_1)$ (GeV)	> 250	> 300	> 350	> 400	> 450	> 500	> 550
$N_\mu^{\text{tot}}$	29666	14125	6573	3176	1666	841	425
$N_\mu^{\text{lost}}$	3350	1484	649	292	152	79	40
$N_e^{\text{lost}}$	4273	2077	958	444	225	110	55
$N_{\tau_h}^{\text{lost}}$	4704	2377	1083	510	249	112	56
Lost-lepton	$12328 \pm 707$	$5939 \pm 366$	$2690 \pm 180$	$1246 \pm 92$	$627 \pm 52$	$301 \pm 29$	$150 \pm 18$

### 5.6.3 QCD Background Estimation

The QCD multijet contribution in the search regions is expected to be small,  $\approx 2\%$ . It is evaluated using simulation, with data/MC correction factors derived from data control regions enriched in multijet events.

The QCD control region is defined using the search region event selection, apart from those cuts that remove the majority of the QCD:  $\Delta\phi(j_1, j_2) < 2.5$  and  $N_{\text{jets}} < 3$ . The  $p_T$  requirement used to count jets is varied between 20 and 80 GeV, as this parameter is sensitive to the number of multijet events satisfying the requirements of the search regions. We further require  $\Delta\phi(p_T^{\text{miss},\mu}, j_2) < 0.3$ , as this sideband is highly populated with multijet events in which the  $p_T^{\text{miss}}$  has been mismeasured. Such events have back-to-back jets where the mismeasured  $p_T^{\text{miss},\mu}$  vector is aligned with the second jet and is in the opposite hemisphere to the leading jet. Figure 5.12 shows a comparison of the data and MC for this control region, where the excess of QCD multijet events is evident at low  $\Delta\phi(p_T^{\text{miss},\mu}, j_2)$ .

The event yields for data and MC in this region are shown in Table 5.12 for each jet counting  $p_T$  threshold and for  $p_T(j_1) > 250$  GeV. The scale factor  $R^{\text{QCD}}$  is defined as

$$R^{\text{QCD}} = \frac{N_{\text{QCD}}^{\text{obs}} - N_{\text{QCD}}^{\text{MCnon-QCD}}}{N_{\text{QCD}}^{\text{pred}}}, \quad (5.10)$$

where  $N_{\text{QCD}}^{\text{obs}}$  is the observed number of events in the QCD control region and  $N_{\text{QCD}}^{\text{MCnon-QCD}}$  is the sum of the non-QCD events, taken from simulation and corrected with data/MC scale factors according to the data-driven estimations given in Section 5.6.1 and 5.6.2 where applicable.  $N_{\text{QCD}}^{\text{pred}}$  is the predicted number of QCD events in the control region, taken from simulation.  $R^{\text{QCD}}$  then estimates the ratio of QCD events in data to QCD events in simulation to give a data/MC scale factor for the QCD prediction from simulation in the search regions.

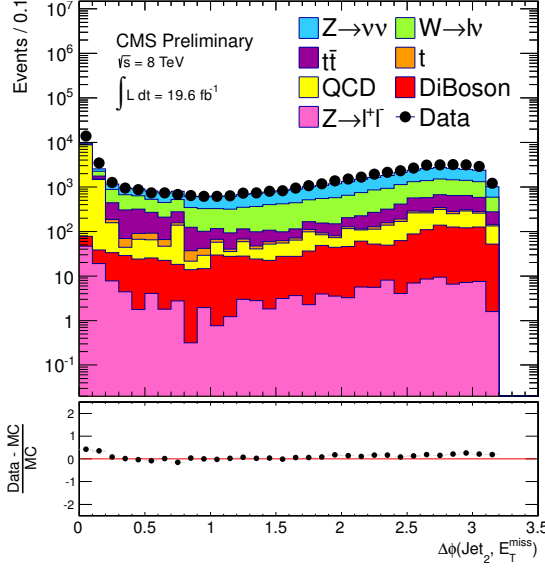


**Figure 5.12:** The QCD rich region dominated by back to back jets,  $\Delta\phi(p_T^{\text{miss},\mu}, j_2) < 0.3$ , shown for a jet counting cut of 60 GeV for  $p_T(j_1) > 250$  GeV.

**Table 5.12:** Event yields from MC and data for  $p_T(j_1) > 250$  GeV and for different values of the  $p_T$  threshold used for jet counting in the QCD rich region  $\Delta\phi(p_T^{\text{miss}}, j_2) < 0.3$ . Relative uncertainty on a scale factor derived from the data is also shown.

Jet $p_T$ (GeV)	Data	MC	QCD	Total Data/MC	$R^{\text{QCD}}$	Uncertainty
> 20	21428	15987	10110	1.340	1.538	0.321
> 30	20568	15141	10089	1.358	1.538	0.325
> 40	19938	14543	10057	1.371	1.536	0.329
> 50	19307	13974	9930	1.382	1.537	0.335
> 60	18708	13522	9852	1.384	1.526	0.341
> 70	18110	12921	9603	1.402	1.540	0.347
> 80	17435	12485	9455	1.397	1.523	0.354

The QCD scale factor  $R^{\text{QCD}}$  in each search region is found by taking the mean scale factor from all the jet counting thresholds. The scale factors applied to the QCD multijet event yield, from simulation, in search region are shown in Table 5.13. A correction factor of 1.53 at  $p_T(j_1) > 250$  GeV is required, decreasing to 1.35 at  $p_T(j_1) > 550$  GeV. This is greater than the factor from the dijet resonance analysis of 1.22 [176], but the search regions here are in a different region of phase space so it is not unexpected.

**Table 5.13:** QCD scale factor derived from QCD rich control region for each inclusive  $p_T(j_1)$  bin with relative error.

$p_T(j_1)$ (GeV)	QCD <sub>s.f.</sub>	Relative Error
250	1.534	0.336
300	1.490	0.336
350	1.465	0.341
400	1.428	0.350
450	1.402	0.359
500	1.365	0.369
550	1.347	0.377

The total relative uncertainties on  $R^{\text{QCD}}$  are shown in Table 5.13<sup>1</sup>. They are due to the statistical uncertainty on the number of events in data (which is negligible) and the systematic uncertainty on the number of non-QCD events in the control regions — a relative uncertainty of 50% is assigned to each non-QCD background. To ensure we give a conservative estimation for the QCD multijet background, a 50% uncertainty on the raw QCD yield from simulation is combined in quadrature with the uncertainty on  $R^{\text{QCD}}$ : total relative uncertainty on the multijet prediction is of order 60%. The final QCD background estimation in the search regions is shown in Table 5.14.

**Table 5.14:** Summary of the estimated total remaining QCD background.

$p_T(j_1)$ (GeV)	> 250	> 300	> 350	> 400	> 450	> 500	> 550
QCD	$786 \pm 473$	$508 \pm 306$	$304 \pm 184$	$162 \pm 99$	$80 \pm 49$	$52 \pm 32$	$28 \pm 18$

To provide a further cross check that the QCD prediction is sensible, we check the agreement for  $\Delta\phi(p_T^{\text{miss}}, j_3)$ . Figure 5.13 shows the distribution for a jet counting threshold of 60 GeV and  $p_T(j_1) > 250$  GeV; data agrees with MC within the assigned uncertainties.

#### 5.6.4 $t\bar{t}$ background estimation

The contribution of  $t\bar{t}$  events in the search regions is predicted to be small,  $\approx 2\%$ . It is estimated using simulation normalized using the Next to Next Leading Order (NNLO) cross section [177], and cross checked using a data control sample enriched in  $t\bar{t}$  events.

<sup>1</sup>The statistical precision listed in this table is arguably too high, as all the numbers are consistent with one another within the errors quoted. In future analyses, perhaps a non- $p_T$  dependent scale factor of  $1.4 \pm 0.4$  would be more appropriate.

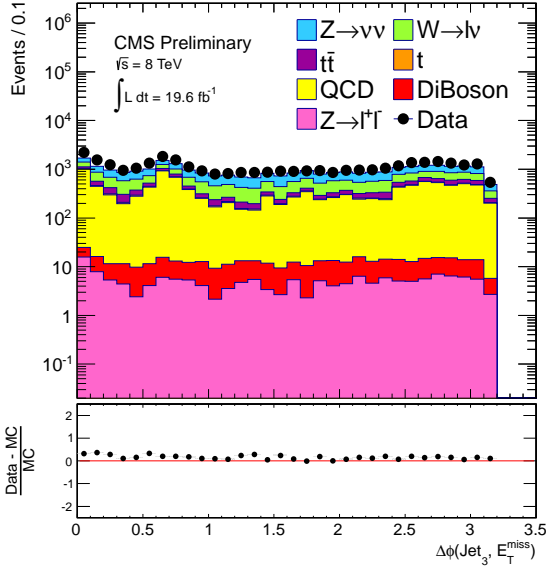


**Figure 5.13:**  $\Delta\phi(p_T^{\text{miss}}, j_3)$ , shown for a jet counting threshold of 60 GeV for  $p_T(j_1) > 250$  GeV.

The data control sample is derived from the same trigger as the search regions, satisfying the selection criteria of  $p_T^{\text{miss},\mu} > 250$  GeV and  $p_T(j_1) > 110$  GeV, along with the event cleaning criteria. In addition,  $\Delta\phi(j_1, j_2) < 2.5$ , and, to select leptonic decays of  $t\bar{t}$  events, a well-identified electron is required, and a loose muon of opposite sign. The invariant mass of the electron-muon system must lie above 60 GeV, removing much of the contribution of  $Z(\ell^+\ell^-) + \text{jets}$  events in the control sample.

The distributions of the invariant mass and  $p_T$  of the electron-muon system are shown in Figure 5.14. The event yields from data and simulation are shown in Table 5.15, before and after the invariant mass cut. Data and simulation are seen to agree well with one another. The scale factor  $R^{t\bar{t}}$  is extracted using an analogous method as for  $R^{\text{QCD}}$ , and has a value of  $0.97 \pm 0.30$ , where the uncertainty is dominated by the systematic uncertainty in the non- $t\bar{t}$  processes in the control sample, which are taken as 50% of each. We therefore find that the NNLO cross section used to normalize the  $t\bar{t}$  simulation describes the data well, and apply a data/MC scaling factor of 1.0.

Although probably over-conservative, the uncertainty on the  $t\bar{t}$  background is taken to be 50% to be consistent with the other background estimations taken from simulation. The 50% relative uncertainty used throughout the analysis is designed to cover any uncertainty in the statistical precision, data/MC scale factors, PDFs, parton showering etc. The exact number is somewhat arbitrary, and is taken to be 50%, but the overall difference

to the result by varying the number is negligible. These are all small backgrounds so the uncertainty on them, be it 50 or 100 or even 200% makes very little difference overall.

**Table 5.15:** Event yields from MC and data for  $t\bar{t}$  background

Requirement	$1e, 1\mu$	$m_T(e\mu) > 60$ GeV
$t\bar{t}$	421	375
Single top	61	55
$Z(\ell^+\ell^-) + \text{jets}$	51	7
Diboson	34	27
$W + \text{jets}$	2	0.5
QCD	0	0
Total background	568	464
Data	554	452
Data/MC	0.98	0.97

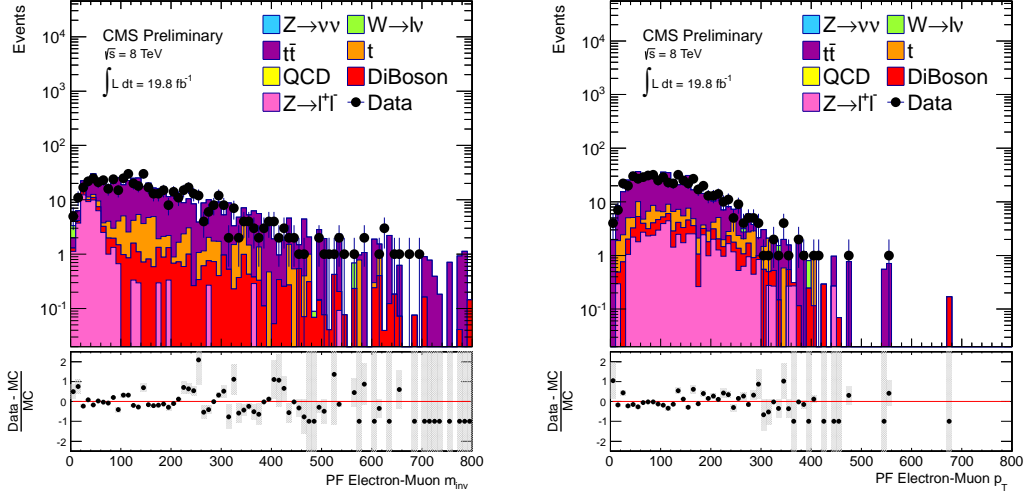


**Figure 5.14:** Invariant mass distribution (left) and  $p_T$  distribution (right) of the  $e\mu$  pair in the  $t\bar{t}$ -enriched control sample.

### 5.6.5 Diboson background estimation

The diboson (WW, WZ and ZZ) backgrounds are estimated using simulation, where the NLO cross sections [178] are used to normalize event yields to the integrated luminosity of the search regions. The diboson backgrounds where one of the bosons is a photon,  $V\gamma$ :  $W\gamma$ ,  $Z(\nu\bar{\nu})\gamma$  and  $Z(\ell^+\ell^-)\gamma$ , are treated inclusively: they are absorbed into the data

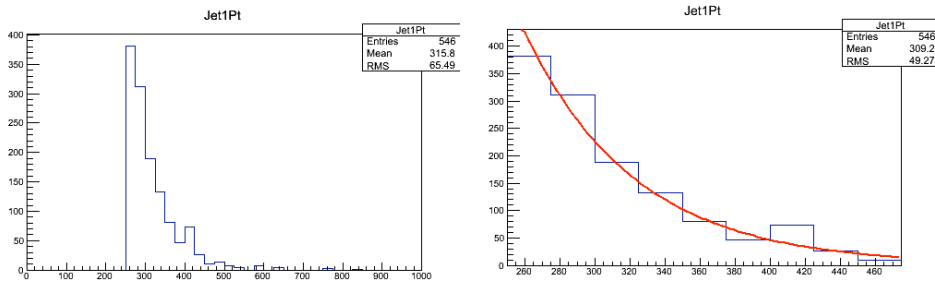
driven estimates of  $W + \text{jets}$  and  $Z(\nu\bar{\nu}) + \text{jets}$ , and into the MC estimate of  $Z(\ell^+\ell^-) + \text{jets}$  respectively.

Table 5.16 shows the difference between treating the  $V\gamma$  backgrounds inclusively as opposed to exclusively — taking their yields in the search regions individually from simulation. The difference in evaluating the  $Z(\nu\bar{\nu}) + \text{jets}$  event yield with and without the inclusion of  $Z(\nu\bar{\nu})\gamma + \text{jets}$  is calculated, in order to give a data-driven estimation of the  $Z(\nu\bar{\nu})\gamma + \text{jets}$  background. This method is compared to the yield from using simulation directly. A similar method is used to compare the yield of  $W\gamma + \text{jets}$  in data and simulation. Both agree within the 50% uncertainty assigned to all numbers taken from simulation.

**Table 5.16:** Inclusive and exclusive methods of treating  $Z(\nu\bar{\nu})\gamma$  and  $W\gamma$  backgrounds. Data driven estimates are calculated to be the difference between the methods, and are compared to event yields from simulation.

$p_T(j_1)$ (GeV)	> 250	> 300	> 350	> 400	> 450	> 500	> 550
$Z(\nu\bar{\nu})\gamma + \text{jets}$							
$Z(\nu\bar{\nu}) + Z(\nu\bar{\nu})\gamma + \text{jets}^{\text{data}}$	$21209 \pm 1115$	$10077 \pm 592$	$4597 \pm 324$	$2250 \pm 197$	$1250 \pm 137$	$663 \pm 94$	$334 \pm 65$
$Z(\nu\bar{\nu}) + \text{jets}^{\text{data}}$	$20104 \pm 1328$	$9508 \pm 715$	$4339 \pm 379$	$2156 \pm 215$	$1200 \pm 145$	$634 \pm 99$	$317 \pm 68$
$Z(\nu\bar{\nu})\gamma + \text{jets}^{\text{data}}$	1105	569	258	94	50	29	17
$Z(\nu\bar{\nu})\gamma + \text{jets}^{\text{MC}}$	1289	595	274	148	50	26	15
Data / MC	0.86	0.96	0.94	0.64	1.00	1.12	1.13
$W\gamma + \text{jets}$							
$W + W\gamma + \text{jets}^{\text{data}}$	$12328 \pm 707$	$5939 \pm 366$	$2690 \pm 180$	$1246 \pm 92$	$627 \pm 52$	$301 \pm 29$	$150 \pm 18$
$W + \text{jets}^{\text{data}}$	$11831 \pm 747$	$5677 \pm 388$	$2562 \pm 188$	$1186 \pm 98$	$592 \pm 53$	$288 \pm 31$	$139 \pm 19$
$W\gamma + \text{jets}^{\text{data}}$	497	262	128	60	35	13	12
$W\gamma + \text{jets}^{\text{MC}}$	503	271	134	62	38	13	11
Data / MC	0.99	0.97	0.96	0.97	0.92	1.00	1.09

A fluctuation in the ratio of data to MC simulation is observed in the estimation of  $Z(\nu\bar{\nu})\gamma + \text{jets}$ , for  $p_T(j_1) > 400$  GeV. This is due to a statistical upward fluctuation in the  $Z(\nu\bar{\nu})\gamma$  simulation around  $p_T = 400$  GeV. ~~Fitting the data/MC numbers in each  $p_T(j_1)$  search region with a straight line, such a fluctuation is not observed and the data/MC ratio at  $p_T(j_1) > 400$  GeV becomes 0.9.~~ This is evident in Figure 5.15 (left); fitting the curve with an exponential function fits the rest of the data points well and smooths out this small excess (right). The simulation is not used at all in the results, and is compared to the number from data purely as a cross check to see that the method of treating the background exclusively and inclusively provides reasonable results. The data/MC ratio is close to one for all of the other search regions, so we are satisfied the method works and proceed to treat the  $V\gamma$  background inclusively.



**Figure 5.15:** The leading jet  $p_T$  spectrum from the  $Z(\nu\bar{\nu})\gamma$  simulation, in the baseline search region; the small increase in events above 400 GeV is evident. The right hand plot shows the zoomed in region which is fitted with an exponential curve in red.

By absorbing  $W\gamma$  and  $Z(\nu\bar{\nu})\gamma$  events into the dominant data driven backgrounds we not only get a better estimation of these backgrounds as we do not rely on the simulation (which does not necessarily represent the data accurately in this area of phase space), we also reduce the uncertainty on the estimations, and in doing so reduce the total uncertainties of the analysis. This is because the yields (in simulation) of  $W\gamma$  and  $Z(\nu\bar{\nu})\gamma$  no longer contribute to  $N_{\mu\mu}^{\text{bkg}}$  and  $N_{\mu}^{\text{bkg}}$ , so the 50% uncertainties on the yields are also no longer included in the uncertainty calculation on these numbers. Instead, they are accounted for within the  $N_{\mu\mu}^{\text{obs}}$  and  $N_{\mu}^{\text{obs}}$  yields with uncertainties calculated as discussed above.

### 5.6.6 Single top quark and Drell–Yan background estimations

Backgrounds due to single top quark events are predicted to be very small, of order 0.5%. Yields are taken directly from simulation and normalized to the approximate NNLO cross sections [177]. The contribution of Drell–Yan  $Z(\ell^+\ell^-) + \text{jets}$  processes in the search regions are predicted to be of a similar size, due to the lepton vetoes - contributing  $\approx 0.5\%$ . It is combined with the background due to  $Z(\ell^+\ell^-)\gamma$  processes, which is negligible and only included for completeness, and evaluated using simulation. An uncertainty of 50% is assigned to these predictions.

## 5.7 Summary

The selection to reduce SM background contribution and maximise possible signal acceptance has been presented. The contribution of SM  $t\bar{t}$  and multijet events in the

search regions is reduced using topological selections. The dominant backgrounds after the complete event selection are from  $Z(\nu\bar{\nu}) + \text{jets}$  and  $W + \text{jets}$  events. These are estimated using muon data control samples enriched in  $Z(\mu\mu)$  and  $W(\mu\nu)$  events. Remaining background from  $t\bar{t}$  and multijet processes are estimated using simulation normalized in data control samples, and small contributions of diboson,  $Z(\ell^+\ell^-)$ , and single top quark events are taken from simulation.

# Chapter 6

## Results and Interpretation

*“In fact, the mere act of opening the box will determine the state of the cat, although in this case there were three determinate states the cat could be in: these being Alive, Dead, and Bloody Furious.”*

— Terry Pratchett, 1948–2015: *Lords and Ladies*

In this chapter, we show the results and interpretations of a search for events containing a single energetic jet and missing transverse momentum, using a data sample collected at 8 TeV by the CMS detector at the LHC and corresponding to an integrated luminosity of  $19.7 \text{ fb}^{-1}$ . Here, the results from the search described in Chapter 5 are shown, and interpreted in terms of simplified models of supersymmetry, particularly for compressed SUSY in the third generation. The results from this counting experiment could similarly be interpreted for many other BSM models.

### 6.1 Results

A summary of the predictions and corresponding uncertainties for all the SM backgrounds, as discussed in Section 5.6 is listed in Table 6.1, and compared to the data in the search regions. The distributions of  $p_T^{\text{miss},\mu}$  and  $p_T(j_1)$  in data as compared to SM predictions in simulation are shown in Figure 6.1. No significant deviation from the SM is observed.

**Table 6.1:** Event yields for the seven inclusive search regions detailed in Chapter 5. The SM background predictions and the data yields correspond to an integrated luminosity of  $19.7 \text{ fb}^{-1}$  and the quoted uncertainties reflect the statistical and systematic contributions, summed in quadrature.

$p_T(j_1)$ (GeV)	> 250	> 300	> 350	> 400	> 450	> 500	> 550
$Z \rightarrow \nu\bar{\nu} + \text{jets}$	$21209 \pm 1115$	$10077 \pm 592$	$4597 \pm 324$	$2250 \pm 197$	$1250 \pm 137$	$663 \pm 94$	$334 \pm 65$
$W + \text{jets}$	$12328 \pm 707$	$5939 \pm 366$	$2690 \pm 180$	$1246 \pm 92$	$627 \pm 52$	$301 \pm 29$	$150 \pm 18$
$t\bar{t}$	$602 \pm 301$	$344 \pm 172$	$178 \pm 89$	$91 \pm 46$	$48 \pm 24$	$27 \pm 14$	$18 \pm 9.0$
$Z \rightarrow \ell^+\ell^- + \text{jets}$	$127 \pm 64$	$75 \pm 38$	$40 \pm 20$	$25 \pm 13$	$17 \pm 8.3$	$11 \pm 5.6$	$7.4 \pm 3.7$
Single top	$172 \pm 86$	$97 \pm 49$	$49 \pm 24$	$21 \pm 10$	$11 \pm 5.7$	$5.2 \pm 2.6$	$3.2 \pm 1.6$
QCD Multijets	$786 \pm 473$	$508 \pm 306$	$304 \pm 184$	$162 \pm 99$	$80 \pm 49$	$52 \pm 32$	$28 \pm 18$
Diboson	$639 \pm 320$	$369 \pm 184$	$206 \pm 103$	$113 \pm 56$	$64 \pm 32$	$36 \pm 18$	$21 \pm 10$
Total SM	$35862 \pm 1474$	$17409 \pm 803$	$8064 \pm 437$	$3907 \pm 250$	$2098 \pm 160$	$1096 \pm 106$	$563 \pm 71$
Data	36582	17646	8119	3896	1898	1003	565

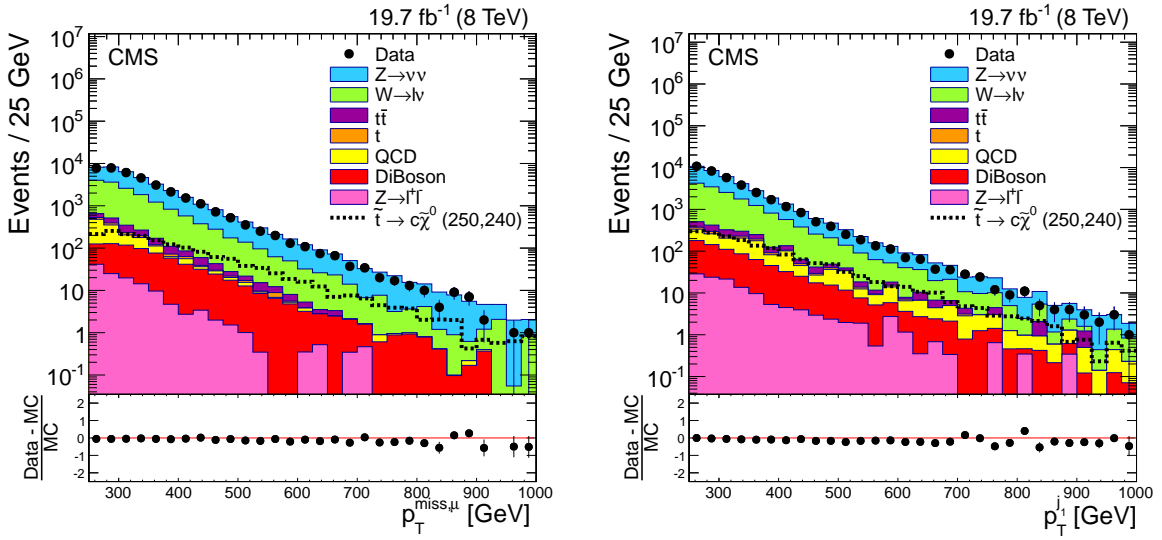


**Figure 6.1:** Distributions of (left)  $p_T^{\text{miss},\mu}$  and (right) leading jet  $p_T$  in the baseline monojet search region,  $p_T(j_1) > 250$  GeV, for data and SM backgrounds. Background distributions are taken from simulation, and normalized to an integrated luminosity of  $19.7 \text{ fb}^{-1}$  using the cross sections shown in Table 5.2. A representative signal distribution for  $\tilde{t} \rightarrow c\tilde{\chi}_1^0$  is also shown (in the dotted line), where  $m_{\tilde{t}} = 250$  GeV and  $m_{\tilde{\chi}_1^0} = 240$  GeV. Statistical uncertainties are shown for the data. Taken from Ref. [5].

## 6.2 Interpretation

No significant deviations from the SM predictions are observed. To interpret the consistency of the observed number of events with the background expectation in the context of compressed SUSY, and also to enable comparison with previous results, we set limits on the production cross section of top and bottom squarks as a function of the top and bottom squark mass and the LSP mass.

Simulation of signal events  $\tilde{t} \rightarrow c\tilde{\chi}_1^0$  and  $\tilde{b} \rightarrow b\tilde{\chi}_1^0$  is necessary to evaluate the sensitivity of the event selection to the SMS models probed, and therefore the compatibility of the results in Table 6.1 to these signatures of new physics.

### 6.2.1 Simulation of signal events

Simulation of signal events is in the SMS [179] framework as described in Section 2.3.4. As the monojet event selection relies on an ISR jet, the acceptance of signal events is low due to the additional factor of  $\alpha_s$  on production cross sections - typically around 1% of events satisfy selection requirements. Therefore, it is necessary to generate many events to ensure uncertainties are not dominated by statistical uncertainties. In addition, scans consist of many points in the  $(m_{\tilde{t}}, m_{\tilde{\chi}_1^0})$  and  $(m_{\tilde{b}}, m_{\tilde{\chi}_1^0})$  mass planes in order to give good coverage across the phase space region of interest. As a result, millions of events are required and the signal MC simulation samples are huge - for example, the  $\tilde{t} \rightarrow c\tilde{\chi}_1^0$  sample takes up disk-space of order 1 TB. Generating these samples is then a computational challenge: it is impractical to use a vast number of computing hours. A faster way to produce MC samples, particularly for signal, was therefore developed in the SUSY group at CMS. So, an alternative method of MC generation has been developed, as compared to the SM background samples detailed in Section 6.2.

Events are generated using MADGRAPH5 and showered with PYTHIA6.4.24 with up to 2 partons. To speed up the generation process, the CMS detector response is simulated using the CMSSW FastSim prescription [156]. It gives an accurate detector response to the physics objects, but takes less than 1/100<sup>th</sup> of the time that the full GEANT4 detector simulation takes. The rate of production is therefore increased by a factor 100, allowing the large samples necessary to be generated. The MLM matching prescription [180], in which partons from the matrix element calculation are matched to jets resulting from the parton shower in order to avoid double counting is used. which matches hard partons

~~from the first stage of simulation to jets produced after hadronization, is used to avoid double counting between the matrix element calculations and parton showering.~~ Top and bottom squark production cross sections are taken from the LHC SUSY Cross Section Working Group [181].

Top squark signal simulation contains events where pair produced top squarks decay via  $\tilde{t} \rightarrow c\tilde{\chi}_1^0$  with 100% branching fraction in the  $(m_{\tilde{t}}, m_{\tilde{t}} - m_{\tilde{\chi}_1^0})$  mass plane from  $m_{\tilde{t}} = 100$  GeV to 350 GeV in steps of 25 GeV, and  $\Delta m_{\tilde{t}} = m_{\tilde{t}} - m_{\tilde{\chi}_1^0} = 10, 20, 30, 40, 60$ , and 80 GeV. There are two additional points at  $m_{\tilde{t}} = 250, 275$  GeV and  $\Delta m_{\tilde{t}} = 5$  GeV to probe the monojet limit towards top squark-LSP degeneracy. An additional set of events at  $m_{\tilde{t}} = 200$  GeV and  $\Delta m_{\tilde{t}} = 10, 80$  GeV were showered with up to 3 partons.

Bottom squark signal simulation contains events where pair produced bottom squarks decay via  $\tilde{b} \rightarrow b\tilde{\chi}_1^0$  with 100% branching fraction in the  $(m_{\tilde{b}}, m_{\tilde{\chi}_1^0})$  mass plane. The scan is less granular, and covers a wider phase space range:  $m_{\tilde{b}} = 100$  GeV to 450 GeV in steps of 25 GeV, so  $m_{\tilde{b}} = 100, 125, 150, 175 \dots 450$  GeV. In the mass plane of the  $\tilde{\chi}_1^0$ ,  $m_{\tilde{\chi}_1^0} = 1, 50, 100 \dots$  GeV, in steps of 50 GeV, for  $m_{\tilde{\chi}_1^0} < m_{\tilde{b}}$ : the  $\tilde{\chi}_1^0$  is clearly always less massive than the  $\tilde{b}$ . For example, for  $m_{\tilde{b}} = 250$  GeV,  $m_{\tilde{\chi}_1^0} = 1, 50, 100, 150, 200$  GeV. There are also points generated close to the degeneracy line, at  $\Delta m_{\tilde{b}} = m_{\tilde{b}} - m_{\tilde{\chi}_1^0} = 10$  GeV, so for the example where  $m_{\tilde{b}} = 250$  GeV, there is an additional mass point at  $m_{\tilde{\chi}_1^0} = 240$  GeV.

## 6.3 Signal acceptance

Here, we refer to signal acceptance as the kinetic acceptance of the signal multiplied by the efficiency of reconstruction.

The signal acceptance in the search regions is calculated for each mass point. Results for the  $\tilde{t}$  signal are shown in Figure 6.2, for a selection of representative values of  $m_{\tilde{t}}$ . As expected, those signal points which have the smallest mass difference  $\Delta m_{\tilde{t}}$  have the greatest signal acceptances, as these look most like a true monojet event. Signal acceptance also increases with  $m_{\tilde{t}}$ . Here, the mass difference  $\Delta m_{\tilde{t}}$  never exceeds 80 GeV.

The signal acceptance in the search regions for the  $\tilde{b}$  signal are shown in Figure 6.3. For the compressed regions, where  $\Delta m_{\tilde{b}} \leq 100$  GeV, we observe a similar behaviour to that seen in Figure 6.2. The lower granularity of this signal compared to the  $\tilde{t}\tilde{t} \rightarrow c\bar{c}\tilde{\chi}_1^0\tilde{\chi}_1^0$  signal is evident as there are fewer values of  $m_{\tilde{\chi}_1^0}$  for each  $m_{\tilde{b}}$  in the compressed regions. For large  $\Delta m_{\tilde{b}}$  relatively large signal acceptances are observed (particularly in the search

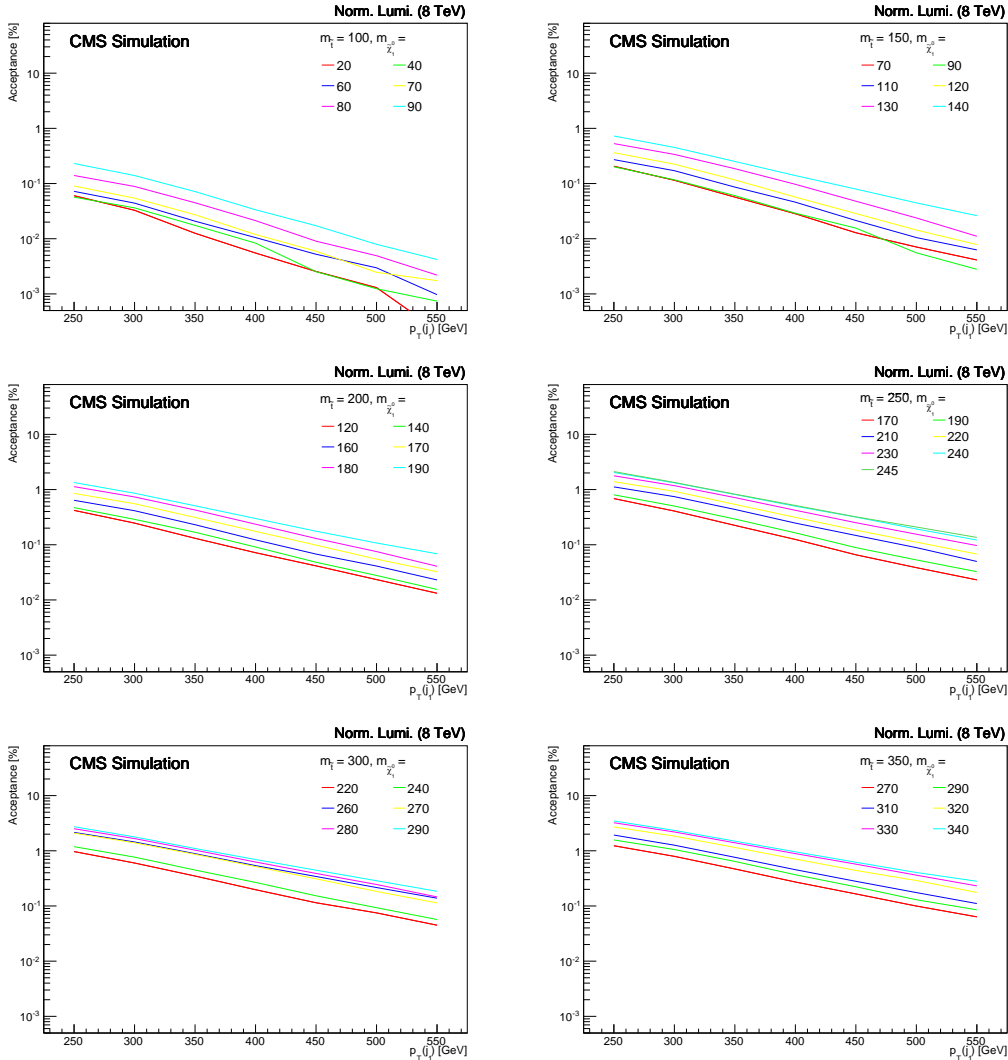


**Figure 6.2:** Signal acceptances in the search regions, at each  $p_T(j_1)$  threshold for the process  $\tilde{t}\tilde{t} \rightarrow c\bar{c}\tilde{\chi}_1^0\tilde{\chi}_1^0$ . Each plot shows a different value of  $m_{\tilde{t}}$ , and various masses of the LSP,  $m_{\tilde{\chi}_1^0}$ . Signal acceptance is greatest when  $m_{\tilde{t}}$  is close to  $m_{\tilde{\chi}_1^0}$ , and increases with increasing  $m_{\tilde{t}}$ .

regions with the lower leading jet  $p_T$  requirements). This is contrary to what we naively expect, as in this area of phase space, outside of the compressed region, events are not monojet-like. The search regions become dominated by dijet events, as sparticle decay products increase in  $p_T$  with increasing  $\Delta m_b$  and more than one jet passes the search region requirements which allow two jets. Acceptance is no longer dependent on energetic ISR jets with the associated factor of  $\alpha_s$ , so is typically higher.

Signal acceptances of some representative mass hypothesis for  $\tilde{t}\tilde{t} \rightarrow c\bar{c}\tilde{\chi}_1^0\tilde{\chi}_1^0$  and  $\tilde{b}\tilde{b} \rightarrow b\bar{b}\tilde{\chi}_1^0\tilde{\chi}_1^0$  signals are shown in Table 6.2 along with their statistical uncertainties.

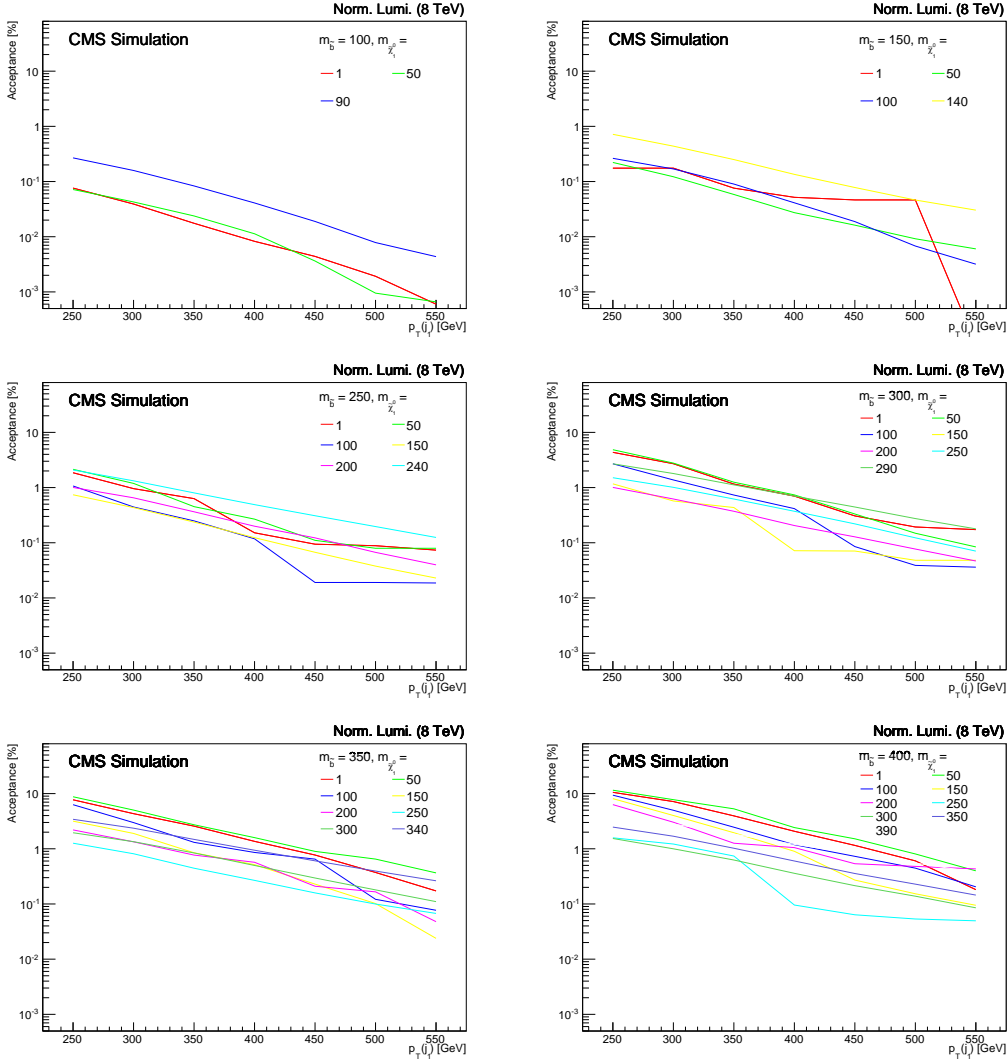


**Figure 6.3:** Signal acceptances in the search regions, at each  $p_T(j_1)$  threshold for the process  $\tilde{b}\tilde{b} \rightarrow b\bar{b}\tilde{\chi}_1^0\tilde{\chi}_1^0$ . Each plot shows a different value of  $m_{\tilde{b}}$ , and various masses of the LSP,  $m_{\tilde{\chi}_1^0}$ . Signal acceptance is greatest when  $m_{\tilde{b}}$  is close to  $m_{\tilde{\chi}_1^0}$ , and increases with increasing  $m_{\tilde{b}}$ . The kinks in the lines are because statistics are low for mass points where  $m_{\tilde{b}} - m_{\tilde{\chi}_1^0} > 100$  GeV, particularly at high leading jet thresholds.

### 6.3.1 Signal acceptance in 2- and 3-parton simulation

The difference in signal acceptance between the 2-parton and 3-parton samples produced for  $\tilde{t}\tilde{t} \rightarrow c\bar{c}\tilde{\chi}_1^0\tilde{\chi}_1^0$  is found to be small; Table 6.3 lists the acceptances for both samples. In the signal regions the differences in the acceptance is, at most, 0.04%, and generally it is less where the analysis is most sensitive (for small mass differences). We conclude that generating 2 or 3 partons with the signal does not have a significant effect on the

**Table 6.2:** Signal acceptance  $\times$  efficiency, shown in %, for each step of the event selection. Two representative mass points are shown;  $(m_{\tilde{b}}, m_{\tilde{\chi}_1^0}) = (250, 240)$  and  $(150, 50)$  GeV for  $\tilde{b}\tilde{b} \rightarrow b\bar{b}\tilde{\chi}_1^0\tilde{\chi}_1^0$  where  $\mathcal{B}(\tilde{b} \rightarrow b\tilde{\chi}_1^0) = 1.0$ , and  $(m_{\tilde{t}}, m_{\tilde{\chi}_1^0}) = (250, 240)$  GeV and  $(200, 120)$  for  $\tilde{t}\tilde{t} \rightarrow c\bar{c}\tilde{\chi}_1^0\tilde{\chi}_1^0$ , where  $\mathcal{B}(\tilde{t} \rightarrow c\tilde{\chi}_1^0) = 1.0$ . Only statistical uncertainties are shown.

Monojet event selection	$\tilde{b}\tilde{b} \rightarrow b\bar{b}\tilde{\chi}_1^0\tilde{\chi}_1^0$		$\tilde{t}\tilde{t} \rightarrow c\bar{c}\tilde{\chi}_1^0\tilde{\chi}_1^0$	
	$\mathcal{B}(\tilde{b} \rightarrow b\tilde{\chi}_1^0) = 1.0$		$\mathcal{B}(\tilde{t} \rightarrow c\tilde{\chi}_1^0) = 1.0$	
	$(250, 240)$ GeV	$(150, 50)$ GeV	$(250, 240)$ GeV	$(200, 120)$ GeV
Event cleaning	$98.61 \pm 0.24$	$98.79 \pm 0.02$	$97.54 \pm 0.14$	$99.21 \pm 0.03$
$p_T^{\text{miss}} > 200$ GeV	$7.41 \pm 0.49$	$2.37 \pm 0.02$	$7.17 \pm 0.25$	$4.29 \pm 0.06$
Noisy events	$6.90 \pm 0.47$	$2.22 \pm 0.02$	$6.68 \pm 0.24$	$4.01 \pm 0.06$
$p_T(j_1) > 110$ GeV	$6.58 \pm 0.46$	$2.08 \pm 0.02$	$6.35 \pm 0.23$	$3.71 \pm 0.06$
$N_{\text{jets}} < 3$	$5.78 \pm 0.44$	$1.39 \pm 0.02$	$5.56 \pm 0.22$	$2.30 \pm 0.04$
$\Delta\phi(j_1, j_2) < 2.5$	$5.58 \pm 0.43$	$1.170 \pm 0.015$	$5.36 \pm 0.21$	$1.96 \pm 0.04$
$\mu$ veto	$5.57 \pm 0.43$	$1.170 \pm 0.015$	$5.36 \pm 0.21$	$1.96 \pm 0.04$
$e$ veto	$5.57 \pm 0.43$	$1.160 \pm 0.015$	$5.36 \pm 0.21$	$1.96 \pm 0.04$
$\tau_h$ veto	$5.52 \pm 0.43$	$1.14 \pm 0.015$	$5.30 \pm 0.21$	$1.93 \pm 0.04$
$p_T^{\text{miss}}$ & $p_T(j_1) > 250$ GeV	$2.08 \pm 0.27$	$0.222 \pm 0.006$	$2.04 \pm 0.13$	$0.42 \pm 0.02$
$p_T(j_1) > 300$ GeV	$1.32 \pm 0.21$	$0.122 \pm 0.005$	$1.32 \pm 0.11$	$0.25 \pm 0.01$
$p_T(j_1) > 350$ GeV	$0.80 \pm 0.17$	$0.058 \pm 0.003$	$0.81 \pm 0.08$	$0.13 \pm 0.01$
$p_T(j_1) > 400$ GeV	$0.49 \pm 0.13$	$0.027 \pm 0.002$	$0.50 \pm 0.07$	$0.072 \pm 0.008$
$p_T(j_1) > 450$ GeV	$0.31 \pm 0.11$	$0.016 \pm 0.002$	$0.32 \pm 0.05$	$0.041 \pm 0.006$
$p_T(j_1) > 500$ GeV	$0.19 \pm 0.08$	$0.009 \pm 0.001$	$0.19 \pm 0.04$	$0.023 \pm 0.005$
$p_T(j_1) > 550$ GeV	$0.12 \pm 0.07$	$0.006 \pm 0.001$	$0.12 \pm 0.03$	$0.013 \pm 0.003$

result. Nevertheless, the differences are accounted for in the uncertainty on the signal acceptance.

### 6.3.2 Systematic Uncertainties on Signal

The selection of signal events (and therefore the signal acceptance) in this analysis relies on a high- $p_T$  ISR jet, so the modelling of ISR must be reliable. The MADGRAPH simulated and measured  $p_T$  spectra of recoiling systems against ISR jets is studied in Ref. [88] for  $Z + \text{jets}$ ,  $t\bar{t}$  and  $WZ$  final states, chosen because such events can be measured with good statistical precision and cover a wide range of phase space. In both data and simulation, the  $p_T$  spectrum of the system which recoils against an ISR jet is measured, and the shapes are compared. The simulation is found to over predict the data by

**Table 6.3:** Acceptances (in %) of 2-parton and 3-parton samples for mass points  $(m_{\tilde{t}}, m_{\tilde{\chi}_1^0}) = (200,190)$  GeV and  $(200,120)$  GeV. The modulus of the differences in the acceptances from the two samples are listed.

Event selection	$(m_{\tilde{t}}, m_{\tilde{\chi}_1^0}) = (200,190)$			$(m_{\tilde{t}}, m_{\tilde{\chi}_1^0}) = (200,120)$		
	2 partons	3 partons	Difference	2 partons	3 partons	Difference
Abnormal events	97.1	97.1	0	99.3	99.19	0.11
$p_T^{\text{miss},\mu} > 200$ GeV	2.74	2.61	0.13	1.84	1.79	0.05
Noise clean	2.58	2.47	0.11	1.75	1.71	0.04
$p_T(j_1) > 110$ GeV	12.53	2.42	0.11	1.71	1.68	0.03
$N_{\text{jets}} < 3$	2.14	2.06	0.08	0.94	0.98	0.04
$\Delta\phi(j_1, j_2) < 2.5$	2.05	1.99	0.06	0.78	0.79	0.01
$e$ veto	2.05	1.99	0.06	0.78	0.79	0.01
$\mu$ veto	2.05	1.99	0.06	0.78	0.79	0.01
$\tau_h$ veto	2.02	1.97	0.05	0.77	0.77	0
$p_T(j_1) > 250$ GeV & $p_T^{\text{miss},\mu} > 250$ GeV	1.32	1.36	0.04	0.43	0.41	0.02
$p_T(j_1) > 300$ GeV	0.86	0.88	0.02	0.25	0.23	0.02
$p_T(j_1) > 350$ GeV	0.51	0.51	0	0.14	0.12	0.02
$p_T(j_1) > 400$ GeV	0.30	0.30	0	0.076	0.063	0.013
$p_T(j_1) > 450$ GeV	0.17	0.18	0.01	0.042	0.025	0.017
$p_T(j_1) > 500$ GeV	0.10	0.10	0	0.024	0.013	0.011
$p_T(j_1) > 550$ GeV	0.067	0.056	0.011	0.014	0.006	0.008

20% for ISR jets with  $p_T > 250$  GeV, see Figure 6.4 which shows the spectrum of the Z + jets system in both data and simulation<sup>1</sup>. All signal acceptances have therefore been weighted by a factor of 0.8 to correct for this difference, and a systematic uncertainty of 20% is assigned to each search region to account for this difference for the high  $p_T$  ISR jets involved.

Other sources of uncertainty on the signal are considered. They are:

- the uncertainty on the JES, which is evaluated by taking the difference in acceptances when the jet  $\vec{p}_T$  is shifted up and down by an  $\eta$  and  $p_T$  dependent factor. The difference in acceptances between varying the energy scale up and down is less than 1% in the signal regions: see Table 6.4;

<sup>1</sup>I had this as the ttbar system before, but the z+jet system goes to higher pt and shows the 0.8 correction behaviour is appropriate - clearly no downward trend above 500GeV

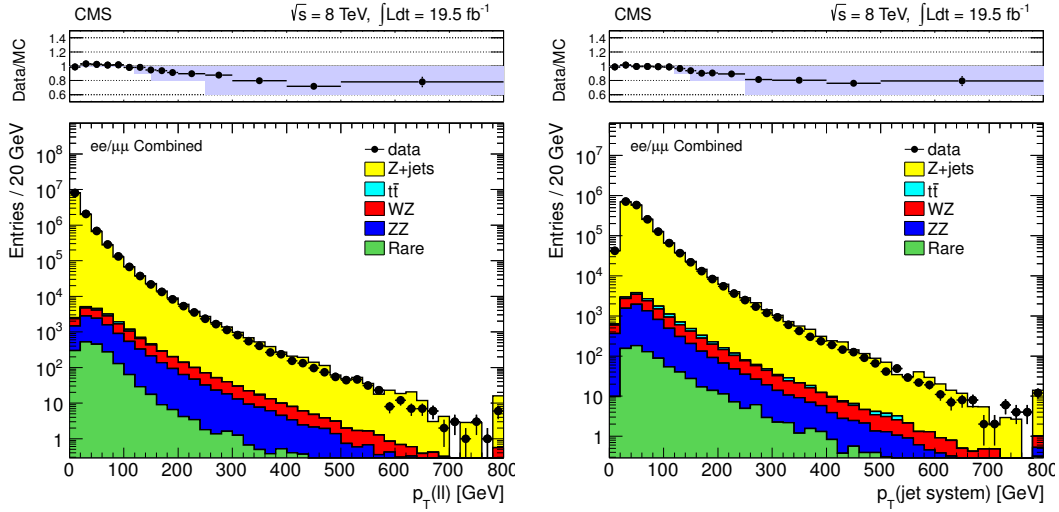


**Figure 6.4:** Taken from [88], the comparison of data to the prediction from simulation of the jet recoil system in  $Z + \text{jets}$  events. The left-hand plot shows the  $p_T$  spectrum of dilepton events in leptonic  $Z$  decays, and the right-hand plot shows the  $p_T$  spectrum of the vector sum of reconstructed jets in hadronic  $Z$  decays. The data/MC ratio, in the top of the figure, shows that for jets with  $p_T > 250$  GeV, the simulation over predicts the data. The shaded band is centred on the weighted MC prediction and indicates the associated uncertainty on the ratio.

- uncertainties on the PDFs. The change in acceptance due to the use of alternative PDFs is less than 2% for a representative signal sample, so a PDF uncertainty of 2% is assigned;
- the difference in acceptance that is obtained from generating signal events with up to 3 partons in MADGRAPH rather than 2 partons (< 1%).

The total uncertainty on the signal in each signal region is taken to be a conservative 25%, and is dominated by the uncertainty due to ISR mis-modelling. The error on the luminosity measurement is 2.6% [182].

## 6.4 Exclusion limits

The  $\text{CL}_s$  method is used to estimate the 95% CL observed upper limit on the signal production cross section in a counting experiment, and corresponding median expected limit with the 1- and 2- standard deviation quantile bands [1, 183]. Given the integrated luminosity, signal acceptance, background expectation and number of observed events (with associated uncertainties), the 95% CL upper limit on the signal cross section is

**Table 6.4:** Acceptances (in %) of signal samples for mass points  $(m_{\tilde{t}}, m_{\tilde{\chi}_1^0}) = (200, 190)$  GeV and  $(200, 120)$  GeV, for when the energy scale is increased and decreased. The modulus of the differences in the acceptances from the two samples are listed.

Search region	$(m_{\tilde{t}}, m_{\tilde{\chi}_1^0}) = (200, 190)$			$(m_{\tilde{t}}, m_{\tilde{\chi}_1^0}) = (200, 120)$		
	JES +	JES -	Difference	JES +	JES -	Difference
$p_T(j_1) > 250$ GeV	1.33	1.33	<0.01	0.42	0.44	0.03
$p_T(j_1) > 300$ GeV	0.88	0.84	0.03	0.26	0.26	<0.01
$p_T(j_1) > 350$ GeV	0.52	0.50	0.03	0.14	0.14	<0.01
$p_T(j_1) > 400$ GeV	0.30	0.29	0.01	0.07	0.08	<0.01
$p_T(j_1) > 450$ GeV	0.18	0.17	0.01	0.04	0.04	<0.01
$p_T(j_1) > 500$ GeV	0.11	0.10	0.01	0.02	0.02	<0.01
$p_T(j_1) > 550$ GeV	0.07	0.06	<0.01	0.02	0.01	<0.01

calculated. This modified-frequentist approach generates a set of pseudo-experiments with the signal plus background, and background only hypotheses, for each mass point and in each search region. The uncertainty on the total background estimation shown in Table 6.1, and uncertainties on signal and integrated luminosity (Section 6.3.2) are treated as a lognormal nuisance parameters. The theoretical top-squark production cross sections, which are equal to the bottom-squark production cross sections, with associated theoretical uncertainties  $\pm 1\sigma_{\text{th}}$  are taken from a collaboration between the ATLAS, CMS and LHC Physics Centre at CERN (LPCC) SUSY working groups. Theory uncertainties are dominated by PDF uncertainties and calculations are detailed in Ref. [181]. Cross section values can be found in Ref. [184]. The 95% CL exclusion limits on production cross sections are compared to the theoretical expectations in order to set lower limits on the top (bottom) squark and LSP masses in the  $(m_{\tilde{t}}, m_{\tilde{\chi}_1^0})$  ( $(m_{\tilde{b}}, m_{\tilde{\chi}_1^0})$ ) mass plane.

Expected 95% CL limits on production cross section, displayed as a function of  $p_T(j_1)$  for a selection of signal mass hypothesis for the  $\tilde{t}\tilde{t} \rightarrow c\bar{c}\tilde{\chi}_1^0\tilde{\chi}_1^0$  signal can be found in Figure 6.5. Each plot shows a particular  $m_{\tilde{t}}$  and the expected limit on cross section uses the SM background expectation alone. Similar plots showing the 95% CL expected limits on production cross section for the  $\tilde{b}\tilde{b} \rightarrow b\bar{b}\tilde{\chi}_1^0\tilde{\chi}_1^0$  signal are shown in Figure 6.6. The signal region where the best (i.e. lowest) expected limit is found is selected as the optimal region in which to set limits for that mass point. Limits are generally fairly flat across the phase space range, for those mass points in the compressed region where  $\Delta m_{\tilde{t}}$  and  $\Delta m_{\tilde{b}} \lesssim 100$  GeV. A fluctuation in the number of  $Z(\mu\mu) + \text{jets}$  events at  $p_T(j_1) > 450$  GeV (see the ‘Data’ row of Table 5.3) leads to a fluctuation in the total

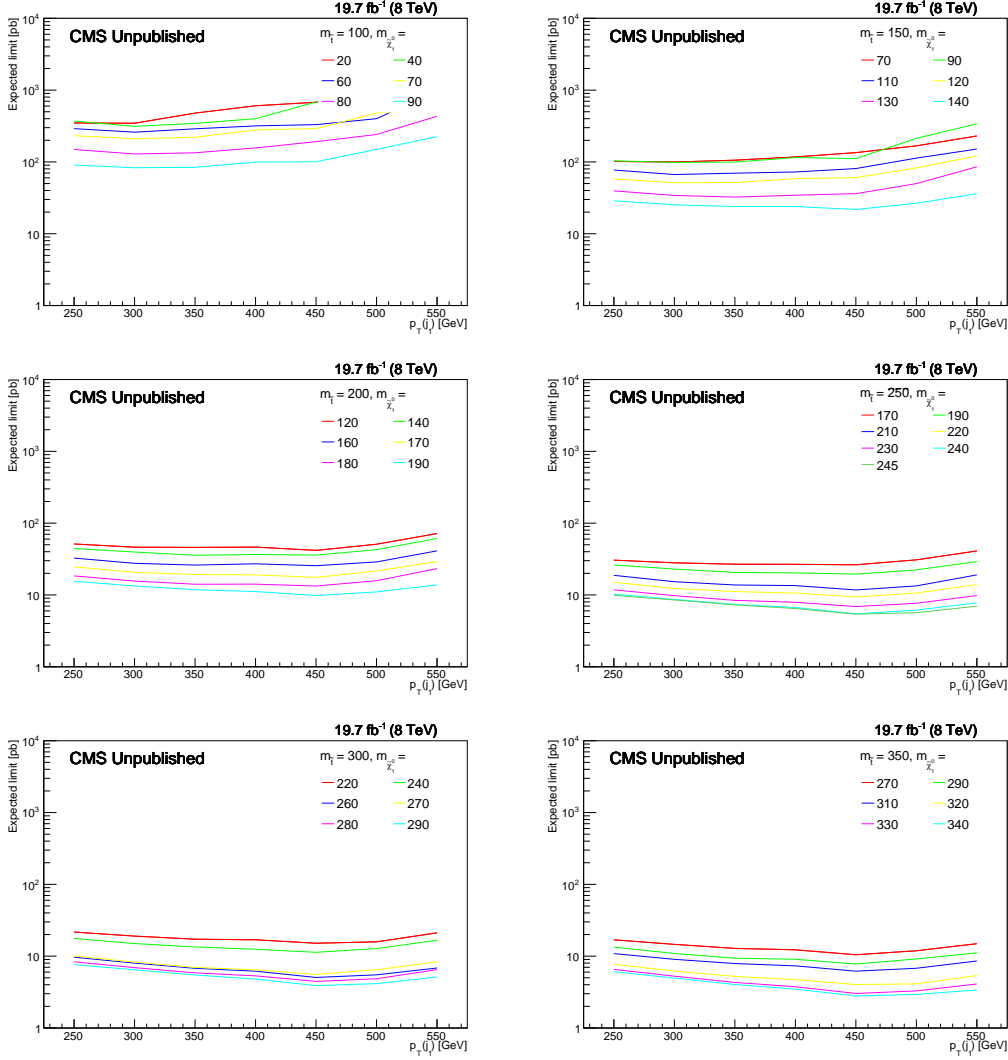


**Figure 6.5:** 95% CL expected limit on top-squark production cross section as a function of  $p_T(j_1)$  GeV (i.e. in each search region). Limits for  $m_{\tilde{t}} = 100, 150, 200, 250, 300$  and  $350$  GeV are shown, where each line corresponds to  $\Delta m_{\tilde{t}} = 10, 20, 30, 40, 60$  and  $80$  GeV.

background expectation in this search region. To ensure smooth limit curves, particularly to avoid unphysical situations where the observed limit curve crosses the theoretical limit curve more than once, we have discounted this signal region from the limit setting procedure.

Outside of the compressed region of phase space in the  $(m_{\tilde{b}}, m_{\tilde{\chi}_1^0})$  mass plane, for some signal points we are not able to set a 95% CL limit on the production cross section in the search regions with the highest  $p_T(j_1)$  thresholds. This is because the acceptance of

such points is very low - these search regions are not sensitive to the dijet event topology described in Section 6.3.

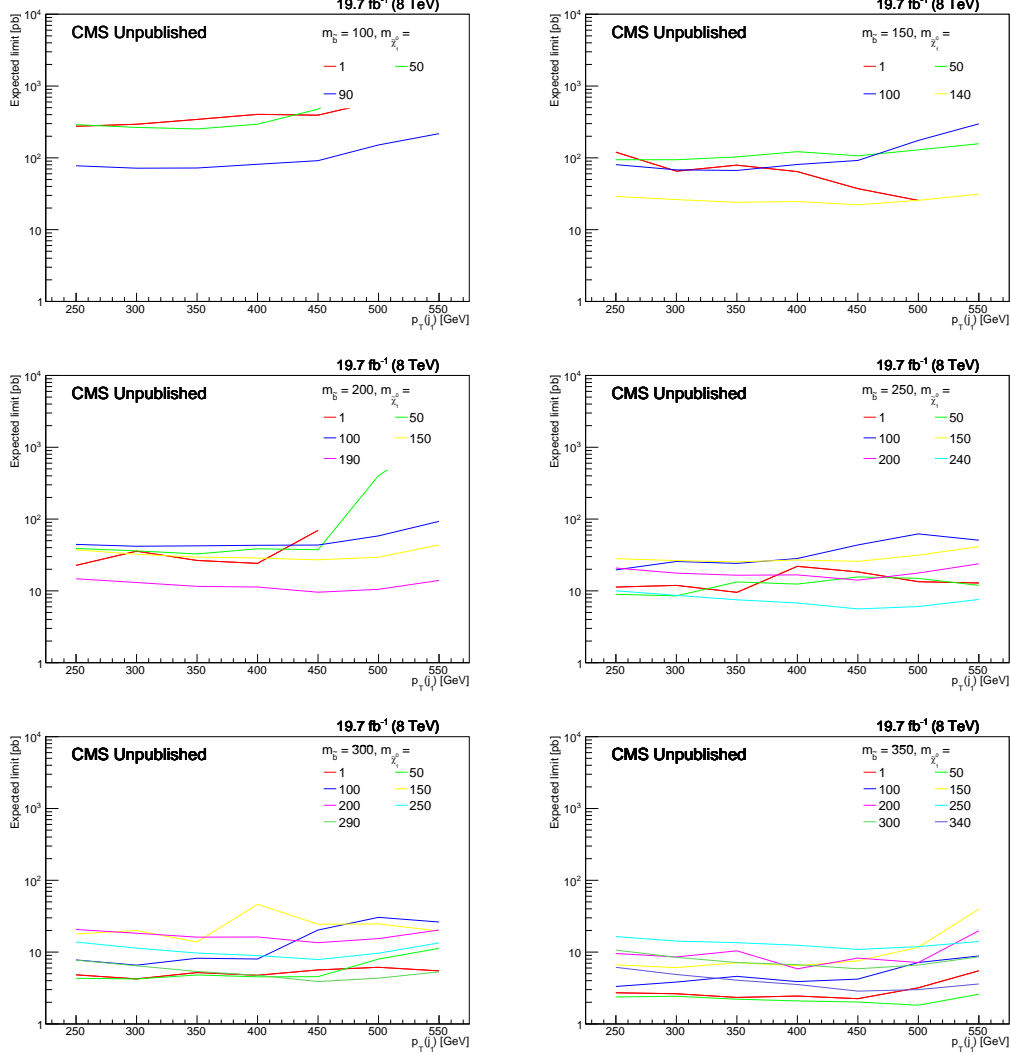


**Figure 6.6:** 95% CL expected limit on bottom-squark production cross section as a function of  $p_T(j_1)$  [GeV] (i.e. in each search region). Limits for  $m_{\tilde{b}} = 100, 150, 200, 250, 300$  and 350 GeV are shown, where each line corresponds to a different  $m_{\tilde{\chi}_1^0}$ .

The temperature plots in Figure 6.7 show the signal acceptance in the search region with the best expected limit for both  $(m_{\tilde{t}}, m_{\tilde{\chi}_1^0})$  and  $(m_{\tilde{b}}, m_{\tilde{\chi}_1^0})$  mass planes. The temperature plots in Figure 6.8 show the best expected 95% CL limit across the phase space range, and Figure 6.9 shows the search region in which this best expected limit is found. We see that typically, harder leading jet cuts give the better limits along the diagonal, where events are dominated by ISR. Also, for larger  $m_{\tilde{t}}$  and  $m_{\tilde{b}}$ , harder jet thresholds give the better limits, as these events are typically more boosted.

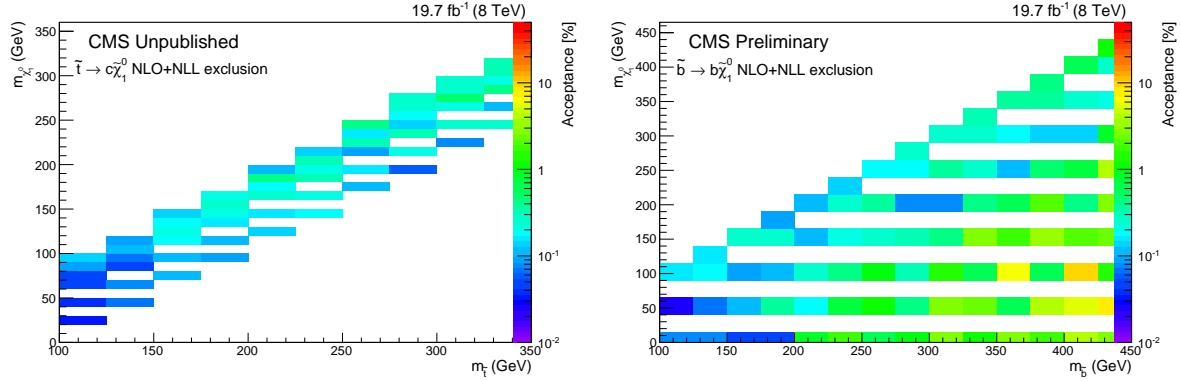


**Figure 6.7:** The temperature plot shows the acceptance of the signal point where the best expected limit is found, across the  $(m_{\tilde{t}}, m_{\tilde{\chi}_1^0})$  (left) and  $(m_{\tilde{b}}, m_{\tilde{\chi}_1^0})$  (right) mass planes.

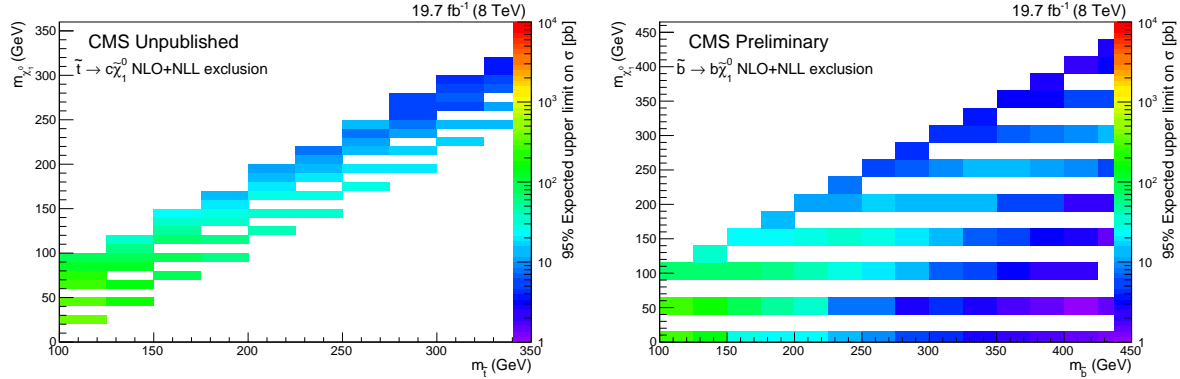


**Figure 6.8:** The temperature plot shows the best expected limit across the  $(m_{\tilde{t}}, m_{\tilde{\chi}_1^0})$  (left) and  $(m_{\tilde{b}}, m_{\tilde{\chi}_1^0})$  (right) mass planes.

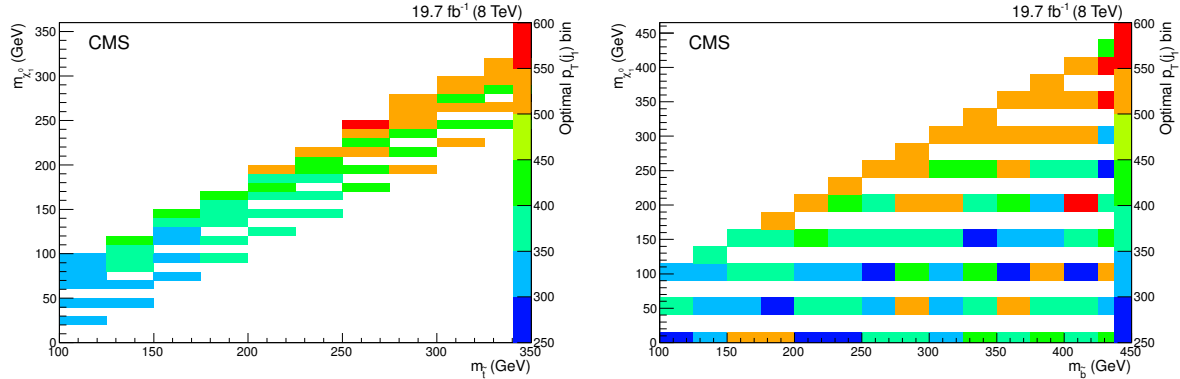


**Figure 6.9:** The temperature plot shows the search region (the  $p_T(j_1)$  threshold) in which the best expected limit is found, across the  $(m_{\tilde{t}}, m_{\tilde{\chi}_1^0})$  (left) and  $(m_{\tilde{b}}, m_{\tilde{\chi}_1^0})$  (right) mass planes. Plots feature in Ref. [5].

Sensitivity outside of the compressed region is expected in the  $(m_{\tilde{b}}, m_{\tilde{\chi}_1^0})$  mass plane. The bottom squark decay  $\tilde{b} \rightarrow b\tilde{\chi}_1^0$  dominates across the mass plane, unlike the top squark decay  $\tilde{t} \rightarrow c\tilde{\chi}_1^0$  which is only valid for the compressed region of phase space. We test the sensitivity of the search criteria for signals where  $\Delta m_{\tilde{b}} > m_W$ , and see larger than naively expected acceptances. To understand these signal acceptances (and resultant 95% CL limits on production cross section) in detail, we study several mass points for which  $m_{\tilde{b}} = 225$  GeV. Figure 6.10 shows the jet multiplicity distributions for  $m_{\tilde{\chi}_1^0} = 1, 50$  and 100 GeV in the baseline search region where all criteria apart from  $N_{\text{jets}} \leq 2$  have been applied.

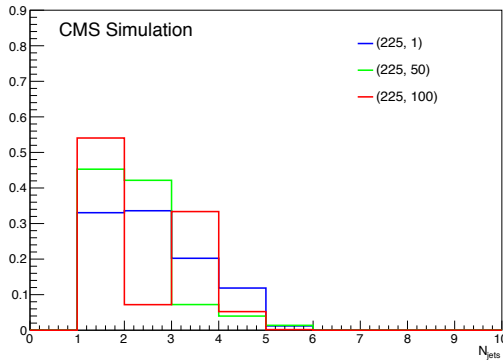


**Figure 6.10:** Normalized distribution of  $N_{\text{jets}}$  for  $\tilde{b} \rightarrow b\tilde{\chi}_1^0$  signal points, in the events satisfying the baseline search region criteria, other than  $N_{\text{jets}} < 3$ . Signal points are labelled as  $(m_{\tilde{b}}, m_{\tilde{\chi}_1^0})$  GeV.

At  $(m_{\tilde{b}}, m_{\tilde{\chi}_1^0}) = (225, 100)$  GeV, most events contain one jet. This could be an ISR jet or a b-jet from the decay of the bottom squark which is energetic enough to pass the  $p_T(j_1)$  requirement of the baseline signal region. A significant number of events contain three jets. The most energetic jet with  $p_T > 250$  GeV originates from one of the b-quark decays (or ISR), and the two softer jets with  $p_T > 60$  GeV originate from the second b quark and ISR (or the two b quarks or otherwise). These trijet events do not satisfy the requirements of the search region and acceptance is reduced.

When  $(m_{\tilde{b}}, m_{\tilde{\chi}_1^0}) = (225, 50)$  GeV most events are classified as having one or two jets. The mass difference  $\Delta m_{\tilde{b}}$  has increased such that both b quarks are sufficiently energetic to pass the jet requirements. Events satisfy the search region requirements once  $N_{\text{jets}} < 3$  is applied and acceptance increases. Search regions are dijet dominated.

At  $(m_{\tilde{b}}, m_{\tilde{\chi}_1^0}) = (225, 1)$  GeV more events have a higher jet multiplicity. The mass difference  $\Delta m_{\tilde{b}}$  is large enough that both b quarks get a significant boost, and satisfy  $p_T(j_1) > 250$  GeV,  $p_T(j_2) > 60$  GeV. There are more events which have supplementary,

relatively soft jets originating from ISR or FSR — and it is these which push the jet multiplicity up. Signal acceptance is then reduced.

Outside of the compressed region, signal acceptance is not dominated by ISR jets. Optimal signal regions typically have lower  $p_T(j_1)$  thresholds, evident in Figure 6.9. Figure 6.11 shows the origin of jets for events that satisfy the baseline search criteria, including the  $N_{\text{jets}} < 3$  requirement, for the various mass points at  $m_{\tilde{b}} = 225$  GeV. The behaviours described above are evident.

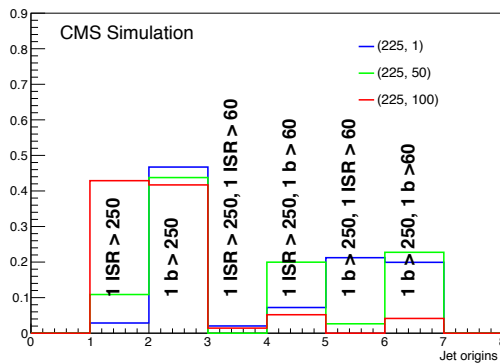


**Figure 6.11:** The topology of events satisfying the baseline search region criteria for  $(m_{\tilde{b}}, m_{\tilde{\chi}_1^0}) = (225, 1), (225, 50)$  and  $(225, 100)$  GeV. The origin of the first and second jet in the event is shown for events with one or two jets. Distributions are normalized to unit area.

Figure 6.12 shows the best 95% CL expected and observed limits on the top-squark production cross section, as a function of the top squark mass for  $\Delta m_{\tilde{t}} = 10, 20, 30, 40, 60$  and 80 GeV. Figure 6.13 shows the similar 95% CL expected and observed limits on the bottom-squark production cross section, as a function of the bottom squark mass for  $\Delta m_{\tilde{b}} = 10$ . As mass points in the remainder of the bottom squark signal sample are produced in a regular pattern in  $(m_{\tilde{b}}, m_{\tilde{\chi}_1^0})$  rather than in  $(m_{\tilde{b}}, \Delta m_{\tilde{b}})$  (as in the  $\tilde{t}\tilde{t} \rightarrow c\bar{c}\tilde{\chi}_1^0\tilde{\chi}_1^0$  case), we show the results for the remainder of  $b\bar{b} \rightarrow b\bar{b}\tilde{\chi}_1^0\tilde{\chi}_1^0$  phase space in a slightly different plane. Figure 6.14 shows the best expected and observed limits for various bottom squark masses as a function of mass difference,  $\Delta m_{\tilde{b}}$ . All plots also show the  $\pm 1, 2\sigma_{\text{exp}}$  bands on the expected limits.

The behaviour in Figure 6.14 where bottom squark limits are low in the compressed region, increase for larger  $\Delta m_{\tilde{b}}$ , and then decrease again is due to the migration of events between bins in jet multiplicity, as described above. The signal topology and search region jet requirements means monojet events, dijet events, and higher jet multiplicities

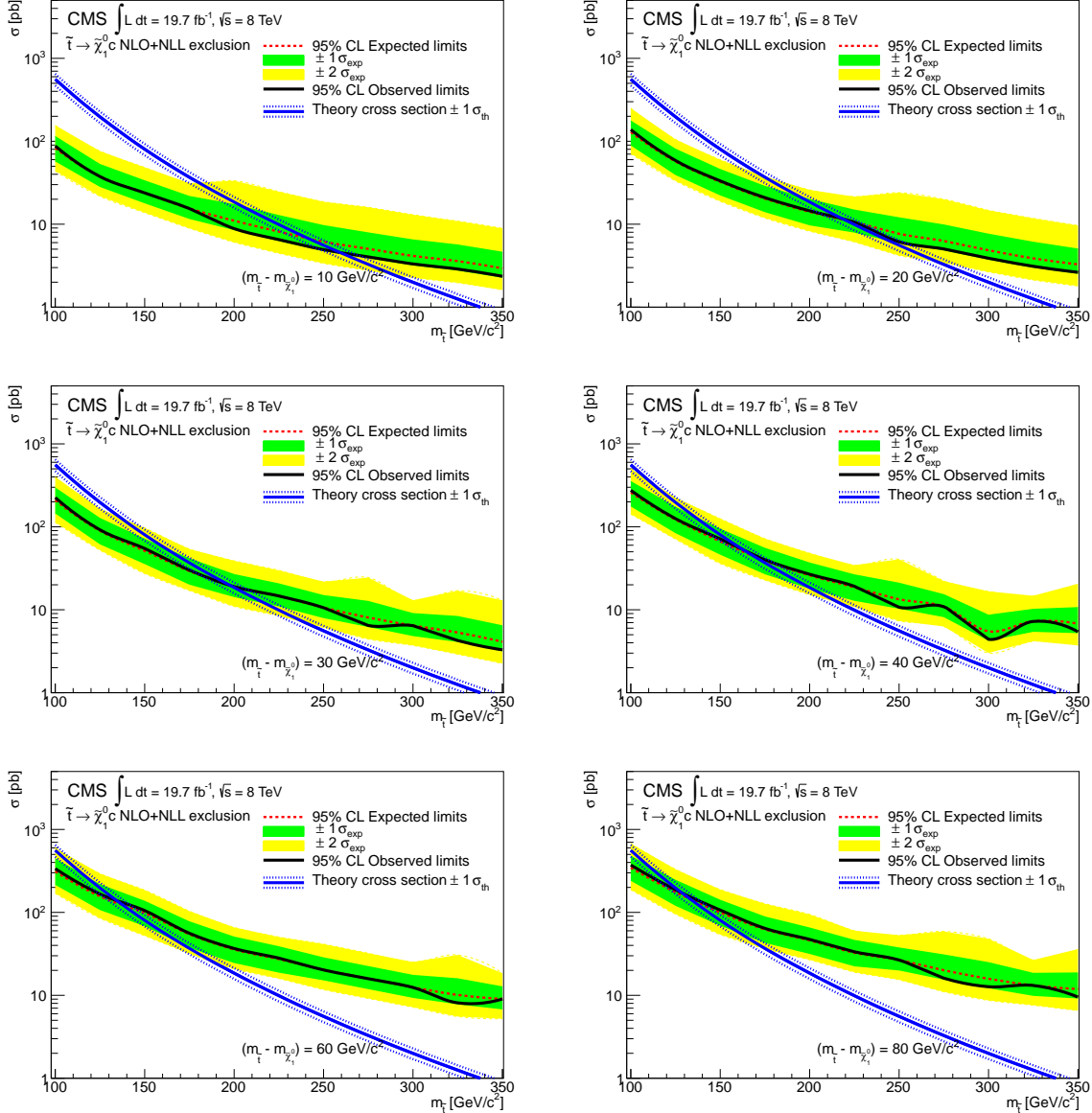


**Figure 6.12:** 95% CL observed and expected limits on the top-squark production cross section as a function of the  $m_{\tilde{t}}$  for  $m_{\tilde{t}} - m_{\tilde{\chi}_1^0} = 10, 20, 30, 40, 60$  and  $80 \text{ GeV}$ . Curves taken from Ref. [4].

dominate in the different regions of phase space and signal acceptance (and hence limits) respond accordingly.

Masses where the observed (expected) limits lie beneath the theory cross section we observe (expect) to exclude. By finding the point of intersection between the observed (expected) and theoretical cross sections, we find the observed (expected) lower limit on the  $m_{\tilde{t}}$  or  $m_{\tilde{b}}$  for a particular value of  $m_{\tilde{\chi}_1^0}$ . Similarly, by finding the intersection between

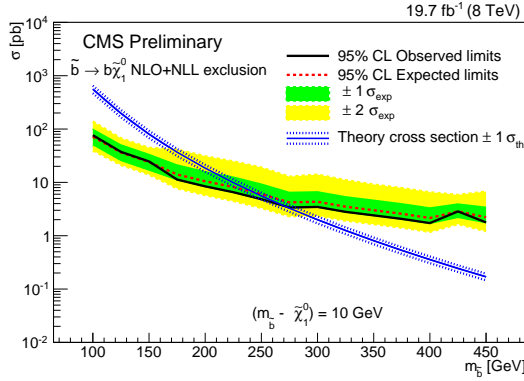


**Figure 6.13:** 95% CL observed and expected limits on the bottom-squark production cross section as a function of  $m_{\tilde{b}}$  for  $m_{\tilde{b}} - m_{\tilde{\chi}_1^0} = 10$  GeV.

the observed ( $\pm 1\sigma_{\text{exp}}$ ) and  $\pm 1\sigma_{\text{th}}$  (theoretical) limits on cross sections, we find the  $\pm 1\sigma_{\text{th}}$  ( $\pm 1\sigma_{\text{exp}}$ ) lower limits on masses. By doing this for every mass point available we build an exclusion contour in the  $(m_{\tilde{t}}, m_{\tilde{\chi}_1^0})$  and  $(m_{\tilde{b}}, m_{\tilde{\chi}_1^0})$  mass planes.

Figure 6.15 shows the 95% CL expected  $\pm 1\sigma_{\text{exp}}$  and observed limits  $\pm 1\sigma_{\text{th}}$  in the  $(m_{\tilde{t}}, m_{\tilde{\chi}_1^0})$  mass plane assuming 100% branching fraction to the top squark decay  $\tilde{t} \rightarrow c\tilde{\chi}_1^0$ . Also shown are previous results from the Tevatron. We are able to exclude the region above a line which goes from approximately  $m_{\tilde{t}} = 130$  GeV,  $m_{\tilde{\chi}_1^0} = 50$  GeV to  $m_{\tilde{t}} = 260$  GeV,  $m_{\tilde{\chi}_1^0} = 255$  GeV. We are able to exclude  $\tilde{t}\tilde{t} \rightarrow c\bar{c}\tilde{\chi}_1^0\tilde{\chi}_1^0$  production for  $m_{\tilde{t}} \leq 260$  GeV and  $\Delta m_{\tilde{t}} \leq 10$  GeV right up to the degeneracy limit.

Similarly, Figure 6.16 shows the 95% CL expected  $\pm 1\sigma_{\text{exp}}$  and observed limits  $\pm 1\sigma_{\text{th}}$  in the  $(m_{\tilde{b}}, m_{\tilde{\chi}_1^0})$  mass plane assuming 100% branching fraction to the bottom squark decay  $\tilde{b} \rightarrow b\tilde{\chi}_1^0$ . We are able to exclude the region above a line which goes from approximately  $m_{\tilde{b}} = 140$  GeV,  $m_{\tilde{\chi}_1^0} = 50$  GeV to  $m_{\tilde{b}} = 270$  GeV,  $m_{\tilde{\chi}_1^0} = 265$  GeV. Further, the region where  $m_{\tilde{b}} < 145$  GeV is excluded for all  $m_{\tilde{\chi}_1^0}$ . We also exclude a region at lower  $m_{\tilde{\chi}_1^0}$  from approximately  $m_{\tilde{b}} = 150$  GeV,  $m_{\tilde{\chi}_1^0} = 40$  GeV to  $m_{\tilde{b}} = 275$  GeV,  $m_{\tilde{\chi}_1^0} = 60$  GeV, above the line extending from  $m_{\tilde{b}} = 175$  GeV,  $m_{\tilde{\chi}_1^0} = 0$  GeV to  $m_{\tilde{b}} = 275$  GeV,  $m_{\tilde{\chi}_1^0} = 40$  GeV. The limit in the compressed region echoes that from the  $(m_{\tilde{t}}, m_{\tilde{\chi}_1^0})$  mass plane: monojet-like events dominate, and sensitivity to events in the region of the mass plane where decay products are very soft is achieved. In the region  $\Delta m_{\tilde{b}} > m_W$ , we set limits on  $m_{\tilde{b}}$  outside the compressed region.

Because the analysis is insensitive to the final state decay products, which are invisible to the event selection within the compressed regions of phase space, the limits can be generalised to any model which has  $\tilde{q} \rightarrow x\tilde{\chi}_1^0$ ; where  $x$  is any decay product invisible

within the event selection – cross sections only need be modified accordingly. Limits are also valid for the most compressed regions of phase space, where  $m_{\tilde{\chi}_1^0}$  approaches  $m_{\tilde{q}}$ .

## 6.5 Summary

A search has been performed for signatures of top and bottom squark production in events with a monojet and large missing transverse momentum, using an integrated luminosity of  $19.7 \text{ fb}^{-1}$  of pp collisions at 8 TeV. The data are found to be in good agreement with expected contributions from SM processes. Limits on top and bottom squark production cross sections in the context of simplified models of supersymmetry are set. Comparisons with the predictions from theory allow limits on third generation squark masses to be set in a mass parameter space where mass splittings between the  $\tilde{t}$  and  $\tilde{b}$  squark and the LSP are less than  $\approx 80$  GeV. These regions have not been probed by previous searches reliant on energetic sparticle decay products: where more than one jet, lepton or photon, as well as large missing energy, is required. We exclude  $\tilde{t}\tilde{t} \rightarrow c\bar{c}\tilde{\chi}_1^0\tilde{\chi}_1^0$  production for  $m_{\tilde{t}} \leq 260$  GeV and  $m_{\tilde{t}} - m_{\tilde{\chi}_1^0} < 10$  GeV and analogously for  $m_{\tilde{t}} \leq 120$  GeV and  $m_{\tilde{t}} - m_{\tilde{\chi}_1^0} < 80$  GeV. We similarly exclude  $\tilde{b}\tilde{b} \rightarrow b\bar{b}\tilde{\chi}_1^0\tilde{\chi}_1^0$  production for  $m_{\tilde{b}} \leq 270$  GeV and  $(m_{\tilde{b}} - m_{\tilde{\chi}_1^0}) < 10$  GeV, with all  $m_{\tilde{\chi}_1^0}$  excluded for  $m_{\tilde{b}} \leq 145$  GeV. A small region of  $\tilde{b}\tilde{b} \rightarrow b\bar{b}\tilde{\chi}_1^0\tilde{\chi}_1^0$  parameter space is excluded for  $m_{\tilde{b}} \leq 270$  GeV and  $m_{\tilde{\chi}_1^0} \approx 50$  GeV. Because the final state jets in this search are invisible, and we are independent of the final state, these limits can be generalized to any model which has  $\tilde{t} \rightarrow x\tilde{\chi}_1^0$  and  $\tilde{b} \rightarrow x\tilde{\chi}_1^0$ , where  $x$  is any state which is invisible within the event selection.

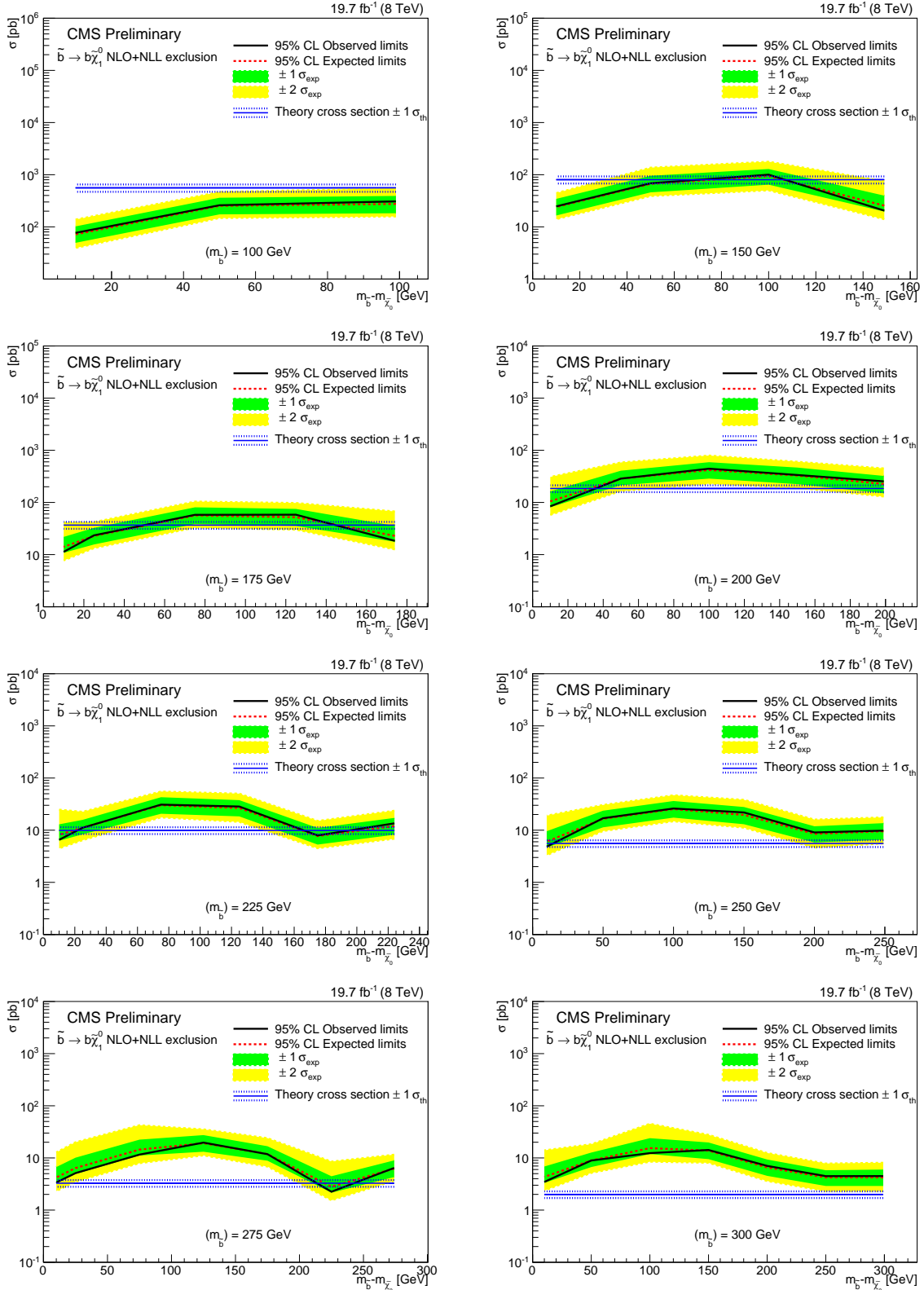


**Figure 6.14:** 95% CL observed and expected limits on the bottom-squark production cross section as a function of the mass difference  $m_b - m_{\tilde{\chi}_1^0}$ , shown for  $m_b = 100, 150, 175, 200, 225$ , and  $275$  GeV. Also shown are the  $\pm 1, 2\sigma_{\text{exp}}$  limits.

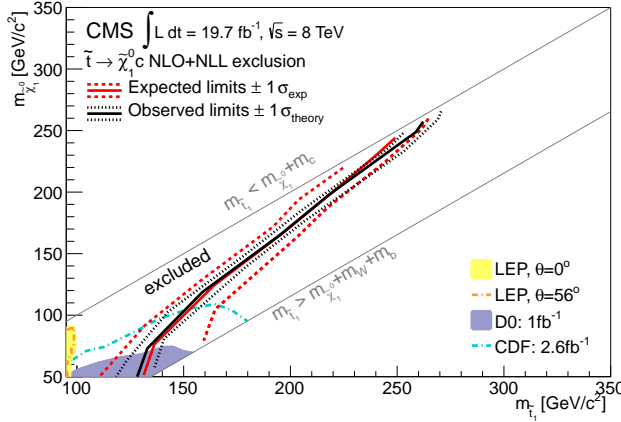


**Figure 6.15:** Expected and observed 95% CL exclusion limits in the  $(m_{\tilde{t}}, m_{\tilde{\chi}_1^0})$  mass plane for top-squark pair production, assuming 100% branching fraction to the decay  $\tilde{t} \rightarrow c\tilde{\chi}_1^0$ . The  $\pm 1\sigma_{exp}$  and  $\pm 1\sigma_{th}$  curves are also shown. The diagonal grey lines mark the borders of the kinematic regimes surrounding the compressed region of phase space. Taken from Ref. [4].

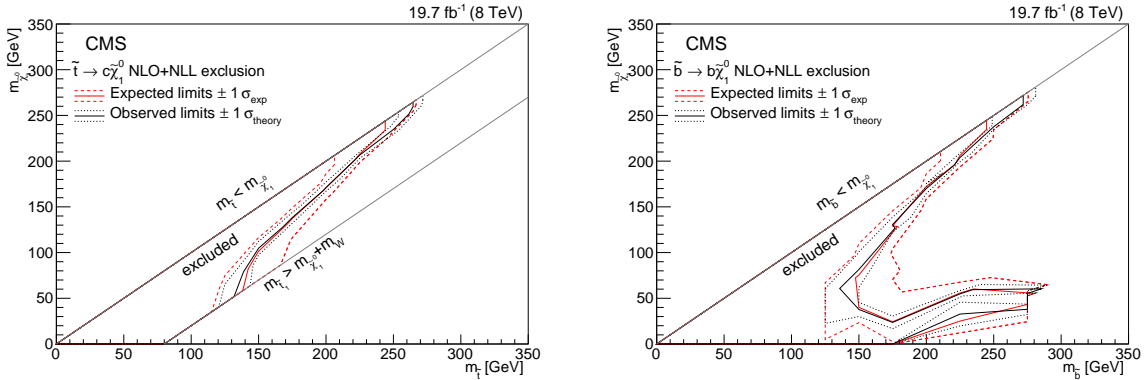


**Figure 6.16:** Observed and expected limits on top-(left) and bottom-(right) squark pair production cross section as a function of the top and bottom squark mass and LSP mass. The top squark limit is the same as the above, only formatted to allow easy comparison between the two limits, which are very similar in the compressed region, as is expected. Additional sensitivity around  $m_{\tilde{b}} \approx 50$  GeV arises from dijet events which satisfy the search region criteria. These curves are those taken from Ref. [5].

# Chapter 7

## Conclusions and Future Outlook

### 7.1 Upgrade L1 Jet Algorithm

The upgrade L1 jet algorithm presented in Chapter 4 showed a marked improvement in spatial and energy resolutions and trigger rates in high PU data, as compared to the current jet algorithm. It is being implemented in the upgraded TMT trigger system installed at CMS during LS1, and will be commissioned this year (2015) ready to come online and replace the current system in 2016. The new trigger is FPGA based, meaning algorithms are flexible to respond to new ideas, algorithm development, physics needs, and changing run conditions. Improvements to the algorithm have already been made, and continue to be worked on.

A better method of calibrating jets to give a uniform response across the calorimeter is necessary, compared to that discussed in Chapter 4, in order to give sharper turn-on curves than the current algorithm. A better PU subtraction method has been developed, which uses a doughnut ring subtraction, rather than the median jet energy. Instead of allowing the somewhat arbitrary 13 jets per event, many more jets (256) are now kept, better taking advantage of the memory storage of new trigger. The jet size has been increased to a diameter of 9 towers, rather than 8, which makes calculating the asymmetry parameters much simpler as there are now an odd number of towers (and so a central one). Alternate clustering algorithms, sub-jets, ratios between hadronic energy and electromagnetic energy deposits, and many other refinements and developments are possible. The jet algorithm will continue to evolve as instantaneous luminosity and PU increase, to enable CMS to maintain and evolve its physics programme.

## 7.2 Search for Compressed SUSY in Monojet Events

The search presented in Chapters 5 and 6 used  $20 \text{ fb}^{-1}$  of integrated luminosity at  $\sqrt{s} = 8 \text{ TeV}$  to set limits in a ‘gap’ in the phase space region of third generation squark vs neutralino mass. Future searches will be able to take advantage of the increased centre-of-mass energy of the LHC, at 13 and 14 TeV, as well as much increased integrated luminosities. As a result, the production cross sections of squarks will be increased, increasing signal acceptance, as well as increasing the mass reach of the search, which is currently limited to 260 GeV or so. The higher statistics will enable lower statistical uncertainties on background estimations as well as open up the possibilities of alternative background estimations.

The dominant uncertainty in the search is due to the statistical uncertainty on the number of  $Z(\mu\mu) + \text{jets}$  events, which is used to estimate the number of  $Z(\nu\bar{\nu}) + \text{jets}$  events — the dominant background. In the  $p_T(j_1) > 450 \text{ GeV}$  search region, the uncertainty on the number of  $Z(\nu\bar{\nu}) + \text{jets}$  events accounts for 85% of the total background uncertainty, and the statistical uncertainty on the  $Z(\mu\mu) + \text{jets}$  event yield accounts for 80% of it. These percentages increase with increasing leading jet threshold. While the increased integrated luminosity will lower this statistical uncertainty, it will also allow alternative methods of estimating the dominant background to be developed. Work is ongoing to probe the effect of using  $W(\mu\nu) + \text{jets}$  events,  $W(e\nu) + \text{jets}$  events, or  $\gamma + \text{jets}$  events, which are not so statistics limited, to estimate the  $Z(\nu\bar{\nu}) + \text{jets}$  background. With these, the systematic uncertainties associated with merging data samples originating from different triggers, and accounting for the various different object reconstruction efficiencies and transfer factors may be less than the statistical uncertainty associated with using  $Z(\mu\mu) + \text{jets}$  events — where the method is much simpler and the same trigger is used for both data and control samples.

Another analysis improvement could be to move to search regions which are binned exclusively, rather than inclusively. In this analysis, it was not clear that doing this gave much advantage in terms of the limits we could set. However, in future, with alternative signal models where different exclusive regions of leading jet  $p_T$  may provide more sensitivity, it could be give advantage.

The search presented here was optimized and interpreted in terms of compressed models of SUSY in the third generation. It could similarly be interpreted in many other BSM new physics models, which give similar final states involving boosted systems and

large  $p_T^{\text{miss}}$ . An obvious re-interpretation is for compressed SUSY more generally, where we do not assume that the third generation is decoupled from the rest, and set limits on the more general  $\tilde{q}$  mass. Production cross sections will be much higher, leading to better limits. It is worth mentioning that in order to be as sensitive as possible in the phase space we have probed, the  $p_T^{\text{miss}}$  requirement should be kept as low as possible. Work was undertaken to understand if signal regions in  $p_T^{\text{miss}}$  rather than leading jet  $p_T$ , as in the more usual ‘monojet’ searches, would give comparable limits. The lowest  $p_T^{\text{miss}}$  bin always gave the best limit, and the mass reach of the search is determined by how low (or high) the  $p_T^{\text{miss}}$  requirement is — which is set by the trigger. Efficient triggering of  $p_T^{\text{miss}}$  both at L1 and the HLT, enabling low rates at the lower  $p_T^{\text{miss}}$  cuts, will therefore allow a good mass reach, for the larger mass differences as well as the most compressed spectra.

The monojet signature is usually employed to search for evidence of DM production. While the traditional searches, with signal regions binned in  $p_T^{\text{miss}}$ , give the best sensitivity to standard DM models, the slightly different topology probed here may be advantageous for alternative DM models, where perhaps a heavier intermediate new particle decays to a DM candidate plus jets. Having as many possible, plausible search regions in which a dark sector may exist is vital if we are to discover what DM is.

The dominant signal uncertainty in the analysis is due to the mismodelling of high  $p_T$  ISR jets in MADGRAPH, which contributes 20% to the systematic uncertainty on the signal acceptance. Better modelling of ISR will decrease this factor.

These factors will allow better search reaches. Better, higher mass limits could be set, with smaller uncertainties — or, possibly, allow for a discovery of new physics in this boosted region of phase space. The search is generic, and model independent, and as the discovery frontier opens up with the LHC providing collisions at increased  $\sqrt{s}$ , could be the discovery channel for a whole host of new physics models.



# Bibliography

- [1] Particle Data Group Collaboration, “Review of Particle Physics”, *Chin. Phys. C* **38** (2014) 090001, doi:10.1088/1674-1137/38/9/090001.
- [2] ATLAS Collaboration, “Observation of a new particle in the search for the Standard Model Higgs boson with the ATLAS detector at the LHC”, *Phys. Lett. B* **716** (2012) 1, doi:10.1016/j.physletb.2012.08.020, arXiv:1207.7214.
- [3] CMS Collaboration, “Observation of a new boson at a mass of 125 GeV with the CMS experiment at the LHC”, *Phys. Lett. B* **716** (2012) 30, doi:10.1016/j.physletb.2012.08.021, arXiv:1207.7235.
- [4] CMS Collaboration Collaboration, “Search for top squarks decaying to a charm quark and a neutralino in events with a jet and missing transverse momentum”, Technical Report CMS-PAS-SUS-13-009, CERN, Geneva, (2014).
- [5] CMS Collaboration, “Searches for third generation squark production in fully hadronic final states in proton-proton collisions at sqrt(s)=8 TeV”, (2015). arXiv:1503.08037. Submitted to *JHEP*.
- [6] CMS, LHCb Collaboration, “Observation of the rare  $B_s^0 \rightarrow \mu^+ \mu^-$  decay from the combined analysis of CMS and LHCb data”, arXiv:1411.4413.
- [7] CMS Collaboration, “Summaries of CMS cross section measurements”. <https://twiki.cern.ch/twiki/bin/view/CMSPublic/PhysicsResultsCombined>. Accessed: 2014-12-20.
- [8] S. Weinberg, “A Model of Leptons”, *Phys. Rev. Lett.* **19** (Nov, 1967) 1264–1266, doi:10.1103/PhysRevLett.19.1264.
- [9] S. Glashow, “Partial Symmetries of Weak Interactions”, *Nucl.Phys.* **22** (1961) doi:10.1016/0029-5582(61)90469-2.
- [10] A. Salam, “Weak and Electromagnetic Interactions”, *Conf.Proc.* **C680519**

- (1968).
- [11] G. Hooft, “Renormalizable Lagrangians for massive Yang-Mills fields”, *Nuclear Physics B* **35** (1971)  
doi:[http://dx.doi.org/10.1016/0550-3213\(71\)90139-8](http://dx.doi.org/10.1016/0550-3213(71)90139-8).
  - [12] P. W. Higgs, “Broken symmetries, massless particles and gauge fields”, *Physics Letters* **12** (1964), no. 2, 132–133,  
doi:[http://dx.doi.org/10.1016/0031-9163\(64\)91136-9](http://dx.doi.org/10.1016/0031-9163(64)91136-9).
  - [13] F. Englert and R. Brout, “Broken Symmetry and the Mass of Gauge Vector Mesons”, *Phys. Rev. Lett.* **13** (Aug, 1964) 321–323,  
doi:[10.1103/PhysRevLett.13.321](https://doi.org/10.1103/PhysRevLett.13.321).
  - [14] P. W. Higgs, “Broken Symmetries and the Masses of Gauge Bosons”, *Phys. Rev. Lett.* **13** (Oct, 1964) 508–509, doi:[10.1103/PhysRevLett.13.508](https://doi.org/10.1103/PhysRevLett.13.508).
  - [15] G. S. Guralnik, C. R. Hagen, and T. W. B. Kibble, “Global Conservation Laws and Massless Particles”, *Phys. Rev. Lett.* **13** (Nov, 1964) 585–587,  
doi:[10.1103/PhysRevLett.13.585](https://doi.org/10.1103/PhysRevLett.13.585).
  - [16] P. W. Higgs, “Spontaneous Symmetry Breakdown without Massless Bosons”, *Phys. Rev.* **145** (May, 1966) 1156–1163, doi:[10.1103/PhysRev.145.1156](https://doi.org/10.1103/PhysRev.145.1156).
  - [17] T. W. B. Kibble, “Symmetry Breaking in Non-Abelian Gauge Theories”, *Phys. Rev.* **155** (Mar, 1967) 1554–1561, doi:[10.1103/PhysRev.155.1554](https://doi.org/10.1103/PhysRev.155.1554).
  - [18] F. Halzen and A. D. Martin, “Quarks and Leptons: An Introductory Course in Modern Particle Physics”. John Wiley and Sons, Philadelphia, 1984.
  - [19] Y. Fukuda, T. Hayakawa, et al., “Measurements of the Solar Neutrino Flux from Super-Kamiokande’s First 300 Days”, *Phys. Rev. Lett.* **81** (Aug, 1998) 1158–1162, doi:[10.1103/PhysRevLett.81.1158](https://doi.org/10.1103/PhysRevLett.81.1158).
  - [20] J. J. Thomson, “XL. Cathode Rays”, *Philosophical Magazine Series 5* **44** (1897), no. 269, 293–316, doi:[10.1080/14786449708621070](https://doi.org/10.1080/14786449708621070),  
arXiv:<http://dx.doi.org/10.1080/14786449708621070>.
  - [21] W. Pauli, “Letter to a physics meeting in Tbingen”.  
<http://microboone-docdb.fnal.gov/cgi-bin/RetrieveFile?docid=953;filename=pauli%20letter1930.pdf>, 1930. Accessed: 2015-01-30, German original and English translation.

- [22] F. Reines and C. L. Cowan, “The Neutrino”, *Nature* **178** (09, 1956) 446–449.
- [23] C. D. Anderson and S. H. Neddermeyer, “Cloud Chamber Observations of Cosmic Rays at 4300 Meters Elevation and Near Sea-Level”, *Phys. Rev.* **50** (Aug, 1936) 263–271, doi:10.1103/PhysRev.50.263.
- [24] J. C. Street and E. C. Stevenson, “New Evidence for the Existence of a Particle of Mass Intermediate Between the Proton and Electron”, *Phys. Rev.* **52** (Nov, 1937) 1003–1004, doi:10.1103/PhysRev.52.1003.
- [25] G. Danby, J.-M. Gaillard, K. Goulian et al., “Observation of High-Energy Neutrino Reactions and the Existence of Two Kinds of Neutrinos”, *Phys. Rev. Lett.* **9** (Jul, 1962) 36–44, doi:10.1103/PhysRevLett.9.36.
- [26] M. Gell-Mann, “A Schematic Model of Baryons and Mesons”, *Phys. Lett.* **8** (1964) 214–215, doi:10.1016/S0031-9163(64)92001-3.
- [27] G. Zweig, “An SU(3) model for strong interaction symmetry and its breaking. Version 2”,.
- [28] E. D. Bloom, D. H. Coward, H. DeStaebler et al., “High-Energy Inelastic  $e - p$  Scattering at  $6^\circ$  and  $10^\circ$ ”, *Phys. Rev. Lett.* **23** (Oct, 1969) 930, doi:10.1103/PhysRevLett.23.930.
- [29] M. Breidenbach, J. I. Friedman, H. W. Kendall et al., “Observed Behavior of Highly Inelastic Electron-Proton Scattering”, *Phys. Rev. Lett.* **23** (Oct, 1969) 935, doi:10.1103/PhysRevLett.23.935.
- [30] S. Glashow, J. Iliopoulos, and L. Maiani, “Weak Interactions with Lepton-Hadron Symmetry”, *Phys. Rev. D* **2** (Oct, 1970) 1285–1292, doi:10.1103/PhysRevD.2.1285.
- [31] J. J. Aubert, U. Becker, P. J. Biggs et al., “Experimental Observation of a Heavy Particle  $J$ ”, *Phys. Rev. Lett.* **33** (Dec, 1974) 1404–1406, doi:10.1103/PhysRevLett.33.1404.
- [32] J. E. Augustin, A. M. Boyarski, M. Breidenbach et al., “Discovery of a Narrow Resonance in  $e^+e^-$  Annihilation”, *Phys. Rev. Lett.* **33** (Dec, 1974) 1406, doi:10.1103/PhysRevLett.33.1406.
- [33] M. L. Perl, G. S. Abrams, A. M. Boyarski et al., “Evidence for Anomalous Lepton Production in  $e^+ - e^-$  Annihilation”, *Phys. Rev. Lett.* **35** (Dec, 1975) 1489–1492,

doi:10.1103/PhysRevLett.35.1489.

- [34] DONUT Collaboration, “Observation of tau neutrino interactions”, *Phys. Lett. B* **504** (2001) 218, doi:10.1016/S0370-2693(01)00307-0,  
arXiv:hep-ex/0012035.
- [35] M. Kobayashi and T. Maskawa, “CP-Violation in the Renormalizable Theory of Weak Interaction”, *Progress of Theoretical Physics* **49** (1973), no. 2, 652–657,  
doi:10.1143/PTP.49.652,  
arXiv:<http://ptp.oxfordjournals.org/content/49/2/652.full.pdf+html>.
- [36] S. W. Herb, D. C. Hom, L. M. Lederman et al., “Observation of a Dimuon Resonance at 9.5 GeV in 400-GeV Proton-Nucleus Collisions”, *Phys. Rev. Lett.* **39** (Aug, 1977) 252–255, doi:10.1103/PhysRevLett.39.252.
- [37] CDF Collaboration, “Observation of Top Quark Production in  $\bar{p}p$  Collisions with the Collider Detector at Fermilab”, *Phys. Rev. Lett.* **74** (Apr, 1995) 2626–2631,  
doi:10.1103/PhysRevLett.74.2626.
- [38] D0 Collaboration, “Search for High Mass Top Quark Production in  $p\bar{p}$  Collisions at  $\sqrt{s} = 1.8$  TeV”, *Phys. Rev. Lett.* **74** (Mar, 1995) 2422,  
doi:10.1103/PhysRevLett.74.2422.
- [39] UA1 Collaboration, “Experimental observation of isolated large transverse energy electrons with associated missing energy at  $s=540$  GeV”, *Phys. Lett. B* **122** (1983), no. 1, 103, doi:[http://dx.doi.org/10.1016/0370-2693\(83\)91177-2](http://dx.doi.org/10.1016/0370-2693(83)91177-2).
- [40] UA2 Collaboration, “Observation of single isolated electrons of high transverse momentum in events with missing transverse energy at the CERN pp collider”, *Phys. Lett. B* **122** (1983), no. 56, 476,  
doi:[http://dx.doi.org/10.1016/0370-2693\(83\)91605-2](http://dx.doi.org/10.1016/0370-2693(83)91605-2).
- [41] UA1 Collaboration, “Experimental observation of lepton pairs of invariant mass around 95 GeV at the CERN SPS collider”, *Phys. Lett. B* **126** (1983), no. 5, 398,  
doi:[http://dx.doi.org/10.1016/0370-2693\(83\)90188-0](http://dx.doi.org/10.1016/0370-2693(83)90188-0).
- [42] UA2 Collaboration, “Evidence for  $Z^0 \rightarrow e^+e^-$  at the CERN pp collider”, *Phys. Lett. B* **129** (1983), no. 12, 130,  
doi:[http://dx.doi.org/10.1016/0370-2693\(83\)90744-X](http://dx.doi.org/10.1016/0370-2693(83)90744-X).
- [43] TASSO Collaboration, “Evidence for planar events in  $e^+e^-$  annihilation at high

- energies”, *Phys. Lett. B* **86** (1979), no. 2, 243,  
[doi:`http://dx.doi.org/10.1016/0370-2693\(79\)90830-X`](http://dx.doi.org/10.1016/0370-2693(79)90830-X).
- [44] MARK–J Collaboration, “Discovery of Three-Jet Events and a Test of Quantum Chromodynamics at PETRA”, *Phys. Rev. Lett.* **43** (Sep, 1979) 830,  
[doi:`10.1103/PhysRevLett.43.830`](https://doi.org/10.1103/PhysRevLett.43.830).
- [45] E. Noether, “Invariante Variationsprobleme”, *Nachrichten von der Gesellschaft der Wissenschaften zu Göttingen, Mathematisch-Physikalische Klasse* **1918** (1918) 235–257.
- [46] N. Cabibbo, “Unitary Symmetry and Leptonic Decays”, *Phys. Rev. Lett.* **10** (Jun, 1963) 531, [doi:`10.1103/PhysRevLett.10.531`](https://doi.org/10.1103/PhysRevLett.10.531).
- [47] SNO Collaboration, “Measurement of the Rate of  $\nu_e + d \rightarrow p + p + e^-$  Interactions Produced by  $^8B$  Solar Neutrinos at the Sudbury Neutrino Observatory”, *Phys. Rev. Lett.* **87** (Jul, 2001) 071301, [doi:`10.1103/PhysRevLett.87.071301`](https://doi.org/10.1103/PhysRevLett.87.071301).
- [48] Super-Kamiokande Collaboration, “Study of the atmospheric neutrino flux in the multi-GeV energy range”, *Phys.Lett.* **B436** (1998) 33–41,  
[doi:`10.1016/S0370-2693\(98\)00876-4`](https://doi.org/10.1016/S0370-2693(98)00876-4), [arXiv:`hep-ex/9805006`](https://arxiv.org/abs/hep-ex/9805006).
- [49] Super-Kamiokande Collaboration, “Evidence for Oscillation of Atmospheric Neutrinos”, *Phys. Rev. Lett.* **81** (Aug, 1998) 1562–1567,  
[doi:`10.1103/PhysRevLett.81.1562`](https://doi.org/10.1103/PhysRevLett.81.1562).
- [50] Daya Bay Collaboration, “Observation of electron-antineutrino disappearance at Daya Bay”, *Phys.Rev.Lett.* **108** (2012) 171803,  
[doi:`10.1103/PhysRevLett.108.171803`](https://doi.org/10.1103/PhysRevLett.108.171803), [arXiv:`1203.1669`](https://arxiv.org/abs/1203.1669).
- [51] Daya Bay Collaboration, “Improved measurement of electron antineutrino disappearance at Daya Bay”, *Chinese Physics C* **37** (2013), no. 1, 011001.
- [52] T2K Collaboration, “Observation of Electron Neutrino Appearance in a Muon Neutrino Beam”, *Phys.Rev.Lett.* **112** (2014) 061802,  
[doi:`10.1103/PhysRevLett.112.061802`](https://doi.org/10.1103/PhysRevLett.112.061802), [arXiv:`1311.4750`](https://arxiv.org/abs/1311.4750).
- [53] T2K Collaboration, “Measurements of neutrino oscillation in appearance and disappearance channels by the T2K experiment with  $6.610^{20}$  protons on target”, *Phys.Rev.* **D91** (2015), no. 7, 072010, [doi:`10.1103/PhysRevD.91.072010`](https://doi.org/10.1103/PhysRevD.91.072010), [arXiv:`1502.01550`](https://arxiv.org/abs/1502.01550).

- [54] E. Corbelli and P. Salucci, “The extended rotation curve and the dark matter halo of M33”, *MNRAS* **311** (2000), no. 2, 441, doi:10.1046/j.1365-8711.2000.03075.x.
- [55] F. W. Dyson, A. S. Eddington, and C. Davidson, “A Determination of the Deflection of Light by the Sun’s Gravitational Field, from Observations Made at the Total Eclipse of May 29, 1919”, *Phil. Trans. A* **220** (1920), no. 571-581, 291, doi:10.1098/rsta.1920.0009.
- [56] R. Massey, T. Kitching, and J. Richard, “The dark matter of gravitational lensing”, *Reports on Progress in Physics* **73** (August, 2010) 086901, doi:10.1088/0034-4885/73/8/086901, arXiv:1001.1739.
- [57] Planck Collaboration Collaboration, “Planck 2013 results. XVI. Cosmological parameters”, *Astron. Astrophys.* **571** (2014) A16, doi:10.1051/0004-6361/201321591, arXiv:1303.5076.
- [58] D. Clowe, M. Bradac, A. H. Gonzalez et al., “A direct empirical proof of the existence of dark matter”, *Astrophys. J.* **648** (2006) L109, doi:10.1086/508162, arXiv:astro-ph/0608407.
- [59] M. Davis, G. Efstathiou, C. S. Frenk et al., “The evolution of large-scale structure in a universe dominated by cold dark matter”, *Astrophys. J.* **292** (1985) 371, doi:10.1086/163168.
- [60] L. Goodenough and D. Hooper, “Possible Evidence For Dark Matter Annihilation In The Inner Milky Way From The Fermi Gamma Ray Space Telescope”, arXiv:0910.2998.
- [61] ALEPH Collaboration, CDF Collaboration, D0 Collaboration, DELPHI Collaboration, L3 Collaboration, OPAL Collaboration, SLD Collaboration, LEP Electroweak Working Group, Tevatron Electroweak Working Group, SLD Electroweak and Heavy Flavour Groups Collaboration, “Precision Electroweak Measurements and Constraints on the Standard Model”, arXiv:1012.2367.
- [62] M. Baak, M. Goebel, J. Haller et al., “The Electroweak Fit of the Standard Model after the Discovery of a New Boson at the LHC”, *Eur. Phys. J. C* **72** (2012) 2205, doi:10.1140/epjc/s10052-012-2205-9, arXiv:1209.2716.
- [63] CMS Collaboration, “Precise determination of the mass of the Higgs boson and tests of compatibility of its couplings with the standard model predictions using

- proton collisions at 7 and 8 TeV”, [arXiv:1412.8662](https://arxiv.org/abs/1412.8662).
- [64] ATLAS Collaboration, “Measurement of the Higgs boson mass from the  $H \rightarrow \gamma\gamma$  and  $H \rightarrow ZZ^* \rightarrow 4\ell$  channels with the ATLAS detector using  $25 \text{ fb}^{-1}$  of  $pp$  collision data”, *Phys. Rev. D* **90** (2014) 052004, [doi:10.1103/PhysRevD.90.052004](https://doi.org/10.1103/PhysRevD.90.052004), [arXiv:1406.3827](https://arxiv.org/abs/1406.3827).
- [65] Y. Golfand and E. Likhtman, “Extension of the Algebra of Poincare Group Generators and Violation of p Invariance”, *JETP Lett.* **13** (1971) 323–326.
- [66] S. P. Martin, “A Supersymmetry primer”, *Adv. Ser. Direct. High Energy Phys.* **21** (2010) 1–153, [doi:10.1142/9789814307505\\_0001](https://doi.org/10.1142/9789814307505_0001), [arXiv:hep-ph/9709356](https://arxiv.org/abs/hep-ph/9709356).
- [67] N. Arkani-Hamed, S. Dimopoulos, and G. Dvali, “The hierarchy problem and new dimensions at a millimeter”, *Phys. Lett. B* **429** (1998), no. 34, 263 – 272, [doi:  
http://dx.doi.org/10.1016/S0370-2693\(98\)00466-3](http://dx.doi.org/10.1016/S0370-2693(98)00466-3).
- [68] R. N. Mohapatra and G. Senjanović, “Neutrino Mass and Spontaneous Parity Nonconservation”, *Phys. Rev. Lett.* **44** (Apr, 1980) 912–915, [doi:10.1103/PhysRevLett.44.912](https://doi.org/10.1103/PhysRevLett.44.912).
- [69] J. Schechter and J. W. F. Valle, “Neutrino masses in  $SU(2) \otimes U(1)$  theories”, *Phys. Rev. D* **22** (November, 1980) 2227–2235, [doi:10.1103/PhysRevD.22.2227](https://doi.org/10.1103/PhysRevD.22.2227).
- [70] M. Schmaltz and D. Tucker-Smith, “Little Higgs review”, *Ann. Rev. Nucl. Part. Sci.* **55** (2005) 229–270, [doi:10.1146/annurev.nucl.55.090704.151502](https://doi.org/10.1146/annurev.nucl.55.090704.151502), [arXiv:hep-ph/0502182](https://arxiv.org/abs/hep-ph/0502182).
- [71] S. Coleman and J. Mandula, “All Possible Symmetries of the  $S$  Matrix”, *Phys. Rev.* **159** (Jul, 1967) 1251, [doi:10.1103/PhysRev.159.1251](https://doi.org/10.1103/PhysRev.159.1251).
- [72] Y. Golfand and E. Likhtman, “Extension of the Algebra of Poincare Group Generators and Violation of p Invariance”, *JETP Lett.* **13** (1971) 323.
- [73] S. Dawson, “SUSY and such”, *NATO Sci.Ser.B* **365** (1997) 33–80, [doi:10.1007/978-1-4615-5963-4\\_2](https://doi.org/10.1007/978-1-4615-5963-4_2), [arXiv:hep-ph/9612229](https://arxiv.org/abs/hep-ph/9612229).
- [74] H. E. Haber, “Introductory low-energy supersymmetry”, [arXiv:hep-ph/9306207](https://arxiv.org/abs/hep-ph/9306207).
- [75] ATLAS Collaboration, “Search for R-parity-violating supersymmetry in events

- with four or more leptons in  $\sqrt{s} = 7$  TeV  $pp$  collisions with the ATLAS detector”, *JHEP* **1212** (2012) 124, doi:10.1007/JHEP12(2012)124, arXiv:1210.4457.
- [76] CMS Collaboration Collaboration, “Search for light stop RPV supersymmetry with three or more leptons and b-tags”, Technical Report CMS-PAS-SUS-13-003, CERN, Geneva, (2013).
- [77] CMS Collaboration, “Search for RPV SUSY in the four-lepton final state”,
- [78] S. Dimopoulos, S. Raby, and F. Wilczek, “Supersymmetry and the Scale of Unification”, *Phys. Rev. D* **24** (1981) 1681–1683, doi:10.1103/PhysRevD.24.1681.
- [79] D. Kazakov, “Beyond the standard model: In search of supersymmetry”, (2000). arXiv:hep-ph/0012288.
- [80] D. Chung, L. Everett, G. Kane et al., “The Soft supersymmetry breaking Lagrangian: Theory and applications”, *Phys. Rept.* **407** (2005) 1–203, doi:10.1016/j.physrep.2004.08.032, arXiv:hep-ph/0312378.
- [81] M. Papucci, J. T. Ruderman, and A. Weiler, “Natural SUSY Endures”, *JHEP* **1209** (2012) 035, doi:10.1007/JHEP09(2012)035, arXiv:1110.6926.
- [82] C. Brust, A. Katz, S. Lawrence et al., “SUSY, the Third Generation and the LHC”, *JHEP* **1203** (2012) 103, doi:10.1007/JHEP03(2012)103, arXiv:1110.6670.
- [83] CMS Collaboration, “Search for new physics in events with same-sign dileptons and  $b$  jets in  $pp$  collisions at  $\sqrt{s} = 8$  TeV”, *JHEP* **1303** (2013) 037, doi:10.1007/JHEP03(2013)037, 10.1007/JHEP07(2013)041, arXiv:1212.6194.
- [84] CMS Collaboration, “Search for gluino mediated bottom- and top-squark production in multijet final states in  $pp$  collisions at 8 TeV”, *Phys. Lett. B* **725** (2013) 243–270, doi:10.1016/j.physletb.2013.06.058, arXiv:1305.2390.
- [85] CMS Collaboration, “Search for new physics in the multijet and missing transverse momentum final state in proton-proton collisions at  $\sqrt{s}= 8$  TeV”, *JHEP* **1406** (2014) 055, doi:10.1007/JHEP06(2014)055, arXiv:1402.4770.
- [86] CMS Collaboration, “Search for supersymmetry in  $pp$  collisions at  $\sqrt{s}=8$  TeV in events with a single lepton, large jet multiplicity, and multiple  $b$  jets”, *Phys. Lett. B* **733** (2014) 328–353, doi:10.1016/j.physletb.2014.04.023,

- arXiv:1311.4937.
- [87] CMS Collaboration, “Search for anomalous production of events with three or more leptons in  $pp$  collisions at  $\sqrt{s} = 8$  TeV”, *Phys. Rev. D* **90** (2014), no. 3, 032006, doi:10.1103/PhysRevD.90.032006, arXiv:1404.5801.
- [88] CMS Collaboration, “Search for top-squark pair production in the single-lepton final state in  $pp$  collisions at  $\sqrt{s} = 8$  TeV”, *Eur. Phys. J. C* **73** (2013), no. 12, 2677, doi:10.1140/epjc/s10052-013-2677-2, arXiv:1308.1586.
- [89] CMS Collaboration, “Search for top squark and higgsino production using diphoton Higgs boson decays”, *Phys. Rev. Lett.* **112** (2014) 161802, doi:10.1103/PhysRevLett.112.161802, arXiv:1312.3310.
- [90] CMS Collaboration, “Search for top-squark pairs decaying into Higgs or Z bosons in  $pp$  collisions at  $\sqrt{s}=8$  TeV”, *Phys. Lett. B* **736** (2014) 371–397, doi:10.1016/j.physletb.2014.07.053, arXiv:1405.3886.
- [91] CMS Collaboration, “Searches for electroweak production of charginos, neutralinos, and sleptons decaying to leptons and W, Z, and Higgs bosons in  $pp$  collisions at 8 TeV”, *Eur. Phys. J. C* **74** (2014), no. 9, 3036, doi:10.1140/epjc/s10052-014-3036-7, arXiv:1405.7570.
- [92] CMS Collaboration, “Search for supersymmetry with razor variables in  $pp$  collisions at  $\sqrt{s}=7$  TeV”, *Phys. Rev. D* **90** (2014), no. 11, 112001, doi:10.1103/PhysRevD.90.112001, arXiv:1405.3961.
- [93] CMS Collaboration, “Search for supersymmetry in hadronic final states with missing transverse energy using the variables  $\alpha_T$  and b-quark multiplicity in  $pp$  collisions at  $\sqrt{s} = 8$  TeV”, *Eur. Phys. J. C* **73** (2013), no. 9, 2568, doi:10.1140/epjc/s10052-013-2568-6, arXiv:1303.2985.
- [94] CMS Collaboration, “Search for supersymmetry in hadronic final states using MT2 in  $pp$  collisions at  $\sqrt{s} = 7$  TeV”, *JHEP* **1210** (2012) 018, doi:10.1007/JHEP10(2012)018, arXiv:1207.1798.
- [95] D. Ghosh, M. Guchait, S. Raychaudhuri et al., “How Constrained is the cMSSM?”, *Phys. Rev. D* **86** (2012) 055007, doi:10.1103/PhysRevD.86.055007, arXiv:1205.2283.
- [96] A. Strumia, “The Fine-tuning price of the early LHC”, *JHEP* **1104** (2011) 073,

- doi:10.1007/JHEP04(2011)073, arXiv:1101.2195.
- [97] CMS Collaboration, “Summary Plots from 7 TeV CMS SUSY analyses”. <https://twiki.cern.ch/twiki/bin/view/CMSPublic/SUSYSMSSummaryPlots7TeV>. Accessed: 2015-01-30.
- [98] N. Arkani-Hamed, P. Schuster, N. Toro et al., “MAMOSET: The Path from LHC Data to the New Standard Model via On-Shell Effective Theories”, arXiv:hep-ph/0703088.
- [99] J. Alwall, P. Schuster, and N. Toro, “Simplified Models for a First Characterization of New Physics at the LHC”, *Phys. Rev. D* **79** (2009) 075020, doi:10.1103/PhysRevD.79.075020, arXiv:0810.3921.
- [100] LHC New Physics Working Group Collaboration, “Simplified Models for LHC New Physics Searches”, *J. Phys. G* **39** (2012) 105005, doi:10.1088/0954-3899/39/10/105005, arXiv:1105.2838.
- [101] CMS Collaboration, “Interpretation of Searches for Supersymmetry with simplified Models”, *Phys. Rev. D* **88** (2013), no. 5, 052017, doi:10.1103/PhysRevD.88.052017, arXiv:1301.2175.
- [102] CMS Collaboration, “Summary Plots from 8 TeV CMS SUSY analyses”. <https://twiki.cern.ch/twiki/pub/CMSPublic/SUSYSMSSummaryPlots8TeV/SUSY2013T2ttT6.pdf>. Accessed: 2015-01-30.
- [103] G. D. Kribs, A. Martin, and A. Menon, “Natural Supersymmetry and Implications for Higgs physics”, *Phys. Rev. D* **88** (2013) 035025, doi:10.1103/PhysRevD.88.035025, arXiv:1305.1313.
- [104] J. A. Casas, J. M. Moreno, S. Robles et al., “What is a Natural SUSY scenario?”, *JHEP* **1506** (2015) 070, doi:10.1007/JHEP06(2015)070, arXiv:1407.6966.
- [105] WMAP Collaboration Collaboration, “First year Wilkinson Microwave Anisotropy Probe (WMAP) observations: Determination of cosmological parameters”, *Astrophys. J. Suppl.* **148** (2003) 175, doi:10.1086/377226, arXiv:astro-ph/0302209.
- [106] S. P. Martin, “Compressed supersymmetry and natural neutralino dark matter from top squark-mediated annihilation to top quarks”, *Phys. Rev. D* **75** (2007) 115005, doi:10.1103/PhysRevD.75.115005, arXiv:hep-ph/0703097.

- [107] S. P. Martin, “The Top squark-mediated annihilation scenario and direct detection of dark matter in compressed supersymmetry”, *Phys. Rev. D* **76** (2007) 095005, doi:10.1103/PhysRevD.76.095005, arXiv:0707.2812.
- [108] C. Balazs, M. S. Carena, and C. Wagner, “Dark matter, light stops and electroweak baryogenesis”, *Phys. Rev. D* **70** (2004) 015007, doi:10.1103/PhysRevD.70.015007, arXiv:hep-ph/0403224.
- [109] M. Drees, M. Hanussek, and J. S. Kim, “Light Stop Searches at the LHC with Monojet Events”, *Phys. Rev. D* **86** (2012) 035024, doi:10.1103/PhysRevD.86.035024, arXiv:1201.5714.
- [110] C. Boehm, A. Djouadi, and M. Drees, “Light scalar top quarks and supersymmetric dark matter”, *Phys. Rev. D* **62** (2000) 035012, doi:10.1103/PhysRevD.62.035012, arXiv:hep-ph/9911496.
- [111] K.-i. Hikasa and M. Kobayashi, “Light scalar top quark at  $e^+e^-$  colliders”, *Phys. Rev. D* **36** (Aug, 1987) 724–732, doi:10.1103/PhysRevD.36.724.
- [112] C. Boehm, A. Djouadi, and Y. Mambrini, “Decays of the lightest top squark”, *Phys. Rev. D* **61** (Apr, 2000) 095006, doi:10.1103/PhysRevD.61.095006.
- [113] L. Evans and P. Bryant, “LHC Machine”, *Journal of Instrumentation* **3** (2008), no. 08, S08001.
- [114] ALICE Collaboration, “The ALICE experiment at the CERN LHC”, *JINST* **3** (2008) S08002, doi:10.1088/1748-0221/3/08/S08002.
- [115] ATLAS Collaboration, “The ATLAS Experiment at the CERN Large Hadron Collider”, *JINST* **3** (2008) S08003, doi:10.1088/1748-0221/3/08/S08003.
- [116] CMS Collaboration, “The CMS experiment at the CERN LHC”, *JINST* **3** (2008) S08004, doi:10.1088/1748-0221/3/08/S08004.
- [117] LHCb Collaboration, “The LHCb Detector at the LHC”, *JINST* **3** (2008) S08005, doi:10.1088/1748-0221/3/08/S08005.
- [118] CMS Collaboration, “Evidence for the direct decay of the 125 GeV Higgs boson to fermions”, *Nature Phys.* **10** (2014) 557–560, doi:10.1038/nphys3005, arXiv:1401.6527.
- [119] CMS Collaboration, “CMS Technical Design Report for the Level-1 Trigger

- Upgrade”, Technical Report CERN-LHCC-2013-011. CMS-TDR-12, CERN, Geneva, (Jun, 2013).
- [120] CMS Collaboration, “CMS Physics: Technical Design Report Volume 1: Detector Performance and Software”, technical design report cms, CERN, (2006).
- [121] M. Cacciari, G. P. Salam, and G. Soyez, “The anti- $k_t$  jet clustering algorithm”, *JHEP* **04** (2008) 063, doi:10.1088/1126-6708/2008/04/063, arXiv:0802.1189.
- [122] CMS Collaboration, “Particle Flow Event Reconstruction in CMS and Performance for Jets, Taus and MET”, CMS Physics Analysis Summary CMS-PAS-PFT-09-001, (2009).
- [123] Aachen-Annecy-Birmingham-CERN-Helsinki-London(QMC)-Paris(CdF)-Riverside-Rome-Rutherford-Saclay(CEN)-Vienna Collaboration, “Experimental observation of isolated large transverse energy electrons with associated missing energy at  $\sqrt{s} = 540$  GeV”, *Phys. Lett. B* **122** (Jan, 1983) 103–116, doi:10.1016/0370-2693(83)91177-2.
- [124] Vienna-Wisconsin Collaboration, Aachen-Amsterdam(NIKHEF)-Annecy-Birmingham-CERN-Harvard-Helsinki-Kiel-London(IC)-London(QMC)-MIT-Padua-Paris(CdF)-Riverside-Rome-Rutherford-Saclay(CEN)-Victoria Collaboration, “Events with large missing transverse energy at the CERN collider: I.  $W \rightarrow \tau\nu$  decay and test of  $\tau - \mu - e$  universality at  $Q^2 = m_W^2$ ”, *Phys. Lett. B* **185** (Nov, 1986) 233–240, doi:10.1016/0370-2693(87)91561-9.
- [125] Vienna-Wisconsin Collaboration, Aachen-Amsterdam(NIKHEF)-Annecy-Birmingham-CERN-Harvard-Helsinki-Kiel-London(IC)-London(QMC)-MIT-Padua-Paris(CdF)-Riverside-Rome-Rutherford-Saclay(CEN)-Victoria Collaboration, “Events with large missing transverse energy at the CERN collider: II. Search for the decays of  $W^+$  into heavy leptons and of  $Z^0$  into non-interacting particles”, *Phys. Lett. B* **185** (Nov, 1986) 241–248, doi:10.1016/0370-2693(87)91562-0.
- [126] CMS Collaboration, “CMS The TriDAS Project: Technical Design Report, Volume 2: Data Acquisition and High-Level Trigger. CMS trigger and data-acquisition project”, technical report, Geneva, (2002).
- [127] R. Frazier, S. Fayer, G. Hall et al., “A demonstration of a Time Multiplexed

- Trigger for the CMS experiment”, *JINST* **7** (2012), no. 01, C01060.
- [128] A. Rose, G. Iles, A. Tapper et al., “Calorimeter Trigger Layer 2 Design and Status”, (2013). EDR Presentation.
- [129] M. Baber, M. Blake, J. Brooke et al., “Development and testing of an upgrade to the CMS level-1 calorimeter trigger”, *JINST* **9** (2014), no. 01, C01006.
- [130] M. Cacciari and G. P. Salam, “Pileup subtraction using jet areas”, *Phys. Lett. B* **659** (2008) 119, doi:10.1016/j.physletb.2007.09.077, arXiv:0707.1378.
- [131] CMS Collaboration, “Search for supersymmetry in hadronic final states with missing transverse energy using the variables  $\alpha_T$  and b-quark multiplicity in pp collisions at  $\sqrt{s} = 8$  TeV”, *Eur. Phys. J. C* **73** (2013) 2568, doi:10.1140/epjc/s10052-013-2568-6, arXiv:1303.2985.
- [132] CMS Collaboration, “Level-1 Calorimeter Trigger Upgrade: Jet and Energy Sum Algorithms and Performance”, (2014). Internal Note.
- [133] A. Delgado and M. Strassler, “A Simple-Minded Unitarity Constraint and an Application to Unparticles”, *Phys. Rev. D* **81** (2010) 056003, doi:10.1103/PhysRevD.81.056003.
- [134] D0 Collaboration, “Search for large extra dimensions via single photon plus missing energy final states at  $\sqrt{s} = 1.96$ -TeV”, *Phys. Rev. Lett.* **101** (2008) 011601, doi:10.1103/PhysRevLett.101.011601, arXiv:0803.2137.
- [135] CDF Collaboration, “Search for large extra dimensions in final states containing one photon or jet and large missing transverse energy produced in  $p\bar{p}$  collisions at  $\sqrt{s} = 1.96$ -TeV”, *Phys. Rev. Lett.* **101** (2008) 181602, doi:10.1103/PhysRevLett.101.181602, arXiv:0807.3132.
- [136] CDF Collaboration, “A Search for dark matter in events with one jet and missing transverse energy in  $p\bar{p}$  collisions at  $\sqrt{s} = 1.96$  TeV”, *Phys. Rev. Lett.* **108** (2012) 211804, doi:10.1103/PhysRevLett.108.211804, arXiv:1203.0742.
- [137] ATLAS Collaboration, “Search for new phenomena with the monojet and missing transverse momentum signature using the ATLAS detector in  $\sqrt{s} = 7$  TeV proton-proton collisions”, *Phys. Lett. B* **705** (2011) 294, doi:10.1016/j.physletb.2011.10.006, arXiv:1106.5327.
- [138] ATLAS Collaboration, “Search for dark matter candidates and large extra

- dimensions in events with a jet and missing transverse momentum with the ATLAS detector”, *JHEP* **1304** (2013) 075, doi:10.1007/JHEP04(2013)075, arXiv:1210.4491.
- [139] CMS Collaboration, “Search for New Physics with a Mono-Jet and Missing Transverse Energy in  $pp$  Collisions at  $\sqrt{s} = 7$  TeV”, *Phys. Rev. Lett.* **107** (2011) 201804, doi:10.1103/PhysRevLett.107.201804, arXiv:1106.4775.
- [140] CMS Collaboration, “Search for dark matter and large extra dimensions in monojet events in  $pp$  collisions at  $\sqrt{s} = 7$  TeV”, *JHEP* **09** (2012) 094, doi:10.1007/JHEP09(2012)094, arXiv:1206.5663.
- [141] CMS Collaboration, “Search for dark matter, extra dimensions, and unparticles in monojet events in proton-proton collisions at  $\sqrt{s} = 8$  TeV”, arXiv:1408.3583.
- [142] OPAL Collaboration, “Photonic events with missing energy in e+ e- collisions at  $S^{**}(1/2) = 189$ -GeV”, *Eur. Phys. J. C* **18** (2000) 253, doi:10.1007/s100520000522, arXiv:hep-ex/0005002.
- [143] A. Heister et al., “Single- and multi-photon production in ee collisions at  $\sqrt{ss}$  up to 209 GeV”, *Eur. Phys. J. C* **28** (2003), no. 1, 1, doi:10.1140/epjc/s2002-01129-7.
- [144] L3 Collaboration Collaboration, “Single photon and multiphoton events with missing energy in  $e^+e^-$  collisions at LEP”, *Phys. Lett. B* **587** (2004) 16, doi:10.1016/j.physletb.2004.01.010, arXiv:hep-ex/0402002.
- [145] DELPHI Collaboration, “Photon events with missing energy in e+ e- collisions at  $s^{**}(1/2) = 130$ -GeV to 209-GeV”, *Eur. Phys. J. C* **38** (2005) 395, doi:10.1140/epjc/s2004-02051-8, arXiv:hep-ex/0406019.
- [146] D0 Collaboration, “Search for large extra dimensions via single photon plus missing energy final states at  $\sqrt{s} = 1.96$ -TeV”, *Phys. Rev. Lett.* **101** (2008) 011601, doi:10.1103/PhysRevLett.101.011601, arXiv:0803.2137.
- [147] CMS Collaboration, “Search for Dark Matter and Large Extra Dimensions in pp Collisions Yielding a Photon and Missing Transverse Energy”, *Phys. Rev. Lett.* **108** (2012) 261803, doi:10.1103/PhysRevLett.108.261803, arXiv:1204.0821.
- [148] ATLAS Collaboration, “Search for dark matter candidates and large extra

- dimensions in events with a photon and missing transverse momentum in  $pp$  collision data at  $\sqrt{s} = 7$  TeV with the ATLAS detector”, *Phys. Rev. Lett.* **110** (2013), no. 1, 011802, doi:10.1103/PhysRevLett.110.011802, arXiv:1209.4625.
- [149] J. Alwall et al., “MadGraph/MadEvent v4: the new web generation”, *JHEP* **09** (2007) 028, doi:10.1088/1126-6708/2007/09/028, arXiv:0706.2334.
- [150] J. Alwall, R. Frederix, S. Frixione et al., “The automated computation of tree-level and next-to-leading order differential cross sections, and their matching to parton shower simulations”, *JHEP* **07** (2014) 079, doi:10.1007/JHEP07(2014)079, arXiv:1405.0301.
- [151] T. Sjöstrand, S. Mrenna, and P. Z. Skands, “PYTHIA 6.4 physics and manual”, *JHEP* **05** (2006) 026, doi:10.1088/1126-6708/2006/05/026, arXiv:hep-ph/0603175.
- [152] T. Sjöstrand, S. Mrenna, and P. Z. Skands, “A Brief Introduction to PYTHIA 8.1”, *Comput. Phys. Commun.* **178** (2008) 852, doi:10.1016/j.cpc.2008.01.036, arXiv:0710.3820.
- [153] R. Field, “Early LHC Underlying Event Data - Findings and Surprises”, arXiv:1010.3558.
- [154] S. Agostinelli, J. Allison, and K. A. et al, “Geant4a simulation toolkit”, *Nucl. Instrum. Meth. A* **506** (2003), no. 3, 250, doi:doi.org/10.1016/S0168-9002(03)01368-8.
- [155] J. Allison et al., “Geant4 developments and applications”, *IEEE 53* **1** (2006) 270, doi:10.1109/TNS.2006.869826.
- [156] CMS Collaboration, “The fast simulation of the CMS detector at LHC”, *J. Phys. Conf. Ser.* **331** (2011) 032049, doi:10.1088/1742-6596/331/3/032049.
- [157] J. Pumplin, D. R. Stump, J. Huston et al., “New Generation of Parton Distributions with Uncertainties from Global QCD Analysis”, *JHEP* **07** (2002) 012, doi:10.1088/1126-6708/2002/07/012, arXiv:hep-ph/0201195.
- [158] S. Alioli, P. Nason, C. Oleari et al., “NLO single-top production matched with shower in POWHEG: s- and t-channel contributions”, *JHEP* **0909** (2009) 111, doi:10.1007/JHEP02(2010)011, 10.1088/1126-6708/2009/09/111,

- arXiv:0907.4076.
- [159] E. Re, “Single-top Wt-channel production matched with parton showers using the POWHEG method”, *Eur.Phys.J. C* **71** (2011) 1547,  
doi:10.1140/epjc/s10052-011-1547-z, arXiv:1009.2450.
- [160] N. Davidson, G. Nanava, T. Przedzinski et al., “Universal Interface of TAUOLA Technical and Physics Documentation”, *Comput. Phys. Commun.* **183** (2012) 821, doi:10.1016/j.cpc.2011.12.009, arXiv:1002.0543.
- [161] S. Höche, F. Krauss, N. Lavesson et al., “Matching parton showers and matrix elements”, (2006). arXiv:hep-ph/0602031. Appear in proceedings of ‘HERA and the LHC: A Workshop on the Implications of HERA for LHC Physics: CERN - DESY Workshop 2004/2005’.
- [162] CMS Collaboration, “Determination of jet energy calibration and transverse momentum resolution in CMS”, *JINST* **6** (2011) P11002,  
doi:10.1088/1748-0221/6/11/P11002, arXiv:1107.4277.
- [163] CMS Collaboration, “Performance of CMS muon reconstruction in pp collision events at  $\sqrt{s} = 7$  TeV”, *J. Inst* **7** (October, 2012) 2P,  
doi:10.1088/1748-0221/7/10/P10002, arXiv:1206.4071.
- [164] CMS Collaboration, “Performance of electron reconstruction and selection with the CMS detector in proton-proton collisions at  $\sqrt{s} = 8$  TeV”, (2015).  
arXiv:1502.02701. Submitted to *JINST*.
- [165] CMS Collaboration, “Search for neutral Higgs bosons decaying to  $\tau$  pairs in  $pp$  collisions at  $\sqrt{s} = 7$  TeV”, *Phys. Lett. B* **713** (2012) 68,  
doi:10.1016/j.physletb.2012.05.028, arXiv:1202.4083.
- [166] CMS Collaboration, “Performance of  $\tau$ -lepton reconstruction and identification in CMS”, *JINST* **7** (2012) 1001, doi:10.1088/1748-0221/7/01/P01001,  
arXiv:1109.6034.
- [167] CMS Collaboration, “CMS tracking performance results from early LHC operation”, *Eur. Phys. J. C* **70** (2010) 1165,  
doi:10.1140/epjc/s10052-010-1491-3, arXiv:1007.1988.
- [168] CMS Collaboration, “Transverse momentum and pseudorapidity distributions of charged hadrons in pp collisions at  $\sqrt{s} = 0.9$  and 2.36 TeV”, *JHEP* **02** (2010)

- 041, doi:[10.1007/JHEP02\(2010\)041](https://doi.org/10.1007/JHEP02(2010)041).
- [169] N. Kidonakis, “Next-to-next-to-leading Soft-Gluon Corrections for the Top Quark Cross Section and Transverse Momentum Distribution”, *Phys. Rev. D* **82** (2010) 114030, doi:[10.1103/PhysRevD.82.114030](https://doi.org/10.1103/PhysRevD.82.114030), arXiv:[1009.4935](https://arxiv.org/abs/1009.4935).
- [170] K. Melnikov and F. Petriello, “Electroweak Gauge Boson Production at hadron colliders through  $O(\alpha(s)^2)$ ”, *Phys. Rev. D* **74** (2006) 114017, doi:[10.1103/PhysRevD.74.114017](https://doi.org/10.1103/PhysRevD.74.114017), arXiv:[hep-ph/0609070](https://arxiv.org/abs/hep-ph/0609070).
- [171] N. Kidonakis, “Next-to-next-to-leading-order collinear and soft gluon corrections for  $t$ -channel single top quark production”, *Phys. Rev. D* **83** (2011) 091503, doi:[10.1103/PhysRevD.83.091503](https://doi.org/10.1103/PhysRevD.83.091503), arXiv:[1103.2792](https://arxiv.org/abs/1103.2792).
- [172] R. Gavin, Y. Li, F. Petriello et al., “W physics at the LHC with FEWZ 2.1”, *Comput. Phys. Commun.* **184** (2013) 208, doi:[10.1016/j.cpc.2012.09.005](https://doi.org/10.1016/j.cpc.2012.09.005), arXiv:[1201.5896](https://arxiv.org/abs/1201.5896).
- [173] N. Kidonakis, “NNLL resummation for  $s$ -channel single top quark production”, *Phys. Rev. D* **81** (2010) 054028, doi:[10.1103/PhysRevD.81.054028](https://doi.org/10.1103/PhysRevD.81.054028), arXiv:[1001.5034](https://arxiv.org/abs/1001.5034).
- [174] N. Kidonakis, “Two-loop soft anomalous dimensions for single top quark associated production with a  $W^-$  or  $H^-$ ”, *Phys. Rev. D* **82** (2010) 054018, doi:[10.1103/PhysRevD.82.054018](https://doi.org/10.1103/PhysRevD.82.054018), arXiv:[1005.4451](https://arxiv.org/abs/1005.4451).
- [175] M. Botje, J. Butterworth, A. Cooper-Sarkar et al., “The PDF4LHC Working Group Interim Recommendations”, (2011). arXiv:[1101.0538](https://arxiv.org/abs/1101.0538).
- [176] CMS Collaboration, “Search for narrow resonances and quantum black holes in inclusive and  $b$ -tagged dijet mass spectra from  $pp$  collisions at  $\sqrt{s} = 7$  TeV”, *JHEP* **1301** (2013) 013, doi:[10.1007/JHEP01\(2013\)013](https://doi.org/10.1007/JHEP01(2013)013), arXiv:[1210.2387](https://arxiv.org/abs/1210.2387).
- [177] N. Kidonakis, “Differential and total cross sections for top pair and single top production”, doi:[10.3204/DESY-PROC-2012-02/251](https://doi.org/10.3204/DESY-PROC-2012-02/251), arXiv:[1205.3453](https://arxiv.org/abs/1205.3453).
- [178] J. M. Campbell, R. K. Ellis, and C. Williams, “Vector boson pair production at the LHC”, *JHEP* **1107** (2011) 018, doi:[10.1007/JHEP07\(2011\)018](https://doi.org/10.1007/JHEP07(2011)018), arXiv:[1105.0020](https://arxiv.org/abs/1105.0020).
- [179] CMS Collaboration, “Interpretation of Searches for Supersymmetry with simplified Models”, arXiv:[1301.2175](https://arxiv.org/abs/1301.2175).

- [180] M. L. Mangano, M. Moretti, F. Piccinini et al., “Matching matrix elements and shower evolution for top-quark production in hadronic collisions”, *JHEP* **0701** (2007) 013, doi:10.1088/1126-6708/2007/01/013, arXiv:hep-ph/0611129.
- [181] M. Krämer, A. Kulesza, R. van der Leeuw et al., “Supersymmetry production cross sections in  $pp$  collisions at  $\sqrt{s} = 7$  TeV”, arXiv:1206.2892.
- [182] CMS Collaboration, “CMS Luminosity Based on Pixel Cluster Counting - Summer 2013 Update”, CMS Physics Analysis Summary CMS-PAS-LUM-13-001, CERN, (2013).
- [183] L. Moneta, K. Cranmer, G. Schott et al., “The RooStats Project”, in *Proceedings of the 13th International Workshop on Advanced Computing and Analysis Techniques in Physics Research (ACAT2010)*. SISSA, 2010. arXiv:1009.1003.
- [184] ATLAS, CMS,  
LPCC Collaboration, “SUSY Cross sections for stop and sbottom quarks at 8 TeV”,  
<https://twiki.cern.ch/twiki/bin/view/LHCPhysics/SUSYCrossSections8TeVstopsbottom>.

# List of Figures

2.1	Combined results from CMS of many SM measurements made at LHC centre-of-mass energies of 7 and 8 TeV, taken from[7]. Theory and experiment agree over a vast range of production cross section values, for many different SM processes. . . . .	6
2.2	Higgs ‘Mexican Hat’ potential . . . . .	16
2.3	Example of a lepton and baryon number interaction which would mediate proton decay. . . . .	22
2.4	The running coupling constants of the electromagnetic, strong and weak forces with increasing energy or decreasing distance. Once SUSY has been added in, the three unify around $10^{16}$ GeV, hinting at a GUT. Taken from [79]. . . . .	24
2.5	The loop contributing to the Higgs mass due to the top quark, left, and the cancellation of the loop due to the top squark, right. . . . .	25
2.6	Example of a SUSY decay chain, in which there are several quarks emitted as well as the LSP. Two of these decay chains will be present in each event due to the pair production of the parent $\tilde{q}$ . . . . .	26
2.7	The limits on the $m_{1/2}, m_0$ CMSSM mass plane from CMS with the full 7 TeV dataset, taken from[97]. . . . .	27
2.8	An example of a SUSY decay of the top squark. This is one of the simplified models probed by CMS at the LHC. . . . .	27
2.9	The limits on the $\tilde{t}, \tilde{\chi}_1^0$ mass plane from CMS at SUSY 2013[102]. . . . .	28

---

2.10 An example SUSY spectrum in the bulk region, left, and for a compressed spectrum, right. The mass difference between the NLSP and the LSP, here the $\tilde{t}$ and $\tilde{\chi}_1^0$ respectively, is much reduced for the compressed scenario.	29
2.11 Feynman diagrams to show two contributing processes to the decays of the top squark: $\tilde{t} \rightarrow c\tilde{\chi}_1^0$ (left) and $\tilde{t} \rightarrow b\tilde{\chi}_1^0 f\bar{f}'$ (right). <a href="#">The intermediate top quark on the right, <math>t^*</math>, is produced off-shell.</a>	31
2.12 Phase space of the top squark and LSP. The grey region is kinematically forbidden: $m_{\tilde{\chi}_1^0} > m_{\tilde{t}}$ is at odds with the LSP definition. The coloured dotted lines and labels define each kinematic region, and the dominant $\tilde{t}$ decays are shown, where we have neglected the four body decay in the region where $m_{\tilde{t}} - m_{\tilde{\chi}_1^0} < m_W$ .	32
3.1 The LHC accelerator ring, showing the locations of the four main experiments at the four collision points.	34
3.2 The CMS detector, with the main subsystems labelled.	37
3.3 The CMS tracker, shown in the $rz$ plane. The pixel detector is shown at the centre of the tracker, closest to the interaction region (shown by the black dot), and the strip detector surrounds it. The different subsystems of the strip detector are shown[116].	40
3.4 The energy resolution (left), transverse and longitudinal impact parameters (center, right) as a function of $ \eta $ for CMS tracker, shown for single muons with $p_T = 1, 10$ and $100$ GeV[116].	40
3.5 Geometric view of the CMS ECAL[116]. Barrel crystals are arranged in modules and supermodules, and endcap crystals arranged in supercrystals. Also shown is the preshower detector.	41
3.6 The energy resolution of an ECAL supercrystal, measured in a test beam. The lower set of points along the dashed line correspond to the energy measured in an array of $3 \times 3$ crystals, where events fall within a $4 \times 4$ mm region in the central crystal[120].	42
3.7 Longitudinal view of the CMS HCal[116]. Locations of the HB, HO, HE and HF are shown with values of $\eta$ . The purple regions represent the muon detectors which further restrict the volume of the HO.	44

---

3.8	The raw energy response (left) and fractional energy resolution (right) as a function of energy, for pions, in team beam data[120]. . . . .	44
3.9	One of the 5 wheels of the barrel of the CMS muon system[116]. Gaseous detectors are embedded in the iron return yoke of the solenoid. . . . .	45
3.10	Muon transverse momentum resolution, shown as a function of muon $p_T$ in the barrel (left) and the endcaps (right)[116]. The resolution of the tracker and muon system is shown, and the enhancement gained by combining the information. Here, and in several of the following plots, the units shown are not natural, indicated by the presence of $c$ in the specified unit. . . . .	46
3.11	A slice of the CMS detector is shown, with various particles, or physics objects, traversing it. By combining information from each of the subdetectors, each of the particles produced in an event can be identified and the whole event reconstructed. . . . .	47
3.12	The relative insensitivity of the anti- $k_t$ algorithm to PU is shown, compared to other common jet algorithms. The distribution of back reaction, corresponding to the net change in $p_T$ to each of the two hardest jets (where each jet has $p_T > 200$ GeV), when adding PU $\sim 25$ to the event, corresponding to LHC running conditions in the next phase of data taking starting in 2015[121]. . . . .	49
3.13	The efficiency of PF jets, and Calo jets, matched to generated jets in the barrel region (left) and the endcap (right), taken from[122]. The superior performance of PF jets is evident because they are more efficiently matched to the generator, “truth” jets, at a lower $p_T$ threshold: termed a sharper turn-on. . . . .	50
3.14	The momentum resolution, $(p_T^{\text{rec}} - p_T^{\text{gen}})/p_T^{\text{gen}}$ of PF jets, and Calo jets, for low energy jets ( $40 \text{ GeV} < p_T < 60 \text{ GeV}$ ) (left) and for high momentum jets ( $300 \text{ GeV} < p_T < 400 \text{ GeV}$ ) (right) in the barrel region, taken from[122]. Not only are the peaks sharper for PF jets, meaning a smaller (and therefore better) overall momentum resolution, but it is also peaking much closer to zero, meaning the jet measurement is much closer to the generated jet momentum. . . . .	50

3.15	The missing transverse momentum resolution, $(p_{T,\text{rec}}^{\text{miss}} - p_{T,\text{gen}}^{\text{miss}})/p_{T,\text{gen}}^{\text{miss}}$ of PF and Calo $p_T^{\text{miss}}$ , taken from[122]. An improved resolution is seen using the PF algorithm, particularly at low values of $p_T^{\text{miss}}$ . At higher $p_T^{\text{miss}}$ values, energy measurements are dominated by the calorimeter resolution and values using the two different methods converge. . . . .	52
3.16	Inclusive pp cross sections ( $\sigma$ ) for basic and rarer physics processes, showing some of the phenomena on the physics programme at CMS. Shown on the right are the interaction rates for LHC design luminosity, $10^{34}\text{cm}^{-2}\text{s}^{-1}$ [126].	54
3.17	Architecture of the L1 trigger. The calorimeter trigger takes inputs from the ECAL, HCAL and HF. The muon trigger takes inputs from the DT, CSCs and RPCs. A decision is made at the L1 GT, using inputs from the GCT and the GMT, of whether to pass an event onto the HLT or discard it.	56
4.1	A possible Run 2 L1 trigger menu, using the current L1 system and algorithms, where $\sqrt{s} = 14\text{ TeV}$ [119]. The numbers here are for illustration purposes only - they are not a proposed trigger menu. In the left hand column, all of the different triggers contributing to the menu are shown. In the centre (right-hand) columns, the projected L1 trigger rate, 95% threshold and plateau efficiency are shown for possible Run 2 running conditions with bunch spacing of 50 ns, $\mathcal{L} = 1.1 \times 10^{34} \text{ cm}^{-2}\text{s}^{-1}$ , PU=50 (25 ns, $\mathcal{L} = 2.2 \times 10^{34} \text{ cm}^{-2}\text{s}^{-1}$ , PU=50). . . . .	60
4.2	Conventional trigger architecture, showing data processing in regions[128]. Here, and in Figure 4.3, ‘TPG’ stands for trigger primitive generators. . .	62
4.3	Time-multiplexed trigger architecture, showing data pipe-lining to different processing nodes[128]. . . . .	64
4.4	Layout of trigger towers in the $r - z$ projection, for $0 < \eta < 3.0$ . Both ECAL and HCAL towers are shown. . . . .	66
4.5	Comparison of the current L1 jet map, left, with the proposed upgrade jet map, showing a $8 \times 8$ square jet, right. . . . .	66

4.6 A few of the overlapping jets of one $4 \times 4$ jet (centre, purple), are shown in red. The window of all of the jet overlaps is shown in blue, measuring $10 \times 10$ . These overlapping jets must be sorted and filtered to keep only the most energetic jet. . . . .	67
4.7 The $p_T$ distribution of L1 jets that have been matched, within a cone of $\Delta R < 0.5$ , to offline jets reconstructed with the anti- $k_t$ algorithm using a radius parameter of 0.5 and calorimeter information as input only. The distribution shown before a $p_T$ and $\eta$ calibration has been applied is shown on the left, and after the calibration has been applied on the right. In both distributions, PU has been subtracted from both jet collections. . .	70
4.8 Resolution in $\eta$ , $\phi$ and $p_T$ for high PU data taken by the CMS detector in 2012. There is a clear improvement with the upgrade jets, plotted in red, in both angular resolutions and energy resolution. These plots can be found in[119]. . . . .	72
4.9 The PU dependency of the L1 jet energy resolution for both the current algorithm and the upgrade algorithm, where the resolution is taken as the RMS of the PU distribution shown in Figure 4.8, for different PU bins. There is a clear improvement with the upgrade jets, plotted in red, which shows independence of PU up to PU $\sim 40$ . . . . .	72
4.10 On the left are the trigger turn on curves for the current jet algorithm and on the right are the trigger turn on curves for the upgrade jet algorithm, for various single jet trigger thresholds, calculated using relatively low PU data. The right hand plot can be found in[119]. . . . .	74
4.11 On the left are the trigger turn on curves for the current jet algorithm and on the right are the trigger turn on curves for the upgrade jet algorithm, for various single jet trigger thresholds, using relatively high PU data. . .	74
4.12 Rates of single, double, triple and quad jet triggers. The single jet trigger shows similar performance to the current system, while the multi-jet trigger show a large reduction in rate. . . . .	77
4.13 Conversion between the L1 jet threshold and the 95% efficiency as measured offline, for the proposed upgrade jet algorithm, using the turn on curves shown in Figure 4.11. . . . .	77

---

4.14 Rates of single, double, triple and quad jet triggers. The single jet trigger shows similar performance to the current system, while the multi-jet trigger show a large reduction in rate. The single and quad jet rate plots can be found in[119]. . . . .	78
4.15 The trigger turn on curves for the $H_T$ variable, left, and the conversion between the L1 $H_T$ threshold and the 95% efficiency as measured offline, using $H_T$ constructed with the proposed upgrade algorithm. . . . .	79
4.16 Rates of $H_T$ triggers, vs L1 threshold (left) and 95% offline threshold (right), where the conversion between L1 threshold and 95% efficiency is taken from Figure 4.15. There is a significant reduction in rates with the proposed upgrade algorithm. . . . .	79
5.1 Feynman diagrams of the signals probed. The top diagram shows the FCNC process $\tilde{t}\bar{t} \rightarrow c\bar{c} \tilde{\chi}_1^0 \tilde{\chi}_1^0$ and the bottom diagram shows the process $\tilde{b}\bar{b} \rightarrow b\bar{b} \tilde{\chi}_1^0 \tilde{\chi}_1^0$ . In both cases, an ISR gluon leads to an energetic jet, and balances the $p_T^{\text{miss}}$ due to LSPs escaping the detector leaving no trace. . .	83
5.2 The trigger efficiency as a function of the $p_T^{\text{miss}}$ (left) and $p_T$ of the leading jet (right). . . . .	85
5.3 Hadronic and EM energy fractions from charged and neutral particles, before clean-up cuts on these quantities are applied. In the leading jet, the charged hadronic energy fraction is required to be $> 20\%$ and the neutral EM and hadronic energy fractions must be $< 70\%$ . In the second leading jet, the neutral EM energy fraction is required to be $< 90\%$ and the neutral hadronic energy fraction must be $< 70\%$ . The shaded band in the ratio plot shows the statistical uncertainty and all distributions are normalized to the cross sections shown in Table 5.2. . . . .	92
5.4 Hadronic and EM energy fractions from charged and neutral particles, after clean-up cuts on these quantities are applied. The shaded band in the ratio plot shows the statistical uncertainty and all distributions are normalized to the cross sections shown in Table 5.2. . . . .	93
5.5 Charm quark $p_T$ spectra for mass splittings across the phase space range, $m_{\tilde{t}} - m_{\tilde{\chi}_1^0} = 10, 30, 80$ GeV, for a top squark mass of 150 GeV. Taken from Ref[5]. . . . .	94

---

5.6 Total $p_T$ of the $\tilde{t}\tilde{t}$ pair for various signal hypotheses, where the mass splitting $m_{\tilde{t}} - m_{\tilde{\chi}_1^0} = 30$ GeV. The $\tilde{t}\tilde{t}$ system has a larger boost for larger $\tilde{t}$ masses. . . . .	95
5.7 Plots of basic selection variables. All figures except for the $p_T$ and $\eta$ of the second leading jet show distributions after all cuts are applied except the one being plotted (the leading jet $p_T$ cut for all plots except the jet $p_T$ and jet $\eta$ is set to 110 GeV). SM backgrounds are taken from simulation and normalized to the integrated luminosity using the cross sections shown in Table 5.2. The error bars in the ratio plots show the statistical uncertainties. . . . .	96
5.8 Plots of selection variables in the baseline search region, where $p_T(j_1) > 250$ GeV. Superimposed are kinematic distributions for the signal $t\bar{t} \rightarrow c\bar{c}\tilde{\chi}_1^0\tilde{\chi}_1^0$ where $m_{\tilde{t}} = 250$ GeV and $m_{\tilde{\chi}_1^0} = 240$ GeV. SM backgrounds are taken from simulation and normalized to the integrated luminosity using the cross sections shown in Table 5.2. The error bars in the ratio plots show the statistical uncertainties. . . . .	97
5.9 Invariant mass and transverse momentum of the dimuon pair in the $Z \rightarrow \mu^+\mu^-$ control sample. . . . .	100
5.10 The ratio of $p_T^{\text{miss},\mu}$ to the $Z$ boson $p_T$ , taken from simulation, in $Z(\mu\mu) + \text{jets}$ and $Z(\nu\bar{\nu}) + \text{jets}$ events. Distributions are normalized to unit area. . . . .	102
5.11 Transverse mass $m_T$ of the muon (left) and $p_T$ of $W^\pm$ candidates in the $W$ mass window, $50 - 100$ GeV in the single muon control sample. . . . .	106
5.12 The QCD rich region dominated by back to back jets, $\Delta\phi(p_T^{\text{miss},\mu}, j_2) < 0.3$ , shown for a jet counting cut of 60 GeV for $p_T(j_1) > 250$ GeV. . . . .	111
5.13 $\Delta\phi(p_T^{\text{miss}}, j_3)$ , shown for a jet counting threshold of 60 GeV for $p_T(j_1) > 250$ GeV. . . . .	113
5.14 Invariant mass distribution (left) and $p_T$ distribution (right) of the $e\mu$ pair in the $t\bar{t}$ -enriched control sample. . . . .	114
5.15 The leading jet $p_T$ spectrum from the $Z(\nu\bar{\nu})\gamma$ simulation, in the baseline search region; the small increase in events above 400 GeV is evident. The right hand plot shows the zoomed in region which is fitted with an exponential curve in red. . . . .	116

6.1 Distributions of (left) $p_T^{\text{miss},\mu}$ and (right) leading jet $p_T$ in the baseline monojet search region, $p_T(j_1) > 250$ GeV, for data and SM backgrounds. Background distributions are taken from simulation, and normalized to an integrated luminosity of $19.7 \text{ fb}^{-1}$ using the cross sections shown in Table 5.2. A representative signal distribution for $\tilde{t} \rightarrow c\tilde{\chi}_1^0$ is also shown (in the dotted line), where $m_{\tilde{t}} = 250$ GeV and $m_{\tilde{\chi}_1^0} = 240$ GeV. Statistical uncertainties are shown for the data. Taken from Ref[5]. . . . .	119
6.2 Signal acceptances in the search regions, at each $p_T(j_1)$ threshold for the process $\tilde{t}\tilde{\bar{t}} \rightarrow c\bar{c}\tilde{\chi}_1^0\tilde{\chi}_1^0$ . Each plot shows a different value of $m_{\tilde{t}}$ , and various masses of the LSP, $m_{\tilde{\chi}_1^0}$ . Signal acceptance is greatest when $m_{\tilde{t}}$ is close to $m_{\tilde{\chi}_1^0}$ , and increases with increasing $m_{\tilde{t}}$ . . . . .	122
6.3 Signal acceptances in the search regions, at each $p_T(j_1)$ threshold for the process $\tilde{b}\tilde{\bar{b}} \rightarrow b\bar{b}\tilde{\chi}_1^0\tilde{\chi}_1^0$ . Each plot shows a different value of $m_{\tilde{b}}$ , and various masses of the LSP, $m_{\tilde{\chi}_1^0}$ . Signal acceptance is greatest when $m_{\tilde{b}}$ is close to $m_{\tilde{\chi}_1^0}$ , and increases with increasing $m_{\tilde{b}}$ . The kinks in the lines are because statistics are low for mass points where $m_{\tilde{b}} - m_{\tilde{\chi}_1^0} > 100$ GeV, particularly at high leading jet thresholds. . . . .	123
6.4 Taken from[88], the comparison of data to the prediction from simulation of the jet recoil system in $Z + \text{jets}$ events. The left-hand plot shows the $p_T$ spectrum of dilepton events in leptonic $Z$ decays, and the right-hand plot shows the $p_T$ spectrum of the vector sum of reconstructed jets in hadronic $Z$ decays. The data/MC ratio, in the top of the figure, shows that for jets with $p_T > 250$ GeV, the simulation over predicts the data. The shaded band is centred on the weighted MC prediction and indicates the associated uncertainty on the ratio. . . . .	126
6.5 95% CL expected limit on top-squark production cross section as a function of $p_T(j_1)\text{GeV}$ (i.e. in each search region). Limits for $m_{\tilde{t}} = 100, 150, 200, 250, 300$ and $350$ GeV are shown, where each line corresponds to $\Delta m_{\tilde{t}} = 10, 20, 30, 40, 60$ and $80$ GeV. . . . .	128
6.6 95% CL expected limit on bottom-squark production cross section as a function of $p_T(j_1)\text{GeV}$ (i.e. in each search region). Limits for $m_{\tilde{b}} = 100, 150, 200, 250, 300$ and $350$ GeV are shown, where each line corresponds to a different $m_{\tilde{\chi}_1^0}$ . . . . .	129

---

6.7	The temperature plot shows the acceptance of the signal point where the best expected limit is found, across the $(m_{\tilde{t}}, m_{\tilde{\chi}_1^0})$ (left) and $(m_{\tilde{b}}, m_{\tilde{\chi}_1^0})$ (right) mass planes. . . . .	130
6.8	The temperature plot shows the best expected limit across the $(m_{\tilde{t}}, m_{\tilde{\chi}_1^0})$ (left) and $(m_{\tilde{b}}, m_{\tilde{\chi}_1^0})$ (right) mass planes. . . . .	130
6.9	The temperature plot shows the search region (the $p_T(j_1)$ threshold) in which the best expected limit is found, across the $(m_{\tilde{t}}, m_{\tilde{\chi}_1^0})$ (left) and $(m_{\tilde{b}}, m_{\tilde{\chi}_1^0})$ (right) mass planes. Plots feature in Ref[5]. . . . .	130
6.10	Normalized distribution of $N_{\text{jets}}$ for $\tilde{b} \rightarrow b\tilde{\chi}_1^0$ signal points, in the events satisfying the baseline search region criteria, other than $N_{\text{jets}} < 3$ . Signal points are labelled as $(m_{\tilde{b}}, m_{\tilde{\chi}_1^0})$ GeV. . . . .	131
6.11	The topology of events satisfying the baseline search region criteria for $(m_{\tilde{b}}, m_{\tilde{\chi}_1^0}) = (225, 1), (225, 50)$ and $(225, 100)$ GeV. The origin of the first and second jet in the event is shown for events with one or two jets. Distributions are normalized to unit area. . . . .	132
6.12	95% CL observed and expected limits on the top-squark production cross section as a function of the $m_{\tilde{t}}$ for $m_{\tilde{t}} - m_{\tilde{\chi}_1^0} = 10, 20, 30, 40, 60$ and $80$ GeV. Curves taken from Ref[4]. . . . .	133
6.13	95% CL observed and expected limits on the bottom-squark production cross section as a function of $m_{\tilde{b}}$ for $m_{\tilde{b}} - m_{\tilde{\chi}_1^0} = 10$ GeV. . . . .	134
6.14	95% CL observed and expected limits on the bottom-squark production cross section as a function of the mass difference $m_{\tilde{b}} - m_{\tilde{\chi}_1^0}$ , shown for $m_{\tilde{b}} = 100, 150, 175, 200, 225$ , and $275$ GeV. Also shown are the $\pm 1, 2\sigma_{\text{exp}}$ limits. . . . .	136
6.15	Expected and observed 95% CL exclusion limits in the $(m_{\tilde{t}}, m_{\tilde{\chi}_1^0})$ mass plane for top-squark pair production, assuming 100% branching fraction to the decay $\tilde{t} \rightarrow c\tilde{\chi}_1^0$ . The $\pm 1\sigma_{\text{exp}}$ and $\pm 1\sigma_{\text{th}}$ curves are also shown. The diagonal grey lines mark the borders of the kinematic regimes surrounding the compressed region of phase space. Taken from Ref[4]. . . . .	137

- 6.16 Observed and expected limits on top-(left) and bottom-(right) squark pair production cross section as a function of the top and bottom squark mass and LSP mass. The top squark limit is the same as the above, only formatted to allow easy comparison between the two limits, which are very similar in the compressed region, as is expected. Additional sensitivity around  $m_{\tilde{b}} \approx 50$  GeV arises from dijet events which satisfy the search region criteria. These curves are those taken from Ref[5]. . . . . 137

# List of Tables

2.1	Summary of the particles of the SM of particle physics. Fermions, of spin- $\frac{1}{2}$ are shown, split into the three generations of leptons and quarks. Masses are taken from Ref[1]. . . . .	7
2.2	Summary of the gauge bosons of the SM. The force carrying bosons of spin-1 are shown, with the Higgs boson to complete the picture. Masses are taken from Ref[1]. . . . .	8
3.1	Alongside typical numbers from Run 1 of LHC operation, two of the possible luminosity performances for LHC after LS1, i.e. for running during Run 2[119]. . . . .	36
3.2	Summary of periods of running of the LHC. . . . .	36
4.1	The 95% efficiency values for various L1 jet transverse momentum thresholds, in GeV, and plateau efficiency values for the current and upgrade algorithm, for turn on curves taken in high PU data and shown in Figure 4.11.	75
5.1	Datasets used in the search, which combine to give a total integrated luminosity of $19.7 \text{ fb}^{-1}$ . . . . .	85
5.2	For illustrative purposes, event yields from different simulated samples for the SM backgrounds at each step of the event selection including the search regions. Backgrounds are obtained directly from simulation and normalized to an integrated luminosity of $19.7 \text{ fb}^{-1}$ using the cross sections shown in the table. . . . .	98

5.3	Event yields for the dimuon control regions in data and MC simulation. 50% uncertainty is assigned to each background (i.e. from $t\bar{t}$ , single top, and diboson events) and these are combined in quadrature to get the total uncertainty on the number of background events in the $Z \rightarrow \mu^+\mu^-$ sample.	99
5.4	The fraction of events that sit in the tail of the $p_T^{\text{miss},\mu}/p_T(Z)$ spectrum, which give correction factors used to predict the $Z \rightarrow \nu\bar{\nu} + \text{jets}$ background.	102
5.5	Observed yields in the dimuon control sample, background yields from non- $Z(\mu\mu)$ processes, $A$ and $\epsilon$ of control sample requirements and the corrected ratio of branching fractions in each of the search regions. . . . .	103
5.6	Summary of the contributions, <a href="#">in %</a> , to the total uncertainty on $Z \rightarrow \nu\bar{\nu}$ + jets background from the various factors used in the data-driven estimation.	104
5.7	<a href="#">The predicted <math>Z(\nu\bar{\nu}) + \text{jets}</math> event yield in each of the search regions, calculated as detailed in the text. The uncertainty contains both systematic and statistical sources.</a> . . . . .	104
5.8	Event yields for the $W \rightarrow \mu\nu$ data control sample with SM backgrounds from MC simulation. A relative uncertainty of 50% is assigned to each background (i.e. from $Z + \text{jets}$ , $t\bar{t}$ , single top, QCD and diboson events) and these are combined in quadrature to get the total uncertainty on the number of background events in the $W \rightarrow \mu\nu$ sample. . . . .	105
5.9	Estimation of the remaining $W + \text{jets}$ background from the lost electron, muon and hadronic tau contributions. . . . .	108
5.10	Summary of the fractional contributions (in %) to the total uncertainty on the $W + \text{jets}$ background from the various factors used to estimate it. . . . .	109
5.11	Summary of the estimated total remaining $W + \text{jets}$ background. . . . .	110
5.12	Event yields from MC and data for $p_T(j_1) > 250$ GeV and for different values of the $p_T$ threshold used for jet counting in the QCD rich region $\Delta\phi(p_T^{\text{miss}}, j_2) < 0.3$ . Relative uncertainty on a scale factor derived from the data is also shown. . . . .	111
5.13	QCD scale factor derived from QCD rich control region for each inclusive $p_T(j_1)$ bin with relative error. . . . .	112
5.14	Summary of the estimated total remaining QCD background. . . . .	112

5.15	Event yields from MC and data for $t\bar{t}$ background . . . . .	114
5.16	Inclusive and exclusive methods of treating $Z(\nu\bar{\nu})\gamma$ and $W\gamma$ backgrounds. Data driven estimates are calculated to be the difference between the methods, and are compared to event yields from simulation. . . . .	115
6.1	Event yields for the seven inclusive search regions detailed in Chapter 5. The SM background predictions and the data yields correspond to an integrated luminosity of $19.7 \text{ fb}^{-1}$ and the quoted uncertainties reflect the statistical and systematic contributions, summed in quadrature. . . . .	119
6.2	Signal acceptance <del>efficiency</del> , shown in %, for each step of the event se- lection. Two representative mass points are shown; $(m_{\tilde{b}}, m_{\tilde{\chi}_1^0}) = (250, 240)$ and $(150, 50) \text{ GeV}$ for $\tilde{b}\tilde{\bar{b}} \rightarrow b\bar{b}\tilde{\chi}_1^0\tilde{\chi}_1^0$ where $\mathcal{B}(\tilde{b} \rightarrow b\tilde{\chi}_1^0) = 1.0$ , and $(m_{\tilde{t}},$ $m_{\tilde{\chi}_1^0}) = (250, 240) \text{ GeV}$ and $(200, 120)$ for $\tilde{t}\tilde{\bar{t}} \rightarrow c\bar{c}\tilde{\chi}_1^0\tilde{\chi}_1^0$ , where $\mathcal{B}(\tilde{t} \rightarrow c\tilde{\chi}_1^0) = 1.0$ . Only statistical uncertainties are shown. . . . .	124
6.3	Acceptances (in %) of 2-parton and 3-parton samples for mass points $(m_{\tilde{t}}, m_{\tilde{\chi}_1^0}) = (200, 190) \text{ GeV}$ and $(200, 120) \text{ GeV}$ . The modulus of the differences in the acceptances from the two samples are listed. . . . .	125
6.4	Acceptances (in %) of signal samples for mass points $(m_{\tilde{t}}, m_{\tilde{\chi}_1^0}) = (200, 190) \text{ GeV}$ and $(200, 120) \text{ GeV}$ , for when the energy scale is increased and decreased. The modulus of the differences in the acceptances from the two samples are listed. . . . .	127

## 1 Acronyms

<b>ADD</b>	Arkani-Hamed, Dimopoulos, and Dvali
<b>ALICE</b>	A Large Ion Collider Experiment
<b>ATLAS</b>	A Toroidal LHC ApparatuS
<b>ASIC</b>	Application Specific Integrated Circuit
<b>BSM</b>	Beyond the Standard Model
<b>CERN</b>	European Organisation for Nuclear Research

<b>CKM</b>	Cabibbo-Kobayashi-Maskawa
<b>CL</b>	Confidence Level
<b>CMB</b>	Cosmic Microwave Background
<b>CMS</b>	Compact Muon Solenoid
<b>CMSSM</b>	Constrained Minimal Supersymmetric Standard Model
<b>CP</b>	Charge Parity
<b>CPT</b>	Charge Parity Time
<b>CSCs</b>	Cathode Strip Chambers
<b>CPU</b>	Computer Processing Unit
<b>DAQ</b>	Data Acquisition System
<b>DIS</b>	Deep Inelastic Scattering
<b>DESY</b>	Deutsches Elektronen-Synchrotron
<b>DM</b>	Dark Matter
<b>DT</b>	Drift Tube
<b>ECAL</b>	Electromagnetic Calorimeter
<b>EB</b>	Electromagnetic Calorimeter Barrel
<b>EE</b>	Electromagnetic Calorimeter Endcap
<b>ES</b>	Electromagnetic Calorimeter pre-Shower
<b>EWK</b>	Electroweak
<b>FCNC</b>	Flavour Changing Neutral Currents
<b>FPGA</b>	Field Programmable Gate Array
<b>FSR</b>	Final State Radiation
<b>GCT</b>	Global Calorimeter Trigger
<b>GMT</b>	Global Muon Trigger
<b>GT</b>	Global Trigger

<b>GUT</b>	Grand Unified Theory
<b>HB</b>	Hadron Barrel
<b>HCAL</b>	Hadronic Calorimeter
<b>HE</b>	Hadron Endcaps
<b>HF</b>	Hadron Forward
<b>HLT</b>	Higher Level Trigger
<b>HO</b>	Hadron Outer
<b>HPD</b>	hybrid photodetectors
<b>HPS</b>	Hadron–Plus–Strips
<b>ISR</b>	Initial State Radiation
<b>JES</b>	Jet Energy Scale
<b>JHEP</b>	Journal of High Energy Physics
<b>L1</b>	Level 1 Trigger
<b>LEP</b>	Large Electron-Positron Collider
<b>LHC</b>	Large Hadron Collider
<b>LHCb</b>	Large Hadron Collider Beauty
<b>LO</b>	Leading Order
<b>LPCC</b>	LHC Physics Centre at CERN
<b>LS1</b>	Long Shutdown 1
<b>LS2</b>	Long Shutdown 2
<b>LSP</b>	Lightest Supersymmetric Particle
<b>MC</b>	Monte Carlo
<b>MSSM</b>	Minimal Supersymmetric Standard Model
<b>NLL</b>	Next to Leading Logarithmic Order
<b>NLO</b>	Next to Leading Order

<b>NLSP</b>	Next-to-Lightest Supersymmetric Particle
<b>NNLO</b>	Next to Next Leading Order
<b>PF</b>	Particle Flow
<b>PS</b>	Proton Synchrotron
<b>PU</b>	pile-up
<b>QED</b>	Quantum Electro-Dynamics
<b>QCD</b>	Quantum Chromo-Dynamics
<b>QFT</b>	Quantum Field Theory
<b>PDFs</b>	Parton Density Functions
<b>RPCs</b>	Resistive Plate Chambers
<b>RCT</b>	Regional Calorimeter Trigger
<b>RF</b>	Radiofrequency
<b>RMT</b>	Regional Muon Trigger
<b>SLAC</b>	Stanford Linear Accelerator Center
<b>SUSY</b>	SUperSYmmetry
<b>SM</b>	Standard Model
<b>SMS</b>	Simplified Model Spectra
<b>SPS</b>	Super Proton Synchrotron
<b>TIB</b>	Tracker Inner Barrel
<b>TEC</b>	Tracker Endcaps
<b>TID</b>	Tracker Inner Disks
<b>TMT</b>	Time-Multiplexed Trigger
<b>TOB</b>	Tracker Outer Barrel
<b>VeV</b>	Vacuum Expectation Value
<b>WIMP</b>	Weakly Interacting Massive Particle

**WMAP**      Wilkinson Microwave Anisotropy Probe

## Changes

Author: anonymous

Added: 132

Deleted: 22

Replaced: 31

Author: per (Robyn Lucas)

Added: 0

Deleted: 0

Replaced: 0